THESIS OF DOCTORAL (PH.D.) DISSERTATION

Copper(II) and (η^5-Cp*)rhodium(III) complexes of some imidazole and pyridine containing ligands

Azza Ahmed Mousad Megahed Hassoon

Supervisors:

Prof. TAMÁS GAJDA

Dr. TAMÁS JAKUSCH

DOCTORAL SCHOOL OF CHEMISTRY
University of Szeged
Faculty of Science and Informatics
Department of Inorganic and Analytical Chemistry

Szeged

2023

TABLE OF CONTENTS

LIST OF ABBREVIATIONS

Materials

MeOH – methanol

DMF – dimethylformamide

TFA – trifluoroacetic acid

TIS – triisopropylsilane

DIC – N,N′ diisopropylcarbodiimide

HEPES – 4-(2-hydroxyethyl)-1-piperazineethanesulfonic acid

MeCN – acetonitrile

Fmoc – 9-fluorenylmethyloxycarbonyl

DTT – dithiothreitol

HOBt – N-hydroxybenzotriazole

Methods

UV-Vis – Ultraviolet-Visible

ESI-MS – Electrospray Ionization Mass Spectrometry

SPPS – Solid Phase Peptide Synthesis

EPR – Electron Paramagnetic Resonance

CD – Circular Dichroism

NMR – Nuclear Magnetic Resonance

HPLC – High Performance Liquid Chromatography

1. INTRODUCTION

Metal ions, particularly transition metals, are well known to play critical roles as protein cofactors in many biological processes, such storage and transport, intracellular signaling processes, catalysis including energy production, or defence against oxidative stress. Metalloproteins, which require one or more metal ions to carry out their functions account for nearly one-third of all known proteins. Metal ion disorder, on the other hand, has been linked to a number of human pathologies. Disturbed copper metabolism, for example, is directly related to Wilson's and Menkes' diseases, but copper homeostasis is also unbalanced in cancer and some similarly widespread neurological disorders such as Alzheimer's and prion diseases.

1.1 Copper ions and the Alzheimer's Disease (AD)

Homeostatic concentrations of essential heavy metals (e.g., copper and zinc) are tightly controlled by intricate buffering systems in living cells. The main Cu-binding proteins in serum are human serum albumin (contains Cu(II)), transcuprein (Cu(II)), and ceruloplasmin (Cu(II)/Cu(I)) [1]. Human high affinity copper uptake protein 1, hCTR1 is in control of the Cu(I) ion transfer across the cell membrane [2]. Several Cu(I) transporters exist within the cell, including antioxidant protein 1 (ATOX1) which delivers Cu(I) through copper-transporting P-type ATPases (ATP7a/b) to different cuproenzymes, -Cu(I) chaperons for cytochrome c oxidase (Cox17), and for Cu,Zn-superoxide dismutase (CCS), as shown in Figure 1.1 [3].

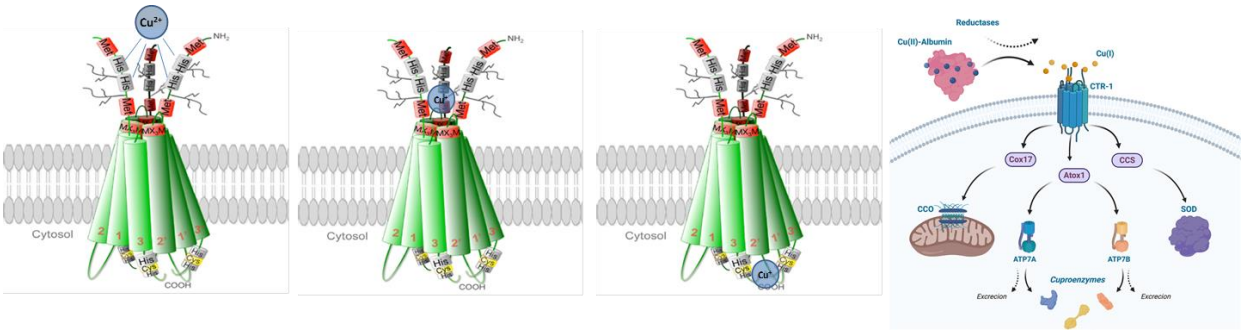

Figure 1.1 Schematic Cu(I) transfer to the cell by hCTR1 protein and Cu(I) distribution by different metallochaperons.[3]

Although, copper is an essential element for any living organisms, primarily acting as a redox enzyme co-factor, the excess of loosely (non-protein) bound Cu can be toxic via different mechanisms, e.g. by production of ROS (Reactive Oxygen Species). Cu dyshomeostasis is

detected in a variety of pathological states. Elevated levels of the kinetically labile Cu(II) pool in serum and urine, for example, have been postulated as diagnostic markers for Wilson's and Alzheimer's disease as a result of ATP7B Cu membrane transporter dysfunction. Alzheimer's disease (AD) is a neurodegenerative disorder and the most common type of dementia. Its main hallmarks include cognitive decline, memory loss, and behaviorial problems. Alzheimer's disease (AD) affects nearly 50 millions of people worldwide, and there is an urgent need for an effective treatment. Amyloid-β (Aβ) peptides are well-known for their potential pathogenic role in the onset of Alzheimer's disease (AD), which is largely associated by the aggregation of these peptides to form oligomers, fibrils, and plaques. The process of amyloid plaque formation and its impact in the pathology of Alzheimer's disease are contentious issues. The deposition of aggregated amyloid-β (Aβ) peptides in senile plaques in brain tissues results in the accumulation of Cu, its concentration ([c_{Cu}] ~390 μM) is ca. five-fold higher than that of in normal age-matched control patients ([c_{Cu}] ~79 μM) [4,5] as shown in Figure 1.2.

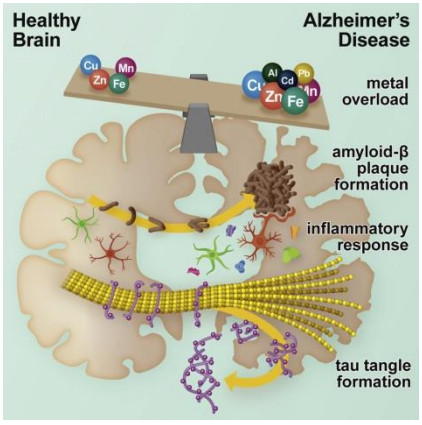

Figure 1.2 Copper accumulation in plaques.[5]

In turn, copper accumulation results in high levels of oxidative stress, abnormal metal homeostasis and impaired mitochondrial functions, all are characteristic for Alzheimer's disease (AD). The amyloid plaques contain Aβ peptides with different lengths, ranging from 39 to 42 amino acids. The most frequent Aβ peptides are $Aβ_{1–40}$ and $Aβ_{1–42}$, with the latter being the most toxic and exhibiting the greatest ability to aggregate. The most important binding sites for copper(II) in Aβ peptides (D1, H6, H13, H14) are found in residues 1–16, therefore it is a suitable model of higher amyloids to investigate their coordination and redox properties with Cu(II) in brain [6]. Stefaniak and Bal [7] recently highlighted the significance of the highly abundant truncated Aβ peptides $Aβ_{4–42}$ [8], which has ATCUN-like binding site.

To date there is no effective cure for Alzheimer's disease (AD), the only available treatments just alleviating the initial pathological symptoms. One potential cure for Alzheimer's disease is to target copper(II) ions to inhibit both aggregation and oxidative stress [9]. However, a general chelation therapy which may aid in the elimination of Cu ion would be ineffective here, clearly a metallochaperon-like function, redistribution is required. For this purpose, numerous ligand families, such as amino-quinoline derivatives, peptide-, aminophenol and aminopyridine-based ligands, have been evaluated in the last two decades [9,10]. Up to now, clear "target" of this redistribution has not been recognized, but redirecting the extracted copper back into the cells seems to be a suitable solution. Considering this pathway, it is possible to predict the conditions that an ideal artificial copper chaperone must meet. To cross the blood-brain barrier, the ligand must be neutral at pH 7.4 [9]. It should be specific for Cu(II), even in the presence of excess Zn(II). Its affinity for Cu(II) should be higher than that of Amyloid β ($\log\beta_{cond} \cong 10–10.3$) [11,12], but lower than that of hCTR1 ($\log\beta_{cond} \cong 13$) [12], which is a copper transporter protein, helping copper to enter into the cell.

1.2 Coordinating properties of peptides containing histidyl residues

The interaction of metal ions with peptides is one of the main research areas of bioinorganic chemistry. This is due to the variety of donor groups in peptide backbone and in the side chains, which results in versatile metal binding properties, together with a great variety of binding affinity and coordination geometry [13]. In this way, metal-peptide complexes are able to mimic the metal ion environment present in most of the relevant metalloproteins [14,15].

Peptides even without coordinating side chains are able to form highly stable complexes with some metal ions (e.g. Cu(II), Ni(II)) by the coordination of their terminal amino and subsequent deprotonated amide nitrogen atoms [16]. However, from bioinorganic (metalloprotein mimicking) point of view, metal complexes with the coordination of (mainly) side chain donor groups are more interesting, since the main donor atoms in the active centres of metalloproteines are of imidazole-N of His, thiolate-S of Cys, and carboxylate-O of Asp and Glu [16]. Among them, the imidazole ring of histidine is probably the most frequent metal binding site. Its effects on the metal binding properties (e.g. structure and thermodynamic stability) are dependent on many factors [16]: on the nature of metal ion, on the number and position of histidine unit(s) in the peptide sequence, and on the presence (or absence) of other potentially

coordinating groups (such as the free amino-terminus, carboxylate (Asp, Glu) or thiolate groups (Cys)).

Peptides with non-protected N-terminal histidine (His-X-Y…. sequences) are able to form the thermodynamically stable 6-membered chelate $\{NH_2,N_{im}\}$, known as histamine-like coordination (Fig.1.3, structure 1). In presence of ligand excess, the bis-complex having $\{2NH_2,2N_{im}\}$ coordination dominates in the solution in a wide pH-range (Fig. 1.3, structure 2). In case of copper(II) the high stability of this bis-complexes suppresses even the copper(II) promoted amide deprotonations [17-19].

Histidine in the second position of the sequence (X-His-Y-Z...) promotes the formation of an amide-bound $\{NH_2,N_{am}^-,N_{im}\}$ coordinated species (Fig. 1.3 structure 3), but prevents the deprotonation of the subsequent amide nitrogens. The metal promoted deprotonation of the N-terminal amide nitrogen occurs at very low pH (~ pH 3 in case of copper(II)), and thus the tridentate (NH_2,N_{am}^-,N_{im}) coordinated species predominates in a wide pH-range [19,20]. More importantly, not only copper(II), but nickel(II), zinc(II) and cobalt(II) are also able to promote the deprotonation of the amide nitrogen of Gly-His and Gly-His-Gly [20,21]. Therefore, these peptides have outstanding metal binding abilities.

Histidine in the third position of the peptide sequence (X-Y-His-Z..) results in strong metal binding ability, too, with high biological relevance. These peptides provide an N-terminal $\{NH_2,N^-,N^-,N_{im}\}$ metal-binding site within a (6,5,5)-membered fused chelate rings (Fig. 1.3, structure (4)), which is also known as the Amino Terminal Copper and Nickel (ATCUN) binding site [22,23]. The $\{NH_2,N^-,N^-,N_{im}\}$ coordination mode is dominant for copper(II) in a wide pH-range around the physiological pH, therefore it has important role in copper(II) trafficking. This binding site is present for example in human serum albumin (Asp-Ala-His-) [24] and endostatine (His-Gly-His-) [25].

Interchain histidines, even in the absence of other coordinating group, may have important role in metal binding. Although, less efficiently as N-terminal amino group, interchain imidazole ring may also serve as anchor for amide coordination, and in this way $\{2N^-,N_{im}\}$ or $\{3N^-,N_{im}\}$ coordinated copper(II) complexes are formed [16].

The presence of several histidine residues in close proximity further increases the metal binding ability. One of the simpliest examples is the HVH peptide, which combines the metal-binding properties of HXY and XYH peptides [26,27]. In the presence of ligand excess bis-

histamine like coordination dominates between pH 4-7, according to the HXY peptides. On the other hand, in equimolar solutions the C-terminal histidine stabilizes the ML species by its additional imidazole binding ({NH_2,2N_{im}}-type coordination), and above pH 6 the ATCUN-like {NH_2,N^-,N^-,N_{im}} coordination is dominant. Two histidine units within the chain provide {N_{im},N^-,N_{im}} or {N_{im},N^-,N^-,N_{im}} (Fig. 1.3, structure (5)) coordination for copper(II) in the physiological pH-range, when zero or one amino acids separate the histidines, respectively [28].

Further increasing the internal histidine umits results in increasing thermodynamic stability of imidazole coordinated complexes for all metal ions, and the {3N_{im}}- or {4N_{im}}-type coordination may become dominant even in the physiological pH-range. In case of copper(II) the stability constants of {2N_{im}}, {3N_{im}} and {4N_{im}} coordinated complexes are ~ 5.5, 7.5, and 9.0 log units [29], respectively, which proves the high metal binding affinity of multi-histidine peptides. Consequently, the {xN_{im}} coordination is frequently observed for large natural multihistidine peptide fragments, including prions or amyloid–β peptides [28].

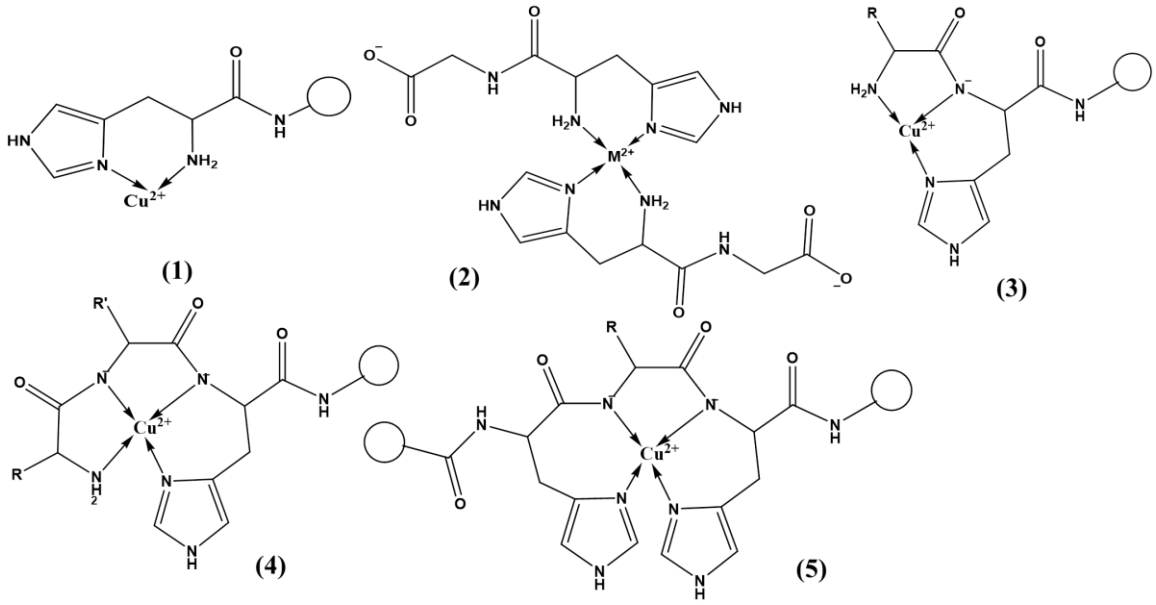

Figure 1.3 Schematic structure of copper(II) complexes ormed in neutral pH in presence of (**1 and 2**) terminal His, (**3**) NH_2-X-His, (**4**) NH_2-X-X-His and (**5**) His-X-His type sequences.

1.2.1 Lytic polysaccharide monooxygenases (LPMOs)

Environmental threats, future energy and chemical shortages necessitate the development of sustainable processes for converting renewable sources into useful chemical compounds. First-generation biofuels derived from starch or sugar are well-established technologies towards

that goal, but their reliance on human food sources (mainly maize) necessitates substitution [30]. The degradation of lignocellulosic biomass is being studied all over the world as an inedible feedstock for producing renewable liquid biofuels due to its low cost, abundance and renewability, and has been proposed as a justifiable solution to produce fuels and other useful chemicals.

Lignocellulose is composed of three polymers (Figure 1.4): lignin (15-30%), hemicellulose (17-32%) and cellulose (38-50%) [31]. Cellulose is a polysaccharide composed of a linear chain of hundreds to thousands of D-glucose units linked by β-1,4 bonds. Lignocellulose (and chitin) is (are) the most abundant biopolymer(s) in Earth, and the agro-industrial sector alone generates massive amounts of cellulosic waste. Despite their enormous potential as a biofuel source, their remarkable recalcitrance to depolymerization has so far hampered their economic use as a feedstock for biofuel production [32]. The recalcitrance of lignocellulose originated mainly from three factors: (i) the glycosidic bond is intrinsically resistant to hydrolytic attack; (ii) these polysaccharides are insoluble in common solvents due to extensive intra-chain hydrogen bonding; (iii) lignocellulose is embedded in a highly complex composite structure formed by lignin, which even more increases its resistant to degradation. These problems amplify each other, making lignocellulose degradation a major biotechnological challenge [30].

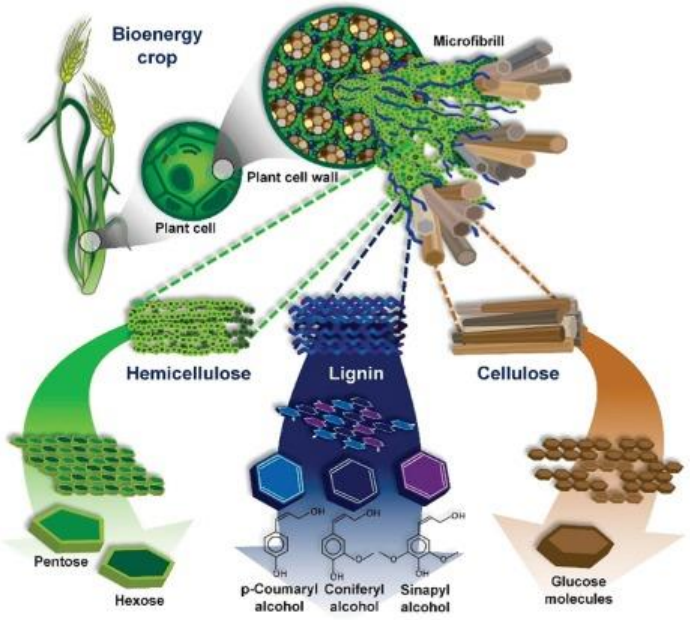

Figure 1.4 Schematic structure of lignocellulose. [31]

To eliminate lignin and allow the action of cellulases on hemicellulose and cellulose polysaccharides, current industrial procedures use high temperatures, high pressures, and strong acids or bases [33]. This pretreatment has long been recognized as the most costly (and polluting) step in the conversion process. On the other hand, plant- or chitin-degrading microorganisms have developed complex arsenals of chemical and enzymatic tools for the degradation of lignocellulose. The recently discovered lytic polysaccharide monooxygenases (Figure 1.5) [34] are among the most important enzymatic tools that play a major role in biomass conversion by oxidative cleavage of glycosidic C-H bonds and, thus, for structural disruption of biopolymers such as chitin and lignocellulose [35]. Therefore, LPMO enzymes opened the door for cellulosic-bioethanol biorefineries that employ commercially and environmentally viable enzyme cocktails. The success of these biorefineries is dependent on the efficiency of the enzymatic saccharification step, which converts lignocellulosic material into soluble sugars. Consequently, the recent inclusion of LPMOs into these enzyme cocktails may present a major breakthrough.

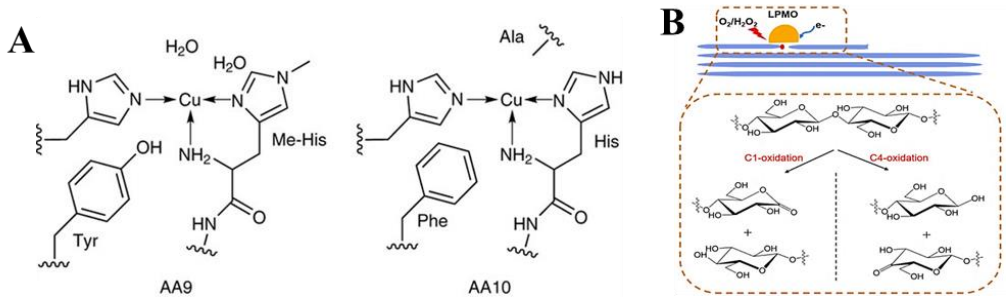

Figure 1.5 Schematic representations of the copper active sites observed in AA9 and AA10 structures (A) [34], Schematic representation of the LPMOs reaction (right) [35].

In copper(II) containing lytic polysaccharide monooxygenases (LPMOs), alternatively called auxiliary activity (AA) family of copper-dependent enzymes, the metal ion is ccordinated by two strictly conserved histidine residues, with one binding bidentate through the N-terminal amine (Fig. 1.5), in a structural motif known as the “histidine brace”. In the reduced form of LPMOs the metal ion has a 3N-coordinated T-shaped geometry, while some additional oxygen donors are coordinated to copper(II) in the oxidized form.

In most LPMO enzymes, a weakly bound (if at all) non-deprotonated tyrosine OH occupies an axial position of copper(II) with Cu−O(Tyr) distances between 2.5 to 3.0 Å. Despite the fact that this Tyr residue is part of a hydrogen-bonding network near the active site, and the

Cu−O(Tyr) distances were reported to shorten (from 2.7 to 2.5 Å) on substrate binding [36], the role of this conserved Tyr-OH is still ambiguous, especially considering the fact that the chitin-active bacterial LPMO family has conserved phenylalanine near the active site, instead of tyrosine [37].

In contrast to typical cellulases, which are hydrolytic enzymes, LPMOs cleave the β-1,4-glycosidic bonds via the oxidation of the C1- or C4 atom in the presence of the co-substrate oxidative agent (Figure 1.5), making the lignocellulose amenable to hydrolases, apparently without the necessity of decrystallization [35,38]. By doing this, LPMOs accelerate the activity of cellulases by up to two orders of magnitude [39], significantly reducing the financial and environmental costs associated with the use of recalcitrant polysaccharides as a feedstock. As a result, research on LPMOs has advanced rapidly, but many questions about their (bio)chemistry, function, mechanism, and application in biorefineries remain. In order to get the maximal benefit of these enzymes, an improved understanding of the chemistry taking place at the active site of these powerful redox proteins is essential. Therefore, the ultimate goal is to understand the mechanism of this uncommon, copper-based chemistry, and perhaps to develop novel catalysts capable of conducting similar reactions and to provide small molecule alternatives to LPMOs. The molecular basis of the functioning of these enzymes is not only related to second-generation biorefineries, but will most likely inspire new catalyst for oxy-functionalization of inert C-H bonds, and a complete understanding of this process is of utmost interest also for fundamental biology.

LPMOs are able to function only by using either O_2 or H_2O_2 as oxidant depending on the conditions [40-42] although dioxygen seems to be their natural co-substrate [37, 41-42]. The possibility of H_2O_2 as the natural co-substrate was raised by Bissaro et al. [43]. Their experiments with labeled hydrogen peroxide ($H_2{}^{18}O_2$) in the presence of a 10-fold molar excess of O_2 revealed that the oxygen atom introduced into the polysaccharide chain originated from H_2O_2 rather than O_2. The incorporation of ^{18}O from $H_2{}^{18}O_2$ into the final product was demonstrated for both AA9s and AA10s as well as for both cellulose and chitin substrates.

Both experimental [44] and computational [41-42,44] studies indicated that in LPMOs a highly reactive Cu(II)-oxyl (Cu(II)-O$^{\bullet}$) species abstracts H-atom from the substrate. QM/MM calculations showed that in case of O_2 co-substrate, a Cu(II)-OO$^{\bullet}$ complex is formed

upon reaction of Cu(I) with O_2 and the protonation of this complex with a subsequent two-electron transfer results (through a Cu(I)···H_2O_2 species), in O−O bond cleavage, and the formation of an Cu(II)-$O^{\bullet}$ active species possibly protonated, that can react with substrate. In the case of H_2O_2 co-substrate, the reaction with LPMO-Cu(I) results in a homolytic O−O cleavage mechanism, and the subsequent formation of the Cu(II)-$O^{\bullet}$ active species. Comparative calculations revealed that the reaction is more favorable with H_2O_2 as co-substrate than with O_2. Overall, most studies indicate that the reactive oxygen species is Cu(II)-$O^{\bullet}$, which can be generated by both O_2- and H_2O_2–driven mechanisms [45,46]. The two mechanisms are interconnected by a common Cu(I)···H_2O_2 intermediate. However, it is important to note, that although the H_2O_2–driven mechanism results in higher rate of substrate oxidation, it results considerably faster protein degradation, too [47].

To date, only five model complexes of lytic polysaccharide monooxygenases (LPMOs) that mimic the 'histidine brace' structural motif have been reported in the literature [48-52], and non of them are peptide derivative. The following concepts were used to design the ligands: (1) the ligand should be a tridentate ligand with two imidazole groups at the *trans* positions to form a **T**-shaped 3N geometry around the bound copper ion; (2) a large twist angle between the two imidazole rings should be maintained as in the enzyme active sites (~ 70°); (3) the ligand should contain imidazole group(s) with acidic N-H proton(s) as the natural enzymes do [51] Nevertheless, pyridine, N-methylimidazole, or N-methylbenzimidazole were also used in some cases instead of imidazole. In the presence of H_2O_2/Et_3N, these models were able to catalyze the oxidative cleavage of the model substrate *p*-nitrophenyl-*β*-D-glucopyranoside or cellobiose.

In 2017, $[(L^{AM})Cu(CH_3CN)]^{2+}$ and $[(L^{IM})Cu(OH_2)]^{2+}$ complexes were prepared and investigated by *Alda et al*. The two ligands (L^{AM} and L^{IM}) provide a tridentate 3N coordination for copper(II) ion, including an N-methylated imidazole and a pyridine rings (Figure 1.6). These complexes have similar structural and spectroscopic properties to the native LPMO enzymes. The LPMO-like activity of the complexes was studied in the presence of hydrogen peroxide (H_2O_2), and *p*-nitrophenyl-*β*-D-glucopyranoside was used as a model substrate. The authors reported particularly stable copper(II)-hydroperoxo intermediates under the conditions used, and applied the Michaelis-Menten kinetics to interpret their kinetic data [48].

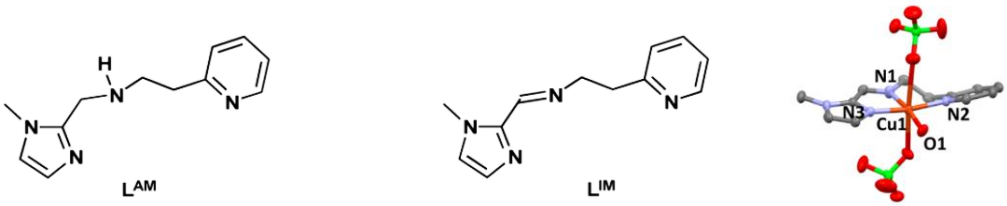

Figure 1.6 Structure of copper(II) complexes and ligands used in ref. [48]

in 2019, Neira *et al.* [49] prepared two copper complexes ([(2BB)Cu^{I}]Otf and [(2BB)-$Cu^{II}(H_2O)_2$](Otf)$_2$) of the tridentate ligand bis[(1-methyl-2-benzimidazolyl)ethyl]-amine (Figure 1.7) as a simple structural model of LPMO active site. This ligand is a good σ-donors and reasonable π-acceptors toward copper ions, and it also provides some steric protection. As a result, the reaction of cuprous complexes and O_2 promotes the formation of free superoxide anions, which are presumably released as a result of solvent displacement from the putative Cu^{II}-superoxo species. The catalytic study indicated that both copper complexes in presence H_2O_2/Et_3N are able to oxidize cellobiose in acetonitrile and in aqueous phosphate buffer solutions, and the final products of the oxidative degradation were sodium gluconate and glucose aldehyde.

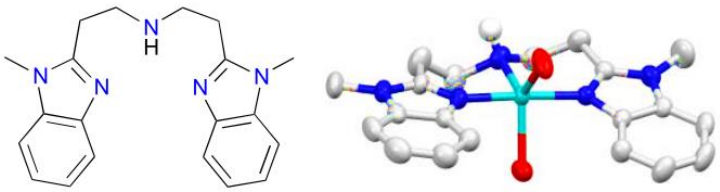

Figure 1.7 Structure of the ligand and its copper(II) complex used in ref. [49]

Sethuraman et al. synthesized and characterized three copper(II) complexes with diazepane backbones (**A**, **B**, and **C**, Figure 1.8) as functional mimics of LPMOs. The ligands have some structural similarities to the 'histidine brace' motif, and their copper(II) complexes exhibit distorted square pyramidal geometry similarly to native LPMOs. These complexes were able to catalyze oxidative cleavage of model substrate *p*-nitrophenyl-*β*-D-glucopyranoside into *p*-nitrophenol and D-allose with a maximum yield up to 78.4% and turnover number (TON) 300. The kinetic study revealed a rate of 3.19 – 5.26×10^{-3} s^{-1}. The reaction was proposed to proceed via Cu^{II}-OOH intermediate. The rate of its formation, which

is accompanied by a ligand to metal charge transfer band at at 375 nm, were obtained between 1.61–9.06×10^{-3} s^{-1} [50].

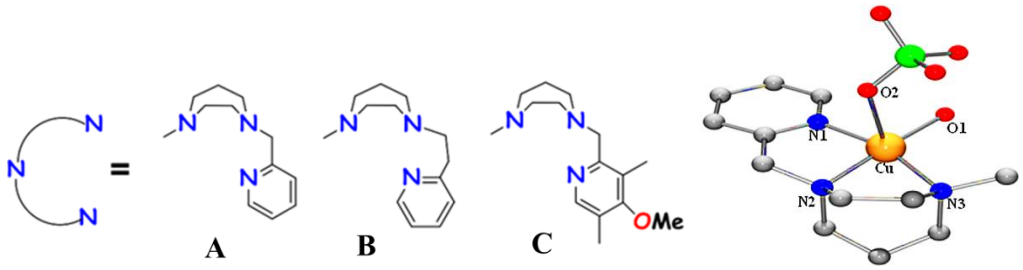

Figure 1.8 Structure of copper(II) complexes and ligands used in ref. [50]

In order to develop an even better functional model of LPMOs, Arisa *at al*. in 2020 [51] prepared the copper(II) complex of (*N*-(2-(1H-imidazol-4-yl)-benzyl)histamine) (LH_3) $Cu^{II}(LH_3)(tfa)_2$ (Figure 1.9), which mimics the 'histidine brace' motif. It is worth mentioning, that this complex shows several similarities to the LPMO enzymes, for example the twist angle between the two imidazole rings is 75° which is very close to the average value of the reported copper(II) sites in LPMOs (72°), spectral properties (λ_{max}, ε, $g_{//}$ and $g_{\perp}$ values), as well as the redox potential of Cu(II)/Cu(I) redox couple (323 mV). The kinetic study of PNPG oxidation in the presence of H_2O_2 as co-substrate showed linear dependence of the observed reaction rate on the concentration of both substrate (PNPG) and the oxidant (H_2O_2). These results indicate that the turn over limiting step of the catalytic reaction is the substrate oxidation step by a reactive species generated by the reaction of the copper (II) complex and H_2O_2 [51].

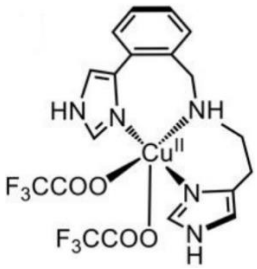

Figure 1.9 Structure of copper(II) complex used in ref. [51]

In 2021, some bis(benzimidazole)amine-based copper complexes (Figure 1.10) with coordination environment and redox potentials similar to those of LPMO enzymes are

reported as efficient catalysts for cellobiose degradation under mild conditions in the presence of H_2O_2/NEt_3 [52]. A Cu^{II}-OOH complex was proposed as an active species, which converted cellobiose up to 67 percent yield.

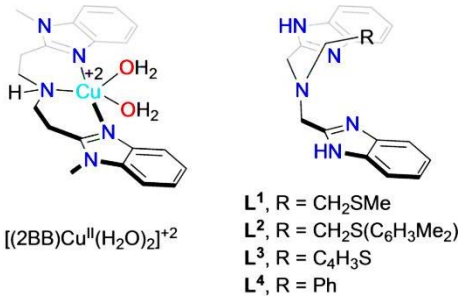

Figure 1.10 Structure of copper(II) complexes and ligands used in ref. [52]

1.2 Half-sandwich Ru(II) and Rh(III) complexes

One of the world's most common causes of death is cancer. During the last few decades, medicinal chemistry has made significant progress towards the development of new chemotherapeutic anticancer agents. Accordingly, considerable effort has been devoted to the development of transition-metal-based compounds, too [53,54]. Cisplatin (cis-$Pt(NH_3)_2Cl_2$), the benchmark drug based on platinum, and its analogues carboplatin and oxaliplatin (Figure 1.11), are by far the most widely used metallodrugs, accounting for 50-70 percent of chemotherapeutic drugs used for the treatment of e.g. ovarian, testicular, lung, and bladder cancers. Although platinum-based antitumor compounds play fundamental roles in the therapy of various solid tumors, increasing drug resistance and the appearance of unwanted side effects of currently available therapies have necessitated the development of new metal-based drugs with fewer side effects, with different mechanisms of action [55,56]. After platinum compounds, titanocene dichloride and budotitane (Figure 1.11) were the first anticancer metallodrugs introduced to clinical trials [57]. Later, ruthenium is recognized as a highly appealing alternative to platinum because many Ru compounds are less toxic and several complexes are highly selective for different cancer cells [58]. Among them, two Ru(III) complexes deserve to be highlighted, NAMI-A and KP1019 (Figure 1.12), which have demonstrated remarkable activities in recently completed phase I clinical trials. Probably, both agents will undergo Phase II clinical trials in the near future [59-62]. Ru(III) cation has several favorable chemical properties that make it particularly useful for rational anticancer drug design. These characteristics include favorable

(slow) ligand-exchange kinetics, the possibility of the formation of +2 and +4 oxidation states in biological environments, and the ability to mimic iron(III) by binding to plasma proteins [58, 63-66]. Besides the above, half-sandwich ruthenium(II) compounds (Figure 1.12) have also attracted great attention, due their promising anticancer properties [67]. In particular, the RAPTA family developed by Dyson and co-workers [68], the RM family developed by the Sadler group [69], and the complexes DW-1 and DW-2, two strong inhibitors of protein kinases developed by Meggers and co-workers [70], have generated considerable interest (Figure 1.12).

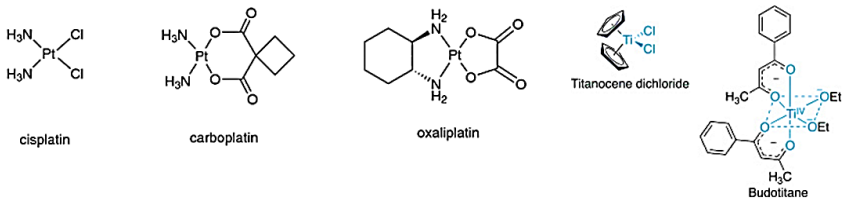

Figure 1.11 Chemical structures of some Pt- and Ti-based anticancer compounds.

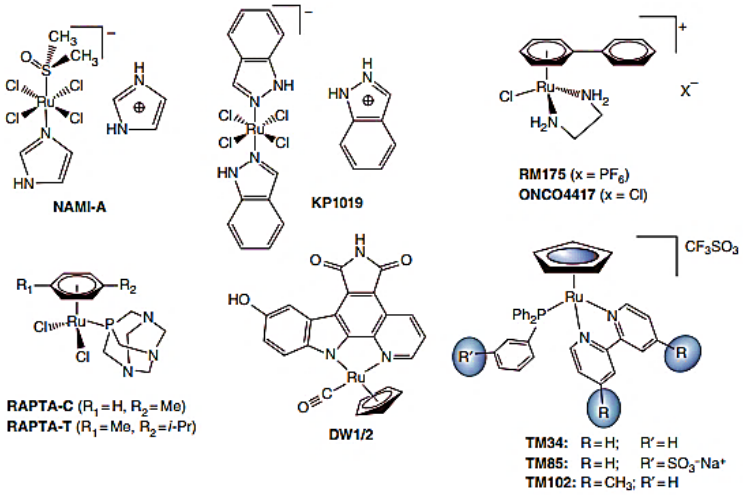

Figure 1.12 Schematic structures of some ruthenium-based compounds with promising anticancer activity

Following the successes of the half-sandwich Ru(II) complexes in the last two decades, analogous complexes of other platinum-group elements ((Rh(III), Os(II), Ir(III)) have also become the focus of anticancer research [71-74]. The results of these studies indicate, that some (η^5-Cp*)Rh(III) and (η^5-Cp*)Ir(III) complexes (Cp* = pentamethylcyclopentadienyl anion) possess important cytotoxicity against several cancer cells [75-81], and in some cases they have higher activity than that of related Ru(II)−arene, or even platinum-based complexes [82,83].

In pseudo-octahedral half-sandwich (also called piano-stool) complexes of d^6 low-spin metal ions, the η^6 or η^5 aromatic ligands occupy three facial coordination sites, leaving the three other facial coordination positions free for the external ligands. The coordination of an arene ring has fundamental effects on the properties of the metal ions: (i) it stabilizes the lower (e.g. Ru(II)) oxidation state, (ii) its strong trans effect considerably increases the rate constant of water exchange (e.g. for (η^5-Cp*)Rh(III) it is $k = 1.6\times10^5$ s^{-1}) as compared to Rh(III) ($k = 2.2\times10^{-9}$ s^{-1}) [84], (iii) the dissociation of arenyl rings from the half-sandwich cation is rather difficult, and the strength of C-M bond can be further increase by the electron-pushing effect of the methyl groups in Cp*, (iv) its lipophilicity facilitates the penetration into the cells.

As a consequence, for Rh(III) mostly (η^5-Cp*)Rh(III) cation coordinated by bidentate (less frequently monodentate) ligands are studied as potential metallodrugs, in which the coordination sphere is saturated by chloride ion(s), known as good leaving-group. The first reported half-sandwich Rh(III) complex with promising anticancer activity was the (η^5-Cp*)Rh(III) analogue of RAPTA-C (Figure 1.12). The complex [(η^5-Cp*)Rh(pta)Cl_2] (pta=1,3,5-triaza-7-phosphaadamantane) exceeded the potency of RAPTA-C and its Os analogue [85], indicating that (η^5-Cp*)Rh(III) cation is also a good platform to develop anticancer metallodrugs.

For example, the (η^5-Cp*)Rh(III) complexes of some benzyhydrazone ligands (e.g. bzhyOH, Figure 1.12) have high cytotoxicity, and more importantly high selectivity towards HCT116 cancer cells [86]. The solution behaviours and anticancer activity of (η^5-Cp*)Rh(III) complexes of several 8-hydroxyquinoline have been studied recently by Enyedy *et al*. [87,88]. The [(η^5-Cp*)RhCl(pphq)] complex (Hpphq = 7-(1-piperidinyl-methyl)-8-hydroxyquinoline, Figure 1.13) showed higher activity against MES-SA human uterine sarcoma and its multidrug-resistant variant than cisplatin [87]. The cytotoxicity and antiproliferative effect of [(η^5-Cp*)RhCl(hqCl-pro)] complex (hqCl-pro = (S)-5-chloro-7-((proline-1-yl)methyl)8-hydroxyquinoline, Fig. 1.13) were more effective against drug resistant Colo 320 adenocarcinoma human cells compared to the drug sensitive Colo 205 cells [88]. The {N,O+P} coordinated [(η^5-Cp*)Rh(pta)(hq)] complex (Figure 1.13) shows somewhat higher activity than cisplatine and considerably higher activity than RAPTA-C against several studied cancer cell lines [89]. Most of the above mentioned and other (η^5-Cp*)Rh(III) complexes of bidentate ligands with (O,O), (O,S), (O,N), (N,N) or (N,S) binding mode possessing notable anticancer activity have recently been reviewed [90].

In addition, its optimal ligand exchange kinetics make (η^5-Cp*)Rh(III) cation suitable drug delivery system for cytotoxins that are too toxic to be delivered directly, or have poor pharmacokinetics, such as curcumin [91]. Besides, some (η^5-Cp*)Rh(III) complexes have promising activity in various other diseases, e.g. they possess important antimalarial [92], antimicrobial [93, 94] and antivirucidal activity, even against SARS-CoV-2 [95]. Unfortunately, the mechanism of action of these half-sandwich Rh(III) (and Ru(II)) complexes is largely unknown.

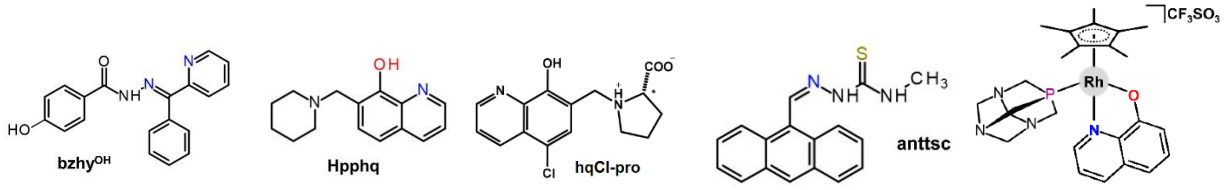

Figure 1.13 Schematic structure of some ligands of which (η^5-Cp*)Rh(III) complexes possess important anticancer activity and the structure of [(η^5-Cp*)Rh(pta)(hq)] complex (see text).

All above mentioned complexes contain one mono- and one bidentate ligands, of which the monodentate is more labile. This allows for the formation of mixed-ligand complex(es) by replacing the monodentate ligand, but this can also be a point of attack to replace the bidentate ligand as well. In this way, even DNA targeting compounds may interact with peptides/proteins during drug-transport, e.g. may undergo ligand substitution reactions especially in the blood plasma, before they reach the target site. Consequently, the reactivity of potential metallodrugs towards biomolecules present in different biological compartments is a crucial parameter for their biodistribution, biotransformation and pharmacokinetic properties. Accordingly, increasing number of studies are available on the protein binding of (η^5-Cp*)Rh(III) ion and its complexes [96,97]. In human blood, serum albumin and transferrin are suggested as the main macromolecular binders of half-sandwich Ru(II) and Rh(III) complexes [98,99]. Beside macromolecules, low molecular mass (LMM) endogenous ligands present in different biological fluids, cells, tissues or organs may also strongly interact with potential metallodrugs, altering their biological/physiological fate. The most obvious imidazole-containing LMM component is histidine itself, its concentration of human serum is ~ 77μM, and is known as one of the major metal binding LMM constituent [100], but several histidine-containing biogenic peptides are known [101] which may also interact with (η^5-Cp*)Rh(III) complexes. There are several

experimental indications of such interactions. For example, the catalytic efficiency of $[(Cp^*)Rh(bpy)(H_2O)]^{2+}$ complex (bpy = bipyridyl), a widely used catalyst in biocatalytic processes to regenerate $NAD^+/NADP^+$ cofactors, is significantly reduced upon interaction with amino acids or peptides [102], mostly in presence of His Cys and Met. Recently, the interaction of several (η^5-Cp*)Rh(III) complexes with human serum albumin (HSA) has been studied in solution [103,104], pointing out the importance of imidazole coordination to these complexes by HSA. Severin's group has developed an indicator-displacement assay (IDA) for the sequence-selective detection of His/Met- containing peptides [105] based on their different binding affinity to (η^5-Cp*)Rh(III) complexes of metal-binding dyes such as azophloxine. Interestingly, the aromatic side chain of tyrosine-containing G-protein-coupled receptor (GPCR) peptides namely, [Tyr^1]-leu-enkephalin, [Tyr^4]-neurotensin(8-13), and [Tyr^3]-octreotide, each of which has a different position for the tyrosine residue can also interact with $[Cp^*Rh(H_2O)_3](OTf)_2$, in water at pH 5−6 [106]. However, to our knowledge, no complete solution themodynamic study on the interaction of (η^5-Cp*)Rh(III) cation with amino acids or peptides are available in the literature. The single related publication deals with (arene)Ru(II)/Rh(III) complexes of peptido-hydroxamic acids [107].

2. Aims

The overall goal of my PhD thesis was to characterize (partly design and synthesize) some amide-containing ligands and to study their metal complexes in order to answer some practical problems. The thesis covers three, at first glance, different topics (see below). However, these areas are connected by the studied metal ions (Cu(II) and (η^5-Cp*)Rh(III)), the amide-containing ligands, and the similar coordination chemical properties of imidazole and pyridine rings.

(i) One potential cure for Alzheimer's disease is to target copper(II) ions to inhibit both aggregation and oxidative stress. However, a general chelation therapy which may aid in the elimination of Cu ion would be ineffective here, clearly a metallochaperon-like function, binding and redistribution is required. Therefore, the goal of my first sub-project was to design artificial metallophores for Alzheimer's disease (AD) therapy, which are specific for Cu(II) even in the presence of excess Zn(II), their copper(II) complexes do not produce ROS, are able to remove Cu(II) ion from its Aβ peptide complexes, and would be able to hand over copper(II) to the membrane transporter hCTR1. To this end, we synthetized and studied the ligands (pyridin-2-ylmethyl)picolinamide (PMPA) and N-(pyridin-2-ylmethyl)-2-((pyridin-2-ylmethyl)amino)acetamide (PDMGA) (see Chart 4.1).

(ii) The catalytic copper in LPMOs is surrounded by a surprisingly simple active center, and is bound to the so-called 'His-brace' motif. It is widely assumed that this motif plays an important role in the efficiency of LPMOs, although their mechanism of action is still not well understood. Beside biochemical investigantions, the study of small molecular models of LPMOs may also help to uncover the catalytic mechanism. Models based on His-peptides as the closest mimics of LPMO active centers may especially useful to reveal some fundamental aspects of the LPMOs' catalytic mechanism that have remained unexplored by synthetic models to date. Therefore, in my PhD work I planned to investigate the thermodynamic stability, structure, and catalytic reactivity of Cu(II) complexes of two histidine-containing peptides, HPH-NH_2 and HPHPY-NH_2 (see Chart 4.3). Proline subunits are used to

separate the histidine and tyrosine moieties, in order to prevent copper(II)-induced amide deprotonation and providing a relatively rigid structure for the ligands.

(iii) Recently, half-sandwich Rh(III) complexes have emerged as intriguing potential anticancer, antimicrobial and antivirucidal agents. These complexes may undergo multiple interactions, especially ligand substitution reactions in biological fluids, before reaching their site of action, which may have fundamental effects on their pharmacokinetic properties. The imidazole coordination is the most frequently detected binding mode of peptides and proteins to half-sandwich Ru(II)/Rh(III) complexes. Therefore, in order to understand the thermodynamic factors governing the binding of half-sandwich Rh(III) cation and its complexes to histidine-containing peptides and proteins, in my PhD work I planned to study the interaction of (η^5-Cp*)Rh(III) cation with imidazole derivatives, with peptides containing histidine in different positions in the sequence, as well as with biogenic His-peptides (see Chart 4.5 and 4.6).

3. Materials and Methods

All starting materials were analytically pure reagents that were not further purified. The peptides GHG-NH_2, HHHG-NH_2, HPH-NH_2 and HPHPY-NH_2 were prepared in our laboratory according to the guidance of Dr. Lívia Fülöp (University of Szeged, Faculty of Medicine, Institute of Medical Chemistry) using solid phase peptide synthesis (SPPS). Analytical HPLC (Agilent 1260 Infinity II), ESI-MS spectrometry on a Thermo Scientific LTQ-XL Mass Spectrometer in a positive ion mode and ^{1}H-NMR (Bruker Ultrashield 500 Plus, in 10% (v/v) D_2O/H_2O mixture) methods were used to confirm the ligand quality and purity (see Appendix Fig. A1). The $A\beta_{1–16}$ and $A\beta_{1–40}$ were synthesized by CASLO. The stock solution of (Cp*)Rh(III) was made from $[(Cp^*)Rh^{III}(\mu\text{-}Cl)Cl]_2$ (Sigma-Aldrich, 97%) and standardized using acid-base titrations. Complexometric analysis was used to determine the concentration of the $CuCl_2$ and $ZnCl_2$ stock solution.

3.1 SYNTHESIS OF THE LIGANDS

3.1.1 Synthesis of the histidine peptides:

GHG-NH_2, HHHG-NH_2, HPH-NH_2 and HPHPY-NH_2 peptides were prepared manually by the standard solid phase synthesis using Fmoc chemistry on a Rink Amide AM resin (0.71mmol/g, Novabiochem) protocol. Coupling was performed in dimethylformamide with a 3-4-fold excess of reagents using DIC/HOBt (N,N′ diisopropylcarbodiimide/hydroxybenzotriazole) as activating agents. Kaiser (ninhydrin) tests were performed after each coupling to assess coupling efficiency. A piperidine/DMF 1:4 (v/v) mixture was used for deprotection. Following the last deprotection step, a mixture of 93% TFA (trifluoroacetic acid), 2.5% H_2O, 2.5% TIS (triisopropylsilane), and 2% DTT (dithiothreitol) was used for 3 hours at 0 °C for the cleveage from the resin. After removing the TFA, the peptide was precipitated in cold diethylether, filtered, washed with diethyl ether, finally dissolved in 50% aqueous acetic acid and lyophilized. The crude product was purified by a Phenomenex Jupiter C18 column, using gradient elution of H_2O:CH_3CN 100:0 v/v to H_2O:CH_3CN 70:30 v/v in a presence of 0.1% TFA. The trifluoroacetate salt of the peptides (~ 50% yield) was obtained as a white solid.

GHG-NH_2: R_t(HPLC) = 3.2 min. Yield: 86.6%. ESI-MS *m/z* calcd for $C_{10}H_{16}N_6O_3$ $[M+H]^+$ 269.14, found 269.14 (z = 1)). ^{1}H NMR (500 MHz, 10% D_2O/H_2O, pH 1.65, δ (ppm): 3.17 (m,

2H, $^{2}H–C_{\beta}H_2$), 3.76 (m, 2H, G-CH_2), 3.84 (d, 2H, G-CH_2), 7.23 (d, 2H, J = 232.5 Hz, C(O)-NH_2), 7.24 (s, 1H, C^5-H), 7.94 (br, 1H, ^{3}G-C(O)-NH), 8.52 (s, 1H, C^2-H), 8.75 (s, 1H, ^{2}H-C(O)-NH)).

HHHG-NH_2: Yield: 70 %. ESI-MS *m/z* calcd for $C_{20}H_{28}N_{11}O_4$ $[M+H]^+$ 486.23, found 486.42 (z = 1)). ^{1}H NMR (500 MHz, 10% D_2O/H_2O, pH 2.0, δ (ppm): 3.13-3.32 (m, 6H, H–$C_{\beta}H_2$), 3.85-3.87, 4.28(t, 3H, H–C_{α}H), 7.02, 7.47 (d, 2H, C(O)-NH_2), 7.25, 7.29, 7.35 (s, 3H, C^5-H), 8.54, 8.55, 8.56 (s, 3H, C^2-H), 8.48, 8.78 (br, 3H, C(O)-NH).

HPH-NH_2: R_t(HPLC) = 7.3 min. Yield: 50%. ESI-MS *m/z* calc.for $C_{17}H_{24}N_8O_3$ $[M + H]^+$ 389.20, found $[M + H]^+$ 389.20 (z = 1) and $[M + 2H]^{2+}$ 195.11 (z = 2). ^{1}H-NMR (500 MHz, D_2O/H_2O) δ(ppm): 1.87–2.38 (m, 8H, Pro-CH_2), 3.26–3.49 (m, 4H, HisCH_2), 3.78–3.83 (m, 2H, Pro N-CH_2), 7.21, 7.62 (d, 2H, $CONH_2$),7.39 (s, 1H, His C_5H), 7.50 (s, 1H, His C_5H), 8.64 (s, 1H, His C_2H), 8.73 (s, 1H, His C_2H), 8.84,8.85 (d, 1H, CONH).

HPHPY-NH_2: R_t(HPLC) = 10.4 min. Yield: 50%. ESI-MS *m/z* calc. for $C_{31}H_{40}N_{10}O_6$ $[M]^+$ 648.31, found $[M+H]^+$ 649.32 (z = 1) and $[M+2H]^{2+}$ 325.16 (z = 2). ^{1}H-NMR (500 MHz, D_2O/H_2O) δ(ppm): 1.79–2.37 (m, 8H, Pro CH_2), 2.97–3.10 (m, 2H, Tyr CH_2), 3.13–3.61 (m, 4H, His CH_2), 3.70–3.82 (m, 4H, Pro N-CH_2), 6.84, 6.86 (d, 2H, Tyr ring CH), 7.04, 7.06 (d, ^{1}H,CONH), 7.17, 7.19 (d, 2H, Tyr ring CH), 7.33 (s, 1H, His C^5H),7.48 (w, 1H, CONH), 7.50 (s, 1H, His C^5H), 8.25, 8.26, 8.75,8.76 (dd, 2H, $CONH_2$), 8.62 (s, 1H, His C^2H), 8.72 (s, 1H, His C^2H)

3.1.2. Synthesis of PMPA

At the first step 0.62 g of picolinic acid (5.0 mmol) solved in 10 mL $SOCl_2$ at reflux temperature under nitrogen atmosphere. The excess of $SOCl_2$ was blown out by the nitrogen flow, the traces were removed under vacuo. The crude product of picolinic acid chloride, without further treatment, was solved in 20 mL of THF and added dropwise to a THF (20 ml) solution of 0.54 g (5.0 mmol) 2-picolylamine at 0°C. After addition of 2.02 g (20.0 mmol) triethylamine, the mixture was stirred during a night at RT. The precipitation (Et_3NHCl) were filtered of, the solvent was removed under vacuo. The crude product was dissolved in 30 ml of CH_2Cl_2, and the solution was washed with aqueous 0.1 M NaOH (3 × 10 ml). After drying ($MgSO_4$) and filtering the organic phase, dry HCl gas was diffused into it. The dihydrochloride form of the ligand PMPA precipitated out in pure form. After filtering and drying under vacuo, the finally mass was

0.7923 g (MW: 286.16, 2.77 mmol, 55.3%) (See Scheme 1). ^{1}H NMR (298 K, D_2O, 500 MHz, pD = ~1.9): δ (ppm from TMS), 4.96 (s 2H), 7.73 (m, 1H), 7.90 (t, 1H), 7.97 (d, 1H), 8.10 (m, 1H), 8.14 (m, 1H), 8.49 (t, 1H), 8.62 (d, 1H), 8.65 (s, 1H). The sign of the amide proton was not observed in D_2O, as it was replaced by deuterium.

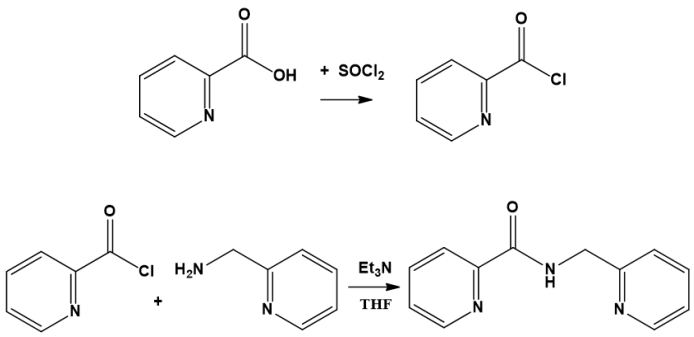

Scheme 1. The steps of the synthesis of the PMPA ligand.

3.1.3. Synthesis of PDMGA

Step 1. Chloroacetyl chloride (600 µL, 7.5 mmol) was dissolved in 20 ml dry CH_2Cl_2 at 0 °C, and a stirred mixture of 2-pycolyl-amine (1.55 ml 15 mmol) and triethylamine (1.2 mL) in 10 ml dry CH_2Cl_2 were added slowly under N_2, the reaction mixture was stirred overnight at room temperature. The reaction mixture was quenched with 10 ml distilled water and then was extracted with 3x20 ml of CH_2Cl_2. The combined organic layer was dried over anhydrous $MgSO_4$, and evaporated to afford crude (~ 0.95%) solid product 0.79 g (4.3 mmol, 57%) N-(2-pyridinylmethyl)acetamide. Crude (~ 95%) N-(2-pyridinylmethyl)acetamide (0.1958 g, ~1.0 mmol) was dissolved in anhydrous CH_3CN (20 ml) containing DIPEA (0.870 ml) and KI (22.2 mg), and was kept at 40 °C under N_2 during 30 min. This mixture was dropwise added (under N_2) to anhydrous CH_3CN (20 ml) containing 0.16 g (1.5 mmol) of 2-picolylamine and was stirred during 48h at RT. Then the resulting mixture filtered over gravity and the solvent was removed under vacuo. The residue was purified by column chromatography using CH_3CN: toluolen : NH_3 (25% in H_2O) (50:50:3) as the eluent. The pure, neutral ligand was unhandleable brown oil, therefore it was solved in CH_3CN and dry HCl gas was diffused into it. The non-stoichiometric hydrochloride form of the ligand PDMGA precipitated out in pure form (130 mg M.W. ~300 g/mol 43%) (See Scheme 2). ^{1}H NMR (D_2O, pD=5.4, 500 MHz) δ (ppm): 8.45 (1H, *J*=4.9 Hz, d), 8.37(1H, *J*=4.8 Hz, d), 7.80(1H, *J*=7.9 Hz, t), 7.77 (1H, *J*=7.8 Hz, t,), 7.41(1H, *J* =

7.9 Hz, d), 7.35(1H, *J* = 6.9 Hz, *J* = 5.5 Hz, dd), 7.29(1H, t, J = 5.9 Hz), 7.28(1H, *J* = 7.7 Hz, d), 4.42 (2H, s), 4.19 (2H, s), 3.79 (2H, s).

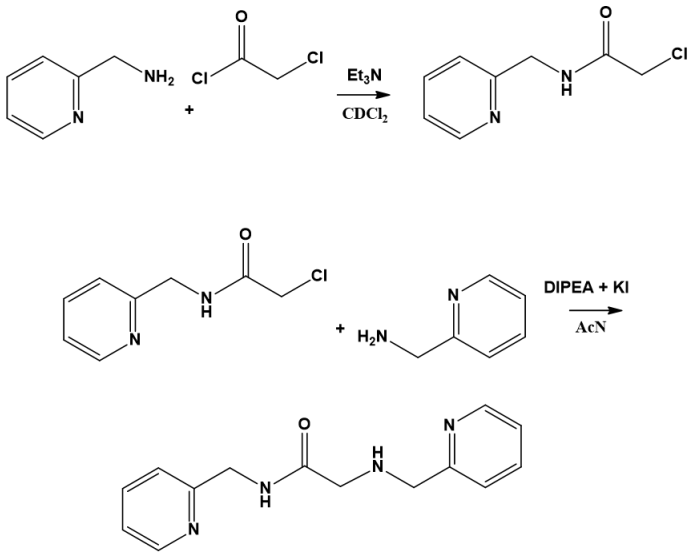

Scheme 2. The steps of the synthesis of the PDMGA ligand.

3.2 Characterization techniques of solution equilibrium and structure

3.2.1 pH-potentiometry

Potentiometric titrations in aqueous solution (*I* = 0.2 M KCl, and *T* = 298.0 0.1 K) under Ar were performed using an automatic titration set consisting of a PC controlled Dosimat 665 (Metrohm) auto-burette and an Orion 710A precision digital pH-meter in order to investigate the protonation and coordination equilibria. Titrations were carried out with a carbonate-free KOH solution (0.10 M, *I* = 0.2 M (KCl)). The Metrohm micro glass electrode (125 mm) was calibrated using a hydrochloric acid titration, and the data were fitted using the modified Nernst-equation **[114]**:

$$E = E_0 + K \cdot \log[H^+] + J_H \cdot [H^+] + \frac{J_{OH} \cdot K_W}{[H^+]}$$

where J_H and J_{OH} are the fitting parameters representing the acidic and alkaline error of the glass electrode, respectively (K_w = $10^{-13.75}$ is the autoprotolysis constant of water **[115]**). The non-linear least squares method was used to compute the parameters. The general equilibrium process characterized the complex formation:

$$pM + qH + rL \overset{ß_{MpHqLr}}{\rightleftharpoons} M_pH_qL_r$$

$$\beta_{M_pH_qL_r} = \frac{[M_pH_qL_r]}{[M]^p[H]^q[L]^r}$$

where M represents the metal ion and L represents the fully deprotonated ligand molecule. Charges have been omitted for clarity. The PSEQUAD computer program [116] was used to calculate the protonation constants of the ligands as well as the formation constants of the complexes. Four independent titrations (50-60 data points per titration) with ligand concentrations ranging from 1.8 to 3.0 × 10^{-3} M were used to calculate the protonation constants. Four to seven independent titrations were used to calculate the complex formation constants (60-70 data points per titration). Metal-to-ligand ratios ranged from 1:6 to 2:1, depending on the ligand. The metal ion concentrations ranged from 0.5 to 3.0 × 10^{-3} M. Titrations were carried out between pH 1.9 and 11.5. The equilibrium was supposed to be achieved when the measured potential changed by less than 0.2 mV within 30 seconds (Cu(II) complexes) and 2 minutes ((η^5-Cp*)Rh(III) complexes). In the latter case the mean waiting time between two doses of titrant solution was 4-6 minutes up to pH 6, 6-30 minutes between pH 6-8 (30 minutes was needed only in the (η^5-Cp*)Rh(III)-GGH system). Above this pH the equilibrium was achieved fearly quickly (6-10 min waiting time) in the (η^5-Cp*)Rh(III)-1-methylimidazole and (η^5-Cp*)Rh(III)-GGA systems, but in all other cases the maximum waiting time (30 minutes) was insufficient to reach the pH-equilibrium. In such cases, the data above pH 8 were evaluated separately, and the formation constants calculated are for informational purposes only (data in square brackets in Table 8-9).

3.2.2 Nuclear Magnetic Resonance (NMR) spectroscopy

NMR spectroscopy is a powerful and widely used technique to study the solution structure of metal complexes. It is especially useful for diamagnetic compounds, such as the (η^5-Cp*)Rh(III) complexes, with low spin d^6 electronic configuration. This method is suitable for studying compounds containing atomic nuclei of which the nuclear spin is different from zero ($I \neq 0$). Such nuclei have a quantized magnetic moment, and under the influence of an external magnetic field, the vector of this magnetic moment may have 2I+1 different positions relative to the direction of the external magnetic field. These positions represent different energy levels, and appropriate excitation radiation (radio frequency) may result transition between these levels (the nucleus is excited, its spin state changes). For a nucleus with spin I = 1/2 (e.g. ^{1}H), the energy of

the excitation radiation can be given by the equation $h\nu = \Delta E = h\gamma B_k/2\pi$ where Bk is the magnitude of external magnetic field, γ is the so-called gyromagnetic factor, which has different values from nucleus to nucleus (isotope to isotope), consequently the nuclei of the different elements can be examined separately. Since the nuclei of molecules are surrounded by electrons, the applied external magnetic field induces diamagnetism in this electron cloud, which results in a slightly different local magnetic field as compared to B_k. The electron cloud around a nucleus is a function of the chemical bonds of the molecule, so a given nucleus in different molecular environment, i.e. surrounded by different electron clouds, has a different resonance frequency in the NMR spectrum. The change of the resonance frequency depending on the molecular environment is called chemical shift.

If the adjacent nuclei have a nuclear spin $I > 0$, obviously their magnetic moments can also have $2I+1$ different orientations compared to the direction of the external magnetic field, which changes the magnitude of the magnetic field in the vicinity of the examined nucleus in a very small but measurable way. This is the so-called spin-spin interaction, which results in the splitting of the signals. The degree of this interaction is characterized by the spin coupling constant. In modern NMR the signals are not detected as an absorption spectrum, but the relaxation of the excited state (the loss of macroscopic magnetization) is monitored. This process is relatively slow (e.g. 0.1-10 s for ^1H). The loss of the macroscopic magnetization in the direction of the external magnetic field is called longitudinal (spin-lattice) relaxation, and the loss of magnetization perpendicular to the external field is called transverse (spin-spin) relaxation, the characteristic time constant for these processes are denoted by T_1 and T_2. The former is closely related to the intensity of the NMR signal, the latter to the signal width. Both relaxations can take place according to several mechanisms, in which fluctuating magnetic fields (with different frequencies) play fundamental roles. Of these, the so-called dipole-dipole interaction, which acts through the space, has usually particular importance. This is inversely proportional to the sixth power of the distance (r^{-6}) between the interacting magnetic dipoles (nuclei). Consequently, the NMR spectroscopy provides four basic information for each detected signal: (i) the signal intensity, which can be directly related to the concentration, (ii) the chemical shift, which provides information about the electron density of the environment of the nucleus, and thus the chemical quality of the atom creating the signal, (iii) the spin-spin coupling constant, which provides information about neighboring groups connected to the studied nucleus through

chemical bonds, and (iv) the T_1 and T_2 relaxation times, which, among others, play a key role in determining the 3-dimensional structure of the molecules.

If the studied compound consists of several nuclei, the so-called 2D-NMR techniques, using special pulse sequences, are more straightforward. During my work, I used the COSY and TOCSY spectroscopy, which may help to uncover the spin-spin interaction within a molecule, as well as the NOESY spectroscopy, which may give structural informations on the studied compound, based on the above mentioned dipole-dipole interactions.

Another important factor is the rate of exchange between different states of the ligand (e.g. bound or unbound to the metal ions). On the NMR time scale these can be fast, transient or slow processes. If the ligand exchange rate is much slower than the relaxation of the studied nuclei, the obtained spectra will contain separate signals for each nuclei in different chemical environment (i.e. separate signals for the free ligand and for the different complexes). In (η^5-Cp*)Rh(III) complexes, fortunately, this is the usual case.

^{1}H NMR experiments were performed on a Bruker Ultrashield 500 Plus instrument. The ligands were dissolved in a 10% (v/v) D_2O/H_2O mixture to have a concentration of 1.5-3 mM, and the desired pH was adjusted with HCl/KOH solution at 298.0 ± 0.1 K and at I = 0.20 M KCl, in the absence or presence of [(η^5-Cp*)$Rh^{III}Cl_3$] at 1:1, 2:3 or 1:4 metal- to-ligand ratios. Methanol was used as an internal reference, using $\delta_{methanol}$ = 3.35 ppm. The data were processed by the Topspin 2.0 software package (Bruker).

3.2.3 Mass Spectrometry (MS)

Mass spectrometry is a very sensitive analytical method, which is based on the formation of gaseous ions and enables their detection and characterization according to their mass and charge, more exactly to their mass/charge (m/z) ratio. During my work mass spectrometric measurements were performed to confirm the identity of the synthetized peptides and to identify the metal complexes present in solution at various pH and metal-to-ligand ratios. ESI-MS spectra were collected on a Q Exactive Plus hybrid quadrupole-orbitrap mass spectrometer (Thermo Scientific, Waltham, MA, USA) equipped with heated electrospray ionization (HESI-II) probe in positive/negative mode and coupled to an Abi 140C Syringe Pump. The samples were prepared in aqueous solution without background electrolyte, applying the appropriate metal-to-ligand ratios and pH. The pH of the solutions was adjusted with aqueous NH_3 and HCl solutions.

3.2.4 UV-visible (UV-Vis) spectroscopy

Ultraviolet-visible (UV-Vis) spectrophotometry can be used to examine substances that contain chromophore groups which absorb light in the 200-800 nm wavelength range. In the case of metal complexes, absorption can be caused by the electronic transitions within the ligand molecules, by the so-called d-d transitions of metal ions, or by the metal-to-ligand/ligand-to-metal charge transfer (MLCT/LMCT) bands. The latter two are related to the number and quality of coordinating donor groups as well as to the geometry around the metal ions, although even the qualitative interpretation of the spectra is not always obvious. In the case of copper(II) there are several experimental 'rules' concerning the position(s) of d-d transitions and the number, quality as well as the geometry of donor groups around the metal ion [111-115]. In the (η^5-Cp*)Rh(III) containing systems the pH dependent UV-Vis spectra are useful (only) to confirm the speciation established by pH-potentiometry. Consequently, pH-dependent UV-Vis spectrometric measurements were performed on Thermo Scientific Evolution 200 and Hewlett Packard 8452A diode array spectrophotometers to gain some equilibrium and structural information on the Rh(III) and Cu(II) complexes. The following systems were studied:

(A) (η^5-Cp*)Rh(III)-GGA and imidazole-containing systems: 0.15 mM of Rh(III); 1:6 or 0.97:1 metal-to-ligand ratios; pH 0.7–11.5; λ: 200–700 nm; pathlength: 1 cm.

(B) Cu(II)-HPH-NH_2 and -HPHPY-NH_2 systems: 0.9-1.8 mM of Cu(II); 1:1 and 1:2 Cu(II)-to-ligand ratios; pH 2–11; λ: 200–900 nm; pathlength: 4 cm.

(C) Cu(II)-PMPA and PDMGA systems: Cu(II) 16 μM; 0.94:1 metal-to-ligand ratio, pH 1–6; λ: 220–360 nm; pathlength: 4 cm.

Using the PSEQUAD computer program [110], the pH-dependent UV-Vis spectra were processed alongside the pH-potentiometric data, calculating logβ values as well as individual UV-Vis spectra of the metal complexes.

3.2.5 Circular dichroism (CD) spectroscopy

CD spectroscopy is used to study chiral compounds based on their different ability to absorb the left- and right-handed circularly polarized light (circular dichroism). In CD spectroscopy the difference of extinction coefficients related to the left- and right-handed circularly polarized light ($\Delta\varepsilon = \varepsilon_{left} - \varepsilon_{right}$) is measured as a function of wavelength (300-800 nm). Although, in metal complexes there can be several reasons for chirality, in fast exchanging copper(II) complexes the most important source is the chirality of the ligands, which may induce

strong chiral perturbation on the d-d and CT bands, mediated by chemical bonds. In this way, CD spectra can provide similar qualitative information on the coordination as the UV-Vis spectroscopy. During my work, the CD spectra of the Cu(II)-HPH-NH_2 and –HPHPY-NH_2 systems were collected in a cell with 4 cm optical pathlength using a a JASCO-J-1500 spectropolarimeter in the wavelength range of 280 to 830 nm. Spectral changes were measured between pH 2 and 11 at 1:1 and 1:2 Cu(II)-to-ligand ratios. The metal ion concentration ranged from 1.2 to 2.4×10^{-3} M. Since the Beer-Lambert law is applicable for the CD spectra, quantitative treatment of the spectra (together with the pH-potentiometric data) using the PSEQUAD computer program [110], enabled us to calculate the logβ values as well as the individual CD spectra of the Cu(II) complexes.

3.2.6 Electron Paramagnetic Resonance (EPR) spectroscopy

EPR spectroscopy is suitable for examining systems with unpaired electrons, such as metal ions and radicals. In terms of its theoretical foundations, EPR spectroscopy shows many similarities to the previously discussed NMR method. In the presence of an external magnetic field, the two possible values of the spin-momentum vector (M_S = +1/2 and –1/2) represent different energy levels, and a transition can occur between them as a result of excitation radiation of suitable energy: $h\nu = \Delta E = g\beta B_k$ (where g is the so-called g-factor, β is the Bohr magneton, Bk is the magnitude of the external magnetic field). The g-factor is characteristic for the chemical environment of the unpaired electron. For an isolated electron g = 2.0023, however, in real systems it can differ significantly from this value due to the spin-orbit interaction of electrons, or the quality and geometry of donor atoms surrounding the metal ion. Their effect on the unpaired electron is not always the same in all directions, therefore g is actually a tensor, i.e. it can take three values (g_x, g_y, g_z) according to the principal axes. In solution phase, the g-values may be averaged due to the fast molecular movements, and the system can be described by a single g_{iso} factor (isotropic spectrum). However, for solid samples, frozen solutions, or for solution samples of large metalloproteins, a single g-value is no longer sufficient. In case of the so-called rhombic spectrum, all three g values are different, in case of the axial spectra two g values ($g_x = g_y = g_\perp$, $g_z = g_{//}$) are sufficient for the correct description.

If the examined metal ion has a nuclear spin $I_M > 0$, the vector of the nuclear spin magnetic moment, similar to that of the electron, may have (2I+1) different positions relative to the

direction of the external magnetic field, which slightly increase or decrease the magnetic field which is sensed by the electron of the investigated metal ion. This results in further splitting of the spectrum, e.g. 2I+1 lines can appear on the isotropic spectra, and a maximum of 3×(2I+1) lines can appear on the rhombic spectra. Real spectra often show less than that, due to the small hyperfine coupling constants (A_M) and the relatively large line widths. If the donor atoms of the ligand coordinated to the metal ion have an inherent nuclear spin $I_L > 0$, the spectrum is further splitted, which can be interpreted in a completely analogous way to the interaction with I_M, As a consequence, this so-called superhyperfine interaction may result in a maximum $(2I_M+1)\times(2I_L+1)$ line. In the case of copper(II) this superhyperfine splitting typically occurs only in the $g_\perp$ range.

A BRUKER EleXsys E500 spectrometer was used to detect the X-band CW-EPR spectra of copper(II) complexes (microwave frequency 9.4 GHz, microwave power 13 mW, modulation amplitude 5 G, modulation frequency 100 kHz).

The following systems were studied both at room temperature and at 77 K:

(A) In Cu(II)-HPH-NH_2 system, seven and ten spectra were measured at different pH values in equimolar (C_{Cu} = 1.24 mmol/L and C_L = 1.30 mmol/L) concentration and at two-fold ligand excess (C_{Cu} = 0.65 mmol/L and C_L = 1.30 mmol/L), respectively.

(B) In Cu(II)-HPHPY-NH_2 system, nine and ten spectra were measured in equimolar solution (C_{Cu} = 1.80 mmol/L and C_L = 1.90 mmol/L) and two-fold ligand excess (C_{Cu} = 0.95 mmol/L and C_L = 1.90 mmol/L), respectively.

(C) In Cu(II)-PMPA system: 13 spectra were recorded at (C_{Cu} = 2.0 mmol/L and C_L = 2.6 mmol/L), and 10 spectra at (C_{Cu} = 1.0 mmol/L and C_L = 7 mmol/L) concentrations, respectively.

(D) In Cu-DPMGA system: 14 spectra were recorded at (C_{Cu} = 2.0 mmol/L and C_L = 2.6 mmol/L), and 20 spectra at (C_{Cu} = 1.0 mmol/L and C_L = 7 mmol/L) concentrations, respectively.

Frozen solution EPR spectra were collected in quartz EPR tubes placed into Dewar containing liquid nitrogen at 77K. To prevent water crystallization 0.05 mL MeOH was added to the 0.2 mL samples. All CW-EPR spectra were simulated using the “epr” software [116]. The anisotropic spectra were analysed by determining the axial g- and A- tensor values ($g_\perp$, $g_\parallel$, $A_\perp^{Cu}$, $A_\parallel^{Cu}$) and the orientation dependent line width parameters. The line width in one orientation was described

with α, β and γ parameters by the equation $\sigma_{MI} = \alpha + \beta M_I + \gamma M_I^2$, where M_I denotes the magnetic quantum number of copper nucleus. Nitrogen splitting was resolved only for one component (CuL_2H_4) where bis-histamine-like coordination was suggested. This spectrum could be fitted by the help of two sets of two equivalent isotropic nitrogen couplings (a_0^N). For the other components, the number of nitrogen couplings corresponding to the coordinating nitrogen was also taken into account as this contributes to the line width. The broad singlet spectra of the dimeric species were treated with isotropic EPR values. For the measurements we used natural $CuCl_2$, therefore the spectra were calculated as the sum of the spectra of ^{63}Cu and ^{65}Cu according to their natural abundances. The "epr" software calculates the copper and nitrogen coupling constants, as well as the relaxation parameters in field units (Gauss = 10^{-4} T).

3.2.7 Spectrofluorometric measurements

Fluorescence spectroscopy can be used to analyze fluorescence of molecules that contain fluorophore groups. Fluorescence occurs when an excited molecule, atom, or nanostructure, relaxes to a lower energy state (usually the ground state) through emission of a photon without a change in electron spin. Steady state fluorescence spectra are when molecules, excited by a constant source of light, emit fluorescence, and the emitted photons, or intensity, are detected as a function of wavelength. A fluorescence emission spectrum is when the excitation wavelength is fixed and the emission wavelength is scanned to get a plot of intensity *vs*. emission wavelength.
The spectrofluorimetry requires low concentration (μM) solutions, and is suitable for studying DNA, proteins and compounds that interact with them. For proteins, there are three fluorescent amino acids: phenylalanine, tyrosine and tryptophan (Trp). We can obtain information about the type and the strength of this interaction. The water soluble amyloid $\beta_{1\text{-}16}$ peptide contains tyrosine residue. Its interaction with copper(II) may affect the intensity of the emission of its tyrosine. Spectrofluorometric spectra in the 290-380 nm range were recorded on a Hitachi 4500 spectrofluorimeter with λ_{ex} at 280 nm using 10 nm/10 nm slit widths in a 1 cm micro quartz cell. The samples contained 10 μM $A\beta_{1-16}$, 12 μM ligand, and variable concentration of Cu(II) at physiological pH.

3.2.8 Electrochemical studies

Cyclic voltammograms of copper(II)-HPH-NH_2 and -HPHPY-NH_2 complexes in the absence and presence of H_2O_2 were recorded by an Autolab PGSTAT 204

potentiostat/galvanostat using a conventional three-electrode system under argon atmosphere in 0.2 M aqueous KCl solutions at 25.0 ±0.1 °C. The cyclic voltammograms were recorded at pH 7.4 and 10.5, at metal-to-ligand ratio 1:1 (c_L = 6.0×10^{-4} M), and were evaluated by Metrohm's Nova software. Before recording the voltammograms, the samples were purged for 15 min with argon. Platinum electrode was used as the working and auxiliary electrode and Ag/AgCl (in 3 M KCl) as reference electrode. E°(Ag/AgCl) versus E°(NHE) (in aqueous solution) is 0.205 V at 25 °C [117]. An aqueous solution of $K_3[Fe(CN)_6]$ ($E_{1/2}$ = + 0.255 V vs. Ag/AgCl) was used to calibrate the electrochemical system.

3.3 Kinetic experiments

Lytic polysaccharide monoxygenases oxidatively cleave the *β*-1,4-glycosidic bonds of polysaccharides, in a process where the C1 or C4 carbon atom of the substrate is oxidized (Fig. 1.5). The LPMO-like activity of our copper(II)-HPH-NH_2 and -HPHPY-NH_2 complexes was studied using *p*-nitrophenyl-*β*-D-glucopyranoside (PNPG) as substrate in presence or absence of H_2O_2, by monitoring the *p*-nitrophenolate anion (ε (400 nm) = 18900 M^{-1}cm^{-1}, p*K* = 6.98(2)) formed during the process (Figure 3.1), on a Thermo Scientific Evolution 200 spectrophotometer at 400 nm.

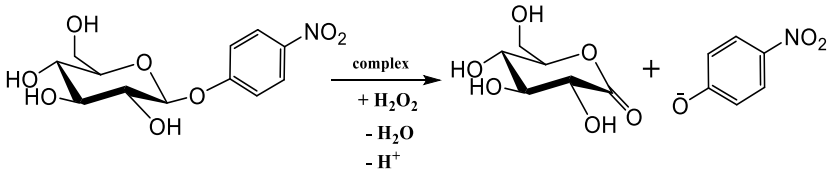

Figure 3.1: Scheme for the conversion of *p*-nitrophenyl-*β*-D-glucopyranoside (PNPG).

The kinetic study was performed at two pH. Beside pH = 10.5 (the pH used in the earlier LPMO mimetic studies [118-120]), we also investigated the enzyme mimetic properties of our complexes at pH = 7.3. The pH of the solutions was kept constant with the help of buffers (pH = 7.4: NaH_2PO_4/Na_2HPO_4, pH = 10.5: $NaHCO_3/Na_2CO_3$). After thermal equilibration (25 °C) of the test solutions containing PNGP, H_2O_2 and buffer in a 1 cm Teflon-plug quartz cuvette, we started our kinetic measurements by adding the necessary amount of the complex stock solution. The initial concentration of PNPG varied from 2.5×10^{-5} M to 0.018 M.

The initial concentration of PNPG varied from 2.5×10^{-5} M to 0.018 M. The initial slope method (≤ 4% conversion) was used to determine the pseudo first order rate constants. The reported data are the average of at least three parallel measurements with a re-producibility better than 10%. Second-order rate constants were obtained from plots of first-order rate constants against the total copper(II) concentration. The parameters of the Michaelis-Menten model (K_M and k_{cat}) were calculated by non-linear least-square method.

The Michaelis-Menten kinetic method was originally introduced to enzymatic reactions. In such reactions (considering only the most simple case) the enzyme (E) and the substrate (S) molecules form an adduct (ES) in a pre-equilibrium step, followed by the conversion of the substrate to product (P) with the regeneration of the enzyme.

$$E + S \underset{k_{-1}}{\overset{k_1}{\rightleftharpoons}} ES \underset{k_{-2}}{\overset{k_2}{\rightleftharpoons}} E + P$$

At the beginning of the reaction [P] ~ 0, and therefore $k_{-2}[E][P] \sim 0$, thus the above equation can be simplified.

$$E + S \underset{k_{-1}}{\overset{k_1}{\rightleftharpoons}} ES \xrightarrow{k_2} E + P$$

Presuming steady-state approximation to the formation and consumption of ES (d[ES]/dt = 0), i.e. $k_1[E][S] = (k_{-1} + k_2)[ES]$, the rate of the reaction can be expressed as

$$\frac{d[p]}{dt} = K[E]_0 = V_0 = k_2[E]_0[S]/([S] + K_M)$$

where $[E]_o$ is the total concentration of the enzyme and K_M is the Michaelis constant: $K_M = [E][S]/[ES]$, which is actually the dissociation constant of the ES complex. In order to apply this methodology, the following conditions must be settled: (i) substrate concentration exceeds considerably the enzyme concentration, (ii) the variation of substrate concentration is negligible during the reaction (which meets the prerequisites of the initial reaction rates method), (iii) the product does not form a stable adduct with the enzyme, (iv) only one substrate molecule can be bound to the enzyme at a time.

Michaelis-Menten mechanism states a linear correlation between the reaction rate and $[E]_o$, but the substrate-dependence is more complex: if $[S]>>K_M$, then the reaction rate becomes independent on [S] ($d[P]/dt = k_2[E]_o$), while at $[S]<<K_M$, the reaction rate increases linearly with

[S] ($d[P]/dt = (k_2/K_M)[E]_o[S]$). Accordingly, the experimental substrate-dependent reaction rate curve is a saturation curve, which can be used to calculate K_M and k_2 (often cited as k_{cat}) parameters by e.g. least squares methods.

3.4 Reactive oxygen species production

The production of ROS was detected by the oxidation of ascorbic acid [121]. A Hewlett Packard 8452A diode array spectrophotometer was used to collect UV-Vis spectra (190-820 nm). The pH was kept at 7.4 using 0.01 M HEPES buffer, the ionic strength was kept at 0.12 M (NaCl) or nearly zero in some cases. In the absence of Aβ, the total volume of the mixtures was 1.5 cm^3, in the presence of Aβ it was only 0.4 cm^3. Both the normal and semi-micro cuvettes had 1.0 cm pathlength. After adjusting the ionic strength, Cu(II)-, Zn(II)-, $Aβ_{1–16}$, and $Aβ_{1–40}$ concentrations, the reaction was initiated by adding ascorbic acid (100 μM) to the solutions. The spectra were measured every 20 seconds for a total of 30 minutes. The reaction rate of ascorbate oxidation was calculated at X_{asc} = 0.8 (X represents absorbance of ascorbic acid) because measuring it close to the initial point was not possible when the reaction was relatively fast. X_{asc} were determined based on absorbance value, compared to a blank sample containing only ascorbic acid and buffer in the same concentration.

4. Results and discussion

4.1 Characterization of copper(II) specific pyridine containing ligands: Potential metallophores for Alzheimer's disease therapy

Up to now, clear "target" of the redistribution of copper has not been recognized, but redirecting the extracted copper back into the cells seems to be a suitable solution. Considering this pathway, it is possible to predict the conditions that an ideal artificial copper chaperone must meet: (A) The ligands has to be neutral at pH 7.4 in order to pass the blood-brain barrier. (B) It should be more selective for Cu(II) than Zn(II). (C) Its affinity for Cu(II) should be higher than that of Amiloid β, but (D) lower than that of hCTR1 in order to take out Cu(II) from the ROS producing plaques and redistrubute into the cell. Therefore, in the first stages of my PhD work, we studied the copper(II) and zinc(II) complexes of two amide containing pyridine derivatives namely, PMPA (**L**^{1}) and PDMGA (**L**^{2}) (see chart 4.1), which were designed to fulfill these conditions.

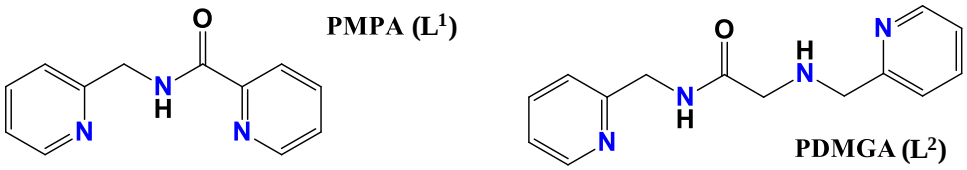

Chart 4.1. Schematic structures of PMPA (**L**^{1}) and PDMGA (**L**^{2}) (taken from [122])

4.1.1 Solution chemical studies[1]

The proton dissociation constants of **L**^{1} and **L**^{2} (listed in Table 1) were determined by pH-potentiometric and ^{1}H-NMR titrations, as well as by UV–Vis spectrophotometry in the acidic region (pH = 1-3). The highest p*K* (= 6.43) of **L**^{2} is related to the secondary amine. Only one pyridine p*K* could be determined by pH-potentiometry for both ligands (pK_a = 4.25 and 4.02 for **L**^{1} and **L**^{2}, respectively), which belong to the pyridine ring of the pyridyl-2-methylamide part of the ligands. The other pyridine ring is very acidic for both ligands, and their p*K* could be determined only by spectrophotometric titration performed between pH 1-3. Similarly acidic p*K*s were determined for the pyridine ring of N-(pyridyl-2-methyl)methylamine (pK_a = 1.4 [123] and 1.78 [124]) and for 2-picolinamide (pK_a = 2.10 [125]).

[1] The text of this chapter is mainly based on ref. [122]

The speciation of copper(II) and zinc(II) with the two ligands was studied at mM concentration. Both ligands form soluble copper(II) and zinc(II) complexes in the studied pH range. One set of stability constants of Cu(II) complexes (Table 1) for both ligands were determined by comparative evaluation of pH-potentiometric and UV-Vis spectroscopic and 2D-EPR measurements (Fig. 4.1, 4.2, 4.3 and 4.4). The stability constants of Zn(II) complexes were determined from pH-metry. The EPR parameters of the Cu(II) complexes are collected in Table 2 and Table 3, while the predicted structures of the Cu(II) complexes are depicted in Chart 4.2.

Table 1 Overall formation constants (logβ) and pK values of the investigated ligands, PMPA and DPMGA, and their complexes formed with Cu(II) and Zn(II) at I = 0.2 mol dm^{-3} KCl and T = 298 K. (taken from [122])

	L^1 = PMPA				**L^2** = PDMGA			
	logβ (3SD)	pK			logβ (3SD)	pK		
H_3L	-	-			12.01(10)	1.57		
H_2L	5.63(20)	1.4			10.46(12)	4.02		
HL	4.25(2)	4.25			6.44(12)	6.44		
	Cu(II)		**Zn(II)**		**Cu(II)**		**Zn(II)**	
	logβ (3SD)	**pK**	**logβ (3SD)**	**pK**	**logβ (3SD)**	**pK**	**logβ (3SD)**	**pK**
MLH	-	-	-	-	13.02(4)	3.54	9.06(15)	3.65
ML	-	-	-	-	9.47(14)	2.82	5.42(5)	7.19
MLH_{-1}	4.08(9)	9.23	-3.59(5)	7.97	6.65(2)	11.3	-1.78(3)	9.00
MLH_{-2}	-5.15(13)		-11.56(4)	-	-4.62(51)	-	-10.77(3)	-
ML_2H_2	-	-	-	-	22.66(7)	3.42	18.29(27)	3.98
ML_2H	-	-	-	-	19.24(9)	3.93	14.31(18)	4.02
ML_2	-	-	-	-	15.31(5)	-	10.29(4)	8.96
ML_2H_{-1}	6.54(45)	8.24	-	-	-	-	1.33(8)	-
ML_2H_{-2}	-1.70(6)	-	-8.22(4)	-	-	-	-	-

Based on the determined stability constants, representative concentration distribution curves were calculated at mM and µM concentrations (Fig 4.1). In mM concentration range *mono*- and *bis*-complexes are also formed (Fig 4.1 a1, b1, c1, d1, chart 4.2). Interestingly, in

excess of the tridentate ligand L^1, above pH 7-8 both metal ions form 6N coordinated bis-complexes ($[MLH_{-1}]^+ + L = [ML_2H_{-2}] + H^+$) with the participation of two deprotonated amide nitrogens (Fig 4.1 a1, b1). The amide deprotonation in zinc complexes is relatively rare phenomenon, while in case of copper(II) the Jahn-Teller distortion, resulting mostly elongated octahedral structure ($g_{\|} > g_{\perp}$), generally prevents the 6N coordination [126]. At μM concentrations the formation of bis-complexes are completely diminished, even at ligand excess (Fig 4.1 a2, b2, c2, d2).

At 77 K the EPR spectrum (Fig. 4.3) of the 6N coordinated $[Cu\mathbf{L}^1{}_2H_{-2}]$ complex shows highly rombic feature and extremely small coupling constant (A_z = 115.8), suggesting that strongly non-equivalent nitrogens are present in the equatorial plane of copper(II), therefore the

Table 2 Isotropic EPR parameters obtained for the different Cu(II)-PMPA and PDMGA complexes. (taken from [122])

L	Species	g_0	A_0	N^-_{amide}	N_{pyr}	N_{amin}	α	β	γ
PMPA	$CuLH_{-1}$	2.1126(1)	70.9(1)	13.2(2)	13.2(1)	-	21.39(1)	-9.16(1)	2.48(1)
	$CuLH_{-2}$	2.1113(1)	51.2(1)	14.1(2)	13.0(1)	-	17.65(1)	-7.50(1)	1.63(1)
	CuL_2H_{-1}	2.0982(2)	65.0(5)	15.5(6)	10.0(4)	-	25.00(1)	-11.30(1)	1.70(1)
	CuL_2H_{-2}	2.1148(2)	33.3(2)	*			36.09(3)	-8.83(3)	-0.10(3)
DPMGA	CuLH	2.1405(1)	59.6(2)	-	11.6(3)	8.2(5)	32.92(1)	-10.10(1)	0.92(1)
	CuL	2.1380(2)	56.3(9)	-	11(2)	6(4)	34.07(2)	-9.58(1)	0.42(1)
	$CuLH_{-1}$	2.1010(1)	72.1(1)	12.2(2)	12.2(1)	7.1(4)	20.50(1)	-8.55(1)	1.93(1)
	$CuLH_{-2}$	2.1158(1)	50.6(2)	12.4(4)	11.7(2)	4(1)	22.06(1)	-9.92(1)	2.24(1)
	CuL_2H_2	2.1152(2)	57(1)	*			14.(2)	-10.69(2)	4.75(2)
	CuL_2H	2.1077(2)	57(2)	*			49.29(2)	-6.66(2)	-1.88(2)
	CuL_2	2.1147(2)	60(1)	-	15(1)	6(2)	31.88(2)	-10.40(2)	7.90(2)

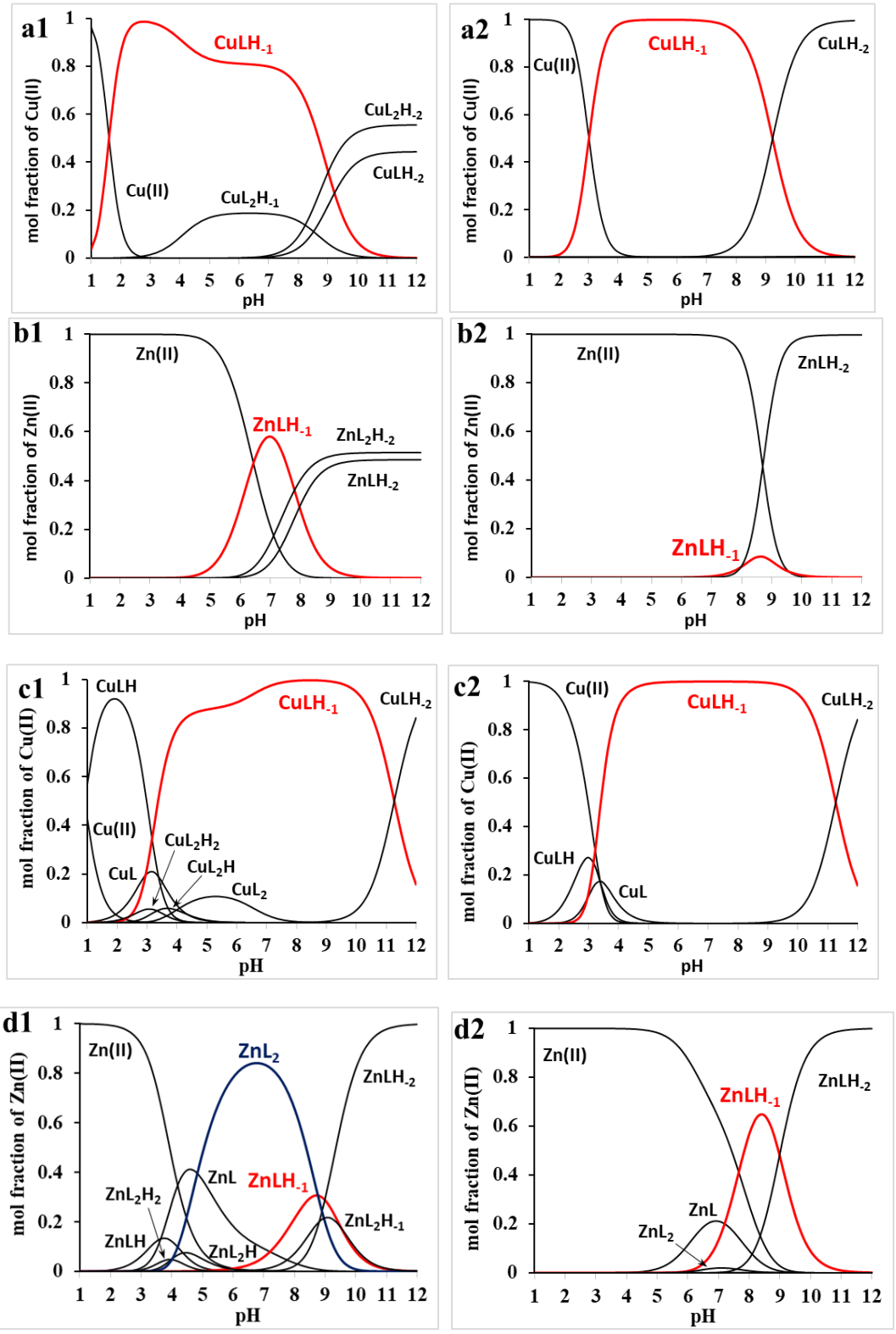

Figure 4.1 Representative concentration distribution curves for PMPA – M(II) (a1/a2 and b1/b2) and for DPMGA – M(II), (c1/c2 and d1/d2) systems at 1:2 metal to ligand ratios. The c(M) = 1 mM (a1/b1/c1/d1) or c(M) = 1 μM (a2/b2/c2/d2) (The bis ligand complex formation at μM metal ion concentration completely suppressed). (taken from [122])

coordination of two pyridine and two deprotonated amide nitrogens in the equatorial plane are expected as shown in Chart 4.2. The structure of the analogous zinc complex is probably similar. The mono-deprotonated *bis*-complex $[Cu\mathbf{L}^{\mathbf{1}}{}_2H_{-1}]^+$ was not detected by pH-metry, it was only identified by the evaluation of pH-dependent EPR spectra measured at room temperature and at high excess of ligand (Fig 4.2). Its proposed structure (Chart 4.2) is based on the published X-ray crystal structures of $Cu\mathbf{L}^{\mathbf{1}}{}_2$ (=$Cu(H_{-1}\mathbf{L}^{\mathbf{1}})(H\mathbf{L}^{\mathbf{1}})$), in which the non-coordinated pyridine ring is protonated [127]. $[ZnL_2H_{-1}]^+$ does not exist in the Zn(II)-PMPA system.

The $[Zn\mathbf{L}^{\mathbf{1}}H_{-1}]^+$ complex is more the seven orders of magnitude less stable than the $[Cu\mathbf{L}^{\mathbf{1}}H_{-1}]^+$, consequently Cu(II) induces the deprotonation of the amide-NH at 5–6 units lower pH than Zn(II). Therefore $[Cu\mathbf{L}^{\mathbf{1}}H_{-1}]^+$ dominates in the solution in a wide pH range, while $[Zn\mathbf{L}^{\mathbf{1}}H_{-1}]^+$ forms only in a narrow pH range, especially at μM concentrations (Fig 4.1 a2, b2). The 3N, amid-coordinated structure of $[Cu\mathbf{L}^{\mathbf{1}}H_{-1}]^+$ (Chart 4.2) is very likely similar to the X-ray structures already published for the *bis*-complex [127] and mixed ligand complexes [128] of PMPA ligand.

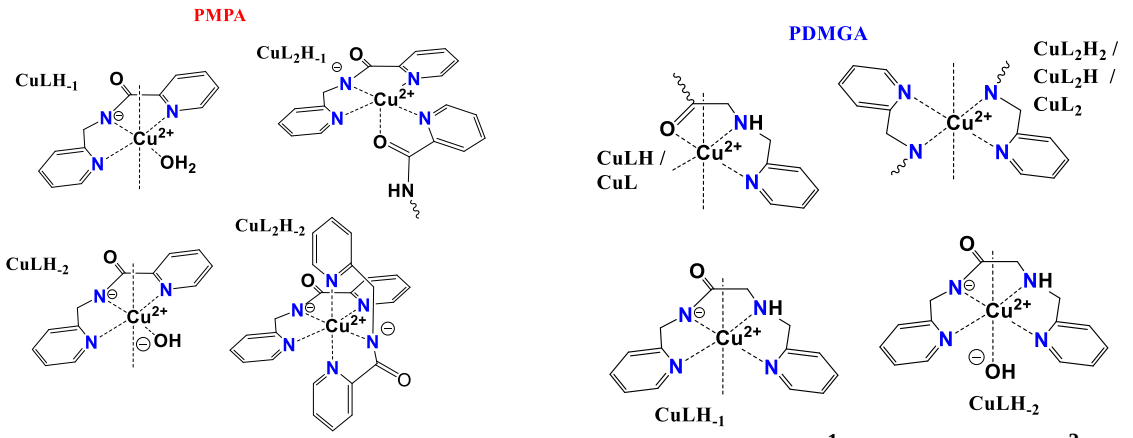

Chart 4.2 Structures of the Cu(II) complexes formed with PMPA ($\mathbf{L}^{\mathbf{1}}$) and PDMGA ($\mathbf{L}^{\mathbf{2}}$). (taken from [122])

At basic pH, further deprotonation was observed ($[M\mathbf{L}^{\mathbf{1}}H_{-1}]^+ \equiv [M\mathbf{L}^{\mathbf{1}}H_{-2}]^0 + H^+$), which is most likely correspond to the deprotonation of a coordinated water molecule ($[M\mathbf{L}^{\mathbf{1}}H_{-2}]^0 \equiv [M(\mathbf{L}^{\mathbf{1}}H_{-1})(OH)]^0$). Interestingly, during this deprotonation the superhyperfine structure of both m_I = +1/2 and +3/2 EPR lines becomes nicely visible. The p*K* of this deprotonation is more than one unit lower in the case of Zn(II) than for Cu(II).

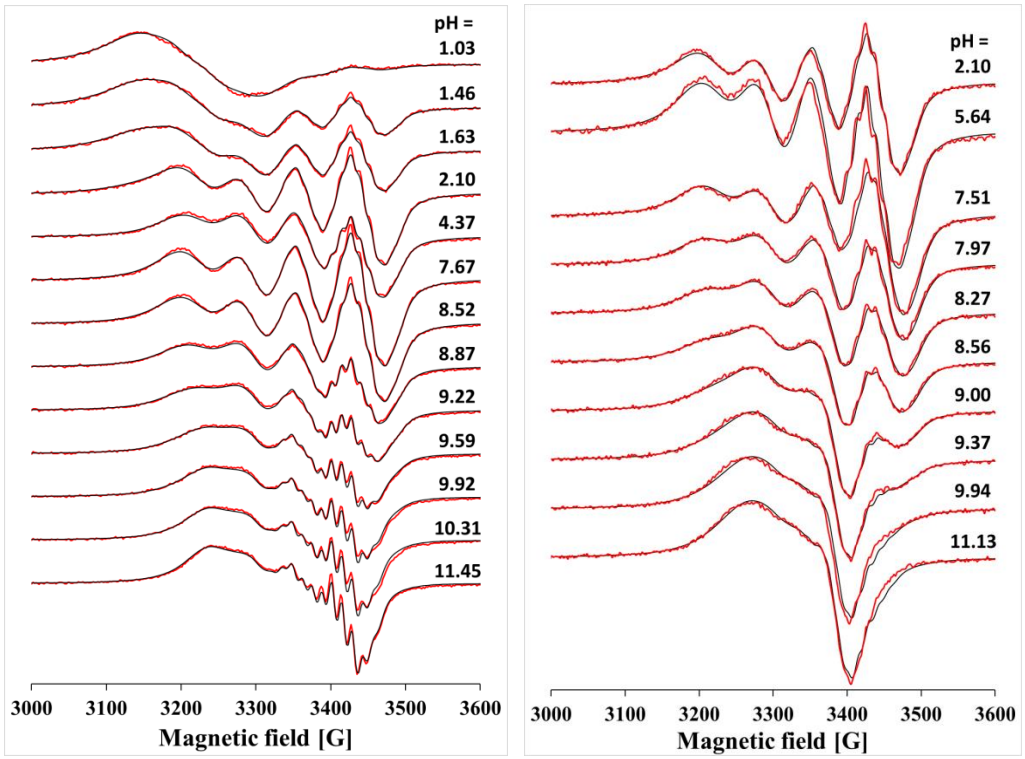

Figure 4.2 Experimental (red) and simulated (black) isotropic EPR spectra recorded at various pH values for the Cu(II)–PMPA system at 1:1.3 (left) or 1:7 (right) metal to ligand ratio{T = 25 ◦C; I = 0.20 M (KCl)}. (taken from [122])

In the M(II)-DPMGA ($\mathbf{L}^2$) system, the speciation (Fig 4.1 c1, d1, c2, d2) proved to be rather complicated since the DPMGA ligand has the ability to coordinate as a bidentate (amino-N, pyridine-N) or tetradentate ligand. Therefore, the combined evaluation of potentiometric and pH-dependent 2D-EPR titrations were used to uncover the equilibrium properties (Fig 4.1 c1, d1, c2, d2, 4.3 and 4.4). At mM concentrations and at ligand excess (Fig 4.1 c1, d1, c2, d2), differently protonated bis-complexes are formed ($[M\mathbf{L}^2{}_2H_2]^{4+} \rightarrow [M\mathbf{L}^2{}_2H]^{3+} \rightarrow [M\mathbf{L}^2{}_2]^{2+}$). The formation constants of these complexes suggest bidentate (amino-N, pyridine-N) or tridentate manner (amino-N, pyridine-N, C=O) coordination of $\mathbf{L}^2$ in these species, which is also supported by the fact that the corresponding pK_s range (3.2–4.02) are close to the non-coordinating pyridine-N (chart 4.2). In addition, the protonation state of $Cu\mathbf{L}^2{}_2H_2$/$Cu\mathbf{L}^2{}_2H$/$Cu\mathbf{L}^2{}_2$ complexes do not show important impact on the EPR parameters (Fig 4.4). In case of zinc(II), the 6N coordinated bis complex $[Zn\mathbf{L}^2{}_2]^{2+}$ is the main species at neutral pH. In case of copper(II), apart the 2N coordinated $Cu\mathbf{L}^2H$, mostly 4N coordinated mono-complexes are formed.

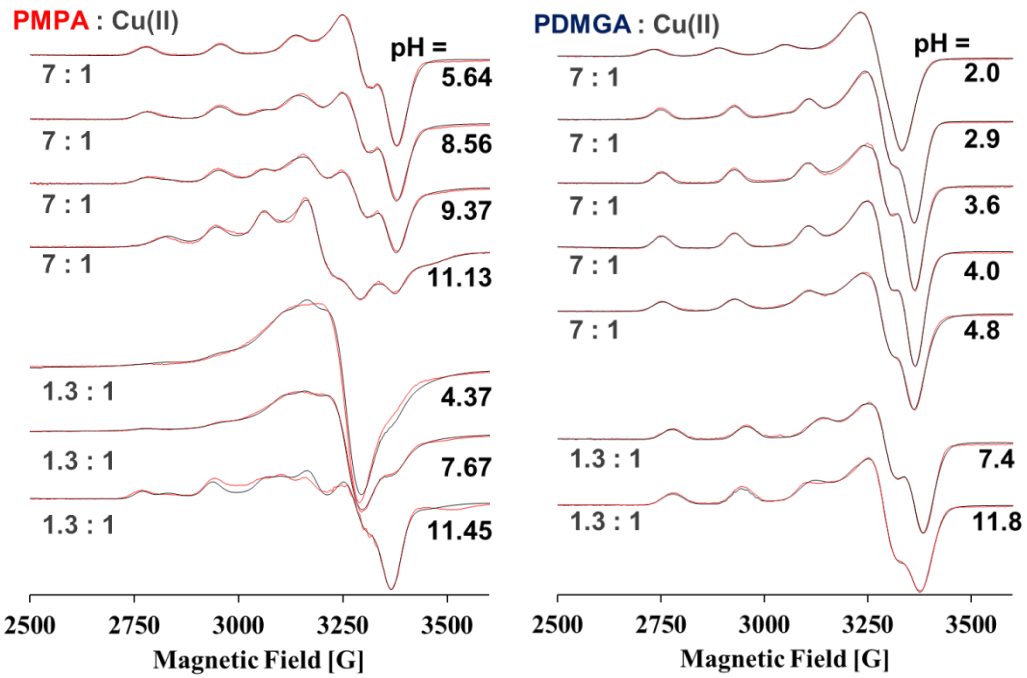

Figure 4.3 Selection of experimental (red) and simulated (black) anisotropic EPR spectra recorded at different metal to ligand ratios and various pH values for the Cu(II)–PMPA and the Cu(II)-PDMGA systems {T = 77 K; I = 0.20 M (KCl)}. (taken from [122])

The published crystal structure of the Zn$\mathbf{L}^{\mathbf{2}}_2$ [129] confirms that Zn(II) ion is surrounded by two $\mathbf{L}^{\mathbf{2}}$ molecules that coordinate in a tridentate manner through pyridine-N, amino-N and amide-O, while the "amide-close" pyridine-N is located far from the zinc ion, resuling in octahedral coordination geometry. An additional deprotonation of $[Zn\mathbf{L}^{\mathbf{2}}_2]^{2+}$ to form $[Zn\mathbf{L}^{\mathbf{2}}_2H_{-1}]^{+}$ complex with pK_a 8.96 is most likely related to the deprotonation of coordinated water molecule $[Zn\mathbf{L}^{\mathbf{2}}_2H_{-1}]^{+} \equiv [Zn\mathbf{L}^{\mathbf{2}}_2OH]^{+}$).

The deprotonation of $[Cu\mathbf{L}^{\mathbf{2}}H]^{3+}$ and $[Cu\mathbf{L}^{\mathbf{2}}]^{2+}$ is highly overlapped (Fig 4.1 c2), suggesting that DPMGA coordinates in tetradentate manner. The formation of these species has no significant effect on the EPR spectra (Fig 4.4), since their spectra overlap with that of the major $[Cu\mathbf{L}^{\mathbf{2}}H_{-1}]^{+}$ complex, which dominates in the solution between pH 3-11. The anisotropic EPR parameters of all Cu(II)-$\mathbf{L}^{\mathbf{2}}$ show axial feature (Table 3), *i.e.* their structures are tetragonal with elongated Jahn-Teller distortion complexes. Consequently, in $[Cu\mathbf{L}^{\mathbf{2}}H_{-1}]^{+}$ the ligand is tetradentately coordinated in the equatorial plane, similarly to the published X-ray structure [129]. The analogous $[Zn\mathbf{L}^{\mathbf{2}}H_{-1}]^{+}$ is nine order of magnitude less stable, and it is major species only between pH 8-9 at μM concentrations (Fig. 4.1 d2). At basic pH, the $[M\mathbf{L}^{\mathbf{2}}H_{-1}]^{+}$ complexes release an additional proton forming a neutral ternary hydroxido species $[M\mathbf{L}^{\mathbf{2}}H_{-2}]^{0}$. The EPR

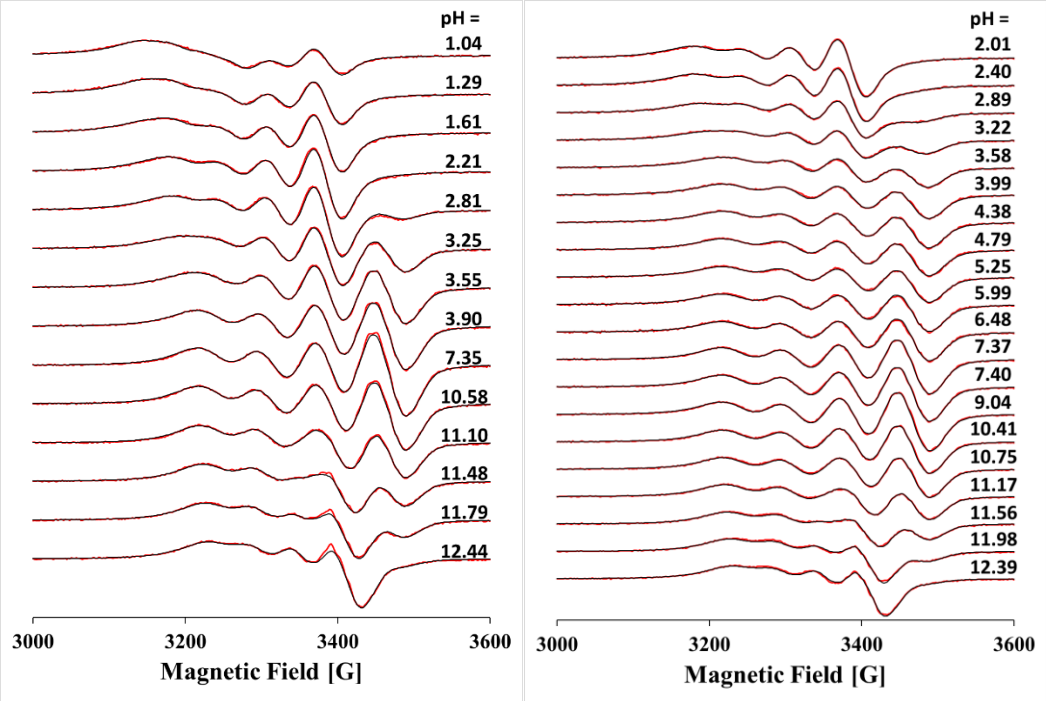

Figure 4.4 Experimental (red) and simulated (black) isotropic EPR spectra recorded at various pH values for the Cu(II)–DPMGA system at 1: 1.3 (left) or 1: 7 (right) metal to ligand ratio{*T* = 25 ˚C; *I* = 0.20 M (KCl)}. (taken from [122])

Table 3 Anisotropic EPR parameters obtained for the different Cu(II)-PMPA and DPMGA complexes. The unit of the coupling constants is Gauss = 0.1 mT. (taken from [122])

L	species	g_x	g_y	g_z	A_x	A_y	A_z
PMPA	$CuLH_{-1}$	2.146		2.212	16.6		195.7
	$CuLH_{-2}$	2.044		2.240	18.5		161.5
	CuL_2H_{-1}	2.047		2.217	19.5		173.9
	CuL_2H_{-2}	2.018	2.097	2.250	77.5	26.9	115.8
DPMGA	CuLH	2.058		2.271	13.1		156.9
	CuL_2H_2	2.053		2.238	20.7		173.9
	CuL_2	2.055		2.240	24.8		169.9
	$CuLH_{-1}$	2.047		2.217	23.5		174.5
	$CuLH_{-2}$	2.054		2.231	30.6		162.9

parameters determined for $[Cu\mathbf{L}^2H_{-2}]^0$ indicate equatorally coordinated hydroxide ion (*i.e.* it should replace a nitrogen). Accordingly, the p*K* of this deprotonation is more than 2 units higher in case of Cu(II) (pK_a = 11.3), tha for Zn(II) (pK_a = 9.00).

The pM == − log [M(II)]) dependence on the ligand concentration (Fig. 4.5) show that the tetradentate ligand ($\mathbf{L}^2$) has three orders of magnitudes greater metal sequestering ability than the tridentate ligand ($\mathbf{L}^1$). Furthermore, both ligands bind copper(II) seven orders of magnitude stronger than zinc(II), implying that our ligands are copper(II) specific even in the presence high excess of Zn(II).

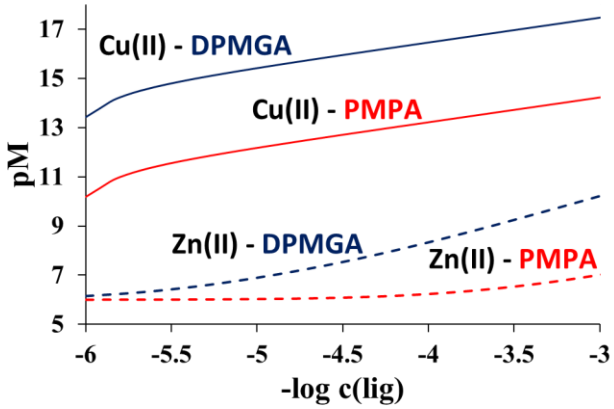

Figure 4.5 Calculated pM = − log [M(II)] values dependence on the ligand concentrations. c(M(II)) = 1 μM; pH = 7.4. (Red/blue line: PMPA/DPMGA and solid/dashed line: Cu(II)/Zn(II)). (taken from [122])

4.1.2. Competition with amyloid β_{1-16}[2]

The water soluble $A\beta_{1-16}$ peptide contains the high affinity copper binding site of amyloid β peptides, and its interaction with copper(II) results in the quenching of its tyrosyl fluorescence. Therefore, direct fluorescence titrations were performed between the ligands and the copper complex of $A\beta_{1-16}$ peptide (Fig. 4.6). These measurements show that both ligands can extract copper from amyloid β_{1-16}, and the tetradentate ligand PDMGA is stronger competitor than the tridentate PMPA.

4.1.3. Inhibition of ROS production[3]

The copper(II) complexes of amyloid peptides induce oxidative stress in the brain. Therefore, the ability of $\mathbf{L}^1$ and $\mathbf{L}^2$ to inhibit the ROS production generated by the interaction of

[2] The text of this chapter is mainly based on ref. [122]
[3] The text of this chapter is mainly based on ref. [122]

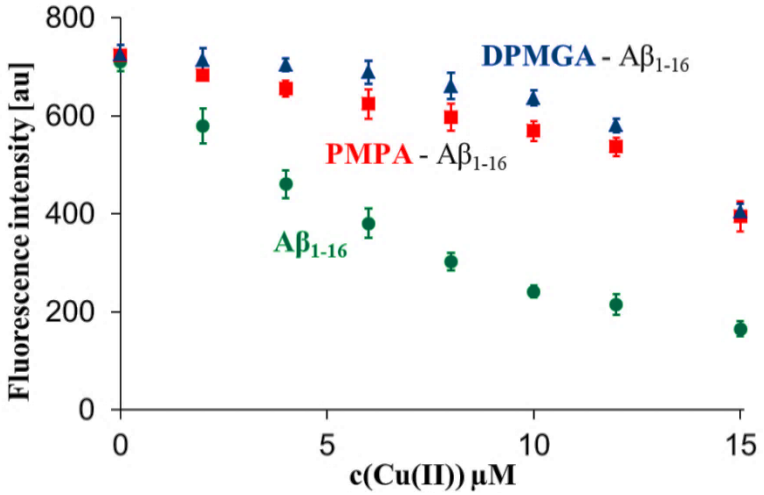

Figure 4.6 Fluorescence of the Tyr residue (λ_{max} = 306 nm, λ_{ex} = 280 nm) of $A\beta_{1-16}$, quenching by Cu(II). (10 µM $A\beta_{1-16}$, 12 µM ligand, pH = 7.4, pathlenght = 1 cm). Average of three independent measurements, the error bars represent the standard deviation. ($A\beta_{1-16}$ itself: green, $\mathbf{L^1}$ - $A\beta_{1-16}$: red and $\mathbf{L^2}$ - $A\beta_{1-16}$: blue). (taken from [122])

copper(II) with ascorbic acid was studied (Fig. 4.7) in order explore the antioxidant activity of our complexes. Beside our ligands, the inhibition ability of other seven relevant ligands (IDPA, DIEN, NTA, TREN, Gly-His, DPA and ENDIP, see Appendix Fig. A3 and Table A1), were also tested, in order to determine the correlation between the inhibition ability and the conditional stability constants (log*K′*) of their Cu(II) complexes. The evaluation of the results showed that the binding of Aβ peptides to Cu(II) itself decreases the rate of ascorbic acid decomposition, indicating that the free copper(II) catalytically more reactive as compared to its Aβ complexes. We observed higher reaction rate in presence of $A\beta_{1-16}$ than $A\beta_{1-40}$ (Fig. 4.8). Six ligands, among them $\mathbf{L^1}$ and $\mathbf{L^2}$, were able to significantly further reduce the rate of ascorbic acid decomposition, and their effect clearly depended on the conditional stability constants (log*K′*) of their Cu(II) complexes **(**Fig. 4.8**)**. The log*K′* (=9.70) of the Cu(II)-IDPA (iminodi(methyl-phosphonic acid) complex is slightly lower than that of the Cu(II)-Aβ species (log*K′* ~10 [11] or ~10.3 [12]), which explains its moderate effect on the reaction.

However, two well-known Cu(II) binder ligands, Gly-His and NTA are exeptions, since these compounds increase the rate of reaction as compred to the Cu(II)-Aβ species. The Cu(II)-GlyHis complex probably catalyze the ROS formation, whereas the Cu(II)-NTA complex most likely forms catalytically active ternary species with $A\beta_{1-16}$. The addition of Zn(II) at concentrations up to 1 mM had no impact on the reaction rates. Considering all these results,

both $\mathbf{L}^1$ and $\mathbf{L}^2$ are capable of removing copper(II) from its Ab complexes, the amyloid peptides and reducing oxidative stress. However, only the tridentate ligand has lower conditional binding constant (log*K'*) than the copper transporter hCTR1, that is only this ligand can hand over copper to the transporter protein. As a result, only $\mathbf{L}^1$ meets the minimal requirements of a potential metallophore.

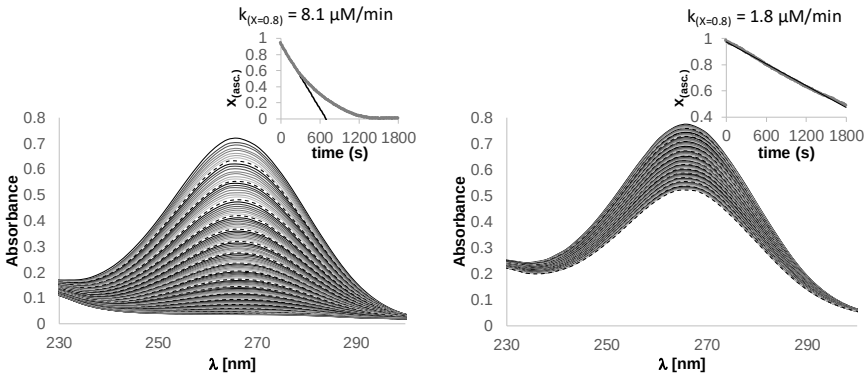

Figure 4.7 The UV-spectra measured during the decomposition of ascorbate in the absence (left) and in the presence (right) of PMPA ($\mathbf{L}^1$). (c(L) = 10.0 µM), at pH = 7.4. c(ascorbate, initial) = 100 µM; c(Cu(II)) = 10 µM; c(Aβ) = 12.0 µM; c(NaCl) = 0.120 M) The reaction rate ($k_{(X=0.8)}$) was determined based on the absorbance at 266 nm when the $X_{(asc.)}$ = 0.8 (see inlets). (taken from [122]

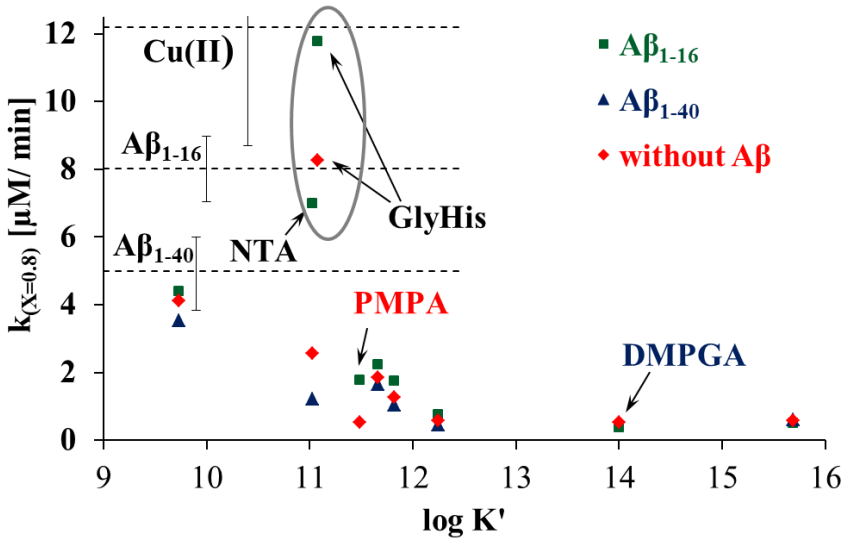

Figure 4.8 Dependence of the observed decomposition rate (µM/min) of ascorbate (at X(abs.) = 0.8) from the conditional stability of the Cu(II)-L complexes (at pH = 7.4); Initial concentrations: c(ascorbate) = 100 µM; c(Cu(II)) = 10 µM; c (L) = 20.0 µM; c(Aβ) = 12.0 µM; c(NaCl) = 0.120 M) (with $A\beta_{1-16}$: green, with $A\beta_{1-40}$: blue: without Aβ: red). (taken from [122])

4.2 Peptide-based chemical models for lytic polysaccharide monooxygenases

The aim of recent project was to design appropriate His-peptides that can closely mimic the LPMO active centres, in order to uncover some valuable information on the roles of (i) the unique His-brace structural motif, and (ii) the presence of axial Tyr residue in the function of LPMOs, unexplored to date by model compounds. To this end, we studied the thermodynamic stability, structure and reactivity of Cu(II) complexes of two histidine containing peptides (Chart 4.3), namely HPH-NH_2 (**L**^{3}) and HPHPY-NH_2 (**L**^{4}) by means of pH potentiometry, UV-Vis, CD, EPR spectroscopy and kinetic investigations. Proline subunits are used to separate the coordination sites, in order to prevent the copper(II) promoted amide deprotonation and to provide relatively rigid structure for the ligands.

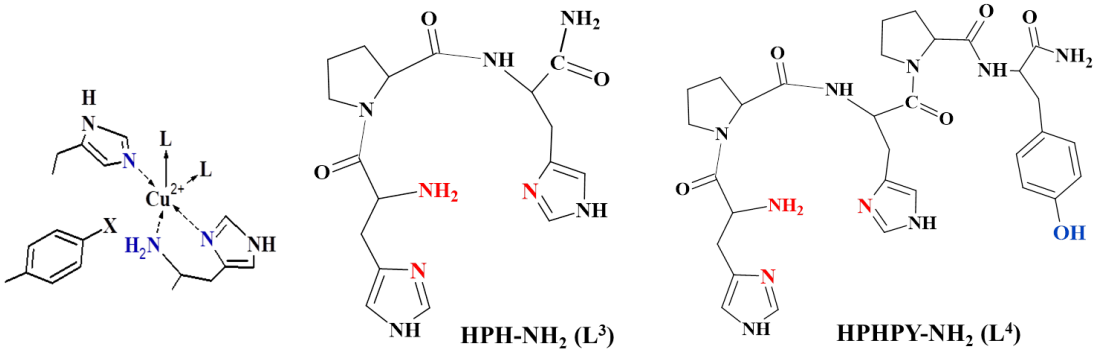

Chart 4.3 Schematic structure of the LPMO's active centre (X = H or OH, L = H_2O or OH^-) and the studied model peptides (taken from [130])

4.2.1 Equilibrium, solution structural and electrochemical studies [4]

The protonation constants of **L**^{3} and **L**^{4} (Table 4) agree well with those of other small histidine peptides [131]. Although the processes are overlapped, the two lowest p*K*s (~ 5.2 and ~ 6.3) belong predominantly to the imidazole ring of the N- and C-terminal His units [132], respectively, those around p*K* ~ 7.5 to the N-terminal amino group, while the highest p*K* (= 9.69) of **L**^{4} is related to the tyrosine phenolic hydroxyl group.

The equilibrium properties of copper(II) complexes (Fig. 4.9) were determined from the combined evaluation of potentiometric, pH-dependent UV-Vis and CD measurements (Figs. 4.10 and 4.11), considering also the EPR spectra obtained both at 77 K (Figs. 4.12, 4.13 and 4.14) and at room temperature (Fig. 4.15). In presence of copper(II) above pH 9.6 (**L**^{4}) and 10.5 (**L**^{3})

[4] The text of this chapter is mainly based on ref. [130]

precipitation was observed, therefore our data were evaluated only up to these pH values. The formation constants determined in this way are listed in Table 4. The coordination properties of

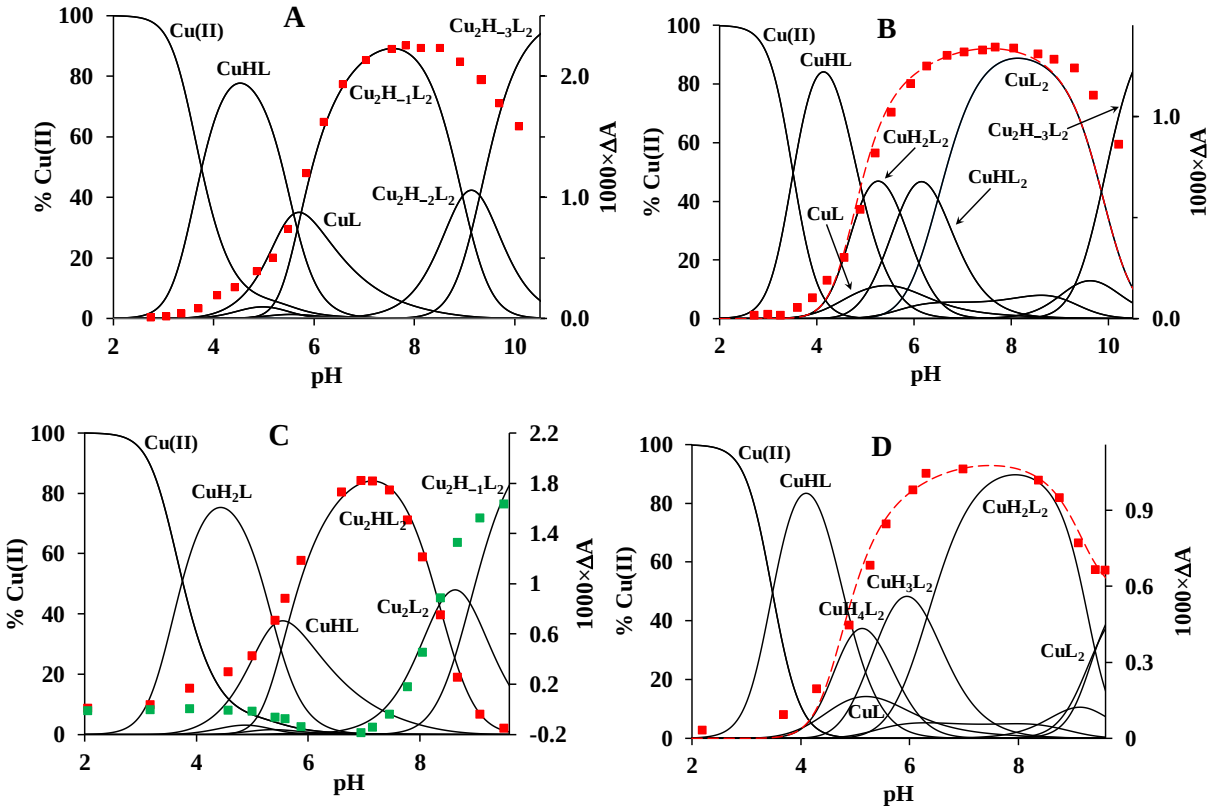

Figure 4.9 Speciation in the Cu(II)-$\mathbf{L}^3$ (A,B) and Cu(II)-$\mathbf{L}^4$ (C,D) systems at 1:1 (A,C) and 1:2 (B,D) metal-to-ligand ratios (T = 298 K, I = 0.2 M KCl, $[L]_{tot}$ = 0.0014 M). Red dotted lines in B and D show the distribution of the sum of *bis*-complexes. Secondary axis: measured CD intensities at 690 (■) and 430 nm (■). (taken from [130])

the two peptides are similar, only the presence of Tyr unit in $\mathbf{L}^4$ makes some difference, therefore in the following the two systems are discussed together.

According to the strong metal-binding ability of histamine-like binding site of N-terminal His units [16,25,132-134], $\{NH_2,N_{im}\}$ coordinated complexes (CuH$\mathbf{L}^3$ and $CuH_2\mathbf{L}^4$) are dominant between pH 3.5-5.0 at both 1:1 and 1:2 metal-to-ligand ratios (Fig 4.9). The basicity corrected formation constants (log β^*_{111} = 8.61 ($\mathbf{L}^3$), log β^*_{121} = 8.58 ($\mathbf{L}^4$)), as well as the spectroscopic data (Table 5) confirm the $\{NH_2,N_{im}\}$ coordination in these complexes. At ligand excess the formation of *bis*-complexes was detected between pH = 5-9 (Fig. 4.9), which are typical for peptides with non-protected N-terminal histidine [16,132-133]. The nearly identical spectral properties (Table 5, Figs. 4.12, 4.13 and 4.14) of these species (CuH_xL_2, where x = 2,1,0

for $\mathbf{L}^3$ and x = 4,3,2 for $\mathbf{L}^4$) suggest *bis*-histamine like {$2NH_2$,$2N_{im}$} coordination (Appendix Fig. A4), which is also supported by their formation constant values, as well as the fact that the corresponding p*K*s are close to those of the imidazole rings at the third position of the free ligands (Table 4).

Table 4. Formation constants and some derived data of the proton and copper(II) complexes of HPH-NH_2 and HPHPY-NH_2 ((estimated errors in parentheses (last digit), I = 0.2 M KCl, T = 298 K).

$\mathbf{L}^3$ = HPH-NH_2			$\mathbf{L}^4$ = HPHPY-NH_2			
Species (pqr)	**log β_{pqr}**	**p*K***	**Species (pqr)**	**log β_{pqr}**	**log β^*_{pqr}**	**p*K***
-	-	-	LH (011)	9.69(1)	-	9.69
LH (011)	7.53(1)	7.53	LH_2 (021)	17.19(1)	-	7.50
LH_2 (021)	13.89(1)	6.36	LH_3 (031)	23.48(1)	-	6.29
LH_3 (031)	19.14(1)	5.25	LH_4 (041)	28.66(1)	-	5.18
CuHL (111)	14.97(1)	5.5	CuH_2L (121)	24.56(1)	14.87	5.4
CuL (101)	9.41(2)	-	CuHL (111)	19.11(1)	22.26	-
$Cu_2H_{-1}L_2$ (2-12)	16.19(2)	8.98	Cu_2HL_2 (212)	35.86(2)	-	8.44
$Cu_2H_{-2}L_2$ (2-22)	7.21(6)	9.34	Cu_2L_2 (202)	27.42(1)	-	8.93
$Cu_2H_{-3}L_2$ (2-32)	-2.14(7)	-	$Cu_2H_{-1}L_2$ (2-12)	18.49(3)	-	-
CuH_2L_2 (122)	27.75(4)	5.76	CuH_4L_2 (142)	46.94(3)	27.56	5.51
$CuHL_2$ (112)	21.99(3)	6.53	CuH_3L_2 (132)	41.43(1)	22.04	6.36
CuL_2 (102)	15.46(8)	-	CuH_2L_2 (122)	35.07(2)	15.68	~ 9.48
			CuL_2 (102)	16.09(9)	-	-

[1] basicity corrected formation constants, corrected by the p*K* of tyrosine phenol group. These data are comparable with the log β_{pqr} values of $\mathbf{L}^1$.

In equimolar solutions, the p*K*s of the {NH_2,N_{im}} coordinated Cu**H**$\mathbf{L}^3$ and $CuH_2\mathbf{L}^4$ complexes (p*K* << 6.3, Table 4), as well as the EPR parameters of Cu$\mathbf{L}^3$ and Cu**H**$\mathbf{L}^4$ (Table 5) clearly indicate an additional nitrogen coordination, *i.e.* the formation of macrochelates with the participation of imidazole rings in the 3rd position of the peptides ({NH_2,2×N_{im}}). However, these complexes have *c.a.* one log unit lower formation constants than the analogous complex of HVH peptide (log β_{101} = 9.41 (HPH) vs. 10.53 (HVH) [132]), indicating more strained macrochelate, probably due to the conformational rigidity of proline unit in the second position. Although Cu$\mathbf{L}^3$ and Cu**H**$\mathbf{L}^4$ are not dominant species at any pH, it is worth mentioning that this coordination mode (Appendix Fig. A4) and the EPR parameters of these species are similar to that of the His-brace motif in LPMO's active centre [135].

Although, the above mentioned complexes are rather usual for copper(II) complexes of peptides with non-protected N-terminal HXH- sequence [16,132-133], the further complex

formation processes are fundamentally different from the systems known so far. The proline unit in the second (and fourth) position in our peptides prevents the formation of fused chelates with

Table 5. Anisotropic EPR parameters of the components obtained by the simulation of frozen solution (77K) spectra of Cu(II)-HPH / HPHPY systems

	Anisotropic EPR parameters[a]				$g_{0,calc}$[c]	UV-Vis λ^{max}_{d-d}	CD
	$g_\perp$	$g_\parallel$	$A_\perp$[b]	$A_\parallel$[b]		(nm)	λ (nm), Δε ($M^{-1}cm^{-1}$)
L^3							
Cu^{2+}	2.084	2.425	5.0	124.6	2.197	830	
CuH_2L[d]	2.067	2.377	18.4	136.7	2.171		
CuHL	2.060	2.305	11.3	169.6	2.142	700	328, –0.15 ; 780, 0.10
CuL	2.060	2.273	12.4	173.8	2.131	688	330, –0.20 ; 770, 0.17
CuH_2L_2	2.053	2.239	17.3	190.1	2.115	636	322, –0.53 ; 680, 0.79
$CuHL_2$	2.053	2.239	17.3	190.1	2.115	638	322, –0.46 ; 685, 0.73
CuL_2	2.052	2.245	18.0	181.3	2.116	640	322, –0.41 ; 690, 0.70
$Cu_2H_{-1}L_2$						622	688, 1.27
$Cu_2H_{-2}L_2$						622	574, –0.20 ; 694, 1.18
$Cu_2H_{-3}L_2$						600	590, –0.25 ; 706, 0.81
L^4							
Cu^{2+}	2.084	2.423	4.9	126.1	2.197	830	
$CuLH_2$	2.060	2.305	9.5	168.9	2.141	700	
CuLH	2.055	2.269	9.9	170.3	2.126	692	328, –0.19 ; 770, 0.19
CuH_4L_2	2.051	2.239	19.4	188.0	2.114	646	324, –0.58 ; 676, 0.68
CuH_3L_2	2.051	2.239	19.4	188.0	2.114	630	324, –0.48 ; 680, 0.67
CuL_2H_2	2.053	2.245	24.5	179.8	2.117	642	324, –0.43 ; 692, 0.62
Cu_2HL_2						624	686, 1.33
Cu_2L_2						622	348, –0.24 ; 436, 0.73 530, 0.57 ; 650, –0.52
$Cu_2H_{-1}L_2$						618	340, –0.45 ; 436, 0.53 530, 0.39 ; 626, –0.32

(a) The experimental error was ± 0.002 for $g_\perp$ and ± 0.001 for $g_\parallel$ and ± $1\cdot10^{-4}$ cm^{-1} for $A_\perp$ and $A_\parallel$. (b) $\times10^{-4}cm^{-1}$. (c) Calculated by the equation $g_{0,calc} = (2g_\perp+g_\parallel)/3$ on the basis of anisotropic values. (d) appeared only at 77 K.

the participation of amide nitrogens, and thus the appearance of ATCUN-type $\{NH_2,2N^-,N_{im}\}$ coordination above pH 5-6, which is the main binding mode of HXH (X≠P) peptides [16,25,132-134]. Surprisingly, in our systems the formation of major complexes around neutral pH requires 3.5 equivalent base consumption with respect to both the ligand and metal ion (Fig. 4.16). This observation can only be interpreted by the formation of a dimer (less probably oligomer) complexes with a composition of $Cu_2H_{-1}\mathbf{L}^3_2$ and $Cu_2H\mathbf{L}^4_2$. The presence of dimer species is further confirmed by our EPR study above pH 5, which show important intensity decrease at

room temperature (Fig. 4.15), and the appearance of a broad singlet signal at 77 K (Figs. 4.13 and 4.14), indicating moderate antiferromagnetic interaction between the metal centres within

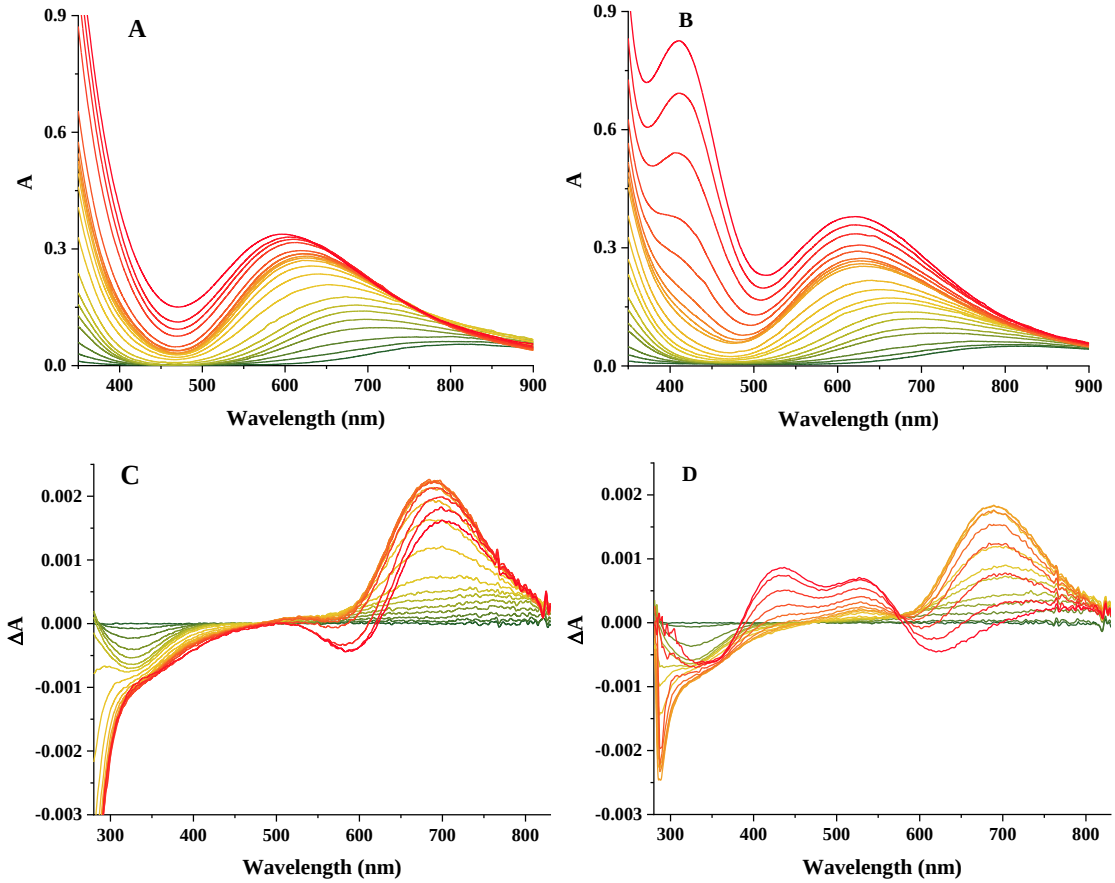

Figure 4.10 pH-dependent UV-Vis (A,B) and Circular Dichroism (C,D) spectra in the Cu(II)-$\mathbf{L}^3$ (A,C) and Cu(II)-$\mathbf{L}^4$ (B,D) systems at 1:1 metal-to-ligand ratios (the pH increases in the green-yellow-red direction, T = 298 K, I = 0.2 M KCl, $[L]_{tot}$ = 0.0014 M). (taken from [130])

the dimer (less probably oligomer) complexes. The spectra of the broad singlet signals change with pH, so they do not refer to rigid dimeric structures, but to structures with pH-dependent copper-copper positions. Typically, such line broadening is caused by the interaction of metal centres at medium distance (5-7 Å) from each other [136]. Since $Cu_2H_{-1}\mathbf{L}^3_2$ and $Cu_2H\mathbf{L}^4_2$ complexes are dominant in a wide pH-range, the single deprotonation per two metal ions should corresponds to a bridge formation between them (*i.e.* amide-deprotonation can be ruled out). Considering that the tyrosine phenols are still protonated in $Cu_2H\mathbf{L}^4_2$ (= $Cu_2H_{-1}(H\mathbf{L}^4)_2$) based on its UV-Vis spectrum (Fig. 4.12), there are only two options for such bridge formation: hydroxido- or imidazolato-bridge. Although, none of these can be completely ruled out, there are

several indirect indications in favour of imidazolato-bridge (Appendix Fig. A4): (i) the d-d transitions are considerably blue-shifted during these deprotonations (Table 5, Fig. 4.10), which

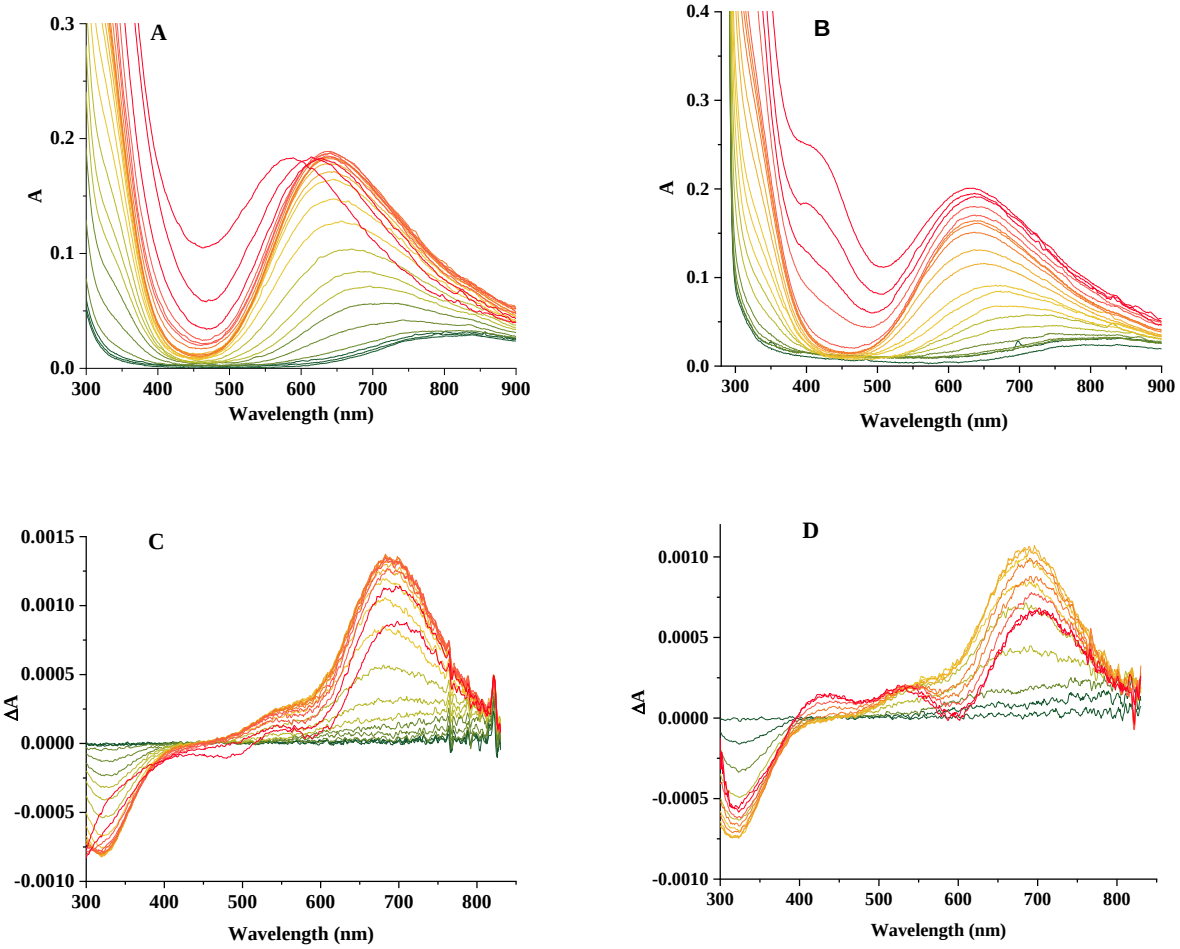

Figure 4.11 pH-dependent UV-Vis (A,B) and Circular Dichroism (C,D) spectra in the Cu(II)-$\mathbf{L}^3$ (A,C) and Cu(II)-$\mathbf{L}^4$ (B,D) systems at 1:2 metal-to-ligand ratios (the pH increases in the green-yellow-red direction, T = 298 K, I = 0.2 M KCl, $[L]_{tot}$ = 0.0014 M,). (taken from [130])

would not be expected for hydroxide coordination, (ii) hydroxido-bridged dinuclear copper(II) centres show strong antiferromagnetic interactions, and are usually EPR silent [137,138], (iii) an imidazolato-bridge creates 5-7 Å copper-copper separation and may produces detectable EPR spectrum [139,140], (iv) the intensity of CD spectra considerably increases during the formation of $Cu_2H_{-1}\mathbf{L}^3_2$ and $Cu_2H\mathbf{L}^4_2$ (Table 5, Fig. 4.10), indicating important additional contribution to the optical activity within the coordination sphere of metal ion, which is less likely in the case of hydroxido-bridge. Although, in the absence of metal ion the deprotonation of neutral imidazole ring takes place at pH > 13, there are several examples in the literature for metal-

promoted deprotonation (*i.e.* imidazolato-bridge formation) around the neural pH-range [141,142].

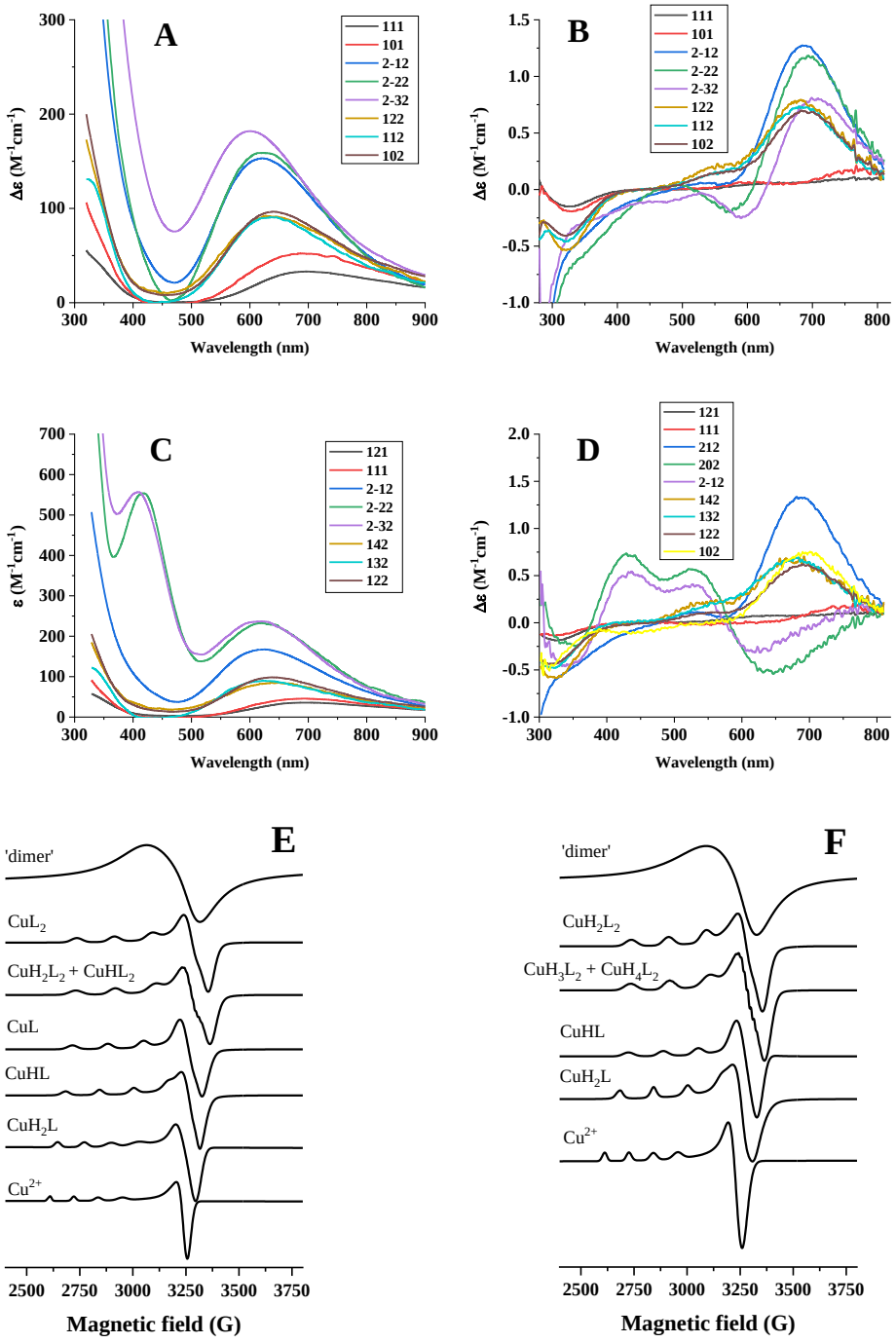

Figure 4.12 Individual UV-Vis (A,C), CD (B,D) and EPR (E,F) spectra of the complexes formed in the Cu(II)-$\mathbf{L}^3$ (A,B,E) and Cu(II)-$\mathbf{L}^4$ (C,D,F) systems. UV-Vis and CD spectra were calculated by the computer program PSEQUAD, while the component EPR spectra were obtained using the 'epr' software. (taken from [130])

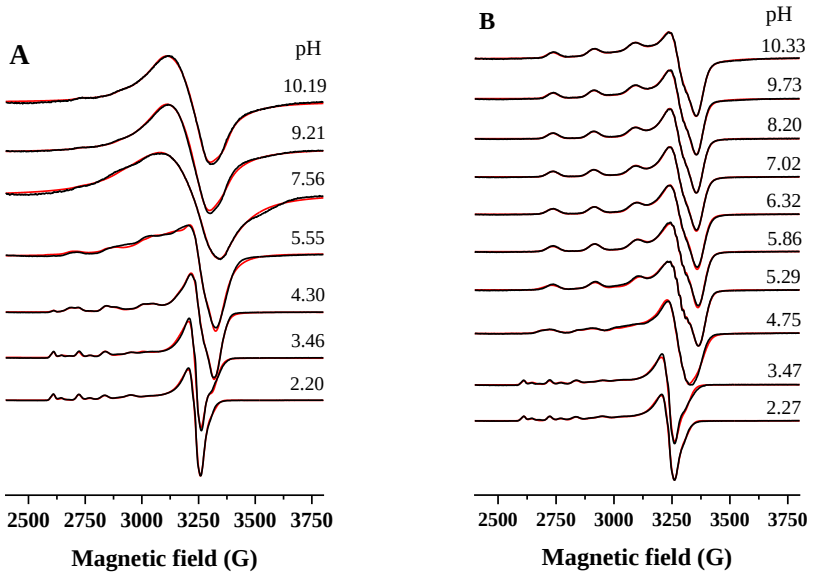

Figure 4.13 Experimental (black) and simulated (red) X-band CW-EPR spectra recorded in Cu(II)-HPH system, in frozen solution (77K), at concentration (A) c_{Cu} = 1.24 mM and c_L = 1.3 mM (beside the dimeric species, small amount of bis-complexes are also present in the pH range 6 – 10),(B) c_{Cu} = 0.65 mM and c_L = 1.3 mM. The spectra were normalized. (taken from [130])

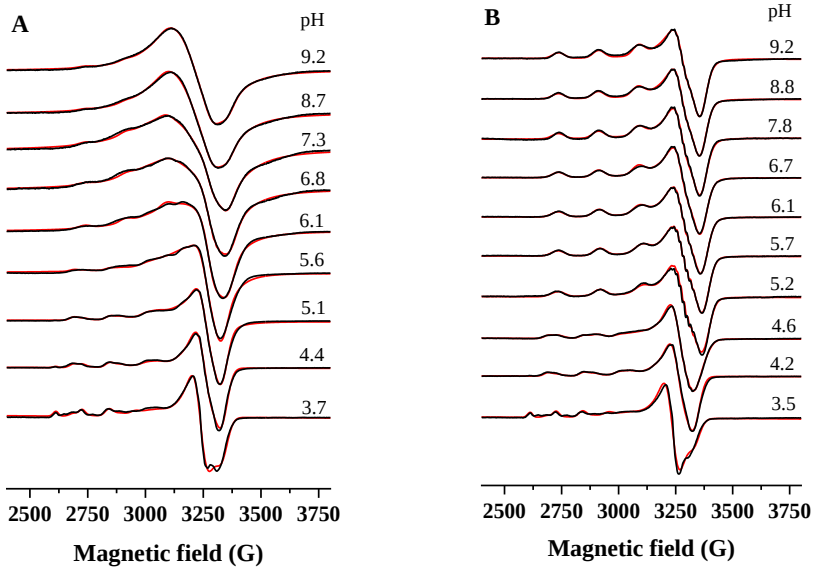

Figure 4.14 Experimental (black) and simulated (red) X-band CW-EPR spectra recorded in Cu(II)-HPHPY system, in frozen solution (77K), at concentration (A) c_{Cu} = 1.80 mM and c_L = 1.9 mM (beside the dimeric species, small amount of *bis*-complexes are also present in the pH range 6 – 10), (B) c_{Cu} = 0.95 mM and c_L = 1.9 mM. The spectra were normalized. (taken from [130])

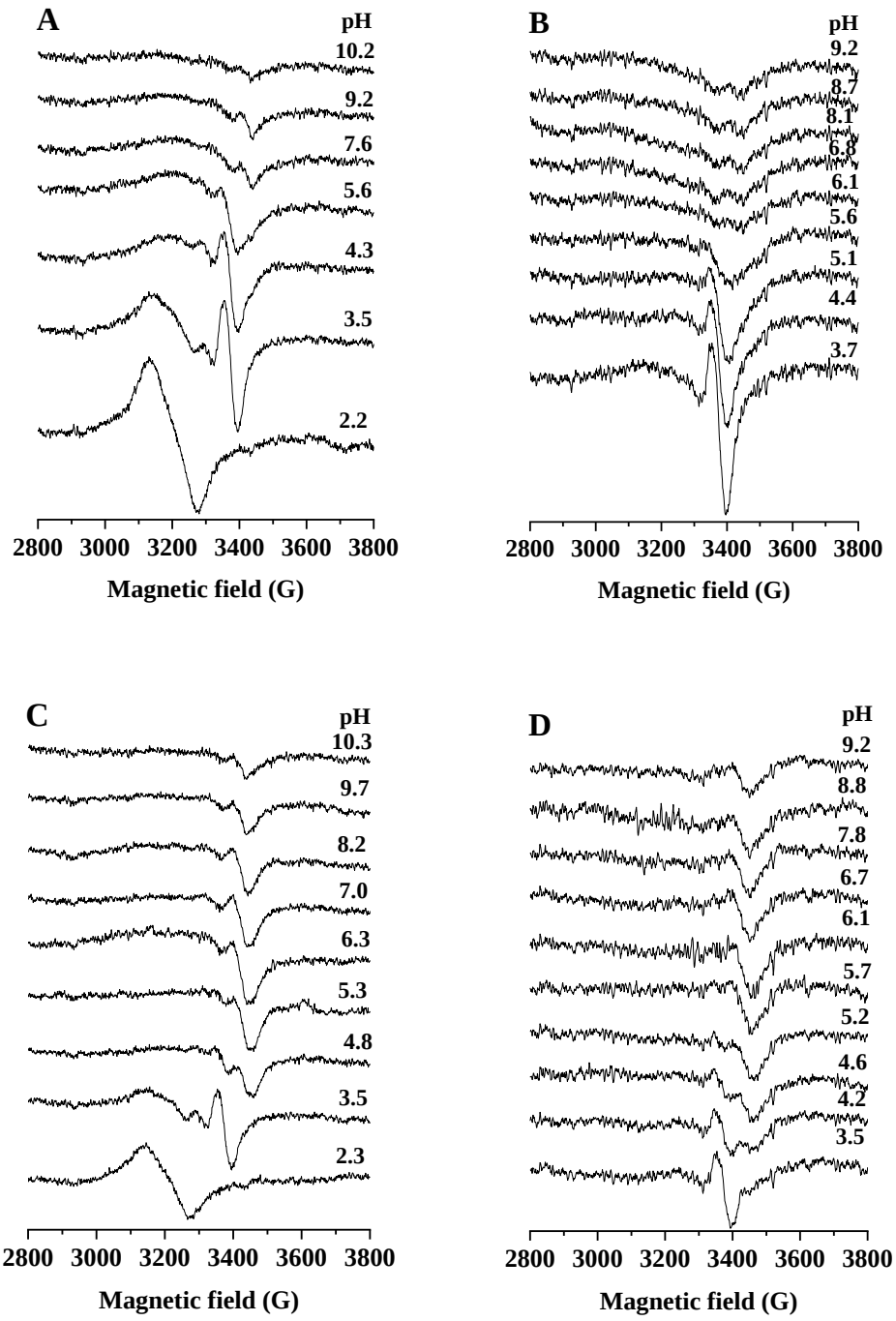

Figure 4.15 Experimental X-band CW-EPR spectra recorded at room temperature in the Cu(II)-$\mathbf{L}^3$ (A,C) and Cu(II)-$\mathbf{L}^4$ (B,D) systems at 1:1 (A,B) and 1:2 (C,D) metal-to-ligand ratios (A: $[Cu(II)]_{tot}$ = 1.24 mM, $[\mathbf{L}^3]_{tot}$ = 1.30 mM, B: $[Cu(II)]_{tot}$ = 0.65 mM, $[\mathbf{L}^4]_{tot}$ = 1.30 mM, C: $[Cu(II)]_{tot}$ = 1.80 mM, $[\mathbf{L}^3]_{tot}$ = 1.90 mM, D: $[Cu(II)]_{tot}$ = 0.95 mM, $[\mathbf{L}^4]_{tot}$ = 1.90 mM). (taken from [130])

Above pH 7 further deprotonations were observed in both equimolar systems. During the process $Cu_2H\mathbf{L}^4_2 = Cu_2\mathbf{L}^4_2 + H^+$, new bands appear between 350-550 nm both in the UV-Vis and CD spectra (Figs. 4.10 and 4.12), which were assigned to phenolate-to-copper(II) charge transfer (CT) transitions. The coordination of C-terminal phenolate obviously induces rearrangement of the peptide within the coordination sphere of copper(II), which explains the fundamental changes also observed in the d-d region of CD spectra (Fig. 4.10D and 4.12). On the other hand, the positions of d-d bands in the visible spectra do not change during the two successive deprotonations ($Cu_2H\mathbf{L}^4_2 \rightarrow Cu_2\mathbf{L}^4_2 \rightarrow Cu_2H_{-1}\mathbf{L}^4_2$). Considering also, that the individual UV-Vis spectra of $Cu_2\mathbf{L}^4_2$ and $Cu_2H_{-1}\mathbf{L}^4_2$ complexes have nearly identical intensity around 410 nm (Fig. 4.12), in both complexes a single phenolate oxygen is coordinated, and the second deprotonation is probably related to the formation of a metal-bound hydroxide ion.

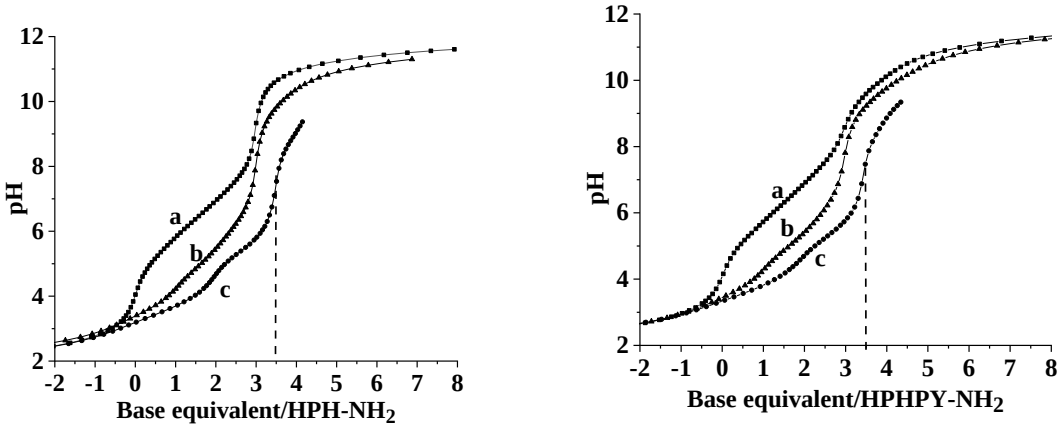

Figure 4.16 Titration curves of the free ligand (a), copper - ligand (II) 1:2 (b) and 1:1 (c) systems as a function of added base equivalent relative to the ligand $\mathbf{L}^3$ (left) and $\mathbf{L}^4$ (right). (taken from [130])

The analogous first deprotonation in presence of $\mathbf{L}^3$ ($Cu_2H_{-1}\mathbf{L}^3_2 \rightarrow Cu_2H_{-2}\mathbf{L}^3_2 + H^+$) does not result notable change neither on the UV-Vis, nor on the CD spectra, which would be expected if an additional nitrogen (e.g. amide) were coordinated. Although the subsequent process ($Cu_2H_{-2}\mathbf{L}^3_2 \rightarrow Cu_2H_{-3}\mathbf{L}^3_2 + H^+$) results in slight shift of both the UV-Vis and CD spectra (Figs. 4.10 and 4.12), considering the analogous sequences of these peptides, we propose hydroxide ion coordination in $Cu_2H_{-2}\mathbf{L}^3_2$ and $Cu_2H_{-3}\mathbf{L}^3_2$, too. Nevertheless, the participation of an N-donor in the second step, perhaps in one of the coordination isomers formed, cannot be ruled out.

Several 1:1 complexes ($[Cu^{I}\mathbf{L}^{3}]^{+}$, $[Cu^{II}\mathbf{L}^{3}+Cl]^{+}$, $[Cu^{II}\mathbf{L}^{4}+Cl]^{+}$, $[Cu^{II}\mathbf{L}^{4}]^{2+}$) were identified in the solutions by ESI-MS, and in the equimolar Cu(II)-$\mathbf{L}^{4}$ system a weak isotopic pattern attributed to the dimer $[Cu^{II}_{2}\mathbf{L}^{2}_{2}+2Cl]^{2+}$ was also found (Appendix Fig. A5).

Although the Cu$\mathbf{L}^{3}$ and CuH$\mathbf{L}^{4}$ complexes, having similar {NH_2,2×N_{im}} coordination mode to the His-brace motif, are not dominant at any pH, and those formed at higher pH have only limited analogy to the LPMO's active centres, we intended to explore the LPMO-like activity of these complexes. To this end, we also studied the electrochemical properties of the 1:1 systems both at pH 7.4 and 10.5 (Fig. 4.17 and Table 6). The copper(II) complexes of the two peptides show similar behaviours, and as expected [143], the cyclic voltammograms indicate quasi-reversible redox processes with rather large separation of cathodic and anodic peaks (Fig. 4.17 and Table 6). In all cases well defined cathodic peaks were observed, while beside the main anodic peaks, weakly developed minor peaks were also observed. The estimated formal redox potentials of the Cu(II)/Cu(I) redox couple for the two peptides are in the range 0.22 – 0.25 V and 0.01 – 0.04 V (vs. Ag/AgCl) at pH 7.4 and 10.5, respectively. These are rather positive values, and are close to the range generally observed for LPMO enzymes [37].

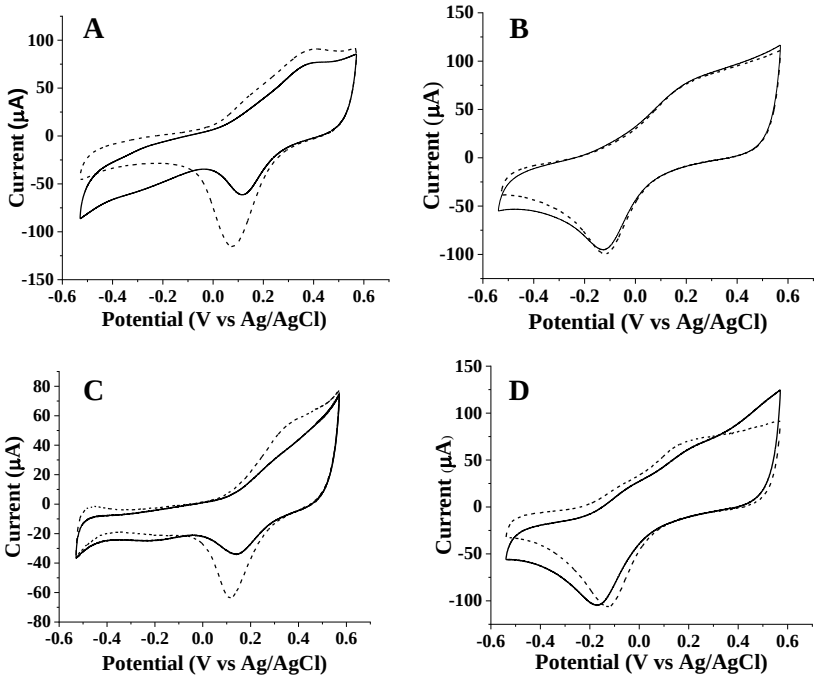

Figure 4.17 Cyclic voltammograms of the Cu(II)-$\mathbf{L}^{3}$ (A,B) and Cu(II)-$\mathbf{L}^{4}$ (C,D) 1:1 systems at pH= 7.4 (A,C) and pH = 10.5 (B,D) in absence (continuous lines) and in presence (dashed lines) of 1.1 equivalent H_2O_2 (T = 298 K, I = 0.2 M KCl, $[L]_{tot}$ = 0.6 mM). (taken from [130])

Table 6. Cathodic and anodic peaks observed by cyclic voltammetry in the Cu(II)-**L**^{3} and Cu(II)-**L**^{4} 1:1 systems ($[Cu(II)]_{tot}$ = 0.6 mM, $[H_2O_2]$ = 0.66 mM, [buffer] = 0.1 M, I = 0.2 M KCl). Potentials are given in V vs. Ag/AgCl electrode.

peptide	pH	1.1 eq. H_2O_2	Ep^{c} (V)	Ep^{mi*} (V)	Ep^{ma**} (V)
L^{3}	7.4	-	0.11	~ 0.16	0.39
		+	0.07	~ 0.16	0.40
	10.5	-	-0.13	-	0.21
		+	-0.12	-	0.21
L^{4}	7.4	-	0.14	-	0.31
		+	0.11	-	0.35
	10.5	-	-0.18	~ -0.03	0.19
		+	-0.13	~ -0.07	0.17

*minor anodic peak
** major anodic peak

4.2.2 Kinetic studies[5]

Our initial goals were only partially achieved by these model systems, the amide deprotonation was efficiently suppressed, but the complexes formed in neutral and alkaline pH show only limited analogy to the 'His-brace' motif. Nevertheless, we attempted to explore the LPMO-like activity of these complexes using the model substrate *p*-nitrophenyl-*β*-D-glucopyranoside (PNPG) at pH 7.4 and 10.5 in the presence of H_2O_2 as a co-substrate. Our preliminary study revealed that the dimer complexes alone result in only very slow hydrolysis of PNPG even at pH 10.5. Although, precipitate formation was detected above pH 9.6 in the Cu(II)-**L**^{4} 1:1 system during our potentiometric study, it was not seen in presence of 100 mM carbonate buffer (pH 10.5) and using 0.05 mM copper concentration. Similarly, at both pH, 10 mM H_2O_2 alone generates the production of insignificant amount of *p*-nitrophenolate. However, in the simultaneous presence of H_2O_2 and Cu(II)-complexes significant LPMO-like activity developed at both pH, which was found to be catalytic (Fig. 4.18). These findings point to oxidative processes, which are also supported by the presence of gluconate in the reaction mixture after 4h reaction time (Fig. 4.19). Remarkably, our systems exhibit significant activity even at pH 7.4, which is a unique feature among the few LPMO model complexes reported to date [48-52]. Nonetheless, at pH 7.4 inactivation of the complexes was noticed above 3 TON (Fig. 4.18A and B), which may be related to the oxidation of peptides by H_2O_2 during such long-term kinetic

[5] The text of this chapter is mainly based on ref. [130]

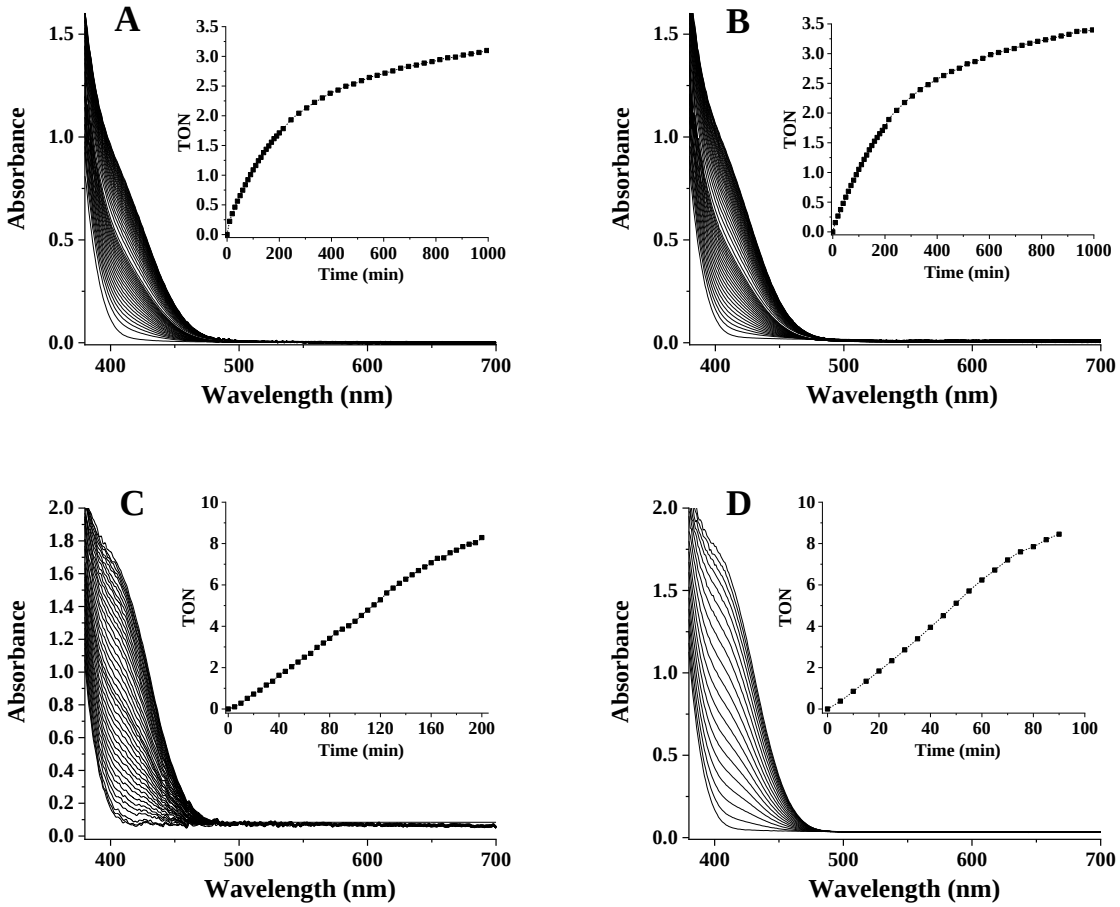

Figure 4.18 Time-dependent formation of *p*-nitrophenolate during the oxidation of PNPG catalysed by the Cu(II)-$\mathbf{L}^3$ (A,C) and Cu(II)-$\mathbf{L}^4$ (B,D) 1:1 systems at pH 7.4 (A,B) and pH 10.5 (C,D); the inserts show the plot of turnover number (TON) as a function of time. (At pH = 7.4: $[H_2O_2]$ = [PNPG] = 20 mM, $[Cu(II)]_{tot}$ = 0.1 mM, 5 mm cuvette; at pH = 10.5 $[H_2O_2]$ = 10 mM, [PNPG] = 5 mM, $[Cu(II)]_{tot}$ = 0.01 mM, 10 mm cuvette) (taken from [130]).

studies, similarly to the native enzymes [47]. It is also noteworthy, that the *bis*-complexes (even in presence of H_2O_2) yield negligible amount of *p*-nitrophenolate (probably due to the presence of dimers in low concentrations).

To obtain more comprehensive kinetic data, we also studied the rate of the reaction as a function of complex, hydrogen-peroxide and substrate concentrations. The observed rate constants of PNPG oxidation show linear dependence on the copper(II) concentration at both pH (Fig. 4.20), and the species formed at pH 10.5 are *c.a.* 5-fold more active than those at neutral pH. We also studied the effect of $CuCl_2$ salt on the PNPG oxidation in the absence of peptides. The observed rates were 7-9-fold smaller as compared to the peptide complexes, and the

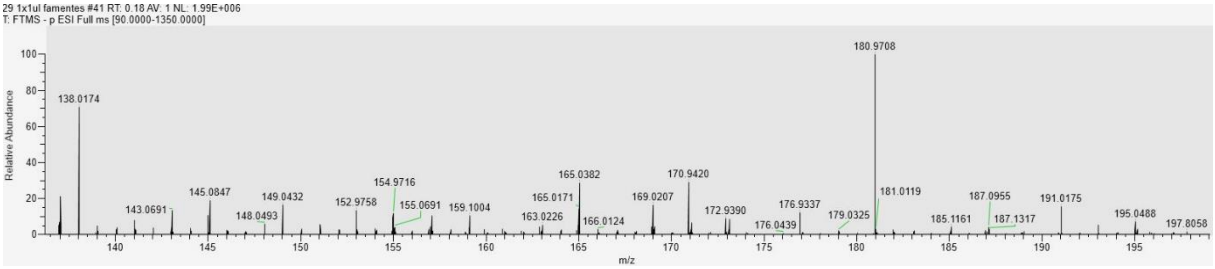

Figure 4.19 ESI-MS spectrum in negative mode of the reaction mixture of PNPG oxidation promoted by the Cu(II)-**L**^{3} system after 4h reaction time (pH = 10.5 [H_2O_2] = 10 mM, [PNPG] = 1 mM, [Cu(II)]$_{tot}$ = 0.05 mM). The peaks at m/z = 138.0174 and 195.0488 corresponds to *p*-nitrophenolate (calc. m/z = 138.0191) and gluconate (calc. m/z = 195.0505) anions, respectively. (taken from [130])

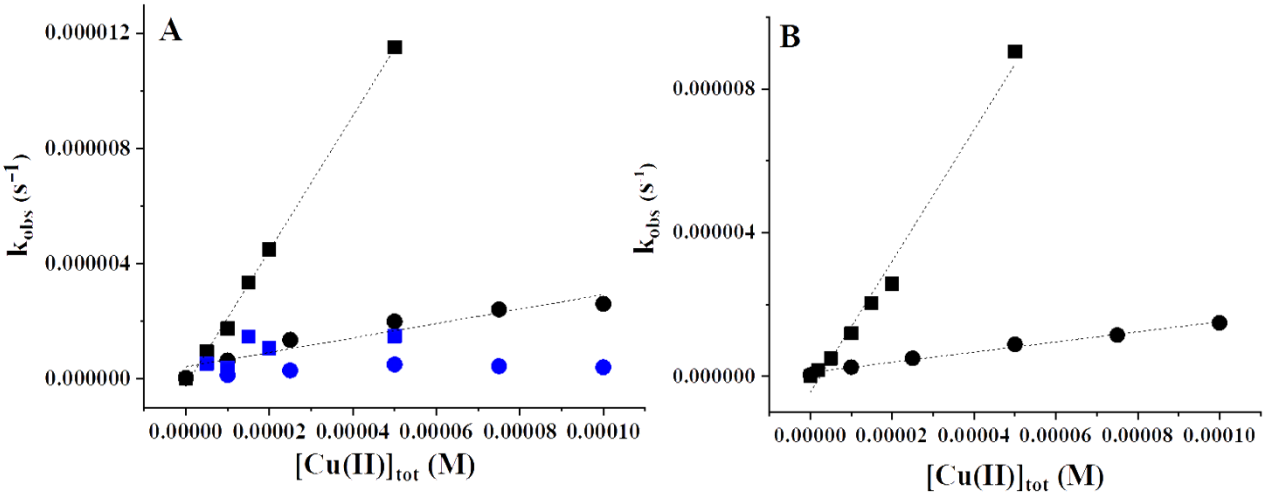

Figure 4.20 Dependence of k_{obs} of PNPG oxidation on the copper(II) concentration in the Cu(II)-**L**^{3} (A) and Cu(II)-**L**^{4} (B) 1:1 systems at pH = 7.4 (●) and 10.5 (■); [PNPG] = [H_2O_2] = 10 mM. (taken from [130])

concentration dependences were found to be rather scattered at both pH (see Fig. 4.20), probably due to the formation of $Cu(OH)_2$ precipitate.

The initial rates of oxidation reveal saturation kinetics with increasing concentration of both H_2O_2 and PNPG (Fig. 4.21). This indicates fast pre-equilibrium between the complex and substrate, as well as co-substrate before the rate determining redox process, therefore the Michaelis-Menten model is applicable in our systems. The corresponding constants thus calculated are summarized in Table 7. At neutral pH no analogous data are available in the literature. At pH 10.5 the k_{cat} values determined by us are similar to the only literature data [48], but the Michaelis constants (K_M) reveal somewhat stronger interaction of our complexes with the substrate, and especially with the co-substrate. More interestingly, our complexes present at pH

7.4 bind the substrate PNPG 10-20-fold more strongly than those at higher pH (Table 7), which can be assigned to the more open coordination environment of Cu(II) at pH 7.4. The comparison between the two peptides reveals some further subtle differences. For example, the k_{cat} values determined at the higher pH increase twice as much for $\mathbf{L}^4$ than for $\mathbf{L}^3$ complexes, as compared to those of the lower pH. The same is true for the strength of interaction ($1/K_M$) with H_2O_2. These data suggest that the LPMO-like activity of $\mathbf{L}^4$ complexes develops more favourably with increasing pH than that of $\mathbf{L}^3$ complexes. This can be due to the steric hindrance of the extra prolyl-tyrosine tail at pH 7.4 (which disappears at higher pH), or to the positive effect of the tyrosine residue in the catalytic mechanism at higher pH. Considering the relatively small differences, in the absence of further information, we propose the former explanation.

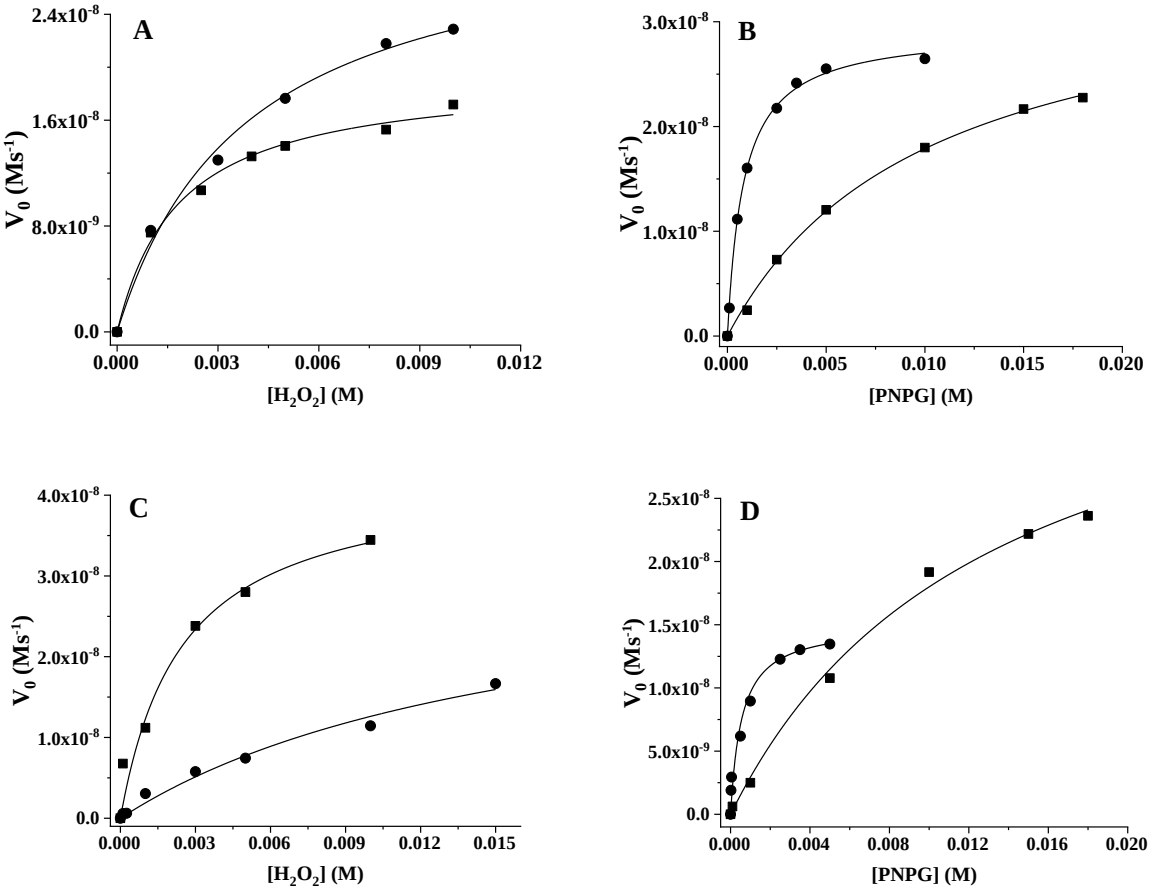

Figure 4.21 Dependence of the initial reaction rates of PNPG oxidation promoted by the Cu(II)-$\mathbf{L}^3$ (A,B) and Cu(II)-$\mathbf{L}^4$ (C,D) 1:1 systems on H_2O_2 (A,C) and PNPG (B,D) concentrations (●: pH 7.3, $[Cu(II)]_{tot}$ = 0.05 mM, ■: pH 10.5, $[Cu(II)]_{tot}$ = 0.01 mM, [PNPG] = 10 mM (A,C), $[H_2O_2]$ = 10 mM (B,D)). Solid lines are calculated from the data in Table 7 (taken from [130]).

Table 7. Michaelis-Menten parameters calculated by non-linear curve fitting from the data depicted in Fig. 4.21. (taken from [130])

(co)substrate	pH	parameter	Cu(II)-HPH	Cu(II)-HPHPY	ref [48]
PNPG	7.4	$10^3 \times k_{cat}$ (s^{-1})	0.59 ± 0.01	0.30 ± 0.01	not available
		K_M (mM)	0.82 ± 0.04	0.56 ± 0.07	
	10.5	$10^3 \times k_{cat}$ (s^{-1})	3.48 ± 0.05	4.17 ± 0.39	3.7
		K_M (mM)	9.44 ± 0.33	13.2 ± 2.4	20
H_2O_2	7.4	$10^3 \times k_{cat}$ (s^{-1})	0.63 ± 0.04	0.68 ± 0.02	not available
		K_M (mM)	3.83 ± 0.63	16.8 ± 0.6	
	10.5	$10^3 \times k_{cat}$ (s^{-1})	1.94 ± 0.08	4.25 ± 0.50	2.5
		K_M (mM)	1.83 ± 0.26	2.50 ± 0.50	30

4.2.3 Interaction of the dimer complexes with hydrogen-peroxide[6]

Since the observed LPMO-like activity requires the presence of H_2O_2, the reaction most probably proceeds via copper(II)-(hydro)peroxo complex(es). Therefore, we also studied the interaction of H_2O_2 and our complexes in the absence of PNPG.

After addition of 1.1 equivalent H_2O_2 to the Cu(II)-**L**^{3} 1:1 system several moderately intense bands appeared on the visible spectra by time both at pH 7.4 and 10.5 (Fig. 4.22). The intensity at 370 (pH 7.4) and at 380 nm (pH 10.5) steadily increases, which is much faster at higher pH. On the other hand, the initial intensity increase of the band at around 550 nm is followed by a decrease after 10 min (at pH 7.4) and 2 min (at pH 10.5). Parallel with these changes typical axial signals appeared on the EPR spectra beside the singlets of dimer species, indicating the partial formation of mononuclear complexes (Fig. 4.23).

The UV-Vis band observed at 370/380 nm is typical for mononuclear end-on Cu(II)-OOH species, and can be assigned to a ligand-to-metal charge transfer (LMCT) transition [144,145]. Indeed, the EPR parameters of the axial spectra determined by deconvolution (Fig. 4.23) are similar to other 3N coordinated mononuclear hydroperoxo complexes with tetragonal/square planar geometry [144,145]. The identity of the transient complex with bands around 550 nm is less clear. Since upon addition of H_2O_2 the coordination of further nitrogen donors to Cu(II) - which would result such a notable blue-shift of d-d bands - is unlikely, these

[6] The text of this chapter is mainly based on ref. [130]

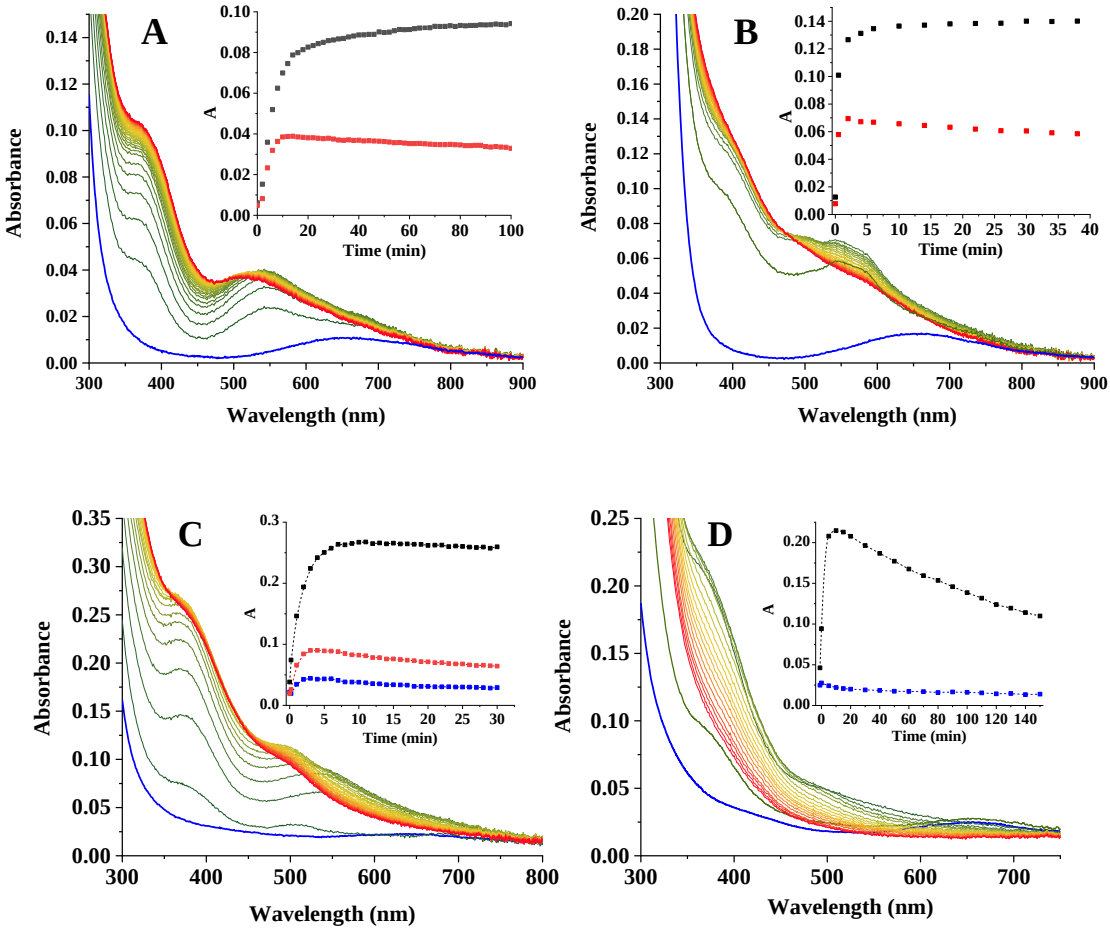

Figure 4.22 Time dependence of UV-Vis spectra of the Cu(II)-$\mathbf{L^3}$ 1:1 systems upon addition of 1.1 equivalent H_2O_2 at (A) pH 7.4 ([Cu(II)] = 0.2 mM, 10 mm cuvette), (B) pH 10.5 ([Cu(II)] = 0.2 mM, 10 mm cuvette); (C) 10 equivalent H_2O_2 at pH 7.4 ([Cu(II)] = 0.2 mM, 10 mm cuvette); (D) 200 equivalent H_2O_2 at pH 7.4 ([Cu(II)] = 0.05 mM, 50 mm cuvette). Blue lines: the initial spectra, green-to-red lines changes upon addition of H_2O_2. Inserts show the time dependence of spectrum intensity at 370 (A,C,D) or 380 (B) nm (black squares), at 550 nm (red squares) and at 650 nm (blue squares). (taken from [130])

transitions can be also assigned to $HOO^{-}\rightarrow$Cu LMCT bands. Several 1,2-peroxo-dicopper(II)complexes have been reported to have LMCT bands around 500-600 nm [146-149]. Therefore, in the absence of other information, tentatively we assigned these LMCT bands to a 1,2-peroxodicopper(II) complexes formed in lower concentrations and being in equilibrium with the mononuclear Cu(II)-OOH species. The interaction with equivalent amount of H_2O_2 only slightly affects the electrochemical (CV) properties of our complexes (Fig. 4.17 and Table 6), indicating that copper remains in its +2 oxidation state.

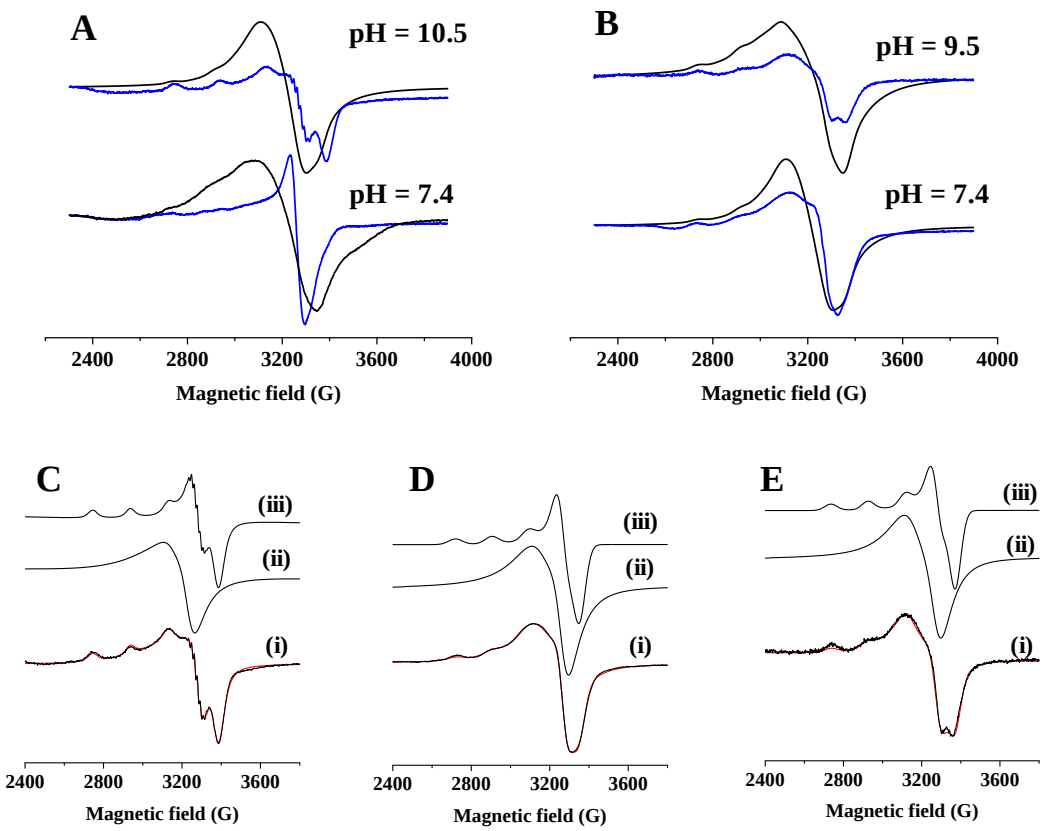

Figure 4.23 A,B: The change of 77K EPR spectra upon addition of 25 eq. H_2O_2 in the Cu(II)-**L**^{3} (A) and Cu(II)-**L**^{4} (B) 1:1 systems. C,D,E: Deconvolution of the EPR spectra obtained after addition of H_2O_2 to the (C) Cu(II)-**L**^{3} at pH 10.5, (D) Cu(II)-**L**^{4} at pH 7.4, (E) Cu(II)-**L**^{4} at pH 9.5; (i) experimental (black) and simulated (red) spectra, (ii) and (iii) are the component spectra of the dimer and monomer complexes, respectively. Isotropic components were described with singlet lines. The EPR parameters of the mononuclear (hydro)peroxo complexes: (C) $g_{\perp}$ = 2.045(2), $g_{\parallel}$ = 2.222(2), $A_{\perp}$ =14(2) G, $A_{\parallel z}$=189(2) G, $A_{N,\perp}$ = 15(2) G; (D) $g_{\perp}$ = 2.058(2), $g_{\parallel}$=2.248(2), $A_{\perp}$=12(5)G, $A_{\parallel}$=182(2)G; (E) $g_{\perp}$ = 2.050(2), $g_{\parallel}$=2.231(2), $A_{\perp}$ = 10(5) G, $A_{\parallel}$ =186(2) G. (taken from [130])

The addition of 10-fold excess of H_2O_2 result in similar behaviours, but faster and more complete formation of the (hydro)peroxo complexes (Fig. 4.22C), indicating the presence of equilibrium systems. However, after 5-10 minutes the intensity of LMCT and even the d-d bands start to slowly decrease, which is more pronounced at 200-fold excess of H_2O_2 (Fig. 4.22D). The transient species with bands around 550 nm, which is tentatively assigned as 1,2-peroxodicopper(II) complex, formed in lesser amount at high excess of H_2O_2 (Fig. 4.22D), as expected for a peroxo-bridged dimer. Based on the above observations, the mononuclear end-on

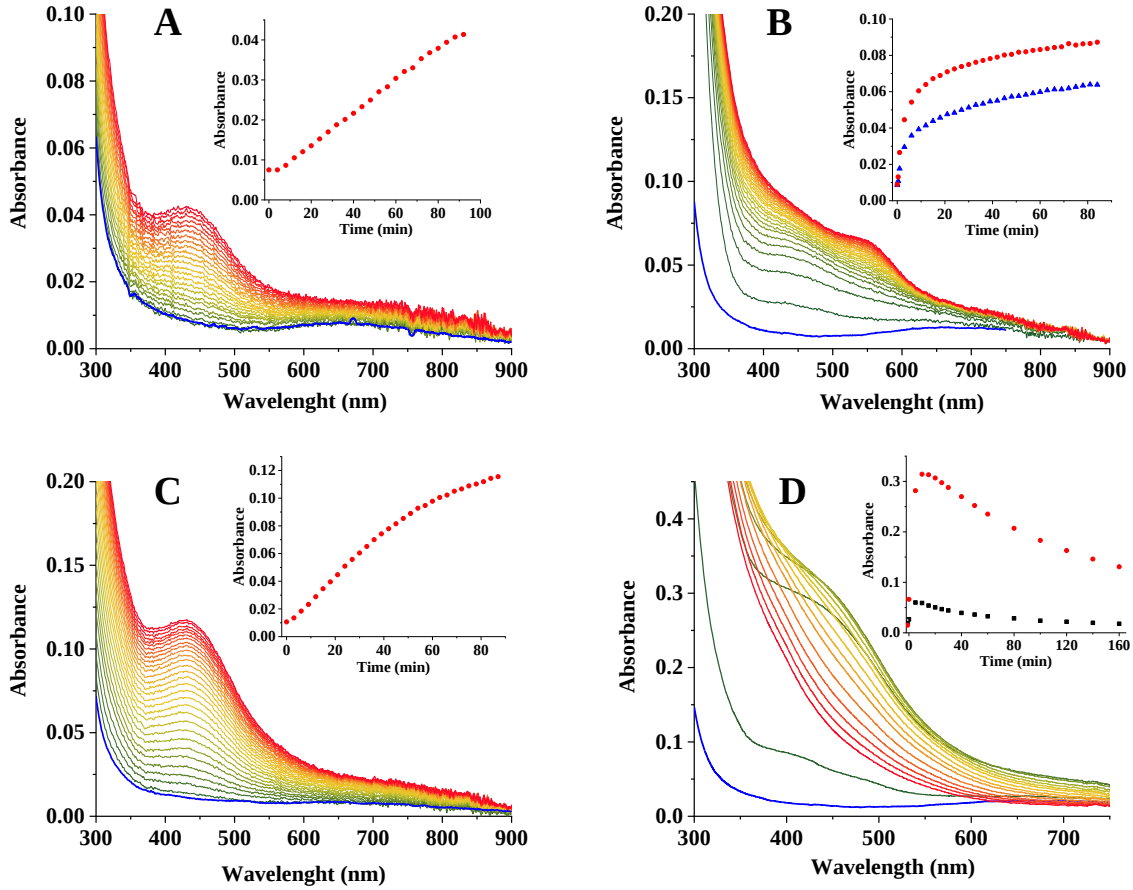

Figure 4.24 Time dependence of UV-Vis spectra of the Cu(II)-$\mathbf{L^4}$ 1:1 systems upon addition of 1.1 eq. (A,B) 10 eq. (C) and 200 eq. H_2O_2 (D) at pH 7.4 (A,C,D) and at 10.5 (B). Blue lines: the initial spectra, green-to-yellow-to-red lines changes upon addition of H_2O_2. Inserts show the time dependence of spectrum intensity at 440 nm (●), 550 nm (▲) and 650 nm (■). ([Cu(II)] = 0.05 mM, 20 mm cuvette (A,B,C) and 50 mm cuvette (D)). (taken from [130])

Cu-OOH species formed in the Cu(II)-HPH system is stable for 1-2 hours at low, but decomposes more rapidly at high H_2O_2 excess. Its decomposition results in the formation of Cu(I) species, as indicated by the intensity decrease of d-d transitions at high H_2O_2 excess (Fig. 4.22D). The reduction of copper(II), at least partly, may due to catalytic disproportionation of H_2O_2 by the Cu(II)/Cu(I) couple, since the amount of dioxygen bubbles detected after longer reaction times was much higher than would be expected from a simple reduction process (~ 0.005 cm^3 under the conditions of Fig. 4.22D).

Basically similar behaviours were observed for the interaction of Cu(II)-$\mathbf{L^4}$ complexes with H_2O_2, too, although the position of the $HOO^- \rightarrow$ Cu LMCT band is somewhat different. The

addition of 1.1 or 10 equivalent H_2O_2 to the Cu(II)-$\mathbf{L^4}$ complexes at pH 7.4, results in the development of an LMCT band at 440 nm (Fig. 4.24A and C). At pH 10.5, an additional band at 550 nm also appeared (Fig. 4.24B). Parallel with these processes the partial formation of mononuclear complexes with axial EPR spectra were also observed (Fig. 4.23B). Similarly to the former system, the (hydro)peroxo complexes formed at low H_2O_2 concentrations are stable for several hours, and the metal ion remains in its +2 oxidation state (Fig. 4.17C and D). Although, the formation of these (hydro)peroxo complexes at low H_2O_2 concentrations is somewhat slower than in the former system, at 200-fold H_2O_2 excess their development and subsequent degradation show similar kinetics (Fig. 4.24D). This degradation also results in the formation of dioxygen bubbles and the decrease of d-d band intensity after longer reaction time. Although the LMCT band at 440 nm is outside the 350-420 nm range typically observed for mononuclear Cu(II)-OOH complexes [150], the single band at 440 nm cannot be clearly assigned to any copper-oxygen species. The addition of H_2O_2 to LPMO enzymes in the absence of substrate may results in the formation of a stable Cu(II)−tyrosyl complex with an absorbance of around 420 nm [47]. This is unlikely in our case, since the characteristic redox process of tyrosyl radicals was absent on the cyclic voltammograms. Therefore, due to the similar behaviours of the two systems, we hypothesize the formation of similar (hydro)peroxo complexes of the two peptides.

4.2.4 Mechanistic considerations[7]

Our data indicate, that the observed Cu(II)-OOH species are one of the key intermediates during the oxidative cleavage, their faster formation at higher pH results in higher rate of transformation. The important role of such Cu(II)-OOH species was also acknowledged in all previous model studies [48-52]. LPMOs are able to function by using either O_2 or H_2O_2 as oxidant depending on the conditions [40-42], although dioxygen seems to be their natural co-substrate [37,41,42]. In both cases Cu(II)-OOH species appears in the proposed catalytic cycles, but experimental [43] and computational studies [44,41,42] indicated that a highly reactive Cu(II)-oxyl species abstracts H-atom from the substrate. In LPMOs the Cu(II)-oxyl radical presumably forms from a Cu(II)-OOH species via a Cu(I)-H_2O_2 adduct, and therefore its formation requires an external electron. The latter is obviously not available in our model systems, but as discussed above, partial reduction of Cu(II) to Cu(I), as well as the formation of dioxygen bubbles were observed

[7] The text of this chapter is mainly based on ref. [130]

after prolonged reaction time in the absence of substrate and at high excess of H_2O_2. However, in presence of PNPG no dioxygen bubbles could be visually observed even at 200-fold excess of H_2O_2 and after longer reaction time. Based on this observation, we speculate, that after the reduction of peptide-bound Cu(II) by H_2O_2, which would produce only a tiny amount of O_2, the resulting Cu(I) complex binds H_2O_2 and enters into a similar catalytic cycle (Chart 4.4), as suggested for the native LPMOs [42]. This assumption is supported by the fact that during the oxidation of PNPG the intensity of d-d transitions completely diminishes after 1-2 TON, but the catalytic cycle continues to work (Fig. 4.25).

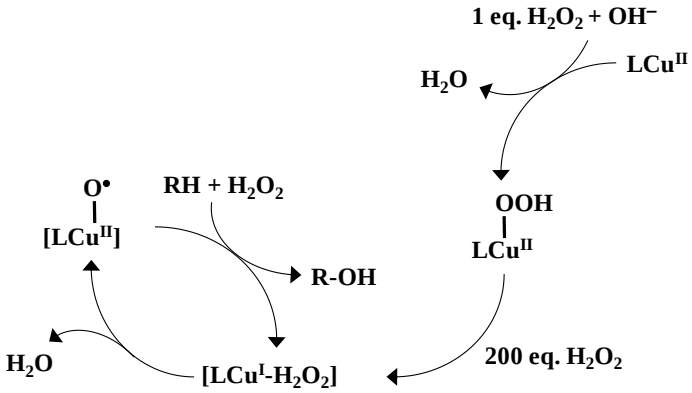

Chart 4.4 Supposed reaction pathway of PNPG (simplified as RH) oxidation by the Cu(II)-peptide complexes (taken from [130])

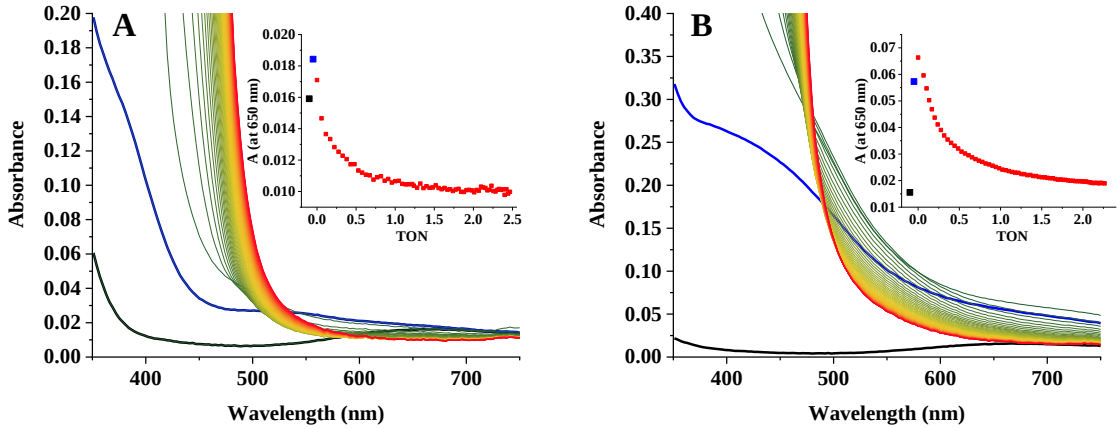

Figure 4.25 UV-Vis spectra of the Cu(II)-$\mathbf{L^3}$ (A) and Cu(II)-$\mathbf{L^4}$ (B) 1:1 systems at pH 7.4 and at [Cu(II)] = [HPH] = 0.05 mM in 50 mm cuvette (black line), + 10 mM H_2O_2 (blue line), + 10 mM PNPG time dependence up to 650 minutes (green-to-red lines); insert show the change of spectrum intensity at 650 nm as a function of turn-over number (TON); initial spectrum (■), + 10 mM H_2O_2 (■), time (TON) dependent changes after addition of 10 mM PNPG (■). TONs were calculated based on the absorbances at 450 nm where $\varepsilon_{\text{p-nitrophenolate}}$ (450nm) ~ 0.2*$\varepsilon_{\text{p-nitrophenolate}}$ (400nm). (taken from [130])

4.3 The interaction of half-sandwich (η^5-Cp*)Rh(III) cation with histidine containing peptides and their ternary species with (N,N) bidentate ligands

In order to uncover the basic solution thermodynamic and coordination properties of imidazole and its derivatives toward half sandwich Rh(III) ion, I studied the interactions of (η^5-Cp*)Rh(III) cation with 13 ligands, which can be divided into two groups. The first group consist simple imidazole compound, synthetic peptides with histidines at different positions and Gly-Gly-Ala (Chart 4.5) a reference peptide containing no histidine. The second group contains some endogenous histidine derivatives, such as histidine itself, thyrotropin-releasing hormone (TRH), carcinine, carnosine and the growth-modulating peptide GHK (Chart 4.6), which are inherently present in the human body. After exploring the binary (η^5-Cp*)Rh(III) complexes of these ligands, we also studied some (η^5-Cp*)Rh(III)-A-B ternary systems (where A = the studied peptides; B = 2,2'-bipyridyl (bpy) or ethylene-diamine (en)), in order to mimic the interaction of the (η^5-Cp*)Rh(III)-based potentially anticancer or drug delivery agents with biogenic peptides and proteins. The protonation constants of these ligands (Table 8 and 9) are in reasonably good agreement with earlier reports and other histidine containing peptides reported in the literature [131].

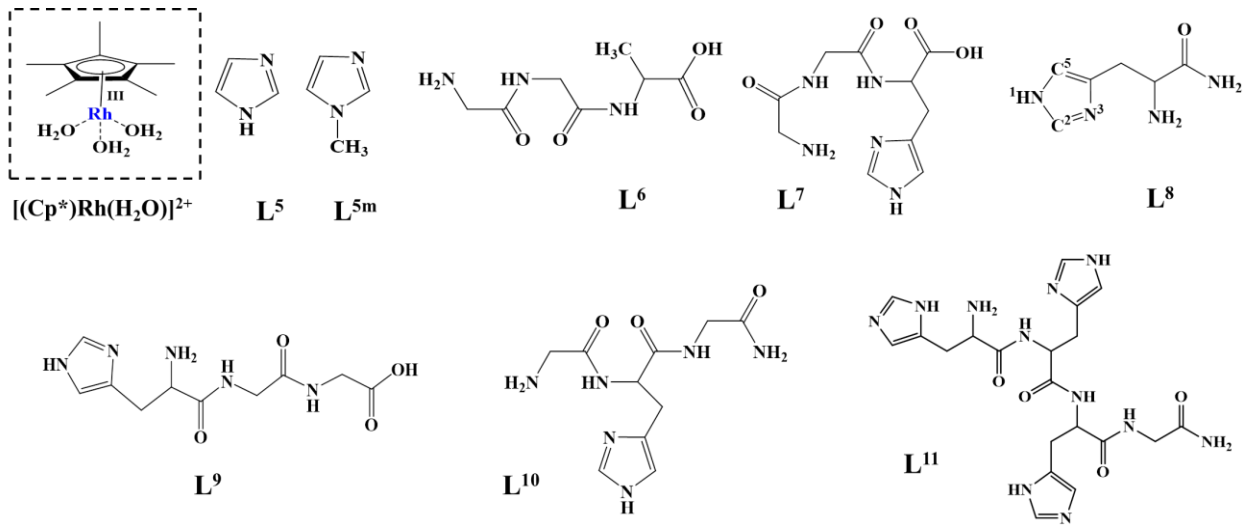

Chart 4.5 Schematic structures of the studied ligands belonging to the first group (the numbering of imidazole ring is shown for $\mathbf{L}^8$) (taken from [151])

4.3.1 Interaction of (η^5-Cp*)Rh(III) with some imidazole derivatives and synthetic histidine containing peptides[8]

4.3.1.1 Interaction of (η^5-Cp*)Rh(III) with imidazole (L^5) and N-methylimidazole (L^{5m})[9]

The monodentate imidazole coordination is the most frequently detected binding mode of peptides and proteins to half-sandwich Ru(II)/Rh(III) complexes [103,152-157], therefore the study of these simple ligands may also help to understand the coordination chemistry of His-containing peptides/proteins. Indeed, (η^5-Cp*)Rh(III) forms rather stable $[ML^{5(m)}]^{2+}$, $[ML_2^{5(m)}]^{2+}$ and $[ML_3^{5(m)}]^{2+}$ complexes (here and in the following M stands for (η^5-Cp*)Rh(III) cation) up to the neutral pH range (Table 8, Fig. 4.26). The formation constants of these parent complexes are nearly identical for the two ligands, and indicate somewhat lower stability than those of the rela-

Table 8. Protonation constants of the studied ligands, formation constants of their (η^5-Cp*)Rh(III) complexes and some derived data (T = 298 K, I = 0.20 M (KCl)), with estimated errors in parentheses (last digit). The constants in square brackets are only indicative values, since the systems were non-equilibrated. (taken from [151])

	log β_{pqr}							
Species(pqr)	**L^5**	**L^{5m}**	**L^6**	**L^7**	**L^8**	**L^9**	**L^{10}**	**L^{11}**
H_4L (041)								24.77(3)
H_3L (031)	-	-	-	17.45(2)	-	16.17(7)	-	19.92(2)
H_2L (021)	-	-	11.25(2)	14.80(1)	12.90(1)	12.89(3)	14.50(2)	14.03(2)
HL (011)	7.02 (1)	7.10 (1)	7.98(1)	8.00(1)	7.48(1)	7.42(1)	8.23(1)	7.56(1)
MH_2L								23.31(1)
MHL (111)	-	-	10.63(8)	13.92(5)	-	14.88(1)	13.98(8)	19.11(1)
ML (101)	5.83(2)	5.94(2)	6.68(3)	9.72(3)	11.09(5)	11.38(1)	-	12.98(1)
ML_2 (102)	10.46(2)	10.68(2)	-	-	-	-	-	–
ML_3 (103)	13.43(3)	13.64(3)	-	-	-	-	-	–
$MH_{-1}L$ (1-11)	-	-	0.88(3)	2.75(4)	5.04(5)	5.89(11)	7.04(4)	–
$MH_{-2}L$ (1-21)	[-10.2]	-	-9.74(3)	[-8.1]	[-5.2]	[-4.6]	[-2.8]	–
$MH_{-1}L_2$ (1-12)	[2.6]	0.39(4)	-	-	-	-	-	–
M_2L (201)								19.49(2)
pK_{NH}, amide	-	-	5.80	6.97	6.05	5.49	~3.5	–
$pM_{7.4}$	6.82	6.89	8.57	10.47	13.07	13.94	14.48	13.44

pM values at pH 7.4 and $10\times c_M = c_L = 10$ μM, T = 25 °C; I = 0.20 M (KCl), where $pM = -\log([M] + 2[M_2(OH)_3] + 2[M_2(OH)_2])$.

[8] The text of this chapter is mainly based on ref [151]
[9] The text of this chapter is mainly based on ref [151]

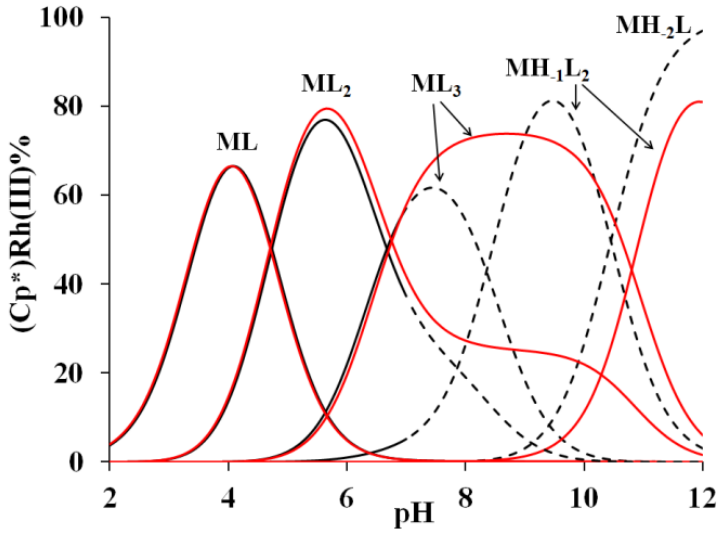

Figure 4.26 Speciation in the (Cp*)Rh(III)-imidazole (**L**^{5}, black) and (Cp*)Rh(III)-1-methylimidazole (**L**^{5m}, red) 1:6 systems (T = 298 K, I = 0.2 M KCl, $[M]_{tot}$ = 0.001 M). Dashed lines show the region of slow processes, where only approximate speciation can be given. (taken from [151])

ted (η^6-*p*-cymene)Ru(II)-**L**^{5m} complexes [158].

Since Rh(III) is diamagnetic (low spin d^6 cation) in all our complexes, NMR is a straightforward method to gain information on the solution structure and also to support the solution speciation. Indeed, all **L**$^{5(m)}$ complexes have slow ligand exchange on the NMR timescale, and thus the changes in speciation can be easily followed (Fig. 4.27). Interestingly, in the (η^5-Cp*)Rh(III)-**L**^{5} system a broad signal appeared at 12 ppm (see the discussion on this signal later) between pH 4–6. Although, up to pH 7 the two systems show nearly identical behaviours, above this pH they are rather differently. In the (η^5-Cp*)Rh(III)-L^{5m} system the complex formation processes are fast enough for equilibrium study even in alkaline solution, where a single additional species, $[MH_{-1}\mathbf{L}^{5m}{}_2]^+$ (= $[M(OH)\mathbf{L}^{5m}{}_2]^+$) could be detected, both by potentiometry and by ^{1}H NMR. On the other hand, in the (η^5-Cp*)Rh(III)-**L**^{5} system the time needed to reach the equilibrium considerably increased above pH 7, which prevented the correct equilibrium description. After 24 h of equilibration at pH > 7 the ^{1}H NMR spectra indicated the formation of a great number of isomers (Fig. 4.27A). Considering the difference between the two ligands, the most plausible reason of isomer formation is the metal-promoted deprotonation and coordination of imidazole N^{1}H group of **L**^{5}, and the subsequent formation of different oligomers

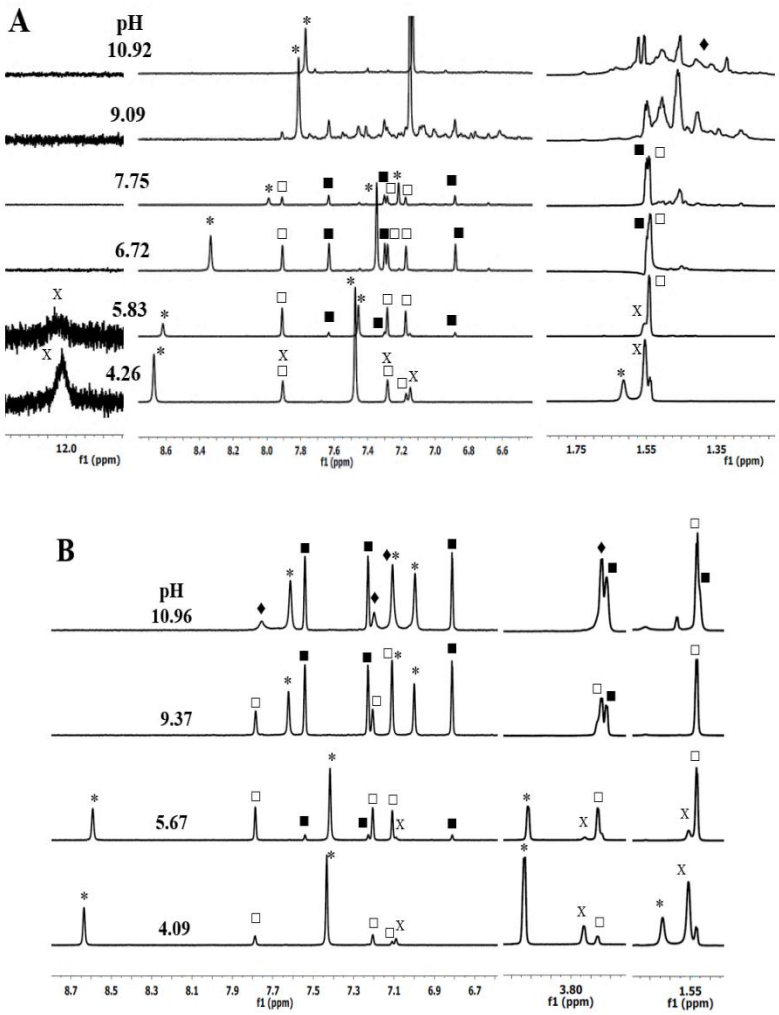

Figure 4.27 pH-dependent ^{1}H NMR spectra of (Cp*)Rh(III)-**L**^{5} (A) and –**L**^{5m} (B) 1:4 systems with the tentative assignment of the signals (* = free ligand or metal ion, × = ML, □ = ML_2, ■ = ML_3, ♦ = $ML_2(OH)$) (taken from [151])

via imidazolato bridges. This would not be very unusual, since the crystal structure of an imidazolato-bridged (η^5-Cp*)Rh(III) complex has been already reported in the literature [159].

4.3.1.2 Interaction of (η^5-Cp*)Rh(III) with GGA (L^6)[10]

In order to assess the effect of histidine moiety of tripeptides on (η^5-Cp*)Rh(III) binding, first we studied the complexes of GGA peptide, having no coordinating side-chain. The combined potentiometric, UV–Vis and NMR results revealed the formation of four species between pH = 2–11 (Table 8, Fig. 4.28). The formation constants obtained reflect surprisingly

[10] The text of this chapter is mainly based on ref [151]

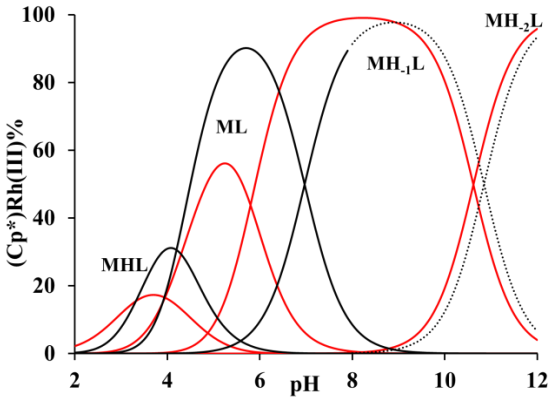

Figure 4.28 Speciation in the (η^5-Cp*)Rh(III)-GGA (**L**^{6}, red lines) and (η^5-Cp*) Rh(III)-GGH (**L**^{7}, black lines) 1/1 systems (T = 298 K, I = 0.2 M KCl, $[M]_{tot}$ = 0.001 M). The lines of uncomplexed metal ion are not shown for clarity. Dashed lines show the region of slow processes, where only approximate speciation can be given. (taken from [151])

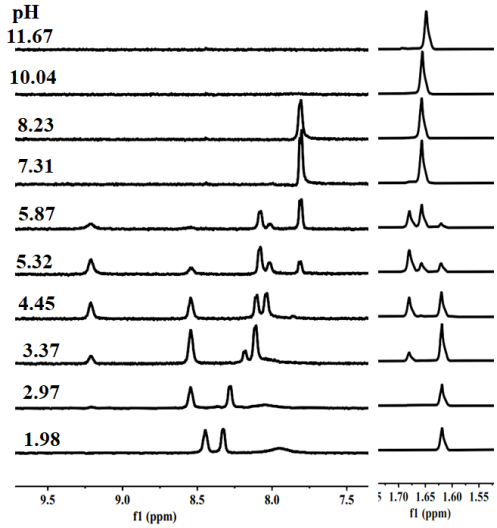

Figure 4.29 Low and high-field parts of pH-dependent ^{1}H NMR spectra of the Rh(Cp*)-GGA (**L**^{6}) 1/1 system (taken from [151])

high (η^5-Cp*)Rh(III) binding affinity of this simple peptide in the physiological pH range. The (η^5-Cp*)Rh(III) promoted deprotonation of N-terminal ammonium group takes places at four units lower pH than in the free ligand, confirming its strong binding to the metal ion. The important down field shift of ^{2}G-NH proton signal (8.55 → 9.22 ppm, see Fig. 4.29) in [M**L**^{6}]$^+$ suggests that beside the ^{1}G amino nitrogen the ^{1}G amide oxygen is also coordinated. The next species ([M**L**^{6}]$^+$ = [MH$_{-1}$**L**^{6}] + H$^+$, pK = 5.80) is dominant in the solution between pH 7–9. Parallel with its formation the signal of ^{2}G amide disappeared from the spectrum (Fig. 4.29), indicating its metal-promoted deprotonation, especially considering the fact, that the signal of ^{3}A amide is still present at pH 7.3. To our knowledge this is the first reported pK for amide nitrogen.

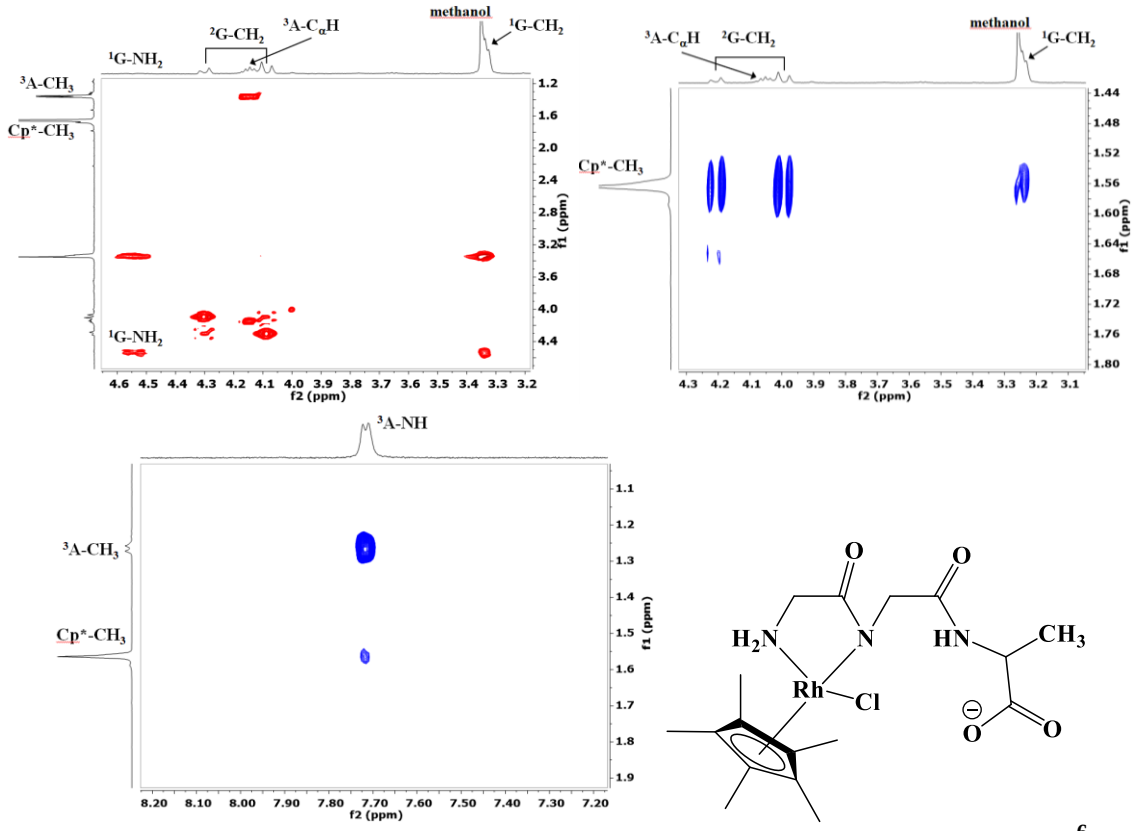

Figure 4.30 Parts of the TOCSY (red) and NOESY (blue) spectra of the (Cp*)Rh(III)-**L**^{6} 1:1 system at pH 7.6 (taken from [151]) and structure of MH_{-1}**L**^{6} complex

deprotonation of simple peptides promoted by a half-sandwich cation. The only related values, which have been determined for (η^5-Cp*)Rh(III) complexes of peptidohydroxamic acids [107], indicate similar pH range for (η^5-Cp*)Rh(III)-promoted amide deprotonation

On the ^{1}H NMR spectrum of [MH_{-1}**L**^{6}] new peaks appeared around 4.45 ppm, which resulted strong cross-peaks with the ^{1}G-CH_2 proton signals on the TOCSY (TOtal Correlation SpectroscopY) spectrum (Fig. 4.30). Consequently, this new peaks belong to the terminal amino group, i.e. its proton-exchange with the solvent slows down considerably upon coordination. The NOESY (Nuclear Overhauser Effect SpectroscopY) spectrum of [MH_{-1}**L**^{6}] revealed cross-peaks between the Cp*-CH_3, ^{1}G-CH_2 and ^{2}G-CH_2 protons, confirming the coordination of ^{1}G-amino and ^{2}G-amide nitrogens. On the other hand, the coordination of C-terminal carboxylate is not supported by our experimental data, i.e. the metal ion is coordinated by a {NH_2,N^- + Cl^-} donor set (Fig. 4.30). Above pH 9 a further deprotonation was observed (pK = 10.62). During this process new set of peaks were not developed, only those of [MH_{-1}**L**^{6}] were shifted, indicating a

fast-exchanging deprotonation. Although, the signal of ^{3}A amide proton disappeared from the spectra above pH 8, it is due to the acceleration of its proton exchange with the bulk water, since the coordination of this amide nitrogen would result in the development of a new set of peaks. The most obvious explanation of this process is the formation of mixed hydroxido complex, *i.e.* $\{NH_2,N^-,OH^-\}$ coordinated $[MH_{-2}\mathbf{L}^{6}]^-$ species.

4.3.1.3 Interaction of (η^5-Cp*)Rh(III) with GGH (L^7)[11]

GGH is an analogue of the N-terminal copper and nickel binding site of human serum albumin. Between pH 3–6 four distinct signals of Cp*-methyl protons can be detected on the ^{1}H NMR spectra (Figure 4.31), two of which belong to $[MH\mathbf{L}^{7}]^{2+}$. This indicates the formation of isomers of this complex, either diastereomers or binding isomers. Surprisingly, two broad signals also appeared at 12.0 and 12.3 ppm on the ^{1}H NMR spectra (Figure 4.31) up to pH 6 in 90% H_2O – 10% D_2O solution, which were absent in 100% D_2O. Similar signals were detected in the acidic pH-range for all imidazole derivatives, except for N-methylimidazole, and can be assigned to the non-coordinated, and therefore protonated NH proton (here probably N^1H, see later) of imidazole ring, whose proton exchange slowed down significantly due to the metal coordination of the other (here probably N^3-) nitrogen. In the present case, the two signals belong to $[MH\mathbf{L}^{7}]^{2+}$ (12.0 ppm) and $[M\mathbf{L}^{7}]^{+}$ (12.3 ppm) complexes. Parallel with the formation of $[M\mathbf{L}^{7}]^{+}$ the signal of ^{2}G-NH is considerably shifted as compared to the free ligand (8.45 → 9.55 ppm, Fig. 4.31). The TOCSY spectrum observed at pH 5.6 indicates unusually high – approximately 400 Hz - inequivalence for the ^{1}G and ^{3}H methylene-protons (Figure 4.32), which is likely due to the involvement of these methylene groups in rather rigid fused chelate ring(s). Remarkably, two peaks at 5.00 and 5.33 ppm are also appeared on the TOCSY spectrum resulting strong cross-peaks with the ^{1}G methylene-protons (Figure 4.32), which therefore belong to the Rh(III) coordinated terminal amino group. Based on the NOESY spectrum, of the two imidazole CH protons, only C^2H is close to the Cp* methyl protons (Figure 4.32), indicating the coordination of N^3-nitrogen. Besides, spatial proximity has been detected between Cp*-CH_3 and ^{3}H-$C_\beta H_2$, as well as between ^{3}H-C^5H and ^{1}G-NH_2 protons (Figure 4.32). All these facts indicate tridentate $\{NH_2,C{=}O,N^3_{im}\}$ type coordination in $[M\mathbf{L}^{7}]^{+}$. Indeed, $[M\mathbf{L}^{7}]^{+}$ has considerably higher thermodynamic stability as compared to $[M\mathbf{L}^{6}]^{+}$ (log β_{101} = 6.68 and 9.71 for $\mathbf{L}^{6}$ and $\mathbf{L}^{7}$,

[11] The text of this chapter is mainly based on ref [151]

respectively), due to the additional imidazole coordination. In turn, the enhanced stability of tridentate coordination in M**L**^{7} results in markedly higher pK for the next deprotonation ([ML]$^{+}$ = [MH$_{-1}$L] + H^{+}, pK_{ML} = 5.80 (**L**^{6}) and 6.98 (**L**^{7}), see Fig. 4.28). During this process the amide proton signal of ^{2}G disappeared from the ^{1}H NMR spectra (Fig. 4.31). Since the ^{3}H amide signals were still detectable, the Rh(III) promoted deprotonation of ^{2}G amide took place during this process. Interestingly, the deprotonation resulted in the duplication of signals, i. e. the formation

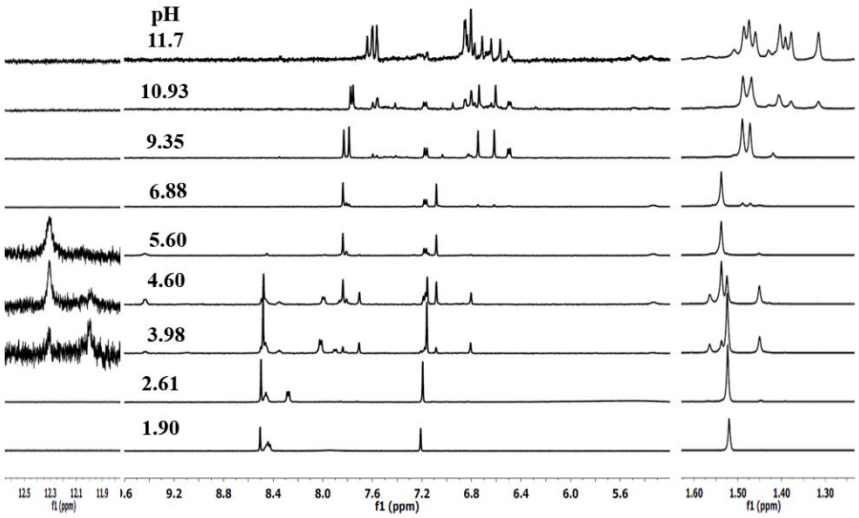

Figure 4.31 Low- and high-field parts of pH-dependent ^{1}H NMR spectra in (Cp*)Rh(III)-GGH (**L**^{7}) 1/1 system (taken from [151])

of two isomers with nearly equal concentrations. The EXSY (EXchange SpectroscopY) spectrum measured at pH 9.2 reflects that these isomers are in conformational or chemical exchange (Fig. 4.33), i.e. are not diastereoisomers. The mass spectrum detected under identical conditions indicates the presence of a monomer and a dimer species in nearly equal amount (Fig. 4.33), thus the exchange is related to the 2[MH$_{-1}$**L**^{7}] = [MH$_{-1}$**L**^{7}]$_{2}$ equilibrium. The pH-metric titration curves can be well fitted by either the monomer or the dimer species, but the parallel refinement of β_{1-11} and β_{2-22} is not possible. However, assuming equal concentration of the monomer and dimer logβ_{1-11} ~ 2.6 and logβ_{2-22} ~ 8.6 can be estimated. Based on the NOESY spectrum, both CH protons of the imidazole ring (C^{2}H and C^{5}H) of both complexes are in spatial proximity to the Cp* methyl protons (Fig. 4.33). This is only possible if the N^{1} nitrogen of imidazole ring is coordinated to Rh(III). In addition, the ^{1}G-CH$_{2}$ protons are also close to the Cp* methyl protons, suggesting {NH$_{2}$,N^{-},N$^{1}_{im}$} type coordination in both species. In one of these complexes the histidine C$_{\beta}$H$_{2}$ protons are slightly, in the other they are considerably inequivalent (Fig. 4.33). In

the monomer complex the imidazole group is part of a 10-membered, rather strained macrochelate ring (Fig. 33E), and its reduced chelate effect allows the formation of dimer species. In $[MH_{-1}\mathbf{L}^7]_2$ the imidazole rings bind to the adjacent (η^5-Cp*)Rh(III), resulting in a more relaxed conformation of the histidine side chains (Fig. 33E), thus the dimer has probably the more equivalent histidine $C_\beta H_2$ protons (signals marked by 'a' in Fig. 4.33). Above pH 8 a further deprotonation was detected (pK ~ 11), but the complex formation processes become too slow for equilibrium study. At pH 11.6 at least nine peaks appeared in the region of Cp* methyl protons (Fig. 4.31), indicating the formation of several isomers, but structural details could not be extracted.

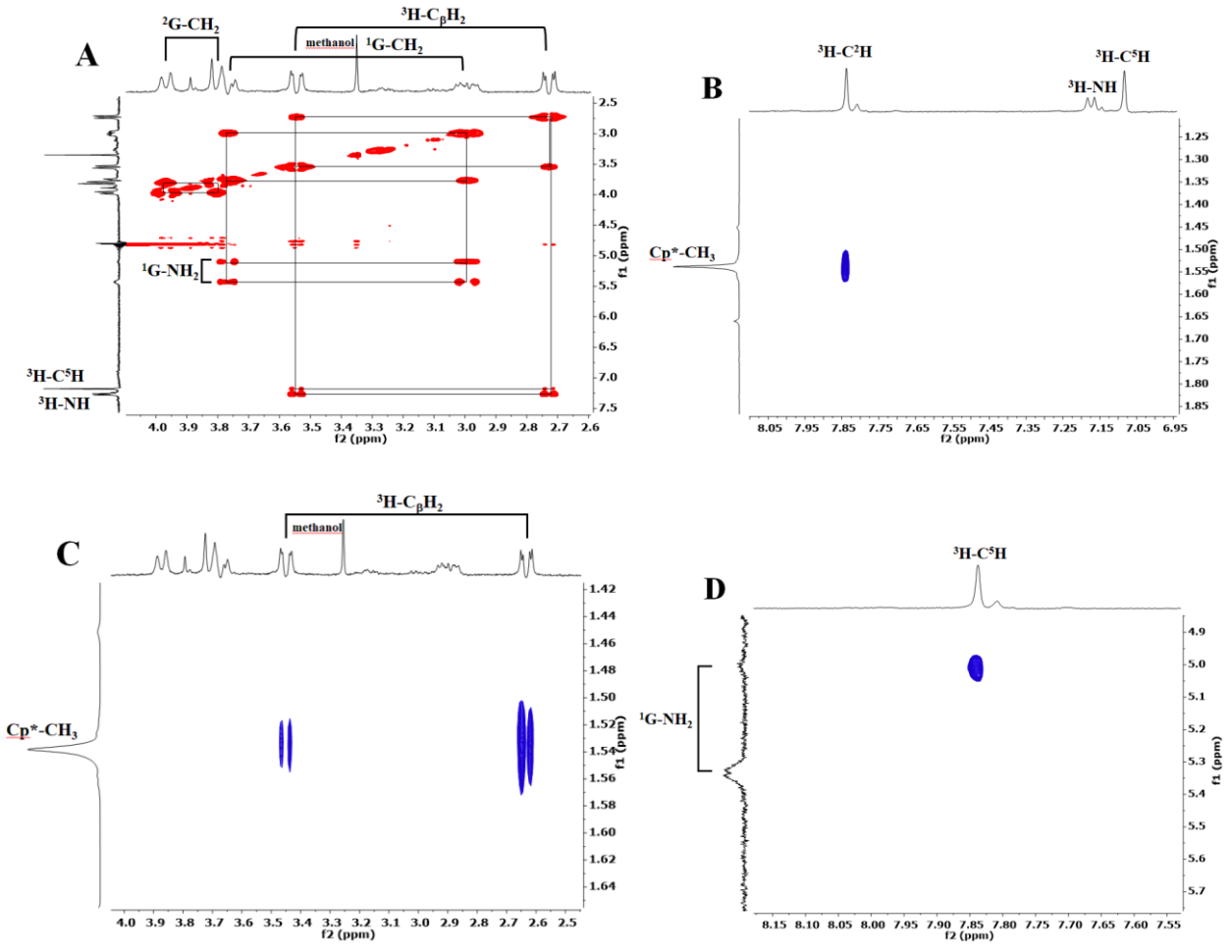

Figure 4.32 Parts of TOCSY (A) and NOESY (B, C, D) spectra of the (Cp*)Rh(III)-$\mathbf{L}^7$ 1:1 system at pH 5.67 (taken from [151])

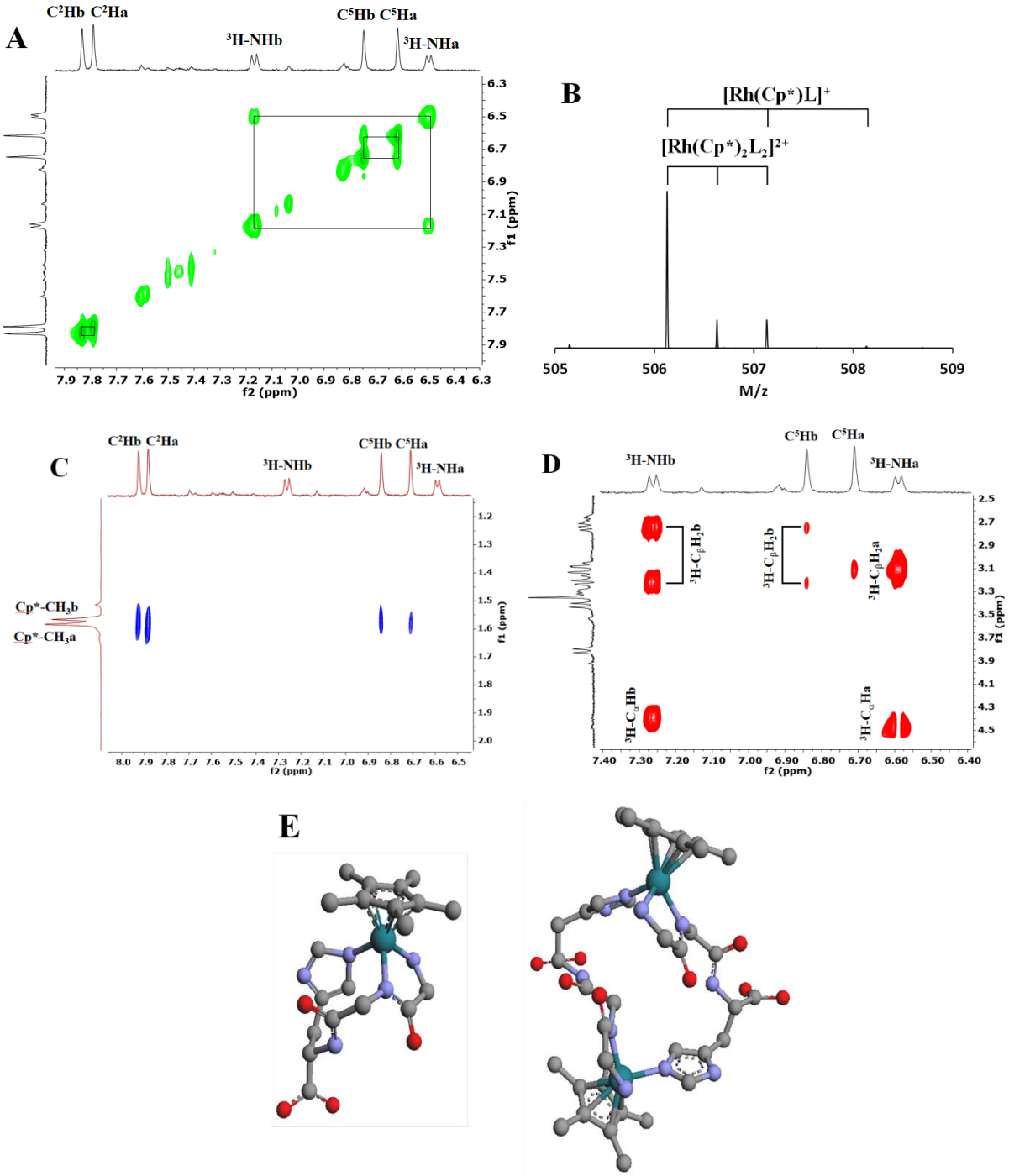

Figure 4.33 Parts of EXSY (A), ESI-MS (B), NOESY (C) and TOCSY (D) spectra of the (η^5-Cp*)Rh(III)-$\mathbf{L}^7$ 1:1 system at pH 9.35 (E) Optimized structures of $MH_{-1}\mathbf{L}^7$ and the dimer $(MH_{-1}\mathbf{L}^7)_2$ complexes (see chapter 4.3.3). (taken from [151])

4.3.1.4 Interaction of (η^5-Cp*)Rh(III) with histidine-amide (L^8) and HGG (L^9)[12]

Both ligands are simple model of N-terminal histidine unit in proteins. In the (η^5-Cp*)Rh(III)-$\mathbf{L}^8$ system three complexes can be identified between pH 2–12 (Table 8, Fig. 4.34). The broad signal related to the N^1H proton of coordinated imidazole ring appeared on the ^1H NMR spectra between pH 2–6 in this case, too (Fig. 4.35). The formation constant of $[M\mathbf{L}^8]^{2+}$ complex is much higher than the analogous values of $[M\mathbf{L}^5]^{2+}$, $[M\mathbf{L}^6]^{+}$ or $[M\mathbf{L}^7]^{+}$, indicating the coordination of both N^3_{im} and amino nitrogens within a 6-membered chelate. Since the resonances of amide protons did not change between pH 2–4, the coordination of carbonyl oxygen is unlikely. Therefore the metal ion in $[M\mathbf{L}^8]^{2+}$ has $\{NH_2, N^3_{im} + Cl^-\}$ donor set, with bidentate, histamine-like coordination of $\mathbf{L}^8$.

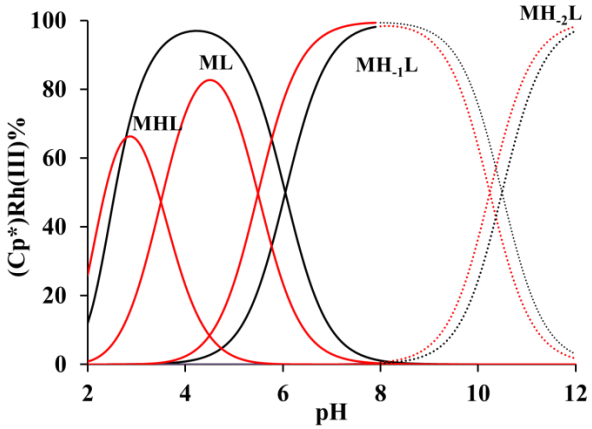

Figure 4.34 Speciation in the (η^5-Cp*)Rh(III)-$\mathbf{L}^8$ (black dashed lines) and (η^5-Cp*)Rh(III)-$\mathbf{L}^9$ (red lines) 1/1 systems (T = 298 K, I = 0.2 M KCl, $[M]_{tot}$ = 0.001 M). The curves of uncomplexed metal ion are not shown for clarity. Dotted lines indicate the region of slow processes, where only approximate speciation can be given (taken from [151])

Above pH 4 a new set of peaks developed on the ^1H NMR spectra (Fig. 4.35), belonging to the $[MH_{-1}\mathbf{L}^8]^+$ species (pK = 6.05). As in the previous cases, new signals appeared on the ^1H NMR spectra close to the water resonance. In fact, the signal closest to water (at 4.90 ppm) is obscured and only its cross peaks appeared on the 2D spectra (Fig. 4.36). The peaks at 4.90 and 5.15 ppm show spatial proximity to the $C_\alpha H$ proton (Fig. 4.36), thus belong to the coordinated amino-NH_2, while the resonance at 5.53 ppm is related to the deprotonated (and coordinated) amide-NH^-. The coordination of these nitrogens is further supported by the spatial proximity of their protons to the Cp*-methyl protons (Fig. 4.36). On the other hand, among the two imidazole

[12] The text of this chapter is mainly based on ref [151]

CH protons, only C^2H shows vicinity to the Cp*-ring, which clearly indicates $\{N^3_{im},NH_2,NH^-\}$binding mode in $[MH_{-1}\mathbf{L^8}]^+$ (Fig. 4.36 and 4.37).

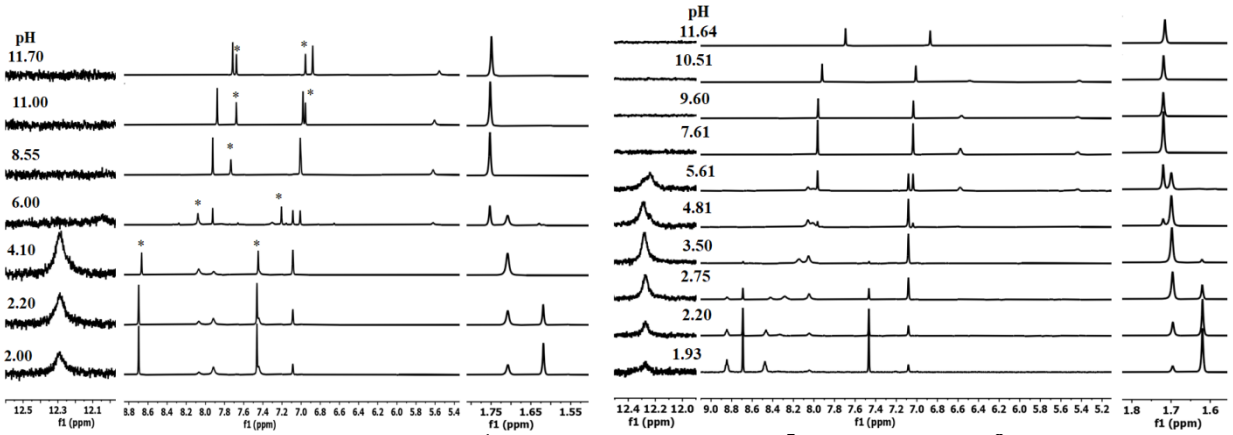

Figure 4.35 Parts of pH-dependent ^{1}H NMR spectra of (η^5-Cp*)Rh(III)-$\mathbf{L^8}$ 2/3 (left) (asterix denotes the signals of the free ligand) and (η^5-Cp*)Rh(III)-$\mathbf{L^9}$ 1/1 (right) systems. (taken from [151])

The (η^5-Cp*)Rh(III)-$\mathbf{L^9}$ system behaves analogously. The formation constants of $[M\mathbf{L^8}]^{2+}$ and $[M\mathbf{L^9}]^+$ complexes are very similar, and the imidazole N^1H proton appeared on the ^{1}H NMR spectra of both $[MH\mathbf{L^9}]^{2+}$ and $[M\mathbf{L^9}]^+$ (Fig. 4.35), confirming the coordination of N^3 nitrogen in these species. The pK of $[MH\mathbf{L^9}]^{2+}$ (pK = 3.50) is close to the pK of carboxylate in the free ligand (Table 8). Consequently, in both $[MH\mathbf{L^9}]^{2+}$ and $[M\mathbf{L^9}]^+$ the ligand binds to the metal ion with histamine-like $\{NH_2,N^3_{im}\}$ coordination, they differ only in the protonation state of the C-terminal carboxylate, remote from the metal ion. During the deprotonation of $[M\mathbf{L^9}]^+$ species (pK = 5.49) the signal of ^{2}G amide proton disappeared from the ^{1}H NMR spectrum. Like in the previous cases, parallel with this amide deprotonation new signals appear near the water, which show strong TOCSY cross-peaks with histidine C^5H, $C_\alpha H$ and $C_\beta H_2$ protons, and therefore belong to the coordinated N-terminal amino group (Fig. 4.38). Among the two imidazole CH protons, only the C^2H proton exhibits spatial proximity to the Cp* methyl protons, thus the N^3 nitrogen of the imidazole ring is coordinated in $MH_{-1}\mathbf{L^9}$. Besides, the ^{1}H-NH_2, ^{2}G-CH_2 and ^{3}G-NH protons are also close to the methyl groups of Cp* ring (Fig. 4.38), confirming the Rh(III)-promoted deprotonation of ^{2}G amide, and therefore the $\{N^3_{im},NH_2,N^-\}$ binding mode in $MH_{-1}\mathbf{L^9}$ (Fig. 4.37). Above pH 8 a further deprotonation was observed in both systems, leading to $MH_{-2}L$ in slow processes. During these deprotonations new set of peaks did not appear, only those already present were shifted (Fig. 4.35), i.e. this deprotonation does not alter the coordination

sphere of Rh(III). Two of such processes may take place, the deprotonation of the amino or imidazole N^1-nitrogens. Since the imidazole C^2H and C^5H protons show the largest shift between pH 8–12, and the signals of coordinated amino group are less affected, this deprotonation is probably related (at least for the most part) to the imidazole N^1-nitrogen.

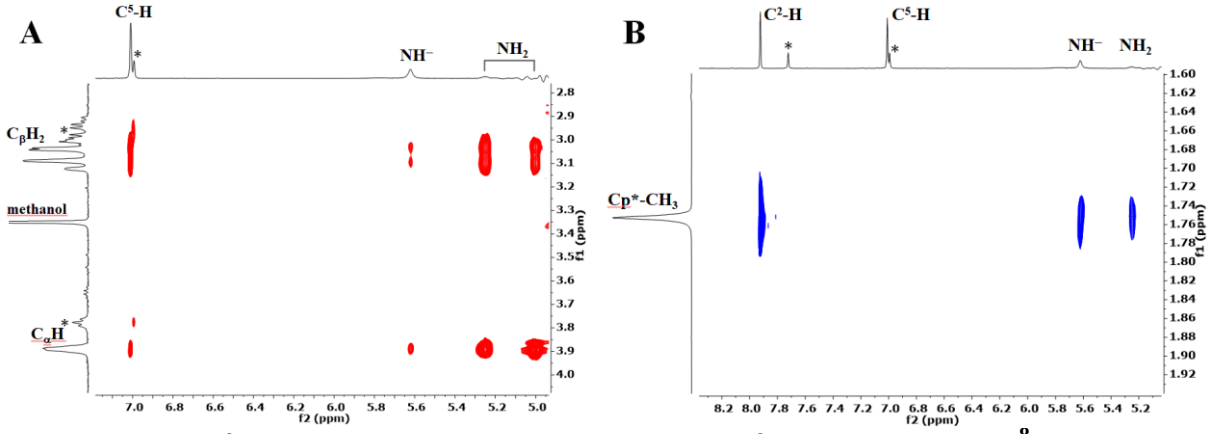

Figure 4.36 Parts of TOCSY (A) and NOESY (B) spectra of the (Cp*)Rh(III)-**L**[8] 1/1 system at pH 7.61. (taken from [151])

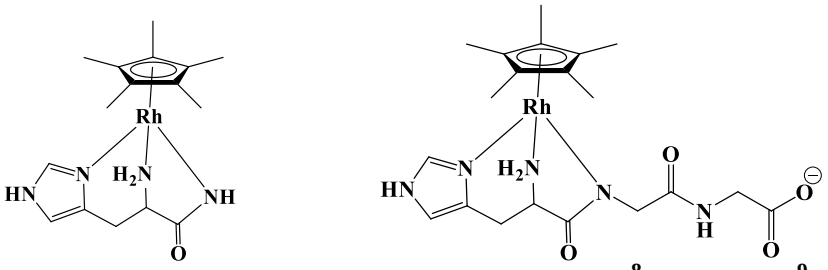

Figure 4.37 Proposed structures of $MH_{-1}L$ species of **L**[8] (left) and **L**[9] (right).

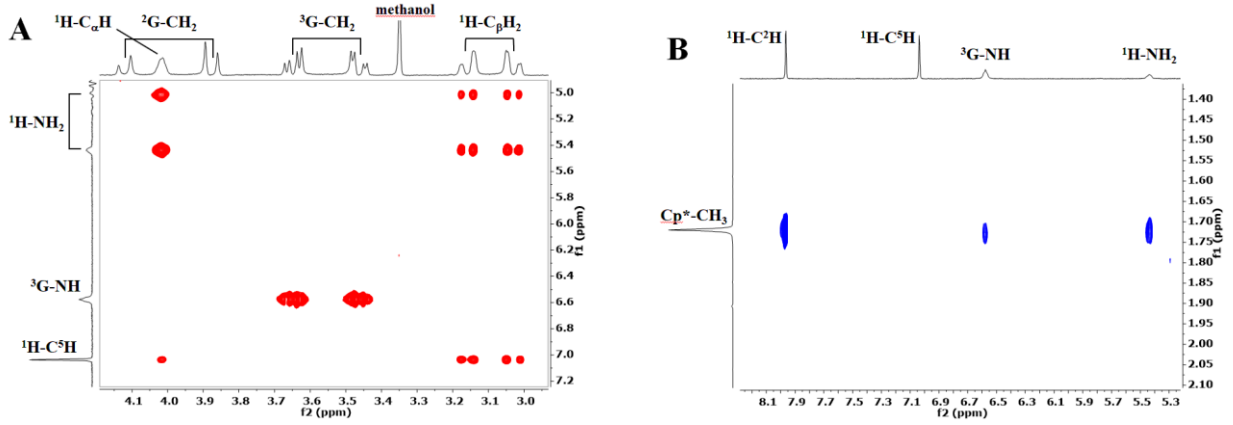

Figure 4.38 Parts of TOCSY (A) and NOESY (B) spectra of the (Cp*)Rh(III)-**L**[9] 1/1 system at pH 7.61. (taken from [151])

4.3.1.5 Interaction of (η^5-Cp*)Rh(III) with GHG-NH_2 (L^{10})[13]

In this peptide the histidine is in the second position, and since it was prepared in our laboratory, the C-terminal carboxylate is amidated. After the formation of a minor species $[MH\mathbf{L}^{10}]^{3+}$ between pH 2–4, two strongly cooperative deprotonations have been detected. Consequently, the formation of $[M\mathbf{L}^{10}]^{2+}$ could not be observed, only that of the subsequent $[MH_{-1}\mathbf{L}^{10}]^{+}$ complex (Fig. 4.39), which is the only species in the solution between pH 4.5–8. Up to pH 4.43 the ^{2}H amide proton gradually disappeared, while the signals of terminal (^{1}G) NH_2 and imidazole N^{1}H protons appeared on the NMR spectra (Figs. 4.40 and 4.41A).

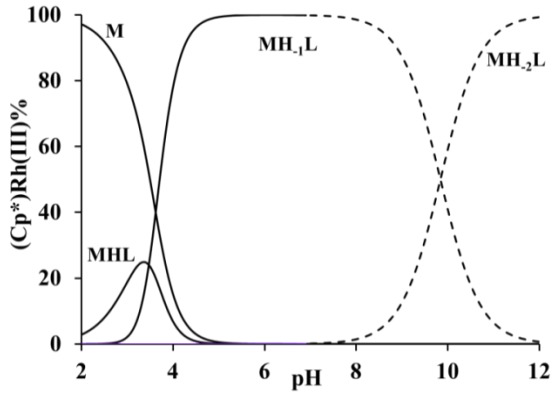

Figure 4.39 Speciation in the (Cp*)Rh(III)-$\mathbf{L}^6$ 1/1 system (T = 298 K, I = 0.2 M KCl, $[M]_{tot}$ = 0.001 M). Dashed lines indicate the region of slow process, where only approximate speciation can be given. (taken from [151])

The NOESY spectrum indicates spatial proximity between the Cp*-methyl and imidazole C^{2}H, ^{3}G amide (Fig. 4.41B), ^{1}G-NH_2, ^{1}G-CH_2 as well as ^{2}H-C$_\beta$H$_2$ protons (Fig. 4.41C). All these facts confirm the {NH_2,N$^-$,N$^3_{im}$} type coordination of peptide in $[MH^{-1}\mathbf{L}^{10}]^{+}$ species as shown in Fig. 4.41E. This is somewhat surprising considering that $\mathbf{L}^{10}$ in this binding mode prefers meridional, while (η^5-Cp*)Rh(III) prefers facial coordination. Therefore, we suspected dimer formation, similar to the case of GGH-OH ($\mathbf{L}^7$). However, the MS spectrum at pH 5 clearly indicates the sole presence of the monomer $[MH_{-1}\mathbf{L}^{10}]^{+}$ complex (Fig. 4.41). The crystal structures of tridentate {NH_2,N$^-$,N$^-$} coordinated (Cp*)Rh(III)-peptide complexes indicate that the central deprotonated amide nitrogen is distorted towards a pyramidal conformation [160]. Similar effect can be expected here, too, but the high thermodynamic stability may over-compensates this conformational strain. Indeed, the potentiometric data show outstanding

[13] The text of this chapter is mainly based on ref [151]

stability of the amide-coordinated complex of **L**[10], its formation takes place at 3–4 units lower pH than in the former systems.

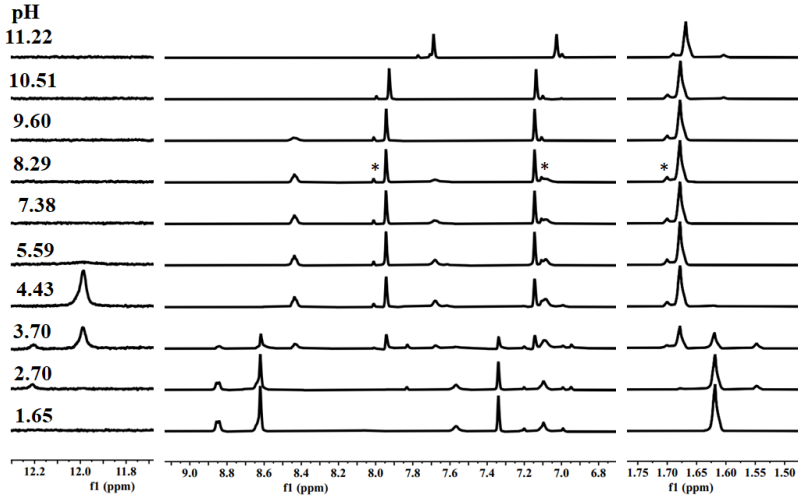

Figure 4.40 Low- and high-field parts of pH-dependent ^{1}H NMR spectra of (Cp*)Rh(III)-**L**[10] 1/1 system (asterix denotes the signals of minor diastereomer, see main text). (taken from [151])

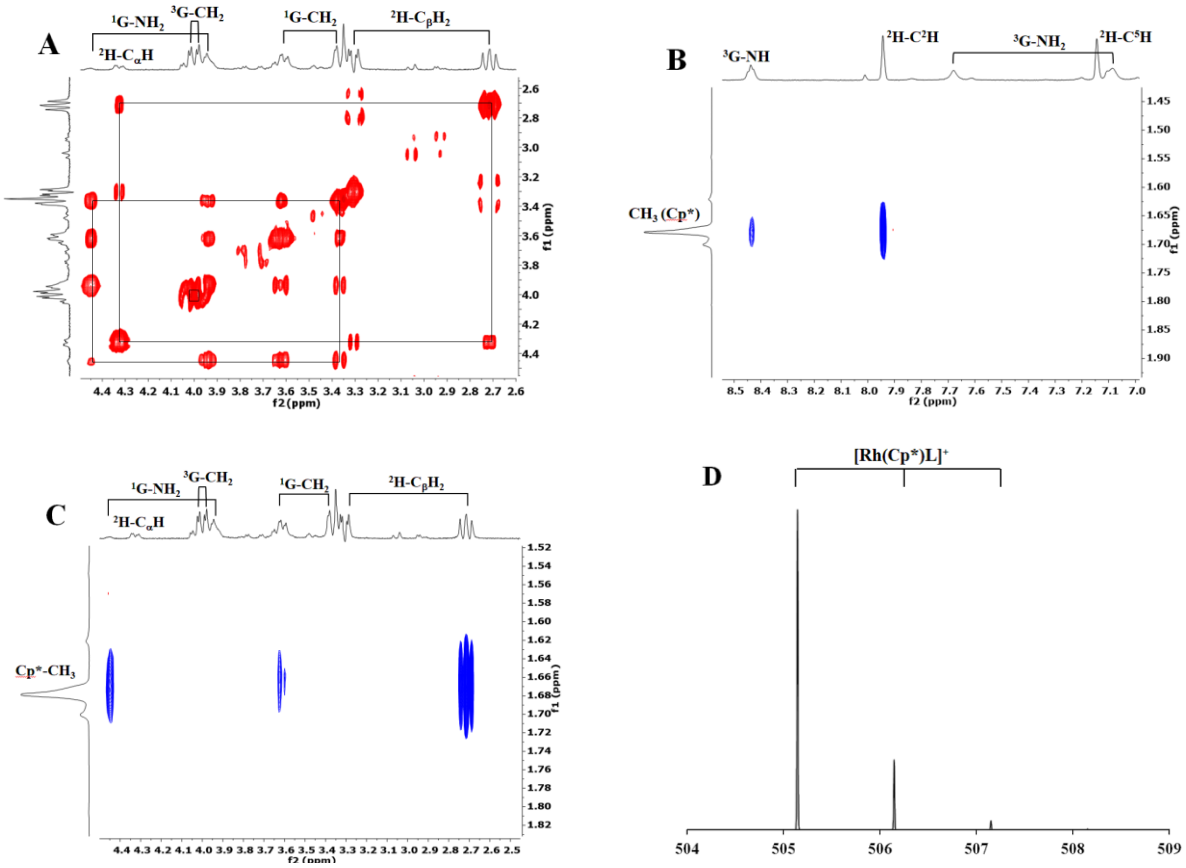

E

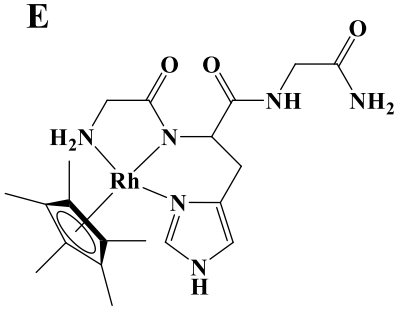

Figure 4.41 Parts of TOCSY (A), NOESY (B,C) at pH 4.43 and ESI-MS at pH 5.4 spectra of the (η^5-Cp*)Rh(III)-$\mathbf{L^{10}}$ 1:1 system at pH 4.43 and proposed structure of $MH_{-1}\mathbf{L^{10}}$ complex (E). (taken from [151])

In this system, too, an additional deprotonation was observed above pH 8, which process was proved to be very slow, the equilibrium was not reached even after several days. In this case, however, the slow complex formation process was further complicated by the slow hydrolysis of the C-terminal amide group, which can be clearly seen on the time dependent MS spectrum at pH 11.04 (see Appendix Fig. A6). This hydrolysis is obviously related to the coordinated metal ion, but the exact mechanism is unknown.

4.3.1.6 Interaction of (η^5-Cp*)Rh(III) with HHHG-NH_2 ($\mathbf{L^{11}}$)

In the previous chapters I studied the effect of the position of histidine unit within the sequence of tripeptides (HGG, HGH, GGH) on the coordination properties toward (η^5-Cp*)Rh(III) cation. A next logical step is to investigate a peptide with histidines in the first three positions. To this end, I synthetized and studied the tetrapeptide HHHG-NH_2, which can be also a good model of multihistidine peptides/proteins present in biological fluids. Due to the higher number of donor sites in this peptide, beside the equimolar system I also studied the interaction in presence of metal ion excess. At 1:1 metal-to-ligand ratio, similarly to the former systems, reliable equilibrium data could be collected only up to pH 8. However, at 2:1 metal-to-ligand ratio the slow kinetics prevented the correct solution study already above pH 5. The combined evaluation of our pH-metric, UV-Vis, MS and NMR data (Figs. 4.42 – 4.46) indicated the formation of three mononuclear and a single binuclear complex in the mentioned pH range. The determined formation constants are listed in Table 8, the calculated distribution curves of the

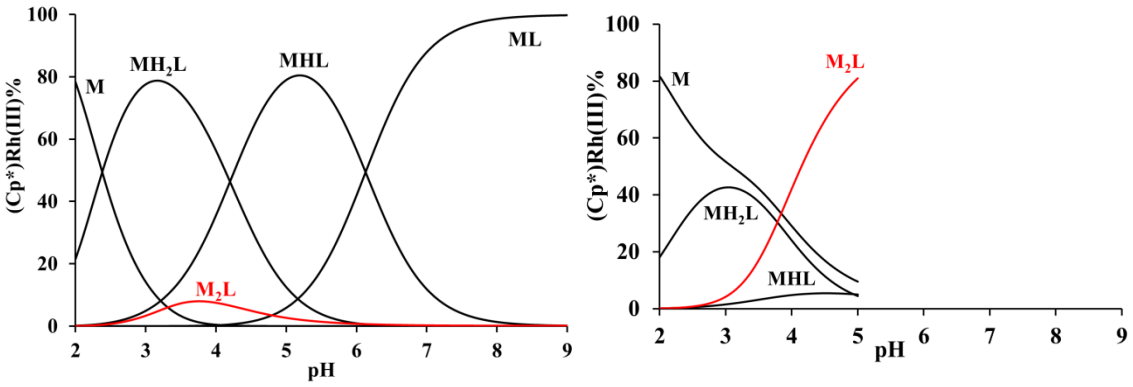

Figure 4.42 Speciation in the (η^5-Cp*)Rh(III)- $\mathbf{L}^{7}$ 1:1 (left) and (η^5-Cp*) Rh(III)- $\mathbf{L}^{11}$ 2:1 (right) systems (T = 298 K, I = 0.2 M KCl, $[M]_{tot}$ = 0.001 M).

complexes are shown in Figure 4.42. Since the ^{1}H NMR signals of the three histidine subunits are significantly overlapped, the complex formation processes can be followed much easier based on the signals of Cp* methyl protons (Fig. 4.43). In the species $[MH_2\mathbf{L}^{11}]^{4+}$, among the amino and 3 imidazole groups two are deprotonated and coordinated. The equilibrium constant for the formation of this complex ($M + H_2\mathbf{L}^{11} = MH_2\mathbf{L}^{11}$, $\log K = \log \beta_{121} - pK_2 - pK_3 = 10.95$) is almost identical to the formation constant of $[M\mathbf{L}^{8}]^{2+}$ species ($\mathbf{L}^{8}$ = histidine amide, $\log \beta_{101} = 11.09$), which would indicate histamine-like $\{NH_2,N^3_{im}\}$ coordination. However, in the pH range of the formation of this complex, two Cp*-methyl signals (● and ○ in Figure 4.43), i.e. two isomers, can be detected. The higher intensity signal (● in Fig. 4.43) shows a similar chemical shift as the $[M\mathbf{L}^{8}]^{2+}$ complex of histidine amide, indicating histamine-like coordination in this isomer. The other isomer (○ in Figure 4.43) is present in the solution nearly ten times lower concentration, and probably related to a *bis*-imidazole coordinated species. Based on the ratio of these isomers, $\log K$ = 9.9 ($M + H_2\mathbf{L}^{11} = MH_2\mathbf{L}^{11}$) can be estimated for the bis-imidazole coordinated species, which agrees well with $\log \beta_{102}$ (=10.46) of imidazole itself (Table 8). The low pK of the next deprotonation ($MH_2\mathbf{L}^{11} = MH\mathbf{L}^{11} + H^+$, p$K$ = 4.20), clearly indicates a further nitrogen coordination in $[MH\mathbf{L}^{11}]^{3+}$. Considering that histamine-like coordination was the dominant in $[MH_2\mathbf{L}^{11}]^{4+}$, a further imidazole coordination, *i.e.* $\{NH_2,2\times N_{im}\}$ binding mode is likely to occur in the $[MH\mathbf{L}^{11}]^{3+}$ complex. However, $[MH\mathbf{L}^{11}]^{3+}$ is also present in two isomeric forms (□ and ■ in Figure 4.43), presumably in addition to the histamine-like binding of N-terminal histidine, the imidazole ring of either the second or third histidine is coordinated ($\{NH_2,^1H\text{-}N_{im},^2H\text{-}N_{im}\}$ or $\{NH_2,^1H\text{-}N_{im},^3H\text{-}N_{im}\}$). These two isomers (two different binding modes) are present in significantly different amounts between pH 4-5 (□ >> ■, see Figure 4.43).

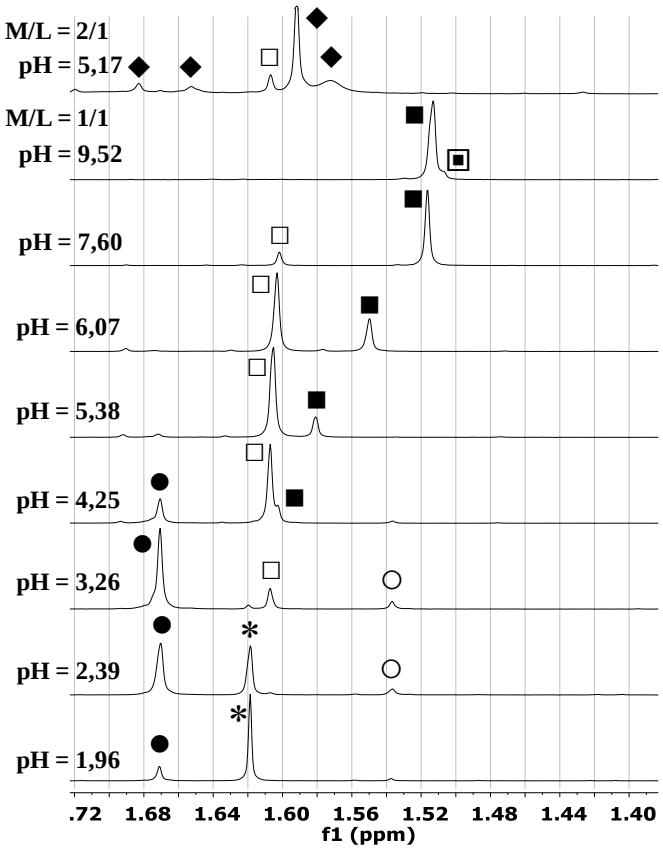

Figure 4.43 pH-dependent ^{1}H NMR spectra of the 1: 1 and 2: 1 (above) systems of (Cp*)Rh(III)-HHHG-NH_2 **L**^{11} in the region of the methyl protons of the Cp* ring (T = 298 K, [L] = 0.0015 M). For an explanation of the signs, see in the text.

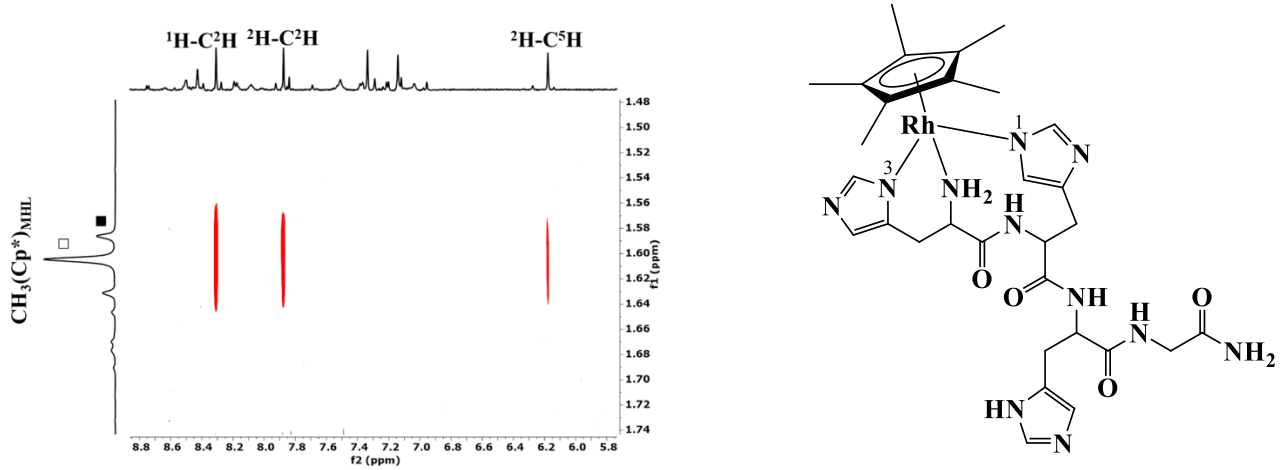

Figure 4.44 Parts of the NOESY spectra of the (Cp*)Rh(III)-**L**^{11} 1:1 system at pH 5.22 (left) and proposed structure of the major MH**L**^{11} isomer (right).

Based on the NOESY spectrum detected at pH 5.2 (Fig. 4.44) the N-terminal histidine of the major isomer is coordinated by its N^{3}_{im} nitrogen (only the C^{2}-H proton shows spatial

proximity to the Cp* methyl protons), while the other histidine (either the second or third) is coordinated monodentately by its N^1_{im} nitrogen (both C^2-H and C^5-H protons are close the the Cp* ring). Surprisingly, however, the Cp* methyl signals of these isomers continuously shift during the $MH\mathbf{L}^{\mathbf{11}} = M\mathbf{L}^{\mathbf{11}} + H^+$ (pK = 6.13) deprotonation. The signal of the major isomer at pH 4-5 (□ in Figure 4.43) shifts only slightly, while the signal of the minor isomer is subjected to a more important shift between pH 5-8. Since these isomers have slow ligand exchange on the NMR timescale (they have separated sets of signals), the continuous pH shift indicates that the deprotonation does not alter the coordination environment of the metal ions, it occurs distant from the metal ions. Consequently, between pH 5-8, the deprotonation of the non-coordinated imidazole ring takes place. The similar coordination environment of the metal ion in $[MH\mathbf{L}^{\mathbf{11}}]^{3+}$ and $[M\mathbf{L}^{\mathbf{11}}]^{2+}$ complexes is also confirmed by the similar individual UV-Vis spectra of these species (Fig. 4.45).

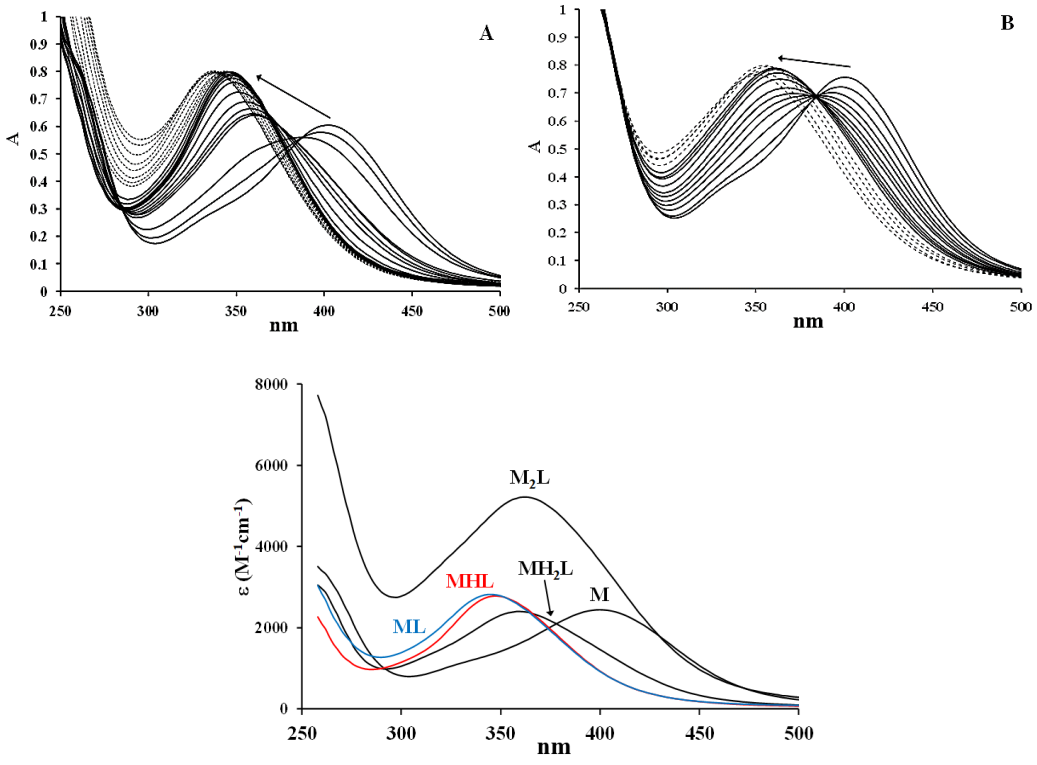

Figure 4.45 pH-dependent UV-Vis spectra of the (η^5-Cp*)Rh(III)-HHHG-NH_2 $\mathbf{L}^{\mathbf{11}}$ systems at 1:1 (A) and 2:1 (B) metal-to-ligand ratio ([(η^5-Cp*) Rh (III)]$_{tot}$ = 0.283 mM (A), 0.340 mM (B)), and the calculated individual UV-Vis spectra of the complexes formed (M = (η^5-Cp*)Rh(III)).

Another interesting fact is that the ratio of these two isomers ({NH_2,^{1}H-N_{im},^{2}H-N_{im}} and {NH_2,^{1}H-N_{im},^{3}H-N_{im}}) changes fundamentally during the MH$\mathbf{L}^{\mathbf{11}}$ = M$\mathbf{L}^{\mathbf{11}}$ + H^+ deprotonation. The signal of the isomer which is dominant at pH = 5 (□ in Figure 4.43), completely disappears at pH 9. At the same time, the intensity of the signal related to the minor isomer at pH 5 ('■' in Figure 4.43) becomes the only detectable signal at pH ~ 8-9. This indicates important conformational change during the $[MH\mathbf{L}^{\mathbf{11}}]^{3+}$ = $[M\mathbf{L}^{\mathbf{11}}]^{2+}$ + H^+ deprotonation. In other words, the binding mode ({NH_2,^{1}H-N_{im},^{2}H-N_{im}} or {NH_2,^{1}H-N_{im},^{3}H-N_{im}}) that results in lower stability for the MH$\mathbf{L}^{\mathbf{11}}$ complex (the isomer marked by '□' in Figure 4.43) becomes the favored one in the M$\mathbf{L}^{\mathbf{11}}$ species. Based on the above observations, we can also speculate on the identity of the more favored binding modes in $[MH\mathbf{L}^{\mathbf{11}}]^{3+}$ and $[M\mathbf{L}^{\mathbf{11}}]^{2+}$. Since the signal of '■' isomer shifted more importantly between pH 4-8, we can assume that the deprotonating (i.e. non-coordinating) histidine is part of the macrochelate ring, since the deprotonation of a histidine unit which is not involved in the mecrochelate ring, *i.e.* is farther from the metal ion, would induce much smaller shift of the Cp* methyl protons. It follows from these considerations that in MH$\mathbf{L}^{\mathbf{11}}$ probably the {NH_2,^{1}H-N_{im},^{2}H-N_{im}} (Fig. 4.44), while in M$\mathbf{L}^{\mathbf{11}}$ the {NH_2,^{1}H-N_{im},^{3}H-N_{im}} binding mode is the more preferred.

Due to the large number of available donor groups in $\mathbf{L}^{\mathbf{11}}$, the formation of dinuclear complexes is also possible. Therefore, we studied the complex formation processes at 2:1 metal-to-ligand ratio, too. The equilibrium data could be evaluated only up to pH 5, since above this point slow kinetics was observed. Our data indicated the formation of $[M_2\mathbf{L}^{\mathbf{11}}]^{4+}$ as the only dinuclear species up to pH 5 (Fig. 4.42). Apart from the intensity, the individual UV-Vis spectra of $[MH_2\mathbf{L}^{\mathbf{11}}]^{3+}$ and $[M_2\mathbf{L}^{\mathbf{11}}]^{4+}$ complexes (Fig. 4.45) are similar, confirming that in both complexes 2–2 nitrogens are coordinated to the metal ions (may be with additional amide oxygens). Four Cp* methyl signals can be assigned to this complex (Fig. 4.43), which indicates the formation of several isomers, but we have no further structural information on these. The formation of dinuclear species was also confirmed by mass spectroscopy (Fig. 4.46). The slow equilibration observed above pH 5 is probably related to the deprotonation of the amide nitrogens of the neutral ligand and the associated significant structural changes.

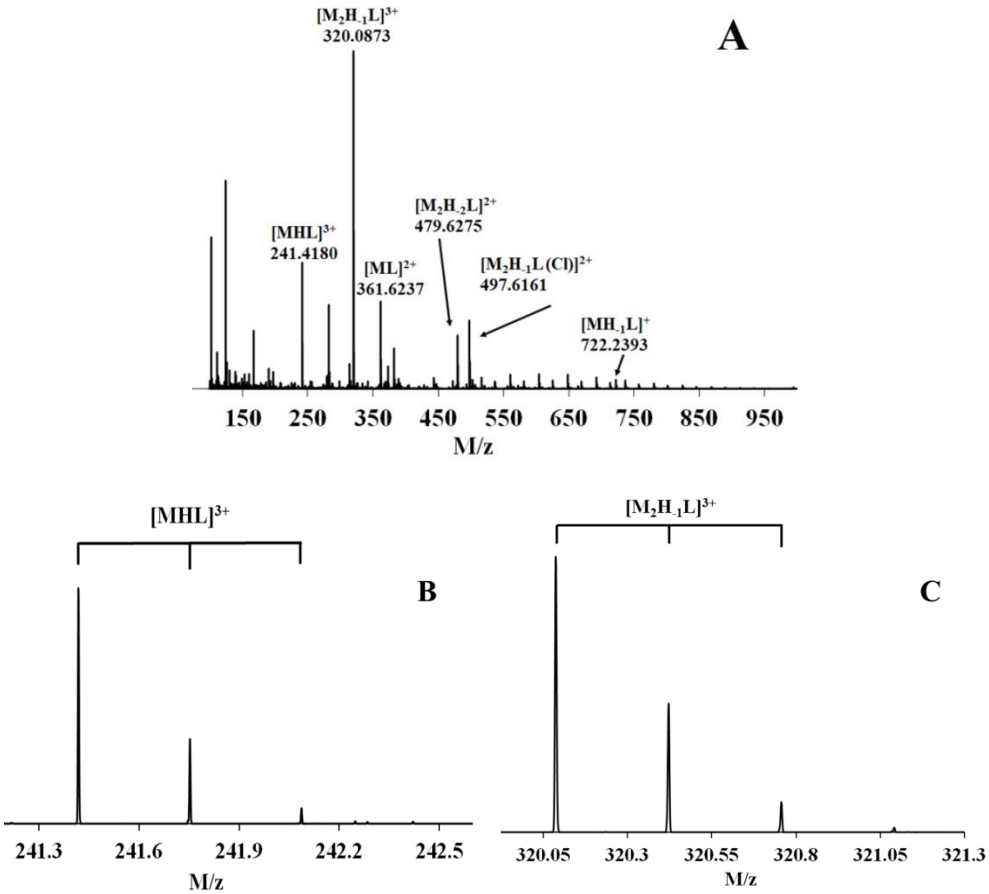

Figure 4.46 ESI-MS spectrum of the Rh(Cp*)-**L**[11] 2/1 system at pH 5.2 (A), isotopic distribution of [M**L**[11]H]$^{3+}$ species (B), [M_2H_{-1}**L**[11]]$^{3+}$ species (C).

4.3.2 Interaction of (η^5-Cp*)Rh(III) cation with endogenous peptides

After establishing the role histidine units and its position on the peptide sequence on the coordination behaviours toward (η^5-Cp*)Rh(III) cation, we studied the solution thermodynamic and solution structural properties of (Cp*)Rh(III) complexes formed with some biologically relevant histidine derivatives present in human body (Histidine **L**[12], Carcinine **L**[13], Carnosine **L**[14], Thyrotropin releasing hormone (TRH**,** pyroGlu-His-Pro-NH_2) **L**[15], and GHK (Gly-His-lys) **L**[16]) (Chart 4.6). In these systems too, we experienced very slow attaintment of equilibrium above pH 7-8, therefore correct solution equilibrium can be given only up to this pH. The solution speciations are based on the combined evaluation of our pH-potentiometric, NMR and MS data. The formation constants determined in this way are reported in Table 9.

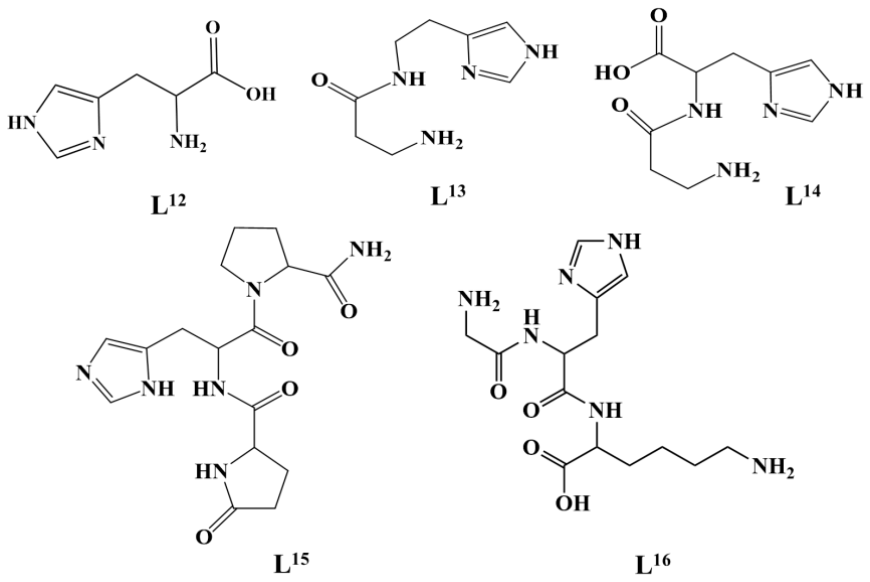

Chart 4.6 Schematic structures of the studied endogenic histidine derivatives.

Table 9. Protonation constants of the studied ligands, formation constants of their (η^5-Cp*)Rh(III) complexes and some derived data (T = 298 K, I = 0.20 M (KCl)), with estimated errors in parentheses (last digit). The constants in square brackets are only indicative values, since the systems were non-equilibrated.

	log β_{pqr}				
Species (pqr)	**L^{12}**	**L^{13}**	**L^{14}**	**L^{15}**	**L^{16}**
H_4L (041)	-	-	-	-	27.88 (4)
H_3L (031)	16.97(7)	-	18.82 (1)	-	25.04 (2)
H_2L (021)	15.21(2)	16.04 (1)	16.14 (1)	-	18.50 (2)
HL (011)	9.12(1)	9.20 (0)	9.37 (1)	6.28(1)	10.56 (1)
MH_2L (121)	-	-	-		24.35 (7)
MHL (111)	-	14.64 (2)	14.97 (1)		20.44 (8)
ML (101)	14.11(6)	8.93 (3)	9.39 (1)	5.38(2)	17.20 (2)
$MH_{-1}L$ (1-11)	4.73(6)	3.42 (2)	3.07 (2)	-	7.10 (3)
$MH_{-2}L$ (1-21)	-	[-7.5]	[-8.1]	-6.49(2)	[-4.7]
M_2L (201)	-	-	-	-	-
ML_2 (102)	-	-	-	9.98(2)	-
$pK_{NH,\ amide}$	-	5.51	6.32	~ 5.94	3.24
$pM^*_{7.4}$	13.32	9.87	9.40	9.25	14.30

pM* values at pH 7.4 and at $c_M = c_L/10$ = 1 μM (T = 25 ◦C; I = 0.20 M (KCl), where pM* = − log([M] + 2[$M_2(OH)_2$] + 2[$M_2(OH)_3$]).

4.3.2.1 Interaction of (η^5-Cp*)Rh(III) with Histidine (L^{12})

Histidine is one of the major low molecular weight metal chelator in blood serum, where its concentration is around 70-125 μM [161]. For example, 4 % of the so-called exchangeable pool of copper in human blood is bound to binary and ternary complexes involving histidine [162]. Depending on the pH, histidine may coordinate to metal ions as mono-, bi- or tridentate ligand [162]. Despite this general finding, only a single species, the $[ML^{12}]^+$ complex could be detected in the solution between pH 1.9-8.0. The presence of this species even at pH 1.9 (*c.a.* 25 %) clearly shows its exceptional thermodynamic stability. The comparison of log β_{101} values of $[ML^{12}]^+$ and the $\{N^3_{im},NH_2+Cl^-\}$ coordinated $[ML^8]^{2+}$ complexes (L^8 = histidine-amide, log β_{101} = 14.11 and 11.09, respectively) indicates an additional, obviously carboxylate coordination,

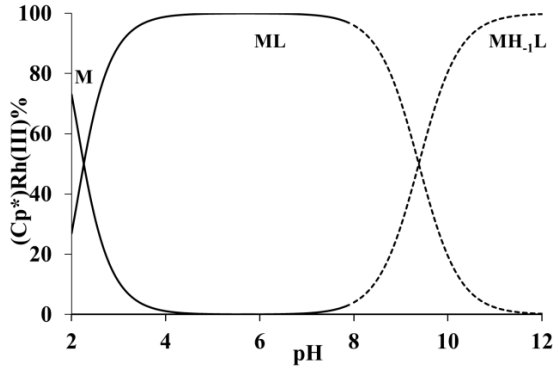

Figur 4.47 Speciation in the (η^5-Cp*)Rh(III)- L^{12} 1:1 systems (T = 298 K, I = 0.2 M KCl, $[M]_{tot}$ = 0.001 M). Dotted lines show the region of slow processes, where only approximate speciation can be given.

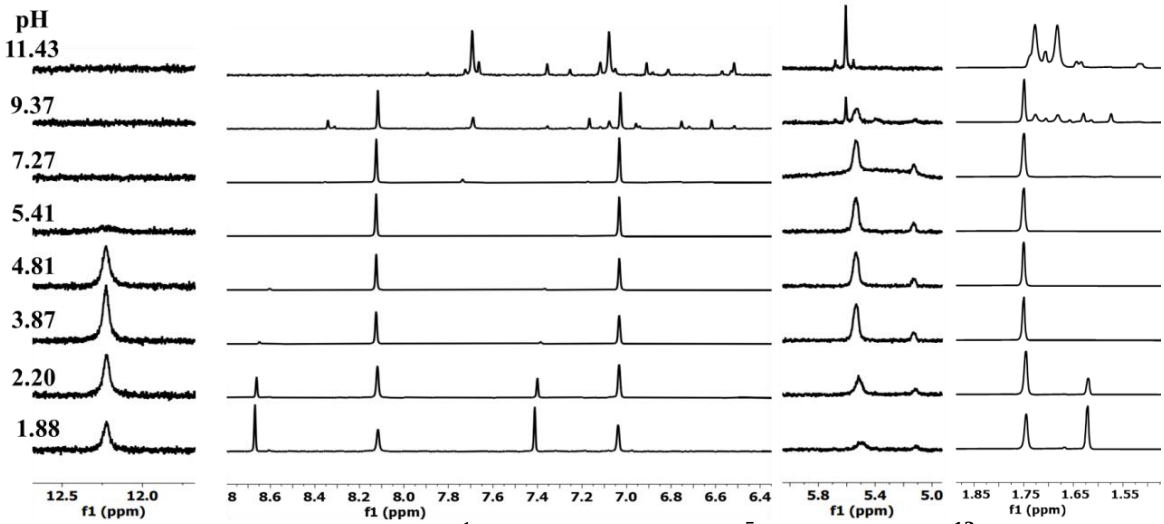

Figure 4.48 Parts of pH-dependent ^{1}H NMR spectra of (η^5-Cp*)Rh(III)-L^{12} 1:1 system

i.e. the tridentate {N^3_{im},NH_2,COO^-} binding mode in [M$\mathbf{L}^{12}$]$^+$.

Like histidine-amide and some other studied ligands, the protonon exchange rate of the imidazole N^1-nitrogen, and the amino group significantly slowed down during coordination, therefore their signals appeared in the NMR spectrum (at 12.2 and 5.54/5.13 ppm, respectively, see Figs. 4.48 and 4.49). The NOESY spectrum detected at pH 5.41 (Fig. 4.49) shows spatial proximity between between the Cp* methyl protons and the imidazole C^2H as well as one of the amino NH_2 protons, which also confirm the coordination of the imidazole N^3- and NH_2-nitrogens.

Above pH 8 a further deprotonation takes place (pK ~ 9.3) leading to [M$H_{-1}\mathbf{L}^{12}$] in slow processes. During this deprotonation several new signals emerged on the ^{1}H NMR spectra (Fig. 4.48), similarly to the (η^5-Cp*)Rh(III)-imidazole system. Therefore, although we have no further structural information, this may imply the formation of imidazolato bridged oligomer species.

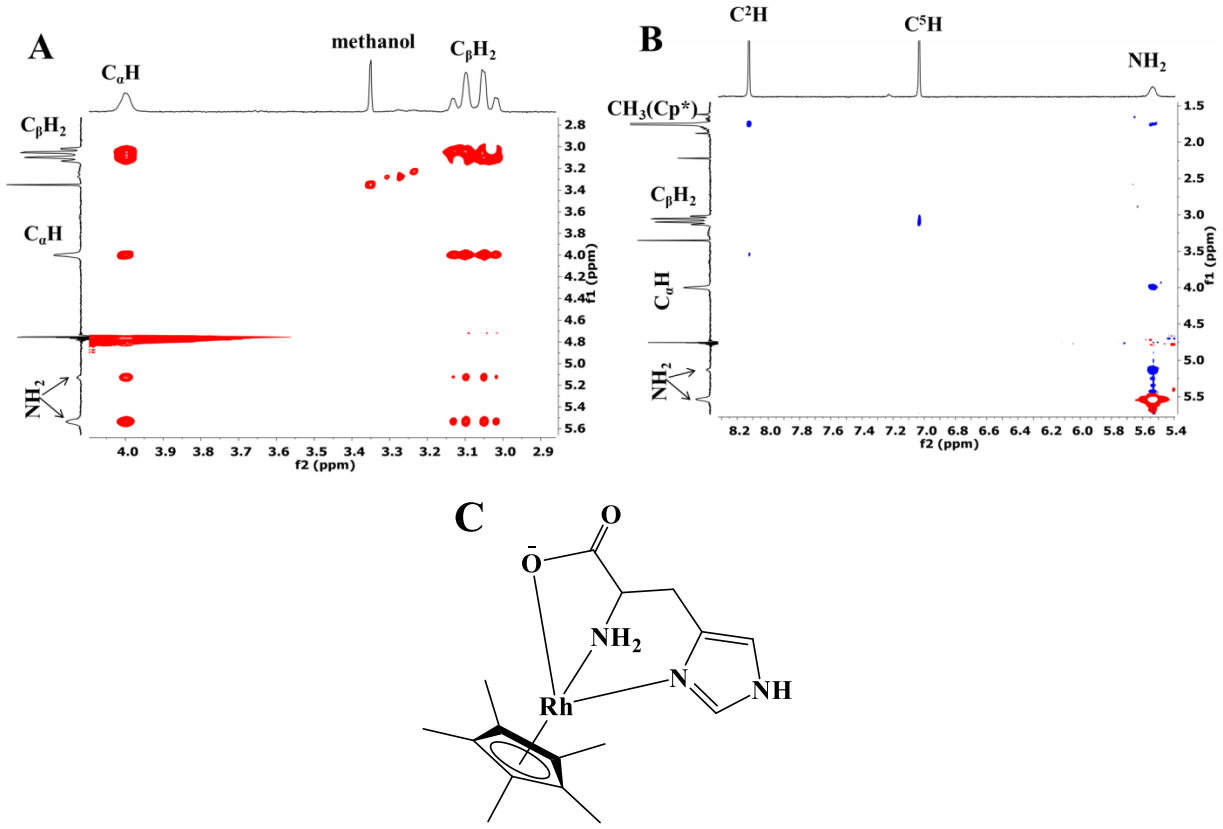

Figure 4.49 Parts of TOCSY (A) and NOESY (B) spectra of the (η^5-Cp*)Rh(III)-$\mathbf{L}^{12}$ 1:1 system at pH 5.41 and proposed structure of M$\mathbf{L}^{12}$ species (C).

4.3.2.2 Interaction of (η^5-Cp*)Rh(III) with Carcinine (L^{13}) and Carnosine (L^{14})

The natural imidazole-containing dipeptides, carcinine (β-alanyl-histamine) and especially carnosine (β-alanyl-histidine) are widely distributed in living tissues and exists at particularly high concentrations in muscle and brain of many animals and humans. Carnosine is one of the most abundant nitrogenous compounds present in the non-protein fraction of vertebrate skeletal muscle (0.5-20 mM) [165-167]. In addition, carnosine has excellent potential to act as a natural antioxidant and anti-inflammatory agents, intracellular buffer in skeletal muscle, as well as free radical scavenger and metal ion chelator. Moreover, it shows antiperoxidative activity on proteins, lipids and DNA. Carcinine exists in multiple histamine-rich mammalian tissues such as heart, kidney, stomach and intestine in levels as high as, or higher than, those reported for carnosine [168,169].

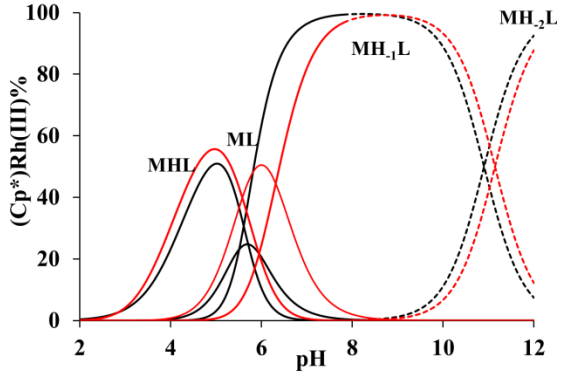

Figure 4.50 Speciation in the (η^5-Cp*)Rh(III)- **L^{13}** (black dashed lines) and (η^5-Cp*) Rh(III)- **L^{14}** (red lines) 1/1 systems (T = 298 K, I = 0.2 M KCl, $[M]_{tot}$ = 0.001 M). The curves of uncomplexed metal ion are not shown for clarity. Dotted lines show the region of slow processes, where only approximate speciation can be given.

The only difference between the two ligands is the presence of a carboxylate group, and therefore a chiral carbon in carnosine (Chart 4.6). Consequently, similar coordination modes can be expected and thus the two ligands are discussed together. The determined formation constants are collected in Table 9, the speciation curves are shown in Fig. 4.50. Between pH 4-5 MHL complexes are formed with both ligands. At this pH the carboxylate group of carnosine is already deprotonated, thus the monoprotonated form signifies that either the amino or imidazole group is coordinated to the metal ion. The NOESY spectrum measured at pH 4.62 indicates that both C^2H and C^5H protons of the imidazole ring are in spatial proximity to the Cp*-methyl protons, *i.e.* the N^1-nitrogen is coordinated to the metal ion in MHL complexes. The imidazole N^1-nitrogen

coordination is characteristic for the monodentate binding of histidine subunits, since the formation of a 5/6/7 membered chelate ring would favor the participation of N^3-nitrogen. Accordingly, although we have no experimental indications on the coordination of carboxylate group of carnosine, the similar stability of the two MHL species indicates monodentate imidazole coordination in these species. Another possible additional binding site is the amide oxygen. Its coordination induces important downfield shift of the corresponding amide proton, as it was seen for GGA and GGH. In the (η^5-Cp*)Rh(III)-carnosine (**L**^{14}) system significant downfield shift of amide proton is observed only between pH 5.5-6.5 (Fig. 4.52), *i.e.* it is associated with [M**L**^{14}]$^+$. During the process MHL = ML + H^+ (p*K* = 5.71 (**L**^{13}) and 5.58 (**L**^{14})), the rhodium induced deprotonation of N-terminal ammonium group takes place at four-unit lower pH than in the free ligands, indicating a relatively strong interaction.

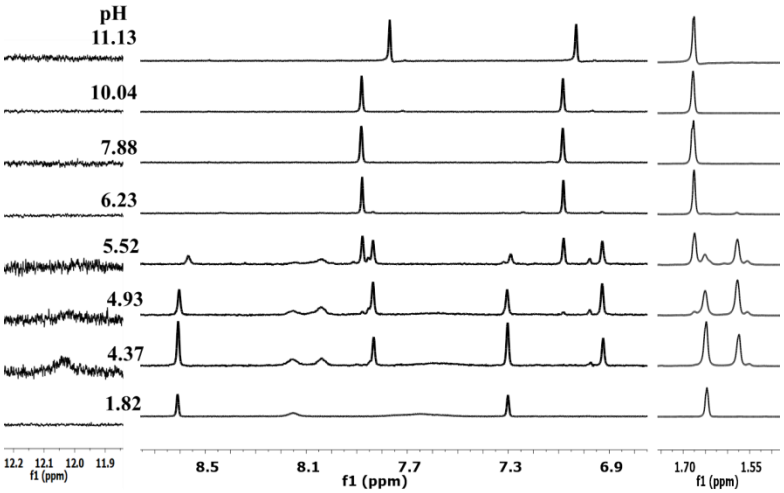

Figure 4.51 Parts of pH-dependent ^{1}H NMR spectra of (η^5-Cp*)Rh(III)-**L**^{13} 1:1 system

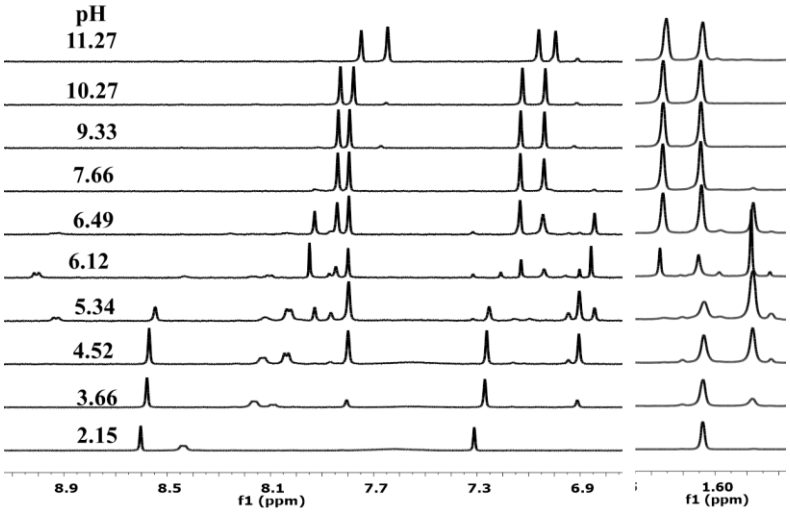

Figure 4.52 Parts of pH-dependent ^{1}H NMR spectra of (η^5-Cp*)Rh(III)-**L**^{14} 1:1 system.

Surprisingly, the NOESY spectrum detected at pH 6.12 (Fig. 4.53) shows the coordination of N^1-nitrogen in $[ML^{14}]^+$, which can be explained by the formation of a 9-membered macrochelate between the amide oxygen and N^1-nitrogen, which does not force the coordination of N^3-nitrogen. Consequently, the $[ML^{14}]^+$ species has a $\{NH_2,C{=}O,N^1_{im}\}$ binding mode. Since the complex $[ML^{13}]^{2+}$ is a minor species at any pH, no structural data can be extracted from the NMR spectra, but we suggest similar coordination mode in the two ML species.

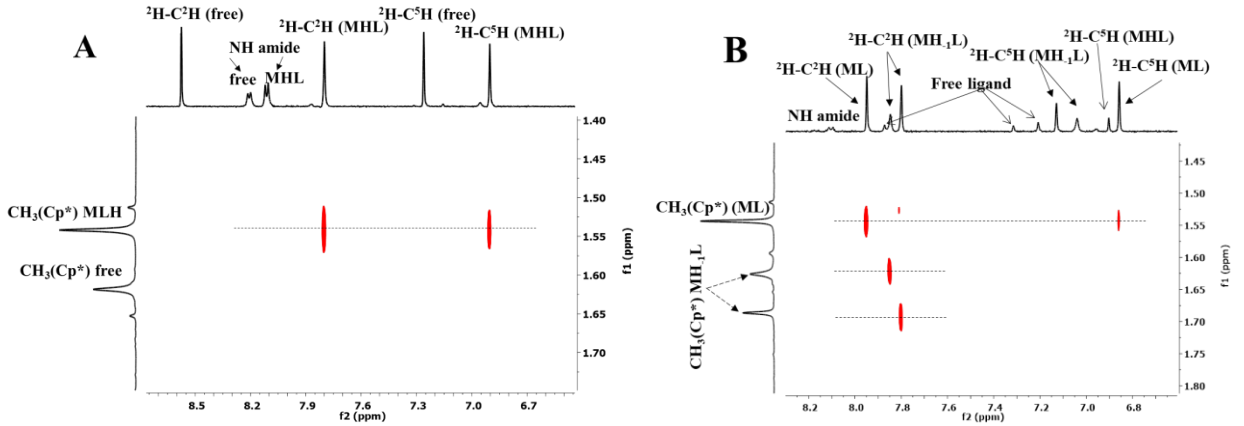

Figure 4.53 Part of NOESY spectrum of the (η^5-Cp*)Rh(III)-$\mathbf{L^{14}}$ 1:1 system at pH 4.62 (A) and pH 6.12 (B).

The subsequent processes ([ML] = $[MH_{-1}L]$ + H^+, pK_{ML} = 5.51 ($\mathbf{L^{13}}$) and 6.32 ($\mathbf{L^{14}}$)) are related to the rhodium promoted amide deprotonation (and coordination). Indeed, between pH 5-7 the signals of amide protons disappeared from the spectra of both systems (Figs. 4.51 and 4.52). The species of carnosine have somewhat higher stability as compared to carcinine. This is probably due to the additional coordination of the carboxylate group, which results in higher stability (logβ = 8.93 for $\mathbf{L^{13}}$ and 9.39 for $\mathbf{L^{14}}$). This extra stabilization can also explain the higher pK of amide deprotonation in the case of carnosine The (NH_2,N^-,N^3_{im}) chelation is the most plausible binding mode in the species $[MH_{-1}L]$ around the neutral pH (Figs. 4.50, 4.54D and 4.55D). The suggested coordination mode of $[MH_{-1}L]$ is supported by the followings: (i) the titration curve (Appendix Fig. A7) shows three ($\mathbf{L^{13}}$) and four ($\mathbf{L^{14}}$) equivalents of base consumption up to pH ~ 8, (ii) during this process the amide proton signal of ^{2}H disappeared from the ^{1}H NMR spectra in both systems (Figs. 4.51 and 4.52), (iii) the signals at 4.34 and 4.83 ppm on TOCSY spectra (Figs. 4.54 and 4.55) have strong cross-peaks with the neighbouring methylene protons of the β-alanine which therefore belong to the Rh(III) coordinated terminal

amino group, (vi) the NOESY spectra of both [$MH_{-1}L$] species revealed cross-peaks between the Cp*-CH_3 and imidazole C^2H, ^2H-$C_\beta H_2$ and β-ala-$C_\beta H_2$ protons (Figs. 4.54 and 4.55).

Interestingly, in the case of carnosine, the amide deprotonation resulted in duplication of NMR signals, which indicates the formation of two isomers with nearly equal concentrations. This could be due to the presence of monomer and dimer species in nearly equal amount, as we have seen in the case of GGH. However, the mass spectrum (Fig. 4.56) detected under identical conditions indicates the presence of only monomer complexes. Consequently, the duplication of signals is related to the formation of diastereoisomers. Since carcinine has no chiral carbon, such diastereoisomerism cannot be observed. By increasing pH above pH 10 further deprotonation process took place leading to the formation of [$MH_{-2}L$] in both systems, which resulted upfield shift of the imidazole C^2H and C^5H protons on the ^1H NMR spectra (Figs. 4.51 and 4.52). Therefore, during these processes probably the imidazole N^1-nitrogens are deprotonated.

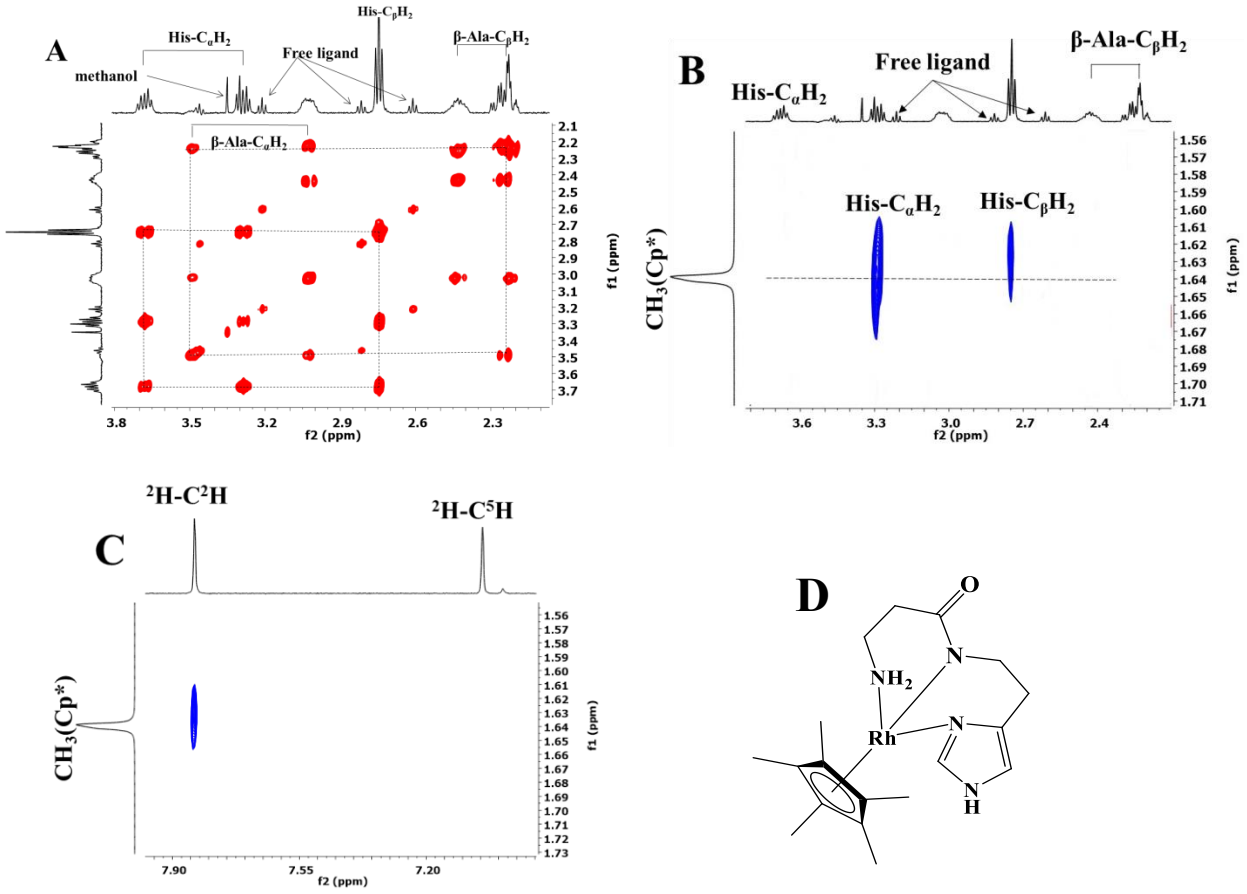

Figure 4.54 Parts of the TOCSY (A) and NOESY (B,C) spectra of the (Cp*)Rh(III)-$\mathbf{L}^{13}$ 1:1 system at pH 8.55 and proposed structure of $MH_{-1}\mathbf{L}^{13}$ (D)

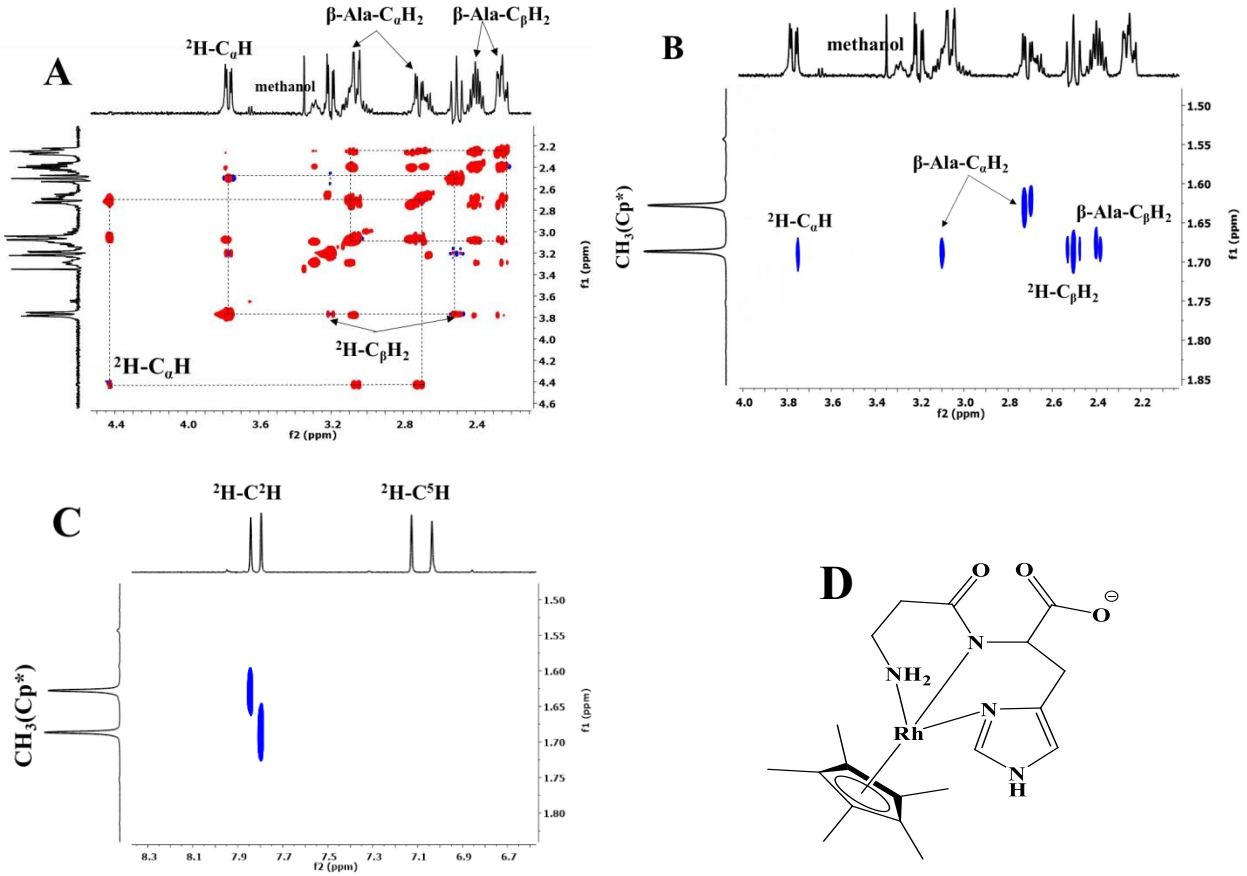

Figure 4.55 Parts of TOCSY (A) and NOESY (B,C) spectra of the (η^5-Cp*)Rh(III)-**L**^{14} 1:1 system at pH 8.30 and proposed structure of MH$_{-1}$**L**^{14} (D)

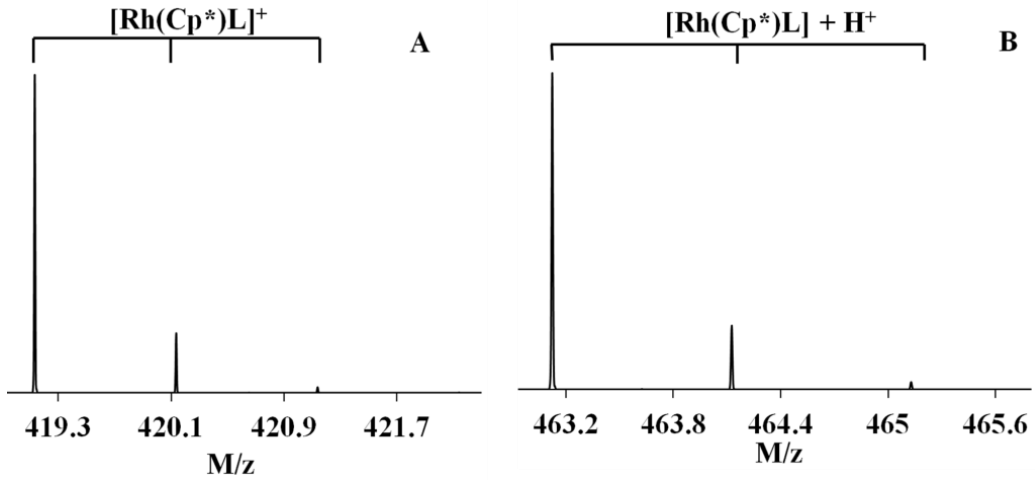

Figure 4.56 Part of ESI-MS spectrum of the Rh(Cp*)- **L**^{13} (A) and Rh(Cp*)- **L**^{14} (B) 1/1 systems at pH 8.7

4.3.2.3 Interaction of (η^5-Cp*)Rh(III) with TRH (L^{15})

Thyrotropin releasing hormone (TRH, pyroGlu-His-Pro-NH_2), a neurohormone synthesized in hypothalamus. It stimulates the synthesis and secretion of thyrotropin (thyroid-stimulating hormone). TRH mainly found in the central nervous system, it improves functional recovery after neurologic dysfunctions, such as brain trauma and epilepsy [170]. In clinical practice it is used to treat spinocerebellar degenerative diseases (e.g. Friedrich's ataxia), and it also has anti-depressant and anti-suicidal properties.

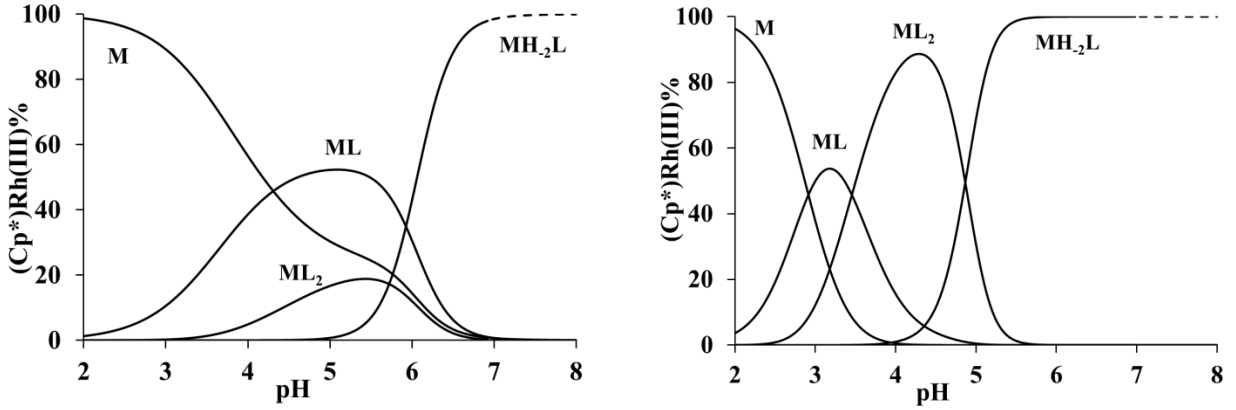

Figure 4.57 Speciation in the (η^5-Cp*)Rh(III)- $\mathbf{L^{15}}$ 1:1 (left) and (η^5-Cp*) Rh(III)- $\mathbf{L^{15}}$ 1:3 (right) systems (T = 298 K, I = 0.2 M KCl, $[M]_{tot}$ = 0.001 M). Dashed lines show the region of slow processes, where only approximate speciation can be given.

The evaluation of our potentiometric data indicated that between pH 2-5 TRH forms $[M\mathbf{L^{15}}]^{2+}$ and $[M\mathbf{L^{15}}_2]^{2+}$ complexes with (η^5-Cp*)Rh(III) cation (Fig. 4.57). The formation of these species can be easily followed on the pH-dependent ^{1}H NMR spectra (Fig. 4.58), too, especially in the region of Cp* methyl and imidazole NH protons (see the signals at 1.513/12.20 ppm for $[M\mathbf{L^{15}}]^{2+}$ and 1.483/12.32 ppm for $[M\mathbf{L^{15}}_2]^{2+}$, respectively). Based on the coordination behavior of the previously discussed ligands and on the structure of TRH, in these complexes the ligand is coordinated monodentately through its N^1-nitrogen (*i.e.* the signals of N^3H are detected at low field). Indeed, the ratio log (K_1/K_2) = log β_{101} – (log β_{102} – log β_{101}) = 0.78 indicates identical binding mode for the first and second ligands (*i.e.* bidentate coordination is unlikely). Considering the size of the ligands, it is somewhat surprising, that log β_{102} (= 9.98) is nearly identical with the log K value of the process M + $H_2\mathbf{L^{11}}$ = $MH_2\mathbf{L^{11}}$ (log K = 9.90) and only slightly smaller than log β_{102} (=10.46) determined for imidazole ($\mathbf{L^5}$).

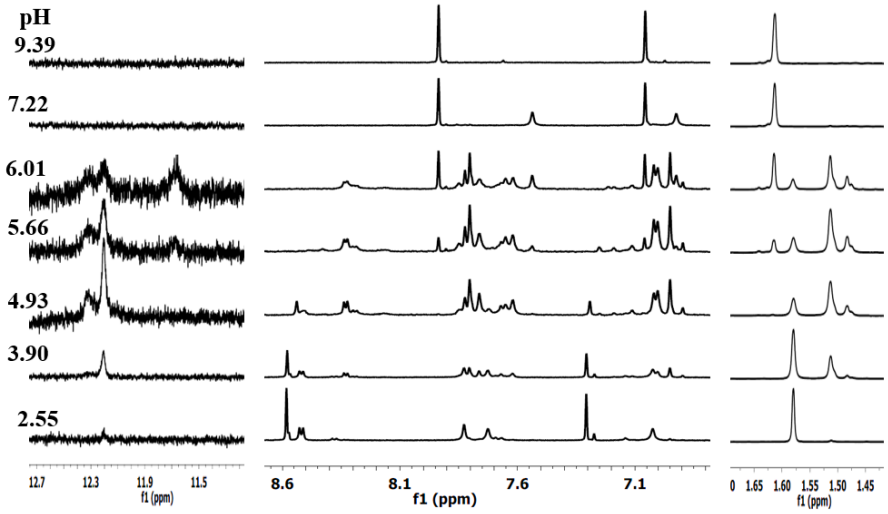

Figure 4.58 Parts of pH-dependent ^{1}H NMR spectra of (η^5-Cp*)Rh(III)-**L**^{15} 1:1 system

Above pH 5 two further equivalent base consumption were detected in a strongly overlapping manner (see Fig. A5), which are related to the highly cooperative deprotonations $[M\mathbf{L}^{15}]^{2+} = [MH_{-2}\mathbf{L}^{15}] + 2H^{+}$. The ESI-MS spectrum observed at pH 7.4 (Fig. 4.59) also support the formation and dominance of the complex $[MH_{-2}\mathbf{L}^{15}]$. Although, $[MH_{-1}\mathbf{L}^{15}]^{+}$ is a necessary intermediate of the above process, it does not form in detectable concentration. Between pH 5-7 the amide protons of the histidyl- and pyroglutamyl residues gradually disappeared from the ^{1}H NMR spectra (Fig. 4.58). The NOESY spectrum measured at pH 7.22 (Fig. 4.60) indicate the coordination of imidazole N^{3}-nitrogen (spatial proximity between Cp*-CH_3 and imidazole C^{2}H protons), i.e. the imidazole ring is part of a 6-membered chelate ring. In addition, the ^{2}H-C$_\beta$H$_2$ and pGlu-C$_\alpha$H protons are also close to the Cp* methyl groups (Fig. 4.60), suggesting that the

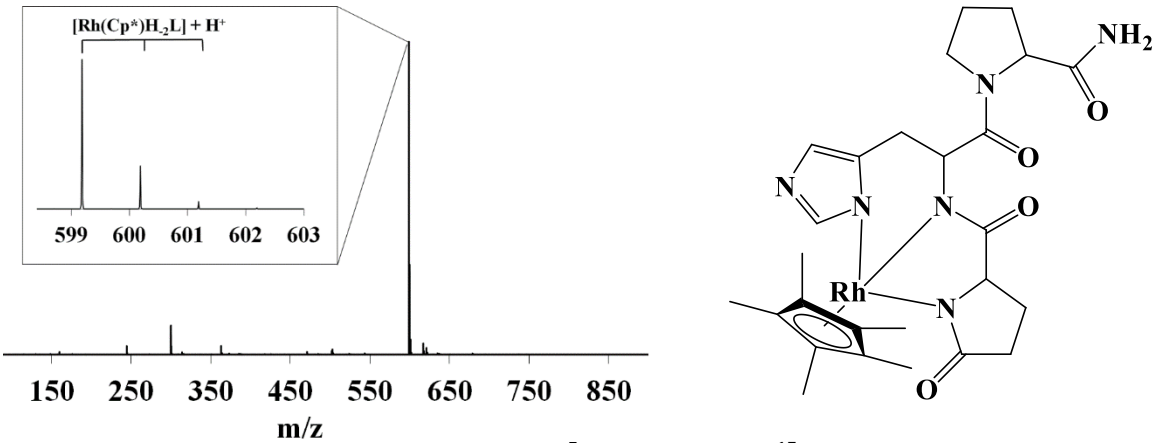

Figure 4.59 ESI-MS spectrum of the (η^5-Cp*)Rh(III)-**L**^{15} 1/1 system at pH 7.4 (left) and structure of $MH_{-2}\mathbf{L}^{15}$ species (right)

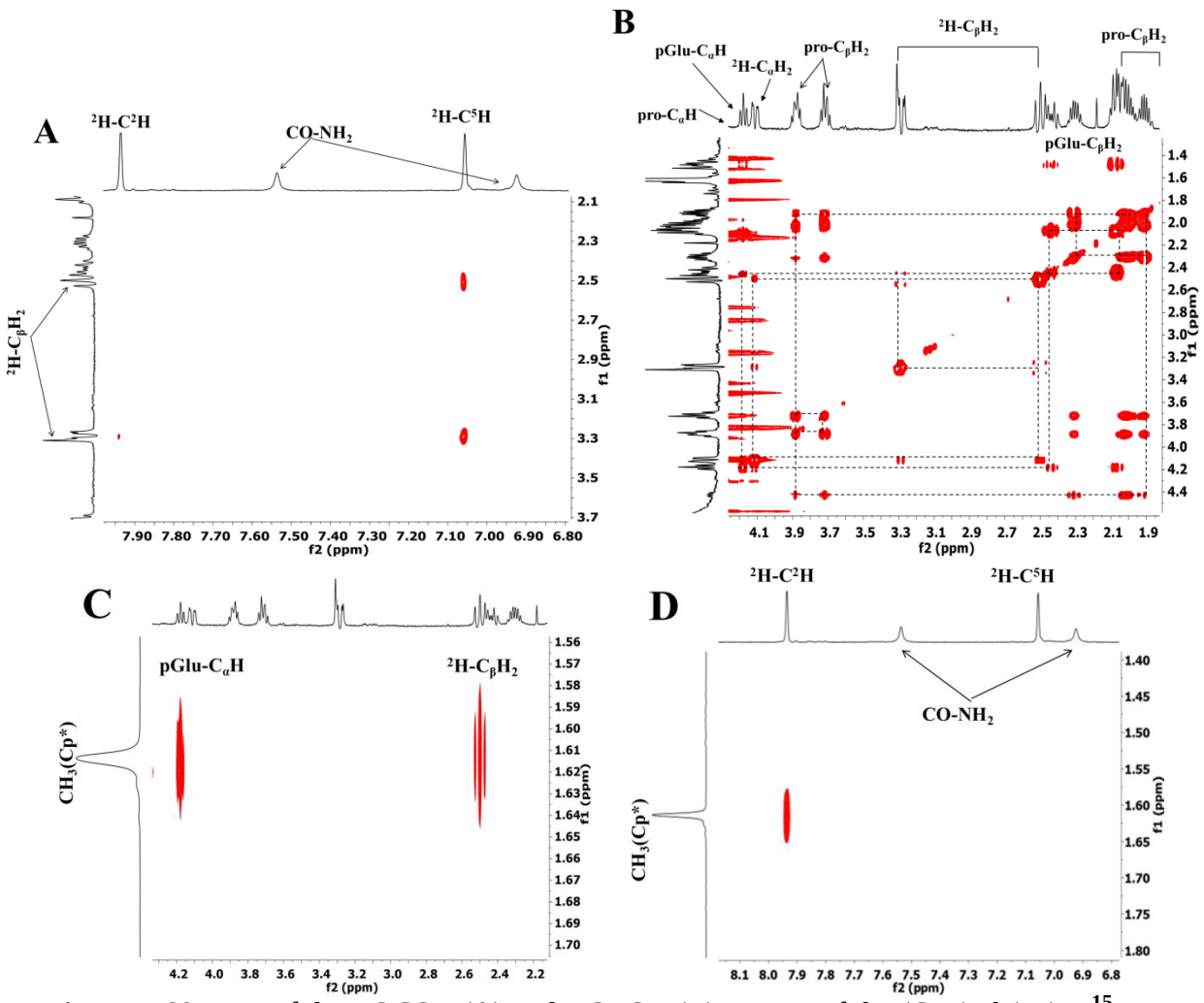

Figure 4.60 Parts of the TOCSY (A) and NOESY (B) spectra of the (Cp*)Rh(III)-**L**^{15} 1:1 system at pH 7.22

peptide backbone surrounds the metal ion. All above mentioned observations are in favor of metal induced deprotonation and coordination of histidyl- and pyroglutamyl amide nitrogens, *i.e.* of {N^3_{im},2×N^-} coordination (Fig. 4.59). Similar coordination mode was reported for the Cu(II) and Ni(II) complexes of TRH formed at neutral pH [171]

4.3.2.4 Interaction of (η^5-Cp*)Rh(III) with GHK (L^{16})

GHK (glycyl-histidyl-lysine) is a naturally occurring tripeptide present in human plasma, saliva and urine. The concentration of GHK in plasma is around 1 μM, but its amount may increase in case of injuries/inflammations. It stimulates the growth of blood vessels and nerve tissues, increases collagen, elastin and glycosaminoglycan synthesis, supports the regeneration of skin, lung, bone and liver tissues, improves the take of transplanted skin, and also possesses anti-

inflammatory, antioxidant and anti-cancer actions. GHK also effective in the treatment of chronic obstructive pulmonary disease (COPD). Furthermore, GHK has very high affinity for copper(II), therefore in human body GHK is present almost exclusively in its Cu(II) complex, *i.e.* almost all above mentioned biological effects are related to the Cu(II)-GHK complex. This interaction may also play an important role in copper ion uptake into cells [172-175].

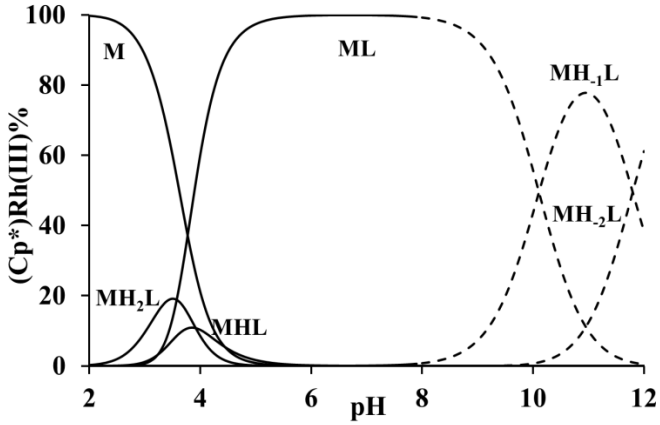

Figure 4.61 Speciation in the (η^5-Cp*)Rh(III)- $\mathbf{L^{16}}$ 1:1 systems (T = 298 K, I = 0.2 M KCl, $[M]_{tot}$ = 0.001 M).

In the (η^5-Cp*)Rh(III)-GHK equimolar system, after the formation of two minor species ($[MH_2\mathbf{L}^{16}]^{3+}$ and $[MH\mathbf{L}^{16}]^{2+}$) a single major complex $[M\mathbf{L}^{16}]^{+}$ is present in the solution between pH 4-8 (Fig. 4.61). The predominance of this species at pH = 5.7 can be clearly seen even on the MS spectrum (Fig. 4.62). During the formation of this species (i) the ^{2}H amide proton gradually disappears from the NMR spectra (Fig. 4.63), (ii) the TOCSY spectrum indicates the appearance of the signals of terminal amino protons (^{1}G-NH_2) around 3.9 and 4.4 (see the strong cross peaks with ^{1}G-CH_2 protons (Fig. 4.64), (iii) up to pH 4.6 one of the imidazole NH proton is also present on the spectra (Fig. 4.63), indicating coordinated imidazole ring. The NOESY spectrum recorded at pH 4.6 shows spatial proximity between the Cp*-methyl and imidazole ^{2}H-C^{2}H as well as ^{2}H-C$_\beta$H$_2$ protons (Fig. 4.64). All these observations are in favour for {NH_2,N^-,N^3_{im}} coordination of GHK, similarly to the analogous copper(II) complex [174]. Indeed, the NOESY crosspeak between ^{2}H-C^{2}H and ^{1}G-NH_2 protons (Fig. 4.64) suggests that the ligand wraps around the metal ion. Accordingly, the rhodium promoted amide deprotonation takes place at very low pH (pK 3.23), close to that of the analogous (η^5-Cp*)Rh(III)-GHG-NH_2 system ($\mathbf{L^{10}}$, pK ~ 3.5), indicating somewhat even higher thermodynamic stability.

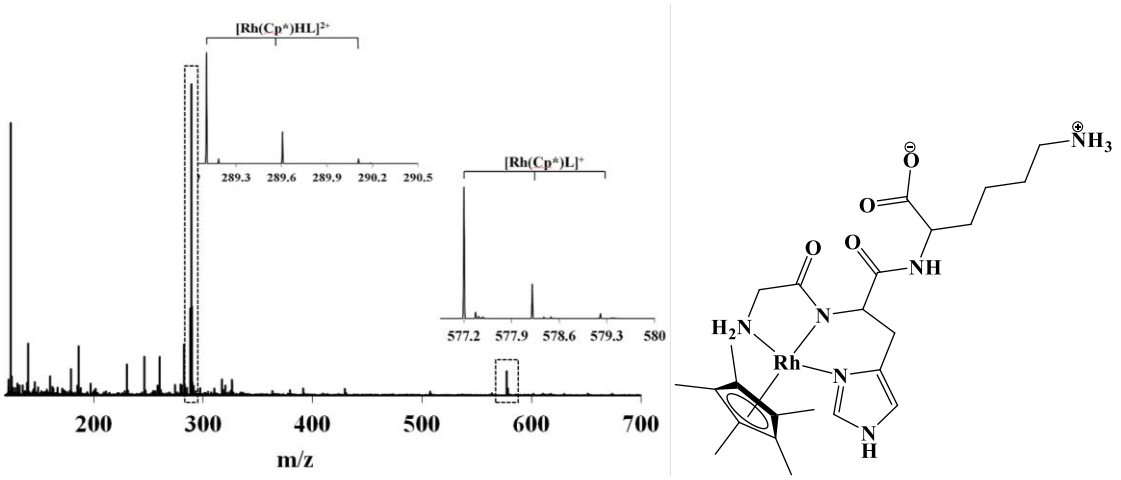

Figure 4.62 Part of ESI-MS spectrum of the Rh(Cp*)- $\mathbf{L^{16}}$ 1/1 system at pH 5.7 (left) and structure of $\mathbf{ML^{16}}$ complex (right).

In $[\mathbf{ML^{16}}]^+$ the side chain amino group of lysine is still protonated, and interestingly the ^{3}K-C$_\varepsilon$H$_2$ protons (next to the amino group) also show spatial proximity to the Cp*-methyl protons (Fig. 4.64). This suggest some ionic interaction between side chain NH_3^+ group and the negatively charged Cp* ring. The deprotonation of this ammonium ion can be well seen on the pH shift of ^{3}K-C$_\varepsilon$H$_2$ proton signals above pH 8 (Fig. 4.63), and its p*K* (= 10.10) is close to that of the free ligand.

Finally, it is worth to mention, that similarly to the $[\mathrm{MH_{-1}L^{10}}]^+$ complex, in the case of $[\mathbf{ML^{16}}]^+$ and $[\mathrm{MH_{-1}L^{16}}]$ species the signals of a minor diastereomer ($R_{Rh}S_{\alpha C}$ or $S_{Rh}S_{\alpha C}$) also appeared on ^{1}H NMR spectra beside the major ones, which can be best seen on the imidazole CH protons (Fig. 4.63).

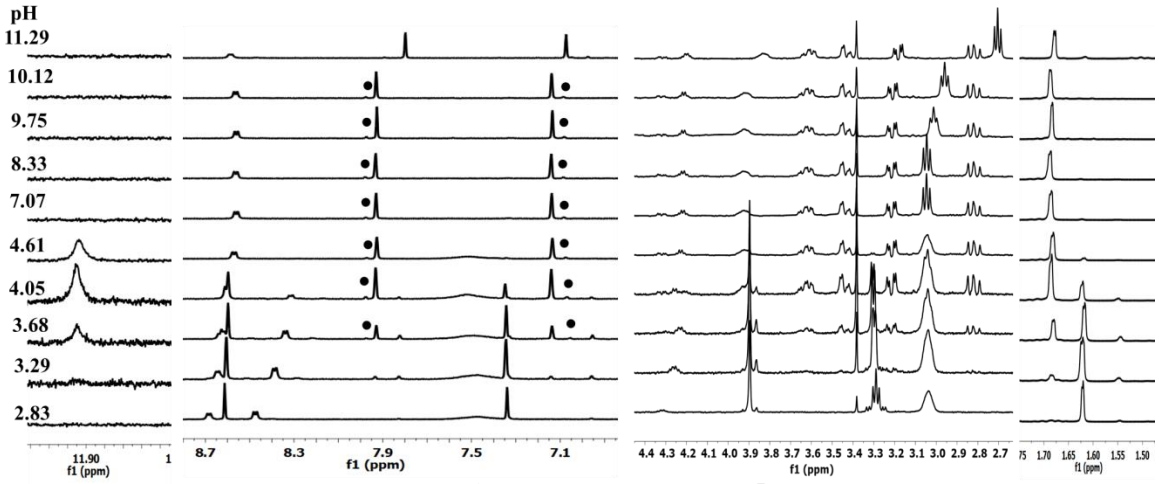

Figure 4.63 Parts of pH-dependent ^{1}H NMR spectra of (η^5-Cp*)Rh(III)-$\mathbf{L^{16}}$ 1:1 system

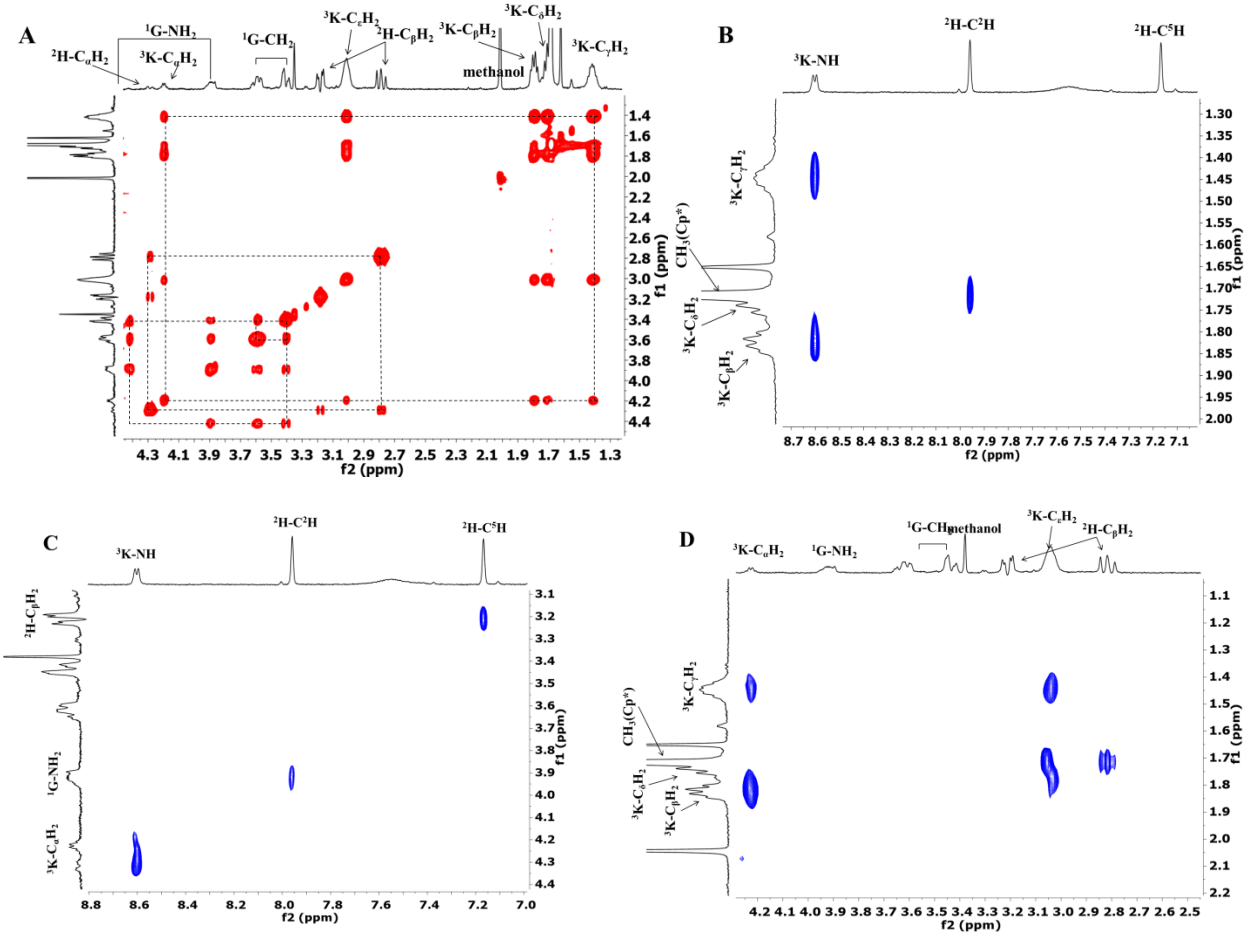

Figure 4.64 Parts of the TOCSY (red) and NOESY (blue) spectra of the (Cp*)Rh(III)-**L**[16] 1:1

4.3.3 Stereoisomerism and geometry optimization[14]

Although, the (η^5-Cp*)Rh(III) cation is well known to form "chiral-at-metal" complexes [176], the presence of two diastereomers on the NMR spectra was detected only in the (η^5-Cp*)Rh(III)-**L**[10] and (η^5-Cp*)Rh(III)-**L**[16] systems. In the other cases, either only one of the two possible diastereomers is formed, or their epimerisation is fast on the NMR timescale. In order to study this behaviour and to determine the most probable solution structures of synthetic peptide complexes present at near physiological pH (mostly $MH_{-1}L$), we performed a computational study using combined molecular mechanical and density functional methods based on the metal-binding sites and proton-proton proximities obtained from the NMR study. This work was performed by Dr. Ferenc Bogár (Institute of Medical Chemistry, University of Szeged), and I

[14] The text of this chapter is mainly based on ref [151]

was not actively involved in these calculations. Therefore, in my thesis I only summarize the final conclusions, the details of this computational study can be find in ref. [151].

Bidentate {NH_2,N^-} coordination of a peptide to (η^5-Cp*)Rh(III) allows fast epimerisation of the Rh(III) centre [177,178], accordingly we detected a single set of NMR peaks for [MH_{-1}**L**^{6}]. This agrees well with the nearly equal energies of the two optimized diastereomers for this species (Fig. A10). On the other hand, tridentate coordination of an L amino acids with $S_{\alpha C}$ absolute configuration results exclusively R configuration for the metal centre [179,180]. Accordingly, our calculation resulted stable structure only for the $R_{Rh}S_{\alpha C}$ diastereomer (Fig. A11) in the case of histidine-amide ([MH_{-1}**L**^{8}]$^+$) and HGG ([MH_{-1}**L**^{9}]). In [MH_{-1}**L**^{7}] the GGH peptide is also coordinated as a tridentate ligand, *i.e.* may give a single diastereomer. However, the 10-membered macrochelate involving the imidazole ring may be sufficiently flexible to still allow rapid epimerization. To nonetheless allow fast epimerisation, which would also result in a single set of NMR peaks. The optimized structure of the two diastereomers (Figs. A10) show rather strained macrochelates, which would likely prevent the rapid epimerisation. The $S_{Rh}S_{\alpha C}$ diastereomer has more severely distorted ^{3}H-amide group (the sum of the bond angles around the peptide nitrogen is 353.6° vs. 357.3°). More importantly, in the $S_{Rh}S_{\alpha C}$ diastereomer the metal ion is far from the plane determined by the imidazole ring (Figs. A10), which is highly unusual for imidazole complexes [181]. Consequently, the single set of NMR peaks for [MH_{-1}**L**^{7}] is probably due to the solely presence of the energetically more stable $R_{Rh}S_{\alpha C}$ diastereomer.

A single set of NMR peaks was detected for the dimer (MH_{-1}**L**^{7})$_2$ species, too. Discarding the possibility of fast epimerisation, this observation indicates that either the $R_{Rh}S_{\alpha C}/R_{Rh}S_{\alpha C}$ or $S_{Rh}S_{\alpha C}/S_{Rh}S_{\alpha C}$ diastereomer is present in the solution. Our calculations indicated lower energy for the $R_{Rh}S_{\alpha C}/R_{Rh}S_{\alpha C}$ diastereomer (Fig. A12), thus probably this isomer is present in the solution.

In the case of [MH_{-1}**L**^{10}]$^+$ we observed two sets of NMR peaks, i.e. the presence of both diastereomers. The isomer ratio is c.a. 8:1, therefore proton-proton proximities could be determined only for the major diastereomer. In this case, none of the optimized geometries could fulfil all NOESY constraints, therefore we neglected the Cp*-CH_3/^{3}H-NH proximity constraint, since the ^{3}H-NH proton is not part of the fused (5,6) chelate rings. The most stable structure obtained in this way for the major isomer was a $R_{Rh}S_{\alpha C}$ diastereomer (Figs. A11), as in all previous cases.

4.3.4 Comparison and interpretation of equilibrium data

Due to the different basicity of the ligands and composition of their complexes, it is more appropriate to calculate the concentration of non-peptide bound metal ion (pM* = − log([M] + 2[$M_2(OH)_2$] + 2[$M_2(OH)_3$]) under identical conditions (pH 7.4 and at 10 × $[M]_{tot}$ = $[L]_{tot}$ = 10^{-5} M), in order to compare the metal ion binding abilities of the studied ligands (see Tables 8 and 9). Obviously, the monodentate $\mathbf{L}^{5}$ and $\mathbf{L}^{5m}$ have the lowest metal binding affinity, which are followed by GGA ($\mathbf{L}^{6}$). At the outset, it is worth noting that in case of GGA and any other simple peptide derivatives, amide coordinated species are present at neutral pH. In certain cases, the (η^5-Cp*)Rh(III) promoted amide deprotonation occur at surprisingly low pH, its p*K* values spread over the range 3.5 – 7.0, and show roughly the reverse order with respect to thermodynamic stability.

The comparison of the pM* values calculated for GGA and GGH (pM* = 8.57 and 10.47, respectively) clearly shows the preference of (η^5-Cp*)Rh(III) toward the imidazole coordination. The metal sequestering ability of histidine containing peptides strongly depends on the position of His unit within the peptide sequence. Such dependency has already been identified for copper(II) complexes (HGG < GHG ≤ GGH [133,182]), however the different structural preferences of the two metal ions resulted in different stability order in the present case, *i.e.* GGH < HGG < GHG. The ATCUN-related GGH is the weakest (η^5-Cp*)Rh(III) binder (Tables 8 and 9), since the exceptional Cu(II) binding ability of GGH ($\mathbf{L}^{7}$) is related to its tetradentate, planar {NH_2,2×N^-,N^3_{im}} coordination mode, but (η^5-Cp*)Rh(III) has only three available binding sites in a facial geometry. HGG ($\mathbf{L}^{9}$), similarly to histidine-amide ($\mathbf{L}^{8}$), provide tridentate facial {NH_2,N_{im},N^-} coordination, therefore these ligands have considerably higher (η^5-Cp*)Rh(III) binding affinity. However, GHG-NH_2 ($\mathbf{L}^{10}$) and GHK ($\mathbf{L}^{16}$) are even stronger (η^5-Cp*)Rh(III) binder. This is somewhat surprising considering that these ligands offer a meridional {NH_2,N^-,N^3_{im}} binding mode. Consequently, in $[MH_{-1}\mathbf{L}^{6}]^+$ and $[M\mathbf{L}^{12}]^+$ the central deprotonated amide nitrogen should be severely distorted towards a pyramidal conformation, but the high thermodynamic stability probably over-compensates this conformational strain.

Carcinine ($\mathbf{L}^{13}$) and carnosine ($\mathbf{L}^{14}$) provide a meridional {NH_2,N^-,N^3_{im}} binding mode, similarly to GHG-NH_2 ($\mathbf{L}^{10}$) and GHK ($\mathbf{L}^{16}$). The only difference between these two group of ligands is the size of the fused chelate rings. At neural pH (6,6) membered chelates are formed in the (η^5-Cp*)Rh(III) complexes of $\mathbf{L}^{13}$ and $\mathbf{L}^{14}$, while (5,6) membered chelates are present in $\mathbf{L}^{10}$

and $\mathbf{L}^{16}$ complexes. This, seemingly small, difference results in a considerably smaller pM* values for carcinine and carnosine (ΔpM* ~ 5). The higher flexibility of the two 6-membered chelates in [$MH_{-1}\mathbf{L}^{14}$] results in the formation of two diastereomers in nearly equal concentrations. In all other systems one of the two possible diastereomers is considerably more favoured energetically than the other.

Although, TRH (pyroGlu-His-Pro-NH_2) also contains histidine in the second position, like GHG-NH_2 ($\mathbf{L}^{10}$) and GHK ($\mathbf{L}^{16}$), no terminal amino group is present in this molecule. The 3N coordination observed at neutral pH requires the simultaneous deprotonation of two amide nitrogens located towards the C-terminal (i.e. $\{N^3_{im},2\times N^-\}$). This and the conformational strain caused by the distorted geometry of the central deprotonated amide nitrogen results in a low pM* value, similar to those of carcinine and carnosine. On the other hand, this example proves that interchain histidine is a suitable anchoring group for amide deprotonation promoted by the (η^5-Cp*)Rh(III) cation.

Interestingly, despite the presence of histidine at the N-terminal position of HHHG, the $\{NH_2,N_{im},N^-\}$ coordination, observed for histidine-amide and HGG, is not formed at neutral pH. Instead, the [$M\mathbf{L}^{11}$]$^{2+}$ complex has a $\{NH_2,2\times N_{im}\}$ binding mode, *i.e.* imidazole coordination is preferred over amide. The pM* values of histidine, histidine-amide, HGG and HHHG-NH_2 are close to each other, thus the histamine-like binding mode complemented by either carboxylate, amide or imidazole coordination results in roughly similar thermodynamic stability.

Among the studied peptides there are several exceptionally strong copper(II) binder (e.g. GHG and GGH), and the physiological effect of some biogenic peptide is strongly related to their copper(II) binding properties (carcinine, carnosine and GHK). Consequently, it is worth to compare the copper(II) and (η^5-Cp*)Rh(III) binding abilities of the studied ligands. Based on the predominance diagrams of the different (η^5-Cp*)Rh(III)-Cu(II)-peptide 1/1/1 ternary systems (Fig. A13) it is clear that (η^5-Cp*)Rh(III) cation has very high affinity towards peptides, in most cases it is greater than that of the well-known peptide-binder copper(II). The only exceptions are the peptides containing the ATCUN motif (XXH), namely GGH ($\mathbf{L}^{7}$) and HHHG-NH_2 ($\mathbf{L}^{11}$). But even in these cases, (η^5-Cp*)Rh(III)-peptide complexes dominate in the solutions up to pH 6, and only above this pH becomes the formation of copper(II) complexes more favoured. This is due to the formation of the tetradentate $\{NH_2,2\times N^-,N^3_{im}\}$ binding mode in copper(II) complexes, which provides higher thermodynamic stability, as the at most tridentate binding mode in

rhodium(III) species. Finally, the two metal ions show similar affinity towards carnosine at the physiological pH, since in this case the tridentate $\{NH_2,N^-,N^3_{im}\}$ binding mode in the Rh(III) complexes can effectively compete with the tetradentate $\{NH_2,N^-,COO^-+N_{im}\}$ coordination formed in the dimer $[Cu_2H_{-2}L_2]$ complex, since it provides less thermodynamic stability than the ATCUN motif. On the other hand, the formation of this dimer species is negligible at the physiologically relevant micromolar concentration range, therefore under this conditions the (η^5-Cp*)Rh(III) complexes dominate in the neutral pH range in case of carnosine, too (see dashed lines in Fig. A13).

4.3.5 Mimicing the interaction of the (η^5-Cp*)Rh(III)-based potentially anticancer or drug delivery agents with peptides [15]

The predominance diagrams (Fig. A13) clearly indicate that most of these peptides, even the copper(II) specific peptides GHK (**L**^{16}), bind rhodium considerably stronger than copper(II). Consequently, such histidine peptides can significantly influence the biospeciation of potentially therapeutic half-sandwich rhodium complexes. In order to prove the actual realization of this possibility, and to mimic the interaction of the (η^5-Cp*)Rh(III)-based potentially anticancer or drug delivery agents with peptides and proteins present in biological fluids, we also studied the (Cp*)Rh(III)-A-B ternary systems (where A = bipyridyl (bpy) or ethylene-diamine (en); B = **L**^{6}, **L**^{7}, **L**^{8}, **L**^{9}, **L**^{10}, **L**^{11}, **L**^{12}, **L**^{13}, **L**^{14}, **L**^{15}, **L**^{16}). The (η^5-Cp*)-bpy and -en complexes are used as two simple representatives of Rh-based potentially anticancer agents. Although, the [Ru(II)(η^6-cymene)(en)Cl]PF_6 and [Ru(II)(η^6-biphenyl)(en)Cl]PF_6 compounds [183], as well as (Cp*)Rh(III) complexes of some (N,N) polypyridyl ligands showed promising in vitro antiproliferative activity [184], the (η^5-Cp*)Rh(III) complexes of ethylene-diamine and bipyridyl possessed negligible effect [184]. On the other hand, the bpy complex possesses moderate antiproliferative effect against A2780 human ovarian cancer cells [185]. Although the (η^5-Cp*)Rh(III)-en/bpy complexes do not have significant anticancer effect, we chose these simple ligands for our study, since their coordination behaviours are basically similar to many other ligands, in fact they have high (Cp*)Rh(III) binding affinity, which was already studied from equilibrium points of view

[15] The text of this chapter is mainly based on ref [151]

[74]. Their pM* values calculated under the conditions given in Table 8-9 are pM* = 12.65 (en) and 13.90 (bpy).

^{1}H-NMR spectra were recorded for the (η^5-Cp*)Rh(III) complexes of en and bpy in the absence and resence of peptides at physiological pH to identify the species formed in the (η^5-Cp*)Rh(III)–en/bpy–ligands (1:1:1) ternary systems after 24-48 h equilibriation at 25 °C. Our data indicated that the weakest binder GGA does not interact, but all histidine derivatives form ternary species with the (η^5-Cp*)Rh(III)-en/bpy complexes (Fig. 4.66). Moreover, in the cases of histidine-amide (**L^{8}**), HGG (**L^{9}**), GHG-NH_2 (**L^{10}**), HHHG-NH_2 (**L^{11}**), histidine (**L^{12}**), TRH (**L^{15}**) and GHK (**L^{16}**) even the signals of binary peptide complexes appeared on the NMR spectra, indicating that these peptides are able to displace ethylene-diamine or bipyridyl from the coordination sphere of (η^5-Cp*)Rh(III) (see Appendix Fig. A14).

The distribution (%) of binary and ternary species in the (η^5-Cp*)Rh(III)-en/bpy-ligand (1:1:1) ternary systems are collected in Table 10. These data also include information on the chemical equilibrium, but due to the unknown values of N-terminal and side-chain amino p*K*s of imidazole coordinated peptides, the correct evaluation of data in Table 10 is not possible. Nevertheless, an estimation of log K = 4.5 ± 0.5 can be given as an average for the monodentate imidazole coordination to the (η^5-Cp*)Rh(III)-en/bpy complexes, This value is considerably higher than log K_3 ~ 3 obtained in the (η^5-Cp*)Rh(III)-**L$^{1(m)}$** systems (Table 8), indicating the preferred formation of such ternary complexes due to some additional (electronic?) interaction(s). This 'extra' stability may result in efficient binding of imidazole side chains of peptides/proteins to the (η^5-Cp*)Rh(III)-based potentially anticancer compounds even under sub-milimolar conditions.

The observed distribution of binary and ternary complexes roughly correlate with the thermodynamic stability or pM* values of the corresponding binary species, however in some cases the deviation is significant. The most striking inconsistency was observed with TRH. The pM* values determined for the (η^5-Cp*)Rh(III)-TRH system (pM* = 9.25) is considerably smaller than those determined for the (η^5-Cp*)Rh(III)-en/bpy systems (pM* = 12.65 (en) and 13.90 (bpy)), *i.e.* binary (η^5-Cp*)Rh(III)-TRH complex should not form in the ternary systems. Nonetheless, after 48h equilibration the signals of the binary (η^5-Cp*)Rh(III)-TRH complex were present on the ^{1}H NMR spectra. Therefore, we repeated our measurements with 2 weeks equilibration time, but the results were the same as before (Fig. 4.65). This is probably related to

an unusual kinetic behaviour of the binary TRH species, *i.e.* relatively fast formation but very slow dissociation.

The NOESY spectra of the ternary systems (some representative example are presented in Appendix Fig. A8 and A9) indicate that in all ternary complexes only the C^2H and C^5H protons of imidazole rings are in spatial proximity to the Cp*-methyl protons. Consequently, in the ternary species these histidine derivatives coordinate monodentately to Rh(III) through their imidazole N^1-nitrogens. This observation also implies that considering only monodentate coordination at neutral pH the imidazole ring has much higher (η^5-Cp*)Rh(III) binding ability than the carboxylate or amino groups.

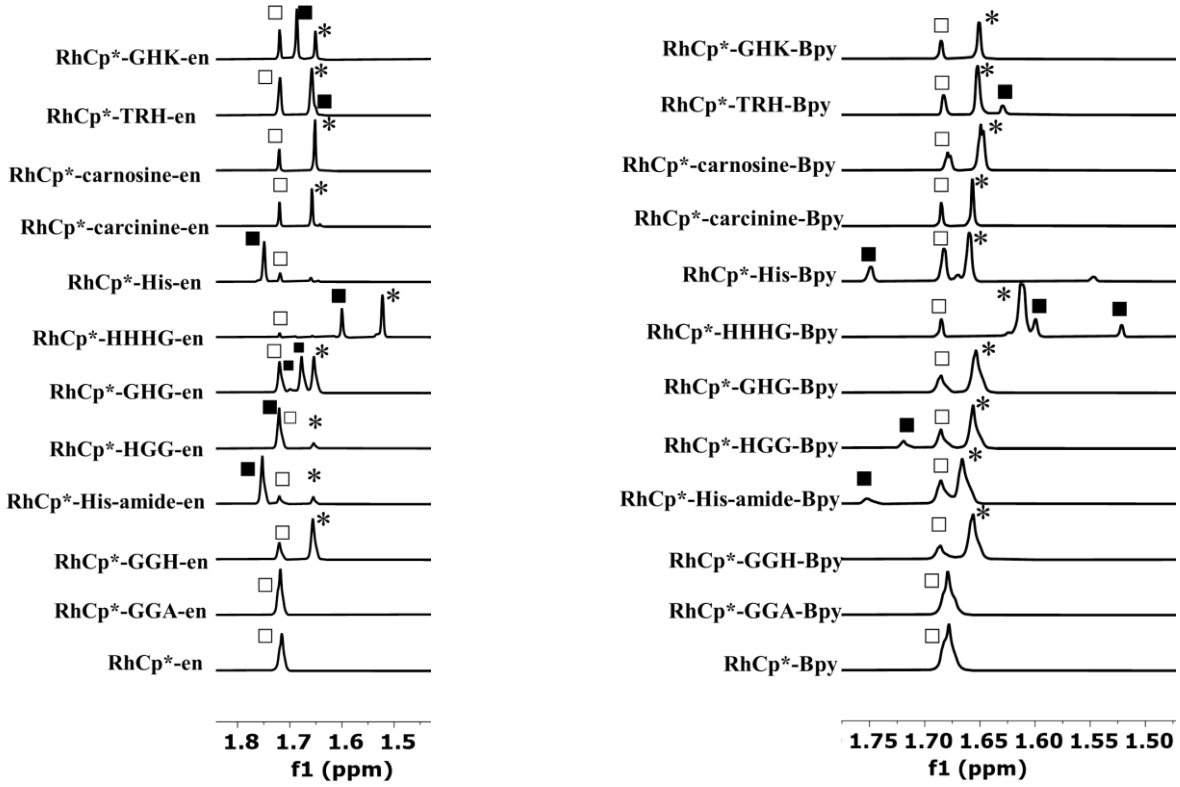

Figure 4.65 ^{1}H NMR signals of Cp*-methyl protons in the (Cp*)Rh(III)-bpy/en binary and different ternary systems (□: MA, *: MAB, ■ : MB).

Table 10. Distribution (%) of the binary and ternary species in the (η^5-Cp*)Rh(III)-en/bpy-histidine derivatives (1:1:1) ternary systems based based of the ^{1}H NMR peak integrals ([(η^5-Cp*)Rh(III)]$^{2+}_{tot}$ = 2 mM, pH = 7.4, *T* = 25 °C, incubation time = 24-48 h (2 weeks for TRH)).

A	B	[RhCp*(A)]%	[RhCp*(B)]%	[RhCp*(A)(B)]%
En	GGA	100	-	-
	GGH	29	-	71
	His-amide	14	74	12
	HGG	-	85	15
	GHG-NH_2	28	38	34
	HHHG-NH_2	5	34	61
	Histidine	18	82	-
	Carcinine	38	-	62
	carnosine	29	-	71
	TRH	40	10	50
	GHK	26	47	26
Bpy	GGA	100	-	-
	GGH	25	-	75
	His-amide	30	8	62
	HGG	27	11	62
	GHG-NH_2	28	-	72
	HHHG-NH_2	12	22	66
	Histidine	34	16	50
	Carcinine	33	-	67
	carnosine	28	-	72
	TRH	23	14	63
	GHK	32	-	68

5. SUMMARY

The overall goal of my PhD thesis was to characterize (partly design and synthesize, too) some amide-containing ligands and to study their metal complexes in order to answer some practical problems. The thesis covers three, at first glance, different topics. However, these areas are interconnected by (i) the amide-group, which is contained in almost all investigated ligands, (ii) the similar coordination chemical properties of imidazole and pyridine rings, and (iii) the studied metal ions (Cu(II) and (η^5-Cp*)Rh(III)). The scientific content and value of this work can be summarized in the following points:

I. Design of specific artificial metallophores for Alzheimer's disease therapy, which are able to transport Cu(II) from its amyloid complexes to the membrane transporter hCTR1.

I designed and synthetized two ligands (PMPA, $\mathbf{L^1}$ and DPMGA, $\mathbf{L^2}$, see Chart 4.1) and studied their Cu(II) and Zn(II) complexes. The comparative evaluation of pH-potentiometric, UV-Vis and EPR spectroscopic data indicated that in mM concentration range, *mono*- and *bis*-complexes, at μM concentrations only *mono*-complexes are formed. In excess of the tridentate PMPA ligand, both metal ions form 6N coordinated *bis*-complexes, with two pyridine and two deprotonated amide nitrogens in the equatorial plane. This is surprising, since the amide deprotonation in zinc complexes is relatively rare phenomenon, while in case of copper(II) the Jahn-Teller distortion generally prevents the 6N coordination. In case of the tetradentate ligand 6N coordination occurs only for zinc in its *bis*-complexes which is the main species at ligand excess and at neutral pH. In case of copper mostly *mono*-complexes are formed, of which the $\{N_{pyr},N^-,NH,N_{pyr}\}$ coordinated $[CuLH_{-1}]^+$ complexes predominate in a wide pH range. The pM dependence on the ligand concentration indicates that the Cu(II) binding ability of the tetradentate DPMGA is three orders of magnitude higher than that of the tridentate PMPA. Furthermore, both ligands bind copper(II) seven orders of magnitude stronger than zinc(II), consequently these ligands are specific for copper(II) even in presence of high excess Zn(II). Our fluorescence titrations proved that both ligands can compete with $A\beta_{1-16}$ for Cu(II), and that the tetradentate DPMGA is more effective competitor than PMPA. However, only the tridentate PMPA has lower conditional binding constant than the copper transporter human CTR1. In addition, we also studied the

ability of PMPA, DPMGA and some other relevant ligands to inhibit the ROS production generated by the raction of copper(II) with ascorbic acid. The results indicated that in contrast to some well-known and strong copper binder ligands, such as Gly-His or NTA, our ligands are indeed able to reduce ROS production. Considering all these observations, only the tridentate PMPA has the properties that are essential to behave as a potential artificial metallophore, *i.e.* able to remove Cu(II) from the redox active Cu(II)-amyloid β species, its Cu(II) complex is redox inactive, and has lower Cu(II) binding affinity as the membrane transporter hCTR1.

II. Design of some His-containing peptides, of which copper(II) complexes can closely mimic the LPMO active centres both from structural and functional points of view.

To this end, I designed and synthetized the HPH-NH_2 ($\mathbf{L^3}$) and HPHPY-NH_2 ($\mathbf{L^4}$) peptides, which possess a binding site similar to the 'His-brace' structural motif, and the additional tyrosine in $\mathbf{L^4}$ may potentially mimic the axial Tyr residues in the active centres of lytic polysaccharide monoxygenases (LPMOs). Proline subunits are used to separate the histidines, in order to prevent the copper(II) promoted amide deprotonation and to provide relatively rigid structure for the ligands. The comparative evaluation of the pH-potentiometric, UV-Vis, CD, ESI-MS and EPR spectroscopic data showed that above pH 5 and in equimolar solutions the complex formation processes are fundamentally different from all copper(II)-peptide systems known so far. Namely, the proline units prevent the formation of the ATCUN-type $\{NH_2,2N^-,N_{im}\}$ coordination above pH 5-6, which is the main binding mode of N-terminally non-protected HXH (X≠P) peptides. Instead, in our systems the imidazolato-bridged $Cu_2H_{-1}(\mathbf{L^3})_2$ and $Cu_2H(\mathbf{L^4})_2$ dimer complexes are dominant in the solution between pH 6-8. Above pH 8 two further deprotonations were observed in both systems. These processes are related to the formation of a metal-bound hydroxide ion, except for the first deprotonation in the Cu(II)-$\mathbf{L^4}$ system, during wich the Tyr-phenolate oxygen binds to the metal ion.

Although our goals were only partially achieved, the amide deprotonation was suppressed, but the complexes formed in neutral and alkaline pH show only limited analogy to the 'His-brace' motif, we attempted to explore the LPMO-like activity of these complexes, especially considering our cyclic voltammetric results which indicated rather positive formal redox potentials for the Cu(II)/Cu(I) redox couple in these complexes both at neutral and at

alkaline pH. To this end, we studied the oxidation of *p*-nitrophenyl-*β*-D-glucopyranoside (PNPG) by H_2O_2 in presence of our complexes both at pH 7.4 and 10.5. The kinetic results indicated that (i) the simultaneous presence of H_2O_2 and copper(II) complexes results in significant, truly catalytic LPMO-like activity even at neutral pH, which is a unique behavior among the LPMO model complexes reported so far, (ii) the Michaelis-Menten model is applicable in our systems. Since the LPMO-like activity most probably proceeds via a copper(II)-peroxo complex, we also studied the interaction of H_2O_2 and our complexes in the absence of PNPG. The analysis UV-Vis and EPR spectra indicated the time-dependent formation of mononuclear Cu(II)-OOH and partly 1,2-peroxodi-copper(II) complexes. These complexes, especially the mononuclear one, are stable for 1-2 hours at low, but decomposes more rapidly at high H_2O_2 excess, yielding Cu(I) species. We propose, that the interaction of this Cu(I) complex(es) with excess of H_2O_2 results in a homolytic O-O bond cleavage and the formation of a highly reactive Cu(II)-oxyl species, which is known to be required for an efficient H-abstraction from the substrate. In this way, we assume a similar catalytic cycle for our model complexes, as suggested recently for the native LPMOs.

III. To explore the most important thermodynamic factors governing the biospeciation of (η^5-Cp*)Rh(III)-based potential metallodrugs in biological fluids.

The monodentate imidazole coordination is the most frequently detected binding mode of peptides and proteins to half-sandwich Ru(II)/Rh(III) complexes, however, to our knowledge, no complete solution themodynamic study on the interaction of (η^5-Cp*)Rh(III) cation or its potential medicinal complexes with amino acids or peptides are available in the literature. Therefore, I studied the interactions of (η^5-Cp*)Rh(III) cation with 11 histidine derivatives, among them biogenic peptides such as carcinine, carnosine, TRH (pGlu-His-Pro-NH_2) and GHK (Gly-His-Lys), as well as with imidazole and Gly-Gly-Ala, which were investigated for comparative purposes. After exploring the binary (η^5-Cp*)Rh(III) complexes of these ligands, we also studied some (η^5-Cp*)Rh(III)-A-B ternary systems (where A = 2,2'-bipyridyl (bpy) or ethylene-diamine (en); B = the studied peptides), in order to mimic the interaction of the (η^5-Cp*)Rh(III)-based potentially anticancer or drug delivery agents with biogenic peptides and proteins. Based on the comparative evaluation of pH-potentiometric, UV-Vis, ^{1}H NMR and MS spectroscopic data, the following general conclusions can be made:

(i) The (η^5-Cp*)Rh(III) cation is able to induce the deprotonation of amide nitrogen well below pH 7 even in case of GGA peptide, having no coordinating side chain.

(ii) The presence histidine units in the peptides results in 2-6 orders of magnitudes stability increase as compared to GGA.

(iii) The (η^5-Cp*)Rh(III) sequestering ability of histidine containing peptides strongly depends on the position and number of His unit within the peptide sequence, the observed order for the monohistidine peptides is as follows: XYH < HXY < XHY. Although, the ATCUN-like GGH is a very strong Cu(II) binder, it forms the least stable (η^5-Cp*)Rh(III) complexes among the His-peptides, because its tetradentate in-plane coordination mode does not fit to the three available facial binding sites of Rh(III). HGG, similarly to histidine-amide, provide tridentate facial {NH_2,N_{im},N^-} coordination, therefore these ligands have considerably higher (η^5-Cp*)Rh(III) binding affinity. However, GHG-NH_2 and GHK are even stronger (η^5-Cp*)Rh(III) binder. This is somewhat surprising considering that these ligands offer a meridional {NH_2,N^-,N^3_{im}} binding mode, while (η^5-Cp*)Rh(III) prefers a facial one. Although, carcinine and carnosine provide similar {NH_2,N^-,N^3_{im}} binding mode as GHG-NH_2 and GHK, the higher the size of their fused chelate rings results in a considerably smaller (η^5-Cp*)Rh(III) binding ability. Although, TRH also contains histidine in the second position, like GHG-NH_2 and GHK, no terminal amino group is present in this molecule. The 3N coordination observed at neutral pH requires the simultaneous deprotonation of two amide nitrogens located towards the C-terminal ({N^3_{im},N^-,N^-} type coordination), which results in a low binding ability, similar to those of carcinine and carnosine. Interestingly, amide coordination was not observed for the multihistidine peptide HHHG.NH_2. Instead, a highly stable {NH_2,N_{im},N_{im}} coordinated species is dominant in the neutral pH. The (η^5-Cp*)Rh(III) binding ability of histidine ({NH_2,N_{im},N_{im}} coordination), histidine-amide and HGG ({NH_2,N_{im},N_{im}} coordination) and HHHG-NH_2 are close to each other, thus the histamine-like binding mode complemented by either carboxylate, amide or imidazole coordination results in roughly similar thermodynamic stability.

(iv) Among the studied peptides there are several exceptionally strong copper(II) binder (e.g. GGH, GHG-NH_2, HHHG-NH_2 and GHK), and the physiological effect of some biogenic peptide is strongly related to their copper(II) binding properties (histidine, carcinine, carnosine and GHK). Consequently, it is worth to compare the copper(II) and (η^5-

Cp*)Rh(III) binding abilities of the studied ligands. Based on the simulated predominance diagrams calculated for the different (η^5-Cp*)Rh(III)-Cu(II)-peptide 1/1/1 ternary systems,it is clear that (η^5-Cp*)Rh(III) cation has very high affinity towards peptides, in most cases greater than that of the well-known peptide-binder copper(II). The only exceptions are the peptides containing the ATCUN motif (XXH), namely GGH and HHHG-NH_2. But even in these cases, (η^5-Cp*)Rh(III)-peptide complexes dominate in the solutions up to pH 6.

(v) The higher flexibility of the two fused 6-membered chelates within the tridentate, {NH_2,N^-,N^3_{im}} coordinated complex of carnosine results in the formation of two diastereomers in nearly equal concentrations. In all other analogous complexes one of the two possible diastereomers (most likely $R_{Rh}S_{\alpha C}$) is considerably more favoured energetically than the other.

(vi) Our detailed ^{1}H NMR study on the different (η^5-Cp*)Rh(III)-en/bpy-peptide ternary systems at physiological pH indicated, that all histidine derivatives form ternary species with the (η^5-Cp*)Rh(III)-en/bpy complexes. Moreover, in the cases of histidine-amide, HGG-OH, GHG-NH_2, HHHG-NH_2, histidine, TRH and GHK even the signals of binary peptide complexes appeared on the NMR spectra, indicating that these peptides are able to displace ethylene-diamine or bipyridyl from the coordination sphere of (η^5-Cp*)Rh(III). These behaviours may have important implication on the biospeciation/ biotransformation of (η^5-Cp*)Rh(III)-based potential metaééodrugs in human bodies.

List of references

[1] Z. K. Mathys, A. R. White, *Adv. Neurobiol*. 18 (**2017**) 199–216.
[2] J. H. Kaplan, E. B. Maryon, *Biophys. J*. 110 (**2016**) 7–13.
[3] J. R. Prohaska, A. A. Gybina, *J. Nutr*. 134 (**2004**) 1003–1006.
[4] A. I. Mot, A. G. Wedd, L. Sinclair, D. R. Brown, S. J. Collins, M. W. Brazier, *Expert. Rev. Neurother*. 11 (**2011**) 1717–1745.
[5] T. J. Huat, J. C. Perna, E. A. Newcombe, N. Valmas, M. Kitazawa, R. Medeiros, *J. Mol. Biol*. 431 (**2019**) 1843-1868.
[6] E. Atrián-Blasco, P. Gonzalez, A. Santoro, B. Alies, P. Faller, C. Hureau, *Coord. Chem. Rev*. 371 (**2018**) 38–55.
[7] E. Stefaniak, W. Bal, *Inorg. Chem*. 58 (**2019**) 13561–13577.
[8] G. Domingo, L. Benussi, C. Saraceno, M. Bertuzzi, R. Nicsanu, A. Longobardi, S. Bellini, A. Cagnotto, M. Salmona, G. Binetti, R. Ghidoni, *Front. Neurosci*. 15 (**2021**) A:708119.
[9] C. Esmieu, D. Guettas, A. Conte-Daban, L. Sabater, P. Faller, C. Hureau, *Inorg. Chem*. 58 (**2019**) 13509–13527.
[10] M. G. Savelieff, G. Nam, J. Kang, H. J. Lee, M. Lee, H. H. Lim, *Chem. Rev*. 119 (**2019**) 1221–1322.
[11] B. Alies, E. Renaglia, M. Rózga, W. Bal, P. Faller, C. Hureau, *Anal. Chem*. 85 (**2013**) 1501–1508.
[12] a) P. Gamez, A. B. Caballero, *AIP Adv*. 5 (**2015**) 092503.
b) E. Stefaniak, D. Płonka, S. C. Drew, K. Bossak-Ahmad, K. L. Haas, M. J. Pushie, P. Faller, N. E. Wezynfeld. W. Bal, *Metallomics*, 10 (**2018**) 1723-1727.
[13] J. Nagaj, K. Stokowa-Sołtys, I. Zawisza, M. Jeżowska-Bojczuk, A. Bonna, W. Bal, *J. Inorg. Biochem*.,119 (**2013**) 85-89.
[14] L. Rulíšek, J. Vondrášek, *J. Inorg. Biochem*. 71 (**1998**) 115–127.
[15] M. Casolaro, M. Chelli, M. Ginanneschi, F. Laschi, L. Messori, M. Muniz-Miranda, A. M. Papini, T. Kowalik-Jankowska, H. Kozłowski, *J. Inorg. Biochem*. 89 (**2002**) 181–190.
[16] I. Sóvágó, C. Kállay, K. Várnagy, *Coord. Chem. Rev*. 256 (**2012**) 2225–2233.
[17] H. Kozlowski, W. Bal, M. Dyba, T. Kowalik-Jankowska, *Coord. Chem. Rev*. 184 (**1999**) 319–346.
[18] G. Brooks, L. D. Pettit, *J. Chem. Soc., Dalton Trans*. (**1975**) 2112.
[19] I. Sóvágó, E. Farkas, A. Gergely, *J. Chem. Soc., Dalton Trans*. (**1982**) 2159-2163.
[20] E. Farkas, I. Sóvágó, A. Gergely, *J. Chem. Soc., Dalton Trans*. (**1983**) 1545-1551.
[21] D. L. Rabenstein, S. A. Daignault, A. A. Isab, A. P. Arnold, M. M. Shoukry, *J. Am. Chem. Soc*. 107 (**1985**) 6435-6439.
[22] N. Camerman, A. Camerman, B. Sarkar, *Can. J. Chem*. 54 (**1976**) 1309.
[23] E. Farkas, I. Sóvágó, T. Kiss, A. Gergely, *J. Chem. Soc., Dalton Trans.* (**1984**) 611-614.
[24] C. Harford, B. Sarkar, *Accounts of chemical research* 30 (**1997**) 123-130.
[25] A. Kolozsi, A. Jancsó, N. V. Nagy, T. Gajda, *J. Inorg. Biochem*. 103 (**2009**) 940-947.
[26] A. Myaria, G. Malandrinos, Y. Deligiannakis, J. C. Plakatouras, N. Hadjiliadis, Z. Nagy, I. Sòvágó, *J. Inorg. Biochem*. 85 (**2001**) 253-261.
[27] B. Bóka, A. Myari, I. Sóvágó, N. Hadjiliadis, *J. Inorg. Biochem.* 98 **(2004**) 113-122.
[28] I. Sóvágó, K. Ősz, *Dalton Trans.* (**200**6), 3841-3854.
[29] C. Kállay, K. Várnagy, G. Malandrinos, N. Hadjiliadis, D. Sanna, I. Sóvágó, *Inorg. Chim. Acta*. 362 (**2009**) 935-945.

[30] G. R. Hemsworth, E. M. Johnston, G. J. Davies, P. H. Walton, *Trends Biotechnol.* 33 (**2015**) 747-761.
[31] S. Imlimthan, P. Figueiredo, H. A. Santos, M. Sarparanta, *Lignin-Based Materials for Biomedical Applications*, (**2021**) 1-34.
[32] J. Jae, G. A. Tompsett, Y.-Chuan Lin, T. R. Carlson, J. Shen, T. Zhang, B. Yang, C. E. Wyman, W. Curtis Conner, G. W. Huber, *Energy Environ. Sci.* 3 (**2010**) 358-365.
[33] M. Thornbury, J. Sicheri, P. Slaine, L. J. Getz, E. Finlayson-Trick, J. Cook, C. Guinard, N. Boudreau, D. Jakeman, J. Rohde, C. McCormick, *PLoS One* 14 (**2019**) e0209221.
[34] G. R. Hemsworth, B. Henrissat, G. J Davies, P. H. Walton, *Nat Chem Biol.* 10 (**2014**) 122–126.
[35] X. Zhou, H. Zhu, *Bioresour. Bioprocess.* 7 (**2020**) 11.
[36] K. E. H. Frandsen, T. J. Simmons, P. Dupree, J.-C. N. Poulsen, G. R. Hemsworth, L. Ciano, E. M. Johnston, M. Tovborg, K. S. Johansen, P. von Freiesleben, L. Marmuse, S. Fort, S. Cottaz, H. Driguez, B. Henrissat, N. Lenfant, F. Tuna, A. Baldansuren, G. J. Davies, L. L. Leggio, P. H. Walton, *Nature Chem. Biol.* 12 (**2016**) 298-303.
[37] K. K. Meier, S. M. Jones, T. Kaper, H. Hansson, M. J. Koetsier, S. Karkehabadi, E. I. Solomon, M. Sandgren, B. Kelemen, *Chem. Rev*. 118 (**2018**) 2593–2635.
[38] V. G. H. Eijsink, D. Petrovic, Z. Forsberg, S. Mekasha, Å. K. Røhr, A. Várnai, B. Bissaro, G. Vaaje-Kolstad, *Biotechnol Biofuels*. 12 (**2019**) 1-16.
[39] P.V. Harris, D. Welner, K. C. McFarland, E. Re, J.-C. Navarro Poulsen, K. Brown, R. Salbo, H. Ding, E. Vlasenko, S. Merino, F. Xu, J. Cherry, S. Larsen, L. L. Leggio, *Biochem.* 49 (**2010**) 3305–3316.
[40] B. Bissaro, Å. K. Røhr, G. Müller, P. Chylenski, M. Skaugen, Z. Forsberg, S. J. Horn, G. Vaaje-Kolstad, V. G. H. Eijsink, *Nat. Chem. Biol*. 13 **(2017**) 1123–1128.
[41] J. A. Hangasky, A. T. Iavarone, M. A. Marletta, *Proc. Natl. Acad. Sci. USA*, 115 (**2018**) 4915–4920.
[42] B. Wang, P. H. Walton, C. Rovira, *ACS Catal.* 9 **(2019**) 4958−4969.
[43] L. Bertini, R. Breglia, M. Lambrughi, P. Fantucci, L. De Gioia, M. Borsari, M. Sola, C. A. Bortolotti, M. Bruschi, *Inorg Chem*. 57 (**2018**) 86−97.
[44] E. A. Span, D. L. M. Suess, M. C. Deller, R. D. Britt, M. A. Marletta, *ACS Chem. Biol.* 12 **(2017**) 1095–1103.
[45] E. D. Hedegård, U. Ryde, *JBIC, J. Biol. Inorg. Chem.* 22 (**2017**) 1029−1037.
[46] E. D. Hedegård, U. Ryde, *Chem. Sci.* 9 (**2018**) 3866−3880.
[47] A. Paradisi, E. M. Johnston, M. Tovborg, C. R. Nicoll, L. Ciano, A. Dowle, J. McMaster, Y. Hancock, G. J. Davies, P. H. Walton, *J. Am. Chem. Soc*. 141 (**2019**) 141, 18585–18599.
[48] A. L. Concia, M. R. Beccia, M. Orio, F. T. Ferre, M. Scarpellini, F. Biaso, B. Guigliarelli, M. Réglier, A.J. Simaan, *Inorg. Chem*. 56 (**2017**) 1023-1026.
[49] A. C. Neira, P. R. Martínez-Alanis, G. Aullón, M. Flores-Alamo, P. Zerón, A. Company, J. Chen, J. B. Kasper, W. R. Browne, E. Nordlander, I. Castillo, *ACS Omega* 4 (**2019**) 10729−10740.
[50] S. Muthuramalingam, D. Maheshwaran, M. Velusamy, R. Mayilmurugan, *J. Catal*. 372 (**2019**) 352–361.
[51] A. Fukatsu, Y. Morimoto, H. Sugimoto, S. Itoh, *Chem. Commun*. 56 (**2020**) 5123-5126.
[52] I. Castillo, A. P. Torres-Flores, D. F. Abad-Aguilar, A. Berlanga-Vázquez, M. Orio, D. Martínez-Otero, *ChemCatChem***.** 13 **(2021**) 4700-4704.
[53] C. X. Zang, S. J. Lippard, Curr. *Opin. Chem. Biol*. 7 (**2003**) 481-489.

[54] D. Wang, S. J. Lippard, *Nat. Rev. Drug Discovery* 4 (**2005**) 307–320.
[55] A. M. Florea, D. Büsselberg, *Cancers* (Basel) 3 **(2011**) 1351–1371.
[56] E. Pérez-Herrero, A. Fernández-Medarde, *Eur. J. Pharm. Biopharm*. 93 (**2015**) 52–79.
[57] P. Köpf-Maier, *Eur. J. Clin. Pharmacol*. 47 (**1994**) 1-16.
[58] G. Süss-Fink, *Dalton Trans*. 39 (**2010**) 1673-1688.
[59] A. H. Velders, A. Bergamo, E. Alessio, E. Zangrando, J. G. Haasnoot, C. Casarsa, M. Cocchietto, S. Zorzet, G. J. Sava, *Med. Chem*. 47 (**2004**) 1110–1121.
[60] C. G. Hartinger, S. Zorbas-Seifried, M. A. Jakupec, B. Kynast, H. Zorbas, B. K. Keppler, *J. Inorg. Biochem*. 100 (**2006**) 891-904.
[61] E. S. Antonarakis, A. Emadi, *Cancer Chemother. Pharmacol*. 66 (**2010**) 1-9.
[62] O. Mazuryk, K. Magiera, B. Rys, F. Suzenet, C. Kieda, M. Brindell, *J. Biol. Inorg. Chem.* 19 (**2014**) 1305–1316.
[63] A. Bergamo, G. Sava, *Chem. Soc. Rev*. 44 (**2015**) 8818-8835.
[64] G. S. Smith, B. Therrien, *Dalton Trans*. 40 (**2011**) 10793–10800.
[65] C. Scolaro, A. Bergamo, L. Brescacin, R. Delfino, M. Cocchietto, G. Laurenczy, T. J. Geldbach, G. Sava, P. J. Dyson, *J. Med. Chem*. 48 (**2005**) 4161-4171.
[66] W. M. Motswainyana, P. A. Ajibade, *Adv. Chem*. 2015 (**2015**) 1-21.
[67] a) S. H. van Rijt, P. J. Sadler, *Drug Discovery Today* 14 (**2009**) 1089–1097;
b) E. S. Antonarakis, A. Emadi, Cancer Chemother. *Pharmacol*. 66 (**2010**) 1–9;
c) W. H. Ang, A. Casini, G. Sava, P. J. Dyson, *J. Organomet. Chem*. 696 (**2011**) 989–998;
d) H.- K. Liu, P. J. Sadler, *Acc. Chem. Res*. 44 (**2011**) 349–359;
e) A. Bergamo, C. Gaiddon, J. H. M. Schellens, J. H. Beijnen, G. Sava, *J. Inorg. Biochem*. 106 (**2012**) 90–99;
f) S. Komeda, A. Casini, *Curr. Top. Med. Chem*. 12 (**2012**) 219–235;
g) G. Gasser, I. Ott, N. Metzler-Nolte, *J. Med. Chem*. 54 (**2011**) 3–25.
[68] C. S. Allardyce, P. J. Dyson, *Platinum Metals Rev*. 45 (**2001**) 62– 69.
[69] R. E. Aird, J. Cummings, A. A. Ritchie, M. Muir, R. E. Morris, H. Chen, P. J. Sadler, D. I. Jodrell, Br. J. *Cancer* 86 (**2002**) 1652– 1657.
[70] a) E. Meggers, G. E. Atilla-Gokcumen, H. Bregman, J. Maksimoska, S. P. Mulcahy, N. Pagano, D. S. Williams, *Synlett*, 8 (**2007**) 1177–1189;
b) K. S. M. Smalley, R. Contractor, N. K. Haass, A. N. Kulp, G. E. Atilla-Gokcumen, D. S. Williams, H. Bregman, K. T. Flaherty, M. S. Soengas, E. Meggers, M. Herlyn, *Cancer Res*. 67 (**2007**) 209–217.
[71] E. Hillard, A. Vessières, F. L. Bideau, D. Plazuk, D. Spera, M. Huche, G. Jaouen, *Chem. Med. Chem*. 1 **(2006**) 551-559.
[72] A. Habtemariam, M. Melchart, R. Fernandez, S. Parsons, I. D. H. Oswald, A. Parkin, F. P. A. Fabbiani, J. E. Davidson, A. Dawson, R. E. Aird, D. I. Jodrell, P. J. Sadler, *J. Med. Chem*. 49 (**2006**) 6858- 6868.
[73] P. J. Dyson, G. Sava, *Dalton Trans*. (**2006**) 1929-1933.
[74] É. A. Enyedy, J. P. Mészáros, O. Dömötör, C. M. Hackl, A. Roller, B. K. Keppler, W. Kandioller, *J. Inorg. Biochem*. 152 **(2015**) 93-103.
[75] Y. Geldmacher, M. Oleszak, W. S. Sheldrick, *Inorg. Chim. Acta*. **393 (**2012) 84−102.
[76] Z. Liu, P. J. Sadler, *Acc. Chem. Res*. 47 **(2014**) 1174−1185.
[77] Z. Liu, A. Habtemariam, A. M. Pizarro, G. J. Clarkson, P. J. Sadler, *Organometallics* 30 **(2011**) 4702−4710.

[78] Z. Liu, A. Habtemariam, A. M. Pizarro, S. A. Fletcher, A. Kisova, O. Vrana, L. Salassa, P. C. Bruijnincx, G. J. Clarkson, V. Brabec, P. J. Sadler, *J. Med. Chem*. 54 **(2011**) 3011−3026.
[79] Z. Liu, I. Romero-Canelón, B. Qamar, J. M. Hearn, A. Habtemariam, N. P. Barry, A. M. Pizarro, G. J. Clarkson, P. J. Sadler, *Angew. Chem., Int. Ed*. 53 **(2014**) 3941−3946.
[80] Y. Geldmacher, K. Splith, I. Kitanovic, H. Alborzinia, S. Can, R. Rubbiani, M. A. Nazif, P. Wefelmeier, A. Prokop, I. Ott, S. Wölfl, I. Neundorf, W. S. Sheldrick. JBIC, *J. Biol. Inorg. Chem*. 17 **(2012**) 631−646.
[81] W. Kandioller, E. Balsano, S. M. Meier, U. Jungwirth, S. Göschl, A. Roller, M. A. Jakupec, W. Berger, B. K. Keppler, C. G. Hartinger, *Chem. Commun*. 49 **(201**3) 3348−3350.
[82] O. Dömötör, S. Aicher, M. Schmidlehner, M. S. Novak, A. Roller, M. A. Jakupec, W. Kandioller, C. G. Hartinger, B. K. Keppler, É. A. Enyedy, *J. Inorg. Biochem*. 134 **(2014**) 57−65.
[83] A. Kurzwernhart, S. Mokesch, E. Klapproth, M. S. Adib-Ravazi, M. A. Jakupec, C. G. Hartinger, W. Kandioller, B. K. Keppler, *Eur. J. Inorg. Chem*. 2016 (**2016**) 240−246.
[84] L. Dadci, H. Elias, U. Frey, A. Hörnig, U. Koelle, A.E. Merbach, H. Paulus, J.S. Schneider, *Inorg. Chem*. 34 (**1995**) 306–315.
[85] A. Dorcier, W.H. Ang, S. Bolano, L. Gonsalvi, L. Juillerat-Jeannerat, G. Laurenczy, M. Peruzzini, A. D. Phillips, F. Zanobini, P. J. Dyson, *Organometallics*, 25 (**2006**) 4090–4096.
[86] L. Shadap, J. L. Tyagi, K. M. Poluri, E. Pinder, R. M. Phillips, *Polyhedron.* 176 (**2020**) 114293.
[87] O. Dömötör, V. F. S. Pape, N.V. May, G. Szakacs, E.A. Enyedy, *Dalton Trans.* 46 (**2017**) 4382–4396.
[88] J. P. Mészáros, J. M. Poljarevic, I. Szatmári, O. Csuvik, F. Fülöp, N. Szoboszlai, G. Spengler, É. A. Enyedy, *Dalton Trans*. 49 (**2020**) 7977-7992.
[89] W. D. J. Tremlett, K. K. H. Tong, T. R. Steel, S. Movassaghi, M. Hanif, S. M. F. Jamieson, T. Sohnel, C. G. Hartinger, *J. Inorg. Biochem.* 199 (**2019**) 110768.
[90] K. Máliková, L. Masaryk, P. Štarha, *Inorganics*, 9 (**2021**) 26.
[91] J. Markham, J. Liang, A. Levina, R. Mak, B. Johannessen, P. Kappen, C. J. Glover, B. Lai, S. Vogt, P. A. Lay, *Eur. J. Inorg. Chem*. 2017 (**2017**) 1812–1823.
[92] M. Mbaba , T. M. Golding, G. S. Smith, *Molecules*, 25 (**2020**) 5276.
[93] C. M. DuChane, L. C. Brown, V. S. Dozier, J. S. Merola, *Organometallics*, 37 (**2018)** 530–538.
[94] S. N. Sovari, F. Zobi, *Chemistry*, 2 (**2020)** 418–452.
[95] C. Chuong, C. M. DuChane, E. M. Webb, P. Rai, J. M. Marano, C. M. Bernier, J. S. Merola, J. Weger-Lucarelli, *Viruses*, 13 (**2021**) 980.
[96] S. Morra, A. Pordea, *Chem. Sci*. 9 (**2018**) 7447-7454.
[97] D. Loreto, A. Merlino, *Coord. Chem. Rev.* 442 (**2021**) 213999.
[98] M. Groessl, M. Terenghi, A. Casini, L. Elviri, R. Lobinski, P. J. Dyson, *J. Anal. At. Spectrom.* 25 (**2010**) 305-313.
[99] G. Berthon, Handbook of Metal Ligand Interactions in Biological Fluids, Vol 1-4; *Marcel Dekker: New York*, **1995**.
[100] O. Dömötör, T. Pivarcsik, J. P. Mészáros, I. Szatmári, F. Fülöp, É. A. Enyedy, *Dalton Trans*. 50 (**2021**) 11918-11930.
[101] J. Moro, D. Tomé, P. Schmidely, T.-C. Demersay, D. Azzout-Marniche, *Nutrients*, 12 (**2020**) 1414.
[102] F. Hollmann, B. Witholt, A. Schmid, *J. Mol. Catal B-Enzym*. 19-20 (**2003**) 167-176
[103] O. Dömötör, É. A. Enyedy, *J. Biol. Inorg. Chem*. 24 (**2019**) 703–719.

[104] O. Dömötör, B. K. Keppler, É. A. Enyedy, *J. Biol. Inorg. Chem*. 27 (**2022**) 315–328.
[105] A. Buryak, K. Severin, *Angew. Chem. Int. Ed*. 43 (**2004**) 4771–4774.
[106] H. B. Albada, F. Wieberneit, I. Dijkgraaf, J. H. Harvey, J. L. Whistler, R. Stoll, N. Metzler-Nolte, R. H. Fish, *J. Am. Chem. Soc*. 134 (**2012**) 10321–10324.
[107] A. Ozsvath, L. Bíro, E. M. Nagy, P. Buglyo, D. Sanna, E. Farkas, *Molecules* 24 (**2019**) 3941.
[108] F. J. C. Rosotti and H. Rosotti, The determination of stability constants, *McGrawHill Book Co*. (**1962**).
[109] E. Högfeldt, Stability Constants of Metal-Ion Complexes, Part A. Inorganic Ligands, Pergamon (**1982**).
[110] L. Zékány, I. Nagypál and G. Peintler, PSEQUAD for chemical equilibria, Technical Software Distributors (**1991**).
[111] E. J. Billo, *Inorg. Nucl. Chem. Lett*. 10 (**1974**) 613-617.
[112] H. Sigel, R. B. Martin, *Chem. Rev*. 82 (**1982**), 385-426.
[113] L. D. Pettit, J. E. Gregor and H. Kozlowski, Perspectives on Bioinorganic Chemistry, *JAI Press* (**1991**).
[114] E. Prenesti, P. G. Daniele, M. Prencipe, G. Ostacoli, *Polyhedron* 18 (**1999**) 3233-3241.
[115] E. Prenesti, P. G. Daniele, S. Berto, S. Toso, *Polyhedron* 25 (**2006**) 2815-2823.
[116] A. Rockenbauer, L. Korecz, *Appl. Magn. Reson.* 10 (**1996**) 29–43.
[117] D.T. Sawyer, A. Sobkowiak, J. L. Roberts, "Electrochemistry for Chemists", 2nd edition, *J. Wiley and Sons Inc*. (**1995**).
[118] C. A. Fowler, F. Sabbadin , L. Ciano, G. R. Hemsworth, L. Elias, N. Bruce, S. McQueen-Mason, G. J. Davies, P. H. Walton, *Biotechnol Biofuels* 12 (**2019**) 1-11.
[119] P. Chylenski, B. Bissaro, M. Sørlie, Å. K. Røhr, A. Várnai, S. J. Horn, V. G. H. Eijsink, *ACS Catal.* 9 (**2019**) 4970-4991.
[120] S. Kuusk, R. Kont, P. Kuusk, A. Heering, M. Sørlie, B. Bissaro, V. G. H. Eijsink, P. Väljamäe, *J. Biol. Chem.* 294 (**2019**) 1516-1528.
[121] T. Chen, X. Wang, Y. He, C. Zhang, Z. Wu, K. Liao, J. Wang, Z. Guo, *Inorg. Chem*. 48 (**2009**) 5801–5809.
[122] T. Jakusch, A. A. Hassoon, T. Kiss, *J. Inorg. Biochem*. 228 (**2021**) 111692.
[123] A. Fischer, M. J. King, F. P. Robinson, *Can. J. Chem*. 56 (**1978**) 3059–3067.
[124] A. Lakatos, É. Zsigó, D. Hollender, N. V. Nagy, L. Fülöp, D. Simon, Z. Bozsó, T. Kiss, *Dalton Trans*. 39 (**2010**) 1302–1315.
[125] R. J. Balahura, *Can. J. Chem*. 52 (**1974**) 1762–1773.
[126] I. Bertini, D. Gatteschi, A. Scozzafava, *Coord. Chem. Rev*. 29 (**1979**) 67–84.
[127] F. Lebon, M. Ledecq, M. Dieu, C. Demazy, J. Remacle, R. Lapouyad, O. Kahn, F. Durant, *J. Inorg. Biochem*. 86 (**2001**) 547–554.
[128] C.-Y. Wu, C.-C. Su, *Polyhedron* 16 (**1997**) 383–392.
[129] L. Zhang, X. Cui, J. Sun, Y. Wang, W. Li, J. Fang, *Bioorg. Med. Chem. Lett*. 23 (**201**3) 3511–3514.
[130] A. A. Hassoon, A. Szorcsik, L. Fülöp, I. Z. Papp, N. May, T. Gajda, *Dalton Trans*. 51 (**2022**) 17241-17254.
[131] L. D. Pettit, K. J. Powell, IUPAC stability constants database, Academic Software, **2008**.
[132] A. Myari, G. Malandrinos, Y. Deligiannakis, J. C. Plakatouras, N. Hadjiliadis, Z. Nagy and I. Sóvágó, *J. Inorg. Biochem.* 85 **(2001**) 253-261.
[133] H. Kozłowski, W. Bal, M. Dyba, T. Kowalik-Jankowska, *Coord. Chem. Rev*. 184

(1999) 319-346.
[134] A. Matera, J. Brasun, M. Cebrat, J. Swiatek-Kozłowska, *Polyhedron*, 27 **(2008**) 1539–1555
[135] V. V. Vu, S. T. Ngo, *Coord. Chem. Rev.* 368 **(2018**) 134-157.
[136] W. R. Hagen, Biomolecular EPR Spectroscopy, CRC Press, Boca Raton, **2008**.
[137] M. S. Haddad, S. R. Wilson, D. J. Hodgson, D. N. Hendrickson, *J. Am. Chem. Soc.* 103 (**1981**) 384-391.
[138] J. F. Folgado, V. Coronado, D. Beltrán-Porter, T. Rojo, A. Fuertes, *J. Chem. Soc. Dalton Trans*. (**1989**) 237-241.
[139] G. Kolks, C. R. Frihart, H. N. Rabinowitz, S. J. Lippard, *J. Am. Chem. Soc*. 98 **(1976**) 5720–5721.
[140] B. Verdejo, S. Blasco, E. García-España, F. Lloret, P. Gaviña, C. Soriano, S. Tatay, H. R. Jiménez, A. Doménech, J. Latorre, *Dalton Trans.* **(2007)** 4726-4737.
[141] I. Török, P. Surdy, A. Rockenbauer, L. Korecz Jr, G. J. A. A. Koolhaas, T. Gajda, *J. Inorg. Biochem*. 71 **(1998**) 7-14.
[142] I. Monte-Pérez, A. M. Sosa, S. Bernès, N. Aliaga-Alcalde, V. M. Ugalde-Saldívar, L. Gasque, *Eur. J. Inorg. Chem*. (**2012**) 4739-4749.
[143] S. Timári, R. Cerea, K. Várnagy, *J. Inorg. Biochem*. 105 **(2011**) 1009–1017.
[144] D. Maiti, A. A. N. Sarjeant, K. D. Karlin, *Inorg. Chem*. 47 **(2008**) 8736-8747.
[145] S. Yamaguchi, H. Masuda, *Sci. Technol. Adv. Mater*. 6 **(2005**) 34–47.
[146] B. Jung, K. D. Karlin, A. D. Zuberbühler, *J. Am. Chem. Soc.* 118 **(1996**) 3763-3764.
[147] L. M. Mirica, X. Ottenwaelder, T. D. P. Stack, *Chem. Rev.*104 (**2004**) 1013-1045.
[148] R. R. Jacobson, Z. Tyeklar, A. Farooq, K. D. Karlin, S. Liu, J. Zubieta, *J. Am. Chem. Soc*. 110 **(1988**) 3692-3693.
[149] Y. Lee, G. Y. Park, H. R. Lucas, P. L. Vajda, K. Kamaraj, M. A. Vance, A. E. Milligan, J. S. Woertink, M. A. Siegler, A. A. Narducci Sarjeant, L. N. Zakharov, A. L. Rheingold, E. I. Solomon, K. D. Karlin, *Inorg. Chem*. 48 **(2009**) 11297–11309.
[150] T. Kamachi, Y.-M. Lee, T. Nishimi, J. Cho, K. Yoshizawa, W. Nam, *J. Phys. Chem. A.* 112 **(2008**) 13102–13108
[151] A. A. Hassoon, A. Szorcsik, F. Bogár, I.Z. Papp, L. Fülöp, Z. Kele, T. Gajda, *J. Inorg. Biochem*. 216 (**2021**) 111330.
[152] A. Casini, G. Mastrobuoni, W. H. Ang, C. Gabbiani, G. Pieraccini, G. Moneti, P. J. Dyson, L. Messori, *ChemMedChem*. 2 (**2007**) 631–635.
[153] A. Merlino, *Coord. Chem. Rev*. 326 (**2016**) 111–134.
[154] B. Wu, M.S. Ong, M. Groessl, Z. Adhireksan, C.G. Hartinger, P.J. Dyson, C. A. Davey, *Chem. Eur. J.* 17 (**2011**) 3562–3566.
[155] Y. Takezawa, P. Bockmann, ¨ N. Sugi, Z. Wang, S. Abe, T. Murakami, T. Hikage, G. Erker, Y. Watanabe, S. Kitagawa, T. Ueno, *Dalton Trans*. 40 (**2011**) 2190–2195.
[156] S. M. Meier, M. Hanif, Z. Adhireksan, V. Pichler, M. Novak, E. Jirkovsky, M. A. Jakupec, V. B. Arion, C. A. Davey, B. K. Keppler, C. G. Hartinger, *Chem. Sci*. 4 (**2013**) 1837.
[157] J. M. Zimbron, T. Heinisch, M. Schmid, D. Hamels, E. S. Nogueira, T. Schirmer, T. R. Ward, *J. Am. Chem. Soc*. 135 (**2013**) 5384–5388.
[158] Z. Bihari, Z. Nagy, P. Buglyo, *J. Organomet. Chem*. 782 (**2015**) 82–88.
[159] M.-L. Lehaire, R. Scopelliti, L. Herdeis, K. Polborn, P. Mayer, K. Severin, *Inorg. Chem.* 43 (**2004**) 1609–1617.

[160] C. Robl, M. Maurus, K. Sünkel, W. Beck, R. Kramer, K. Polborn, *Chem. Eur. J.* 2 (**1996**) 1518–1526.
[161] M. Duran, Amino Acids in *Laboratory Guide to the Methods in Biochemical Genetics* 53–89, Eds. N. Blau, M. Duran, K. M. Gibson, *Springer-Verlag Berlin Heidelberg* (**2008).**
[162] P. Deschamps, P. P. Kulkarni, M. Gautam-Basak, B. Sarkar, *Coord. Chem. Rev*. 249 (**2005**) 895–909.
[163] T. G. Scrase, M. J. O'Neill, A. J. Peel, P. W. Senior, P. D. Matthews, H. Shi, S. R. Boss, P. D. Barker, *Inorg. Chem*. 54 (**2015)** 3118−3124.
[164] F. A. Egbewande, L. E. H. Paul, B. Therrien J. Furrer, *Eur. J. Inorg. Chem*. (**2014)** 1174–1184.
[165] K. G. Crush, *Comp. Biochem. Physiol*. 34 **(1970**) 3-30.
[166] S. M. Greene, F. L. Margolis, M. Grillo, H. Fisher, *Eur. J. Pharmacol*. 99 (**1984**) 79-84.
[167] A. A. Bnldyrev, S. E. Severin, *Adv. Enzyme Regul*. 30 (**1990**) 175-194.
[168] T. Gajda, B. Henry, J. J. Delpuech, *J. Chem. Soc. Dalton Trans*. 0 (**1992**) 2313-2319.
[169] Zs. Árkosi, Z. Paksi, L. Korecz, T. Gajda, B. Henry and A. Rockenbauer, *J. Inorg. Biochem*. 98 (**2004**) 1995-2005.
[170] Y. Sun, X. Lu, M. Gershengorn, *J. Mol. Endocrinol*. 30 (**2003)** 87–97.
[171] G. Formicka-Kozlowska, M. Bezer, L. D. Pettit, *J. Inorg. Biochem*. 18 (**1983**) 335-347.
[172] L. Pickart, J. H. Freedman, W. J. Loker, J. Peisach , C. M. Perkins , R. E. Stenkamp , B. Weinstein, *Nature*, 288 **(1980**) 715–717.
[173] J. D. Campbell, J. E. McDonough, J. E. Zeskind, *Genome Medicine*, 4 (**2012**) article 67.
[174] (a) L. Pickart, J. M. Vasquez-Soltero, A. Margolina, *BioMed Res. Int*. (**2014**) Article ID 151479;
(b) L. Pickart, A. Margolina, *Int. J. Mol. Sci*. 19 (**2018**) 1987.
[175] C. Hureau, H. Eury, R. Guillot, C. Bijani, S. Sayen,P.-L. Solari, E. Guillon, P. Faller, P. Dorlet, *Chem. Eur. J*. 17 (**2011**) 10151 – 10160.
[176] E. B. Bauer, *Chem. Soc. Rev*. 41 (**2012**) 3153–3167.
[177] K. Severin, R. Bergs, W. Beck, *Angew. Chem. Int. Ed. Eng*. 37 (**1998**) 1634–1654.
[178] W. Beck, R. Kramer, *Angew. Chem. Int. Ed. Eng*. 30 (**1991**) 1467–1469.
[179] F. A. Egbewande, L. E. H. Paul, B. Therrien J. Furrer, *Eur. J. Inorg. Chem*. (**2014)** 1174–1184.
[180] W. S. Sheldrick, S. Heeb**,** *J. Organomet. Chem.* 377 (**1989**) 357–366.
[181] P. Chakrabarti, *Protein Eng. Des. Sel*. 4 (**1990**) 57–63.
[182] I. Sovago, K. Varnagy, N. Lihi, A. Grenacs, *Coord. Chem. Rev.* 327–328 (**2016**) 43–54.
[183] P. Zhang, P. J. Sadler, *J. Organomet. Chem*. 839 (**2017**) 5–14.
[184] M. A. Scharwitz, I. Ott, Y. Geldmacher, R. Gust, W. S. Sheldrick, *J. Organomet. Chem.* 693 (**2008**) 2299–2309.
[185] J. J. Soldevila-Barreda, A. Habtemariam, I. Romero-Canelón, P. J. Sadler, *J. Inorg. Biochem*. 153 (**2015**) 322–333.

ACKNOWLEDGEMENTS

First of all, thank God, Allah, the beneficent, the merciful for helping me to accomplish this work. I would like to express my sincere gratitude to my main supervisor, Prof. Tamás Gajda for his continuous help, support and motivation, as well as for his effective help in applications and publishing papers. His guidance helped me in all the time of research and writing of this thesis.

My deepest gratitude goes to my co-supervisor, Dr. Tamás Jakusch. His joining in the direction of my work was a real inspiration; I am thankful for his valuable help around my experiments, as well as for the scientific discussions.

I am thankful to Dr. Éva Enyedy and Dr. Gábor Galbács, as the current and the former Head of Department, for allowing me to carry out my PhD work in the department.

I am especially thankful to Dr. Nóra May from the Hungarian Academy of Science, for her help in the EPR measurements and evaluations, and also to Dr. Attila Szorcsik, for his help in the laboratory concerning my experiments.

I am grateful to all the members of the Bioinorganic Research Group of the Chemistry Institute at University of Szeged for their help and the nice working atmosphere.

I would like to thank my family and friends for their support, patience, and inspiration that I was given during my study.

Last but not the least, I would like to acknowledge the financial support provided by the Hungarian National Research, Development and Innovation Office (NKFIH K_16/120130, GINOP 2.3.2-15-2016-00038), Stipendium Hungaricum and Cultural Affairs & Mission Sector in Egypt.

PUBLICATION LIST

Identification number in the Hungarian Collection of Scientific Publications (MTMT): 10078296

Publications related to the dissertation:

1. **Azza A. Hassoon**, Attila Szorcsik, Ferenc Bogár, Ibolya Z. Papp, Lívia Fülöp, Zoltán Kele, Tamás Gajda, The interaction of half-sandwich (η^5-Cp*)Rh(III) cation with histidine containing peptides and their ternary species with (N,N) bidentate ligands,

J. Inorg. Biochem., 216 (**2021**) 111330. IF= 4.336

2. Tamás Jakusch, **Azza A. Hassoon**, Tamás Kiss, Characterization of copper(II) specific pyridine containing ligands: Potential metallophores for Alzheimer's disease therapy

J. Inorg. Biochem., 228 (**2021**) 111692. IF= 4.336

3. **Azza A. Hassoon**, Attila Szorcsik, Lívia Fülöp, Ibolya Zita Papp, Nóra May, Tamás Gajda, Peptide-based chemical models for lytic polysaccharide monooxygenases,

Dalton Trans., 51 (**2022**) 17241-17254. IF= 4.569

∑IF = 13.241

Oral presentations and posters related to the dissertation:

1. **Azza A. Hassoon**, Attila Szorcsik, Ibolya Zita Papp, Lívia Fülöp, Zoltán Kele and Tamás Gajda: Interaction of half-Sandwich (Cp*)Rh(III) cation with Histidine-containing peptides and their ternary species with (N,N) bidentate ligands, 54th Colloquium on Complex Chemistry and Meeting of the Coordination Chemistry Working Group of the Hungarian Academy of Sciences, 26-27 May 2021. online, Hungary. **(Oral lecture)**
2. **Hassoon Azza**, Szorcsik Attila, Bogár Ferenc, Zita Papp Ibolya, Fülöp Lívia, Kele Zoltán, Gajda Tamás: Interaction of Half-Sandwich (Cp*)Rh(III) Cation with Histidine-Containing Peptides and Their Ternary Species with (N,N) Bidentate

Ligands, Spring Wind Conference, 28-30 May 2021. online, University of Miskolc, Hungary. **(Oral lecture)**

3. **Azza A. HASSOON**, Abdelrahman AHMED, Péter BORSOS, Attila SZORCSIK, Lívia FÜLÖP, Nóra MAY, Tamás GAJDA : Copper(II) complexes of HPH-NH and HPHPY-NH as structural and functional models of lytic polysaccharide monooxygenases, International Symposium Thermodynamics of Metal Complexes, ISMEC, 16-18 June 2021, online, Białystok, Poland. **(Oral lecture)**
4. **Azza A. HASSOON**, Attila SZORCSIK, Lívia FÜLÖP, Nóra MAY, Tamás GAJDA, International Conference on Metal-Binding Peptides: Methodologies and Applications MBP, Copper complexes as bioinspired models for lytic polysaccharide monooxygenases (LPMO), 5-8 July 2022, Nancy, France. **(Oral lecture)**
5. **Azza Hassoon** and Tamás Gajda, RSC Inorganic Reaction Mechanisms Discussion Group Conference (RSC_IRMG), Pharmacokinetics of the interaction of half-sandwich (Cp*)Rh(III) cation with methionine-containing peptides and their ternary species with (N,N) bidentate ligands, 13-14 Sep 2022, online, London, UK. **(Oral lecture)**
6. **Azza A. HASSOON**, Attila SZORCSIK, Lívia FÜLÖP, Nóra MAY, Tamás GAJDA, Anglo German Inorganic Chemistry conference (AGICHEM), 9-10 September 2021, online, London, UK. **(poster)**
7. **Azza A. HASSOON**, Attila SZORCSIK, Lívia FÜLÖP, Nóra MAY, Tamás GAJDA: Symposium of the Spanish Royal Society of Chemistry (RSEQ), Copper(II) complexes of HPH-NH and HPHPY-NH as structural and functional models of lytic polysaccharide monooxygenases, International Symposium Thermodynamics of Metal Complexes, 9-10 September 2021, online, Spain. **(poster)**
8. **Azza A. HASSOON**, Nóra MAY, Tamás GAJDA, 2022 #RSCPoster Twitter Conference, Copper complexes as bioinspired models for lytic polysaccharide monooxygenases (LPMO), 1-2 March 2022, online, London, UK **(poster)**
9. **Azza A. HASSOON**, Attila SZORCSIK, Tamás GAJDA, Chemical biology symposium 2022, CRITICAL FACTORS AFFECTING THE INTERACTION OF HALF-SANDWICH (Cp*)Rh(III) CATION WITH HISTIDINE AND METHIONINE PEPTIDES, 9 May 2022, online, London, UK. **(poster)**

Appendix

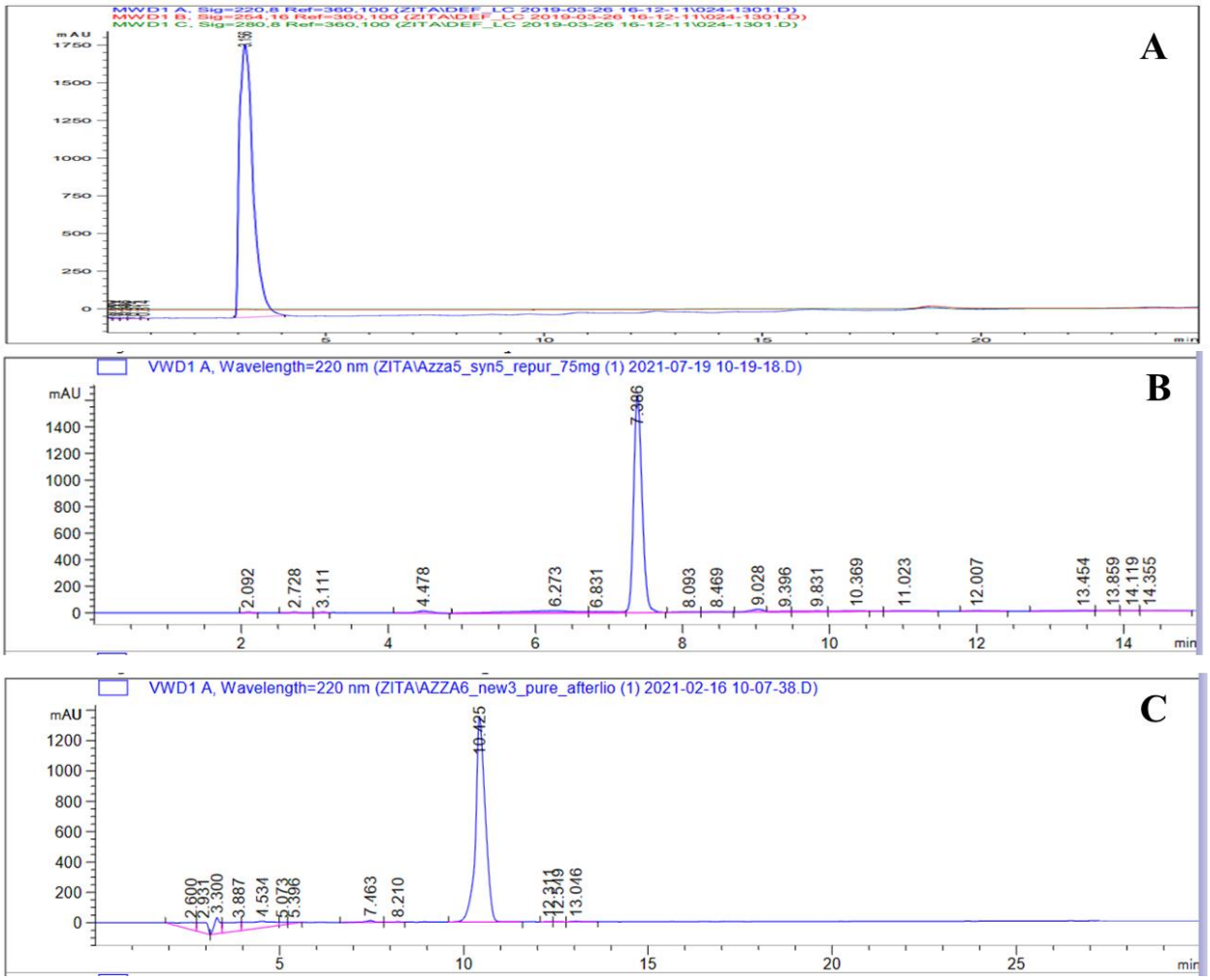
MWD1 A, Sig=220,8 Ref=360,100 (ZITA\DEF_LC 2019-03-26 16-12-11\024-1301.D)
MWD1 B, Sig=254,16 Ref=360,100 (ZITA\DEF_LC 2019-03-26 16-12-11\024-1301.D)
MWD1 C, Sig=280,8 Ref=360,100 (ZITA\DEF_LC 2019-03-26 16-12-11\024-1301.D)
mAU
min
A
VWD1 A, Wavelength=220 nm (ZITA\Azza5_syn5_repur_75mg (1) 2021-07-19 10-19-18.D)
B
7.396
2.092
2.728
3.111
4.478
6.273
6.831
8.093
8.469
9.028
9.396
9.831
10.369
11.023
12.007
13.454
13.859
14.119
14.355
VWD1 A, Wavelength=220 nm (ZITA\AZZA6_new3_pure_afterlio (1) 2021-02-16 10-07-38.D)
C
10.425
2.600
2.931
3.300
3.887
4.534
5.073
5.396
7.463
8.210
12.311
12.519
13.046

D

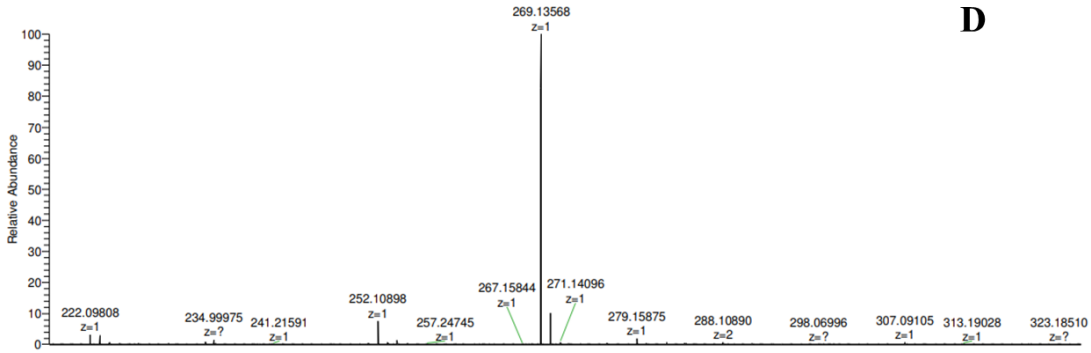

E

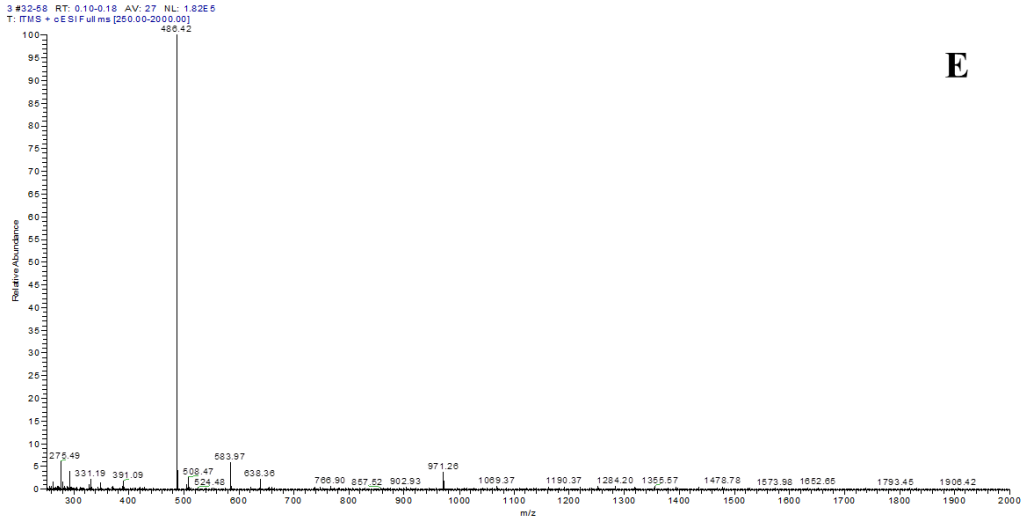

1-5 1000x #490 RT: 2.15 AV: 1 NL: 1.14E+008
T: FTMS + p ESI Full ms [100.0000-1500.0000]

F

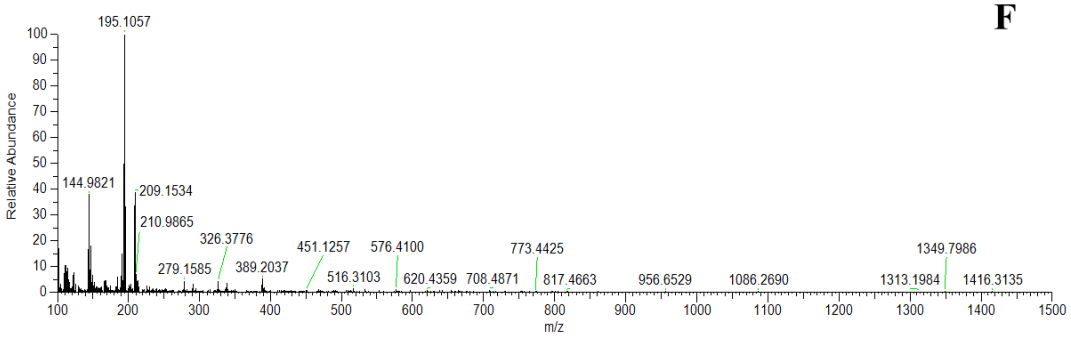

1-5 1000x #582 RT: 2.55 AV: 1 NL: 4.59E+008
T: FTMS + p ESI Full ms [100.0000-1500.0000]

G

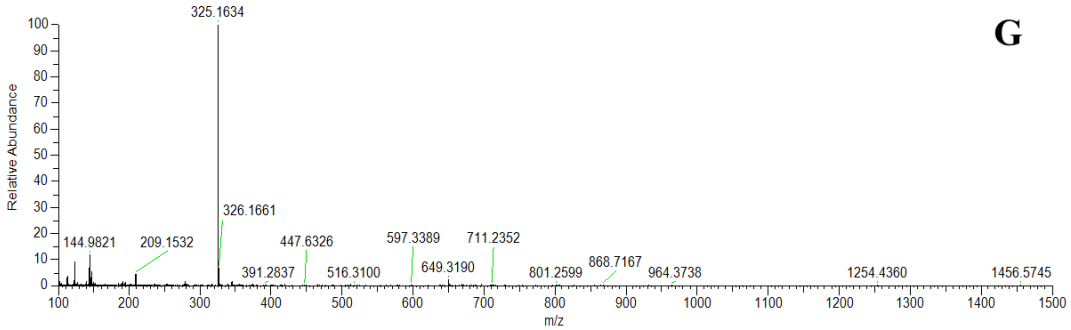

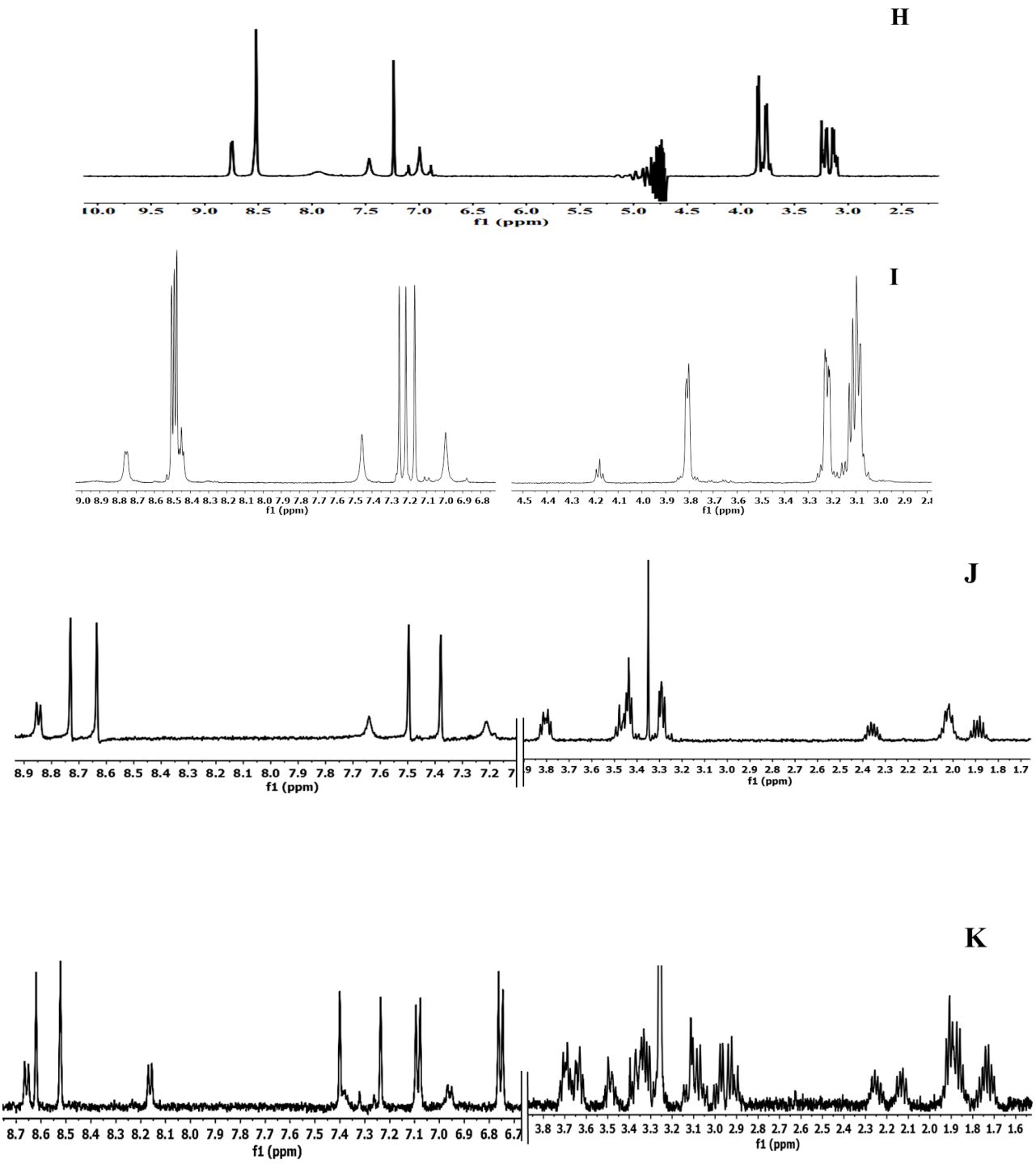

Figure A1 Analytical HPLC chromatograms (A,B,C), HR ESI-MS (D,E,F,G) and ^{1}H NMR (H,I,J,K) spectra of the purified GHG-NH_2 (A,D,H), HHHG-NH_2 (E,I), HPH-NH_2 (B,F,J) and HPHPY-NH_2 (C,G,K) peptides. (taken from [130] and [151])

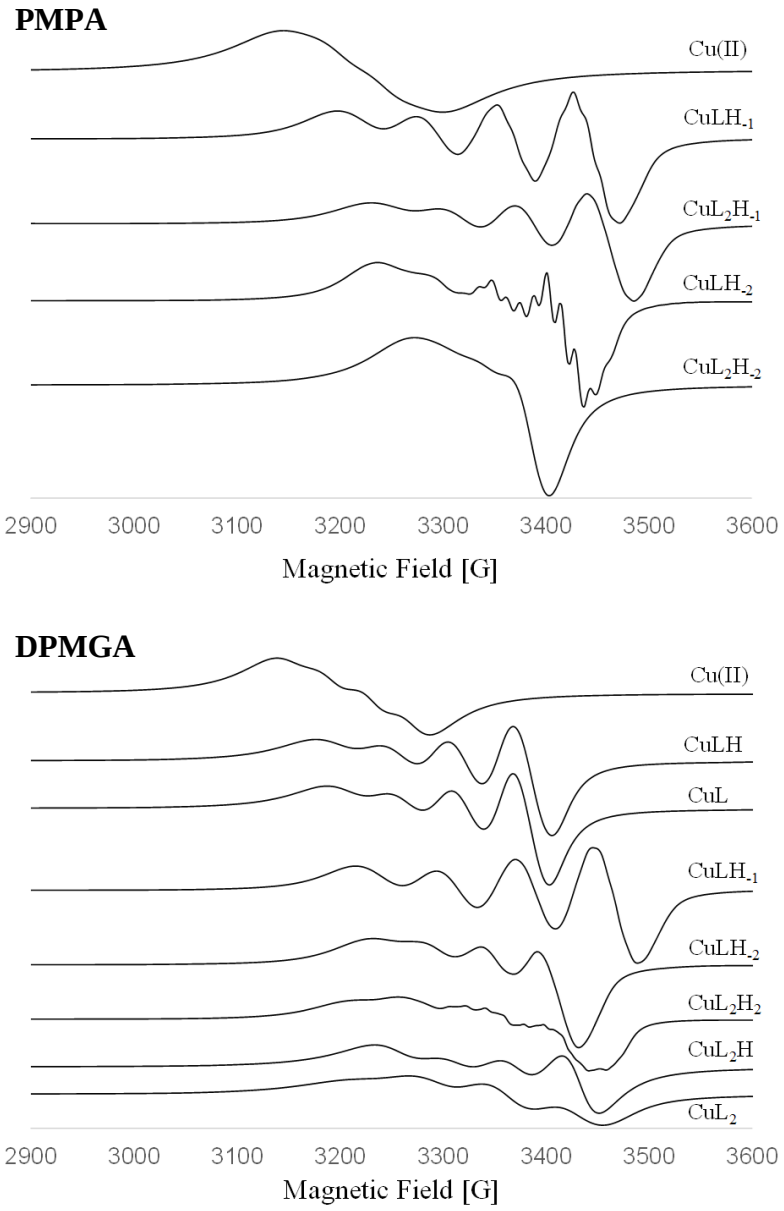

Figure A2 Simulated isotropic EPR spectra of the individual Cu(II) complexes. (taken from [122])

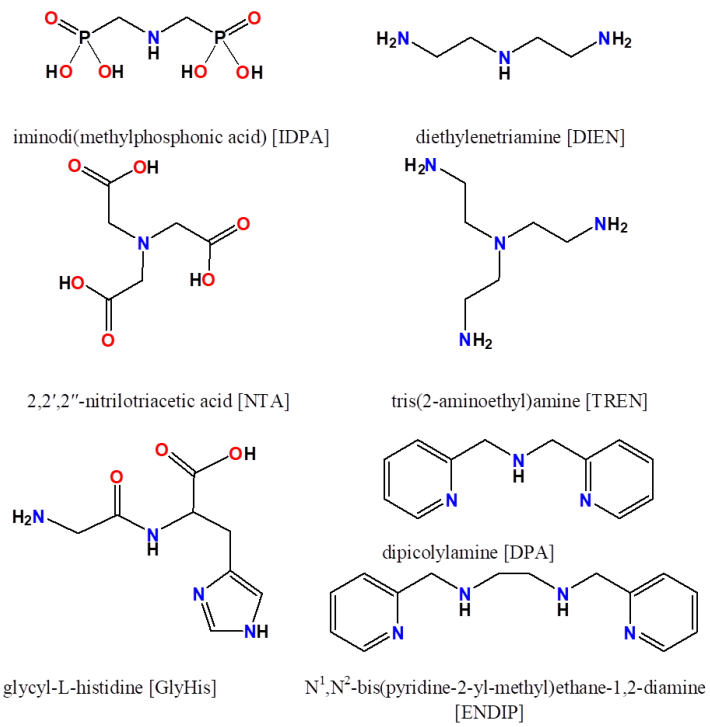

Figure A3 The schematic structure of the additional seven ligands which were also tested (in addition to PMPA and DPMGA) for their ability of inhibition of ROS production of CuAβ in the presence of ascorbate. (taken from [122])

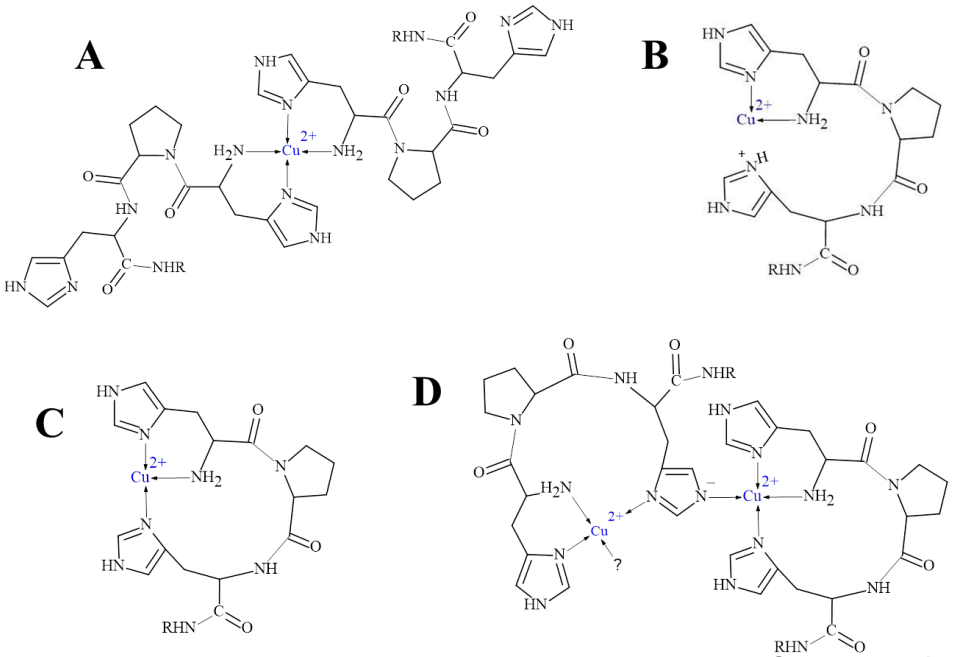

Figure A4 Proposed structres of (A) bis complexes CuH_xL_2 (B) $CuHL^3$ or CuH_2L^4 (C) CuL^3 or $CuHL^4$ (D) $Cu_2H_{-1}L^3_2$ or $Cu_2HL^4_2$

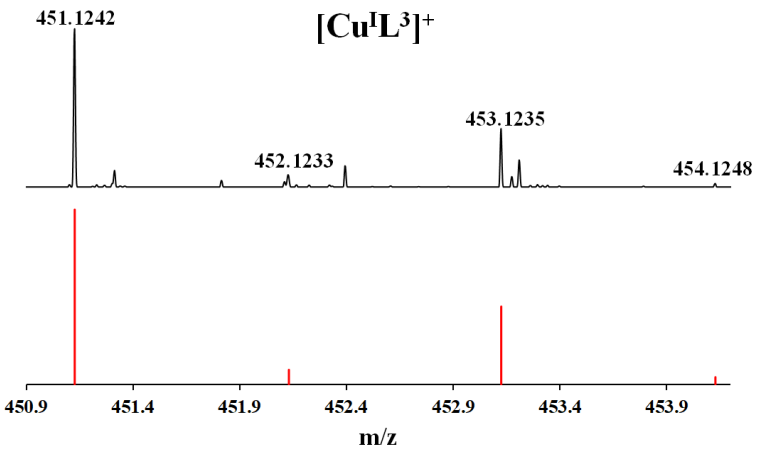
[Cu^I L^3]^+
451.1242
452.1233
453.1235
454.1248
450.9
451.4
451.9
452.4
452.9
453.4
453.9
m/z

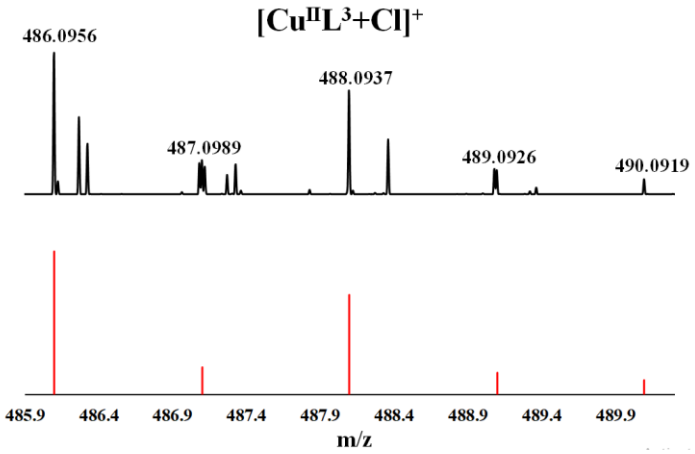
[Cu^II L^3+Cl]^+
486.0956
487.0989
488.0937
489.0926
490.0919
485.9
486.4
486.9
487.4
487.9
488.4
488.9
489.4
489.9
m/z

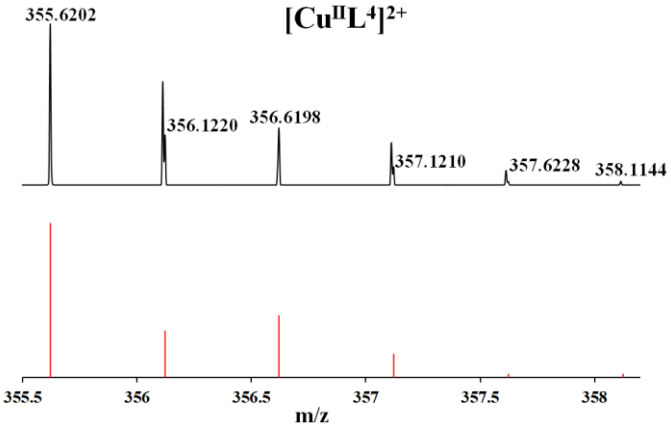
[Cu^II L^4]^2+
355.6202
356.1220
356.6198
357.1210
357.6228
358.1144
355.5
356
356.5
357
357.5
358
m/z

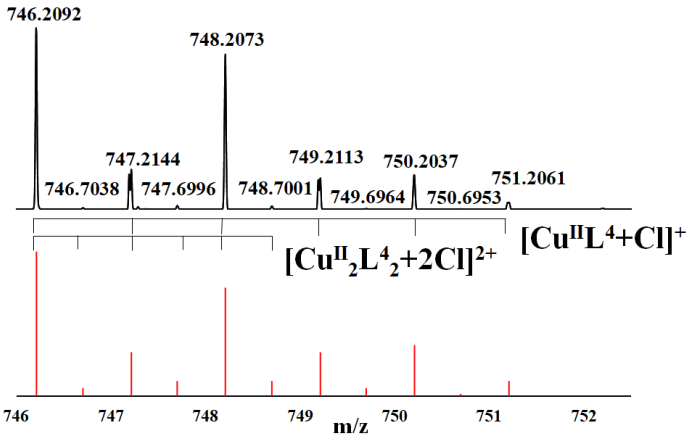

Figure A5 Monomer and dimer complexes identified on the ESI-MS spectra. The peaks related to the dimer $[Cu^{II}_2\mathbf{L}^{4}_2+2Cl]^{2+}$ complex (bottom) have notable lower intensity than those of the monomer species. (taken from [130])

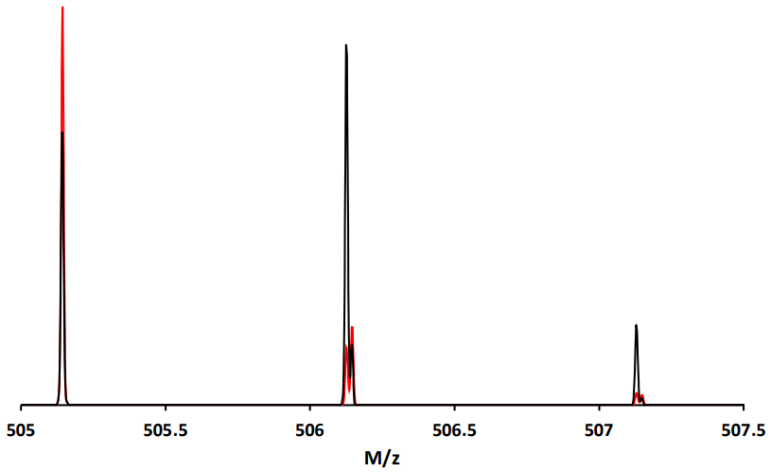

Figure A6 ESI-MS spectrum of the Rh(Cp*)-GHG-NH_2 1/1 system at pH 11.04 after 1 day (red) and 6 days (black) of preparation. The hydrolysis of C-terminal amide ($-CONH_2 \rightarrow -COOH$) resulted in the increase of molecular weight by 0.984 units. (taken from [151])

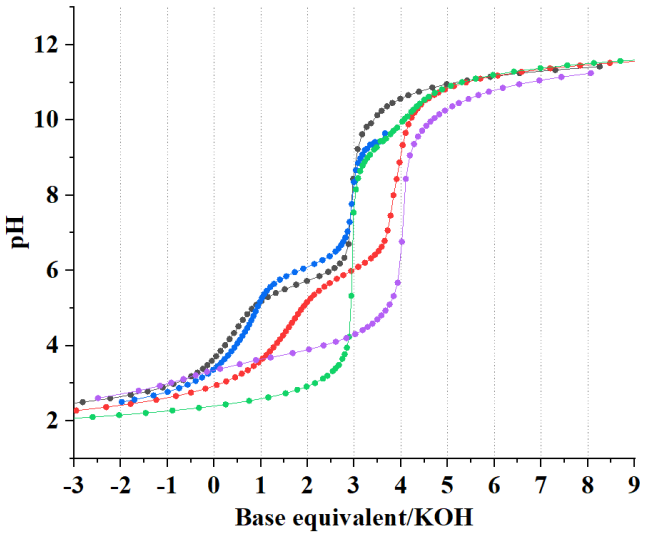

Figure A7. Titration curves of the [(Cp*)$Rh^{III}Cl_3$] at 1:1 metal-to-ligand ratio of ● carcinine, ● Carnocine, ●TRH, ● Histidine, ● GHK systems as a function of added base equivalent relative to the ligand.

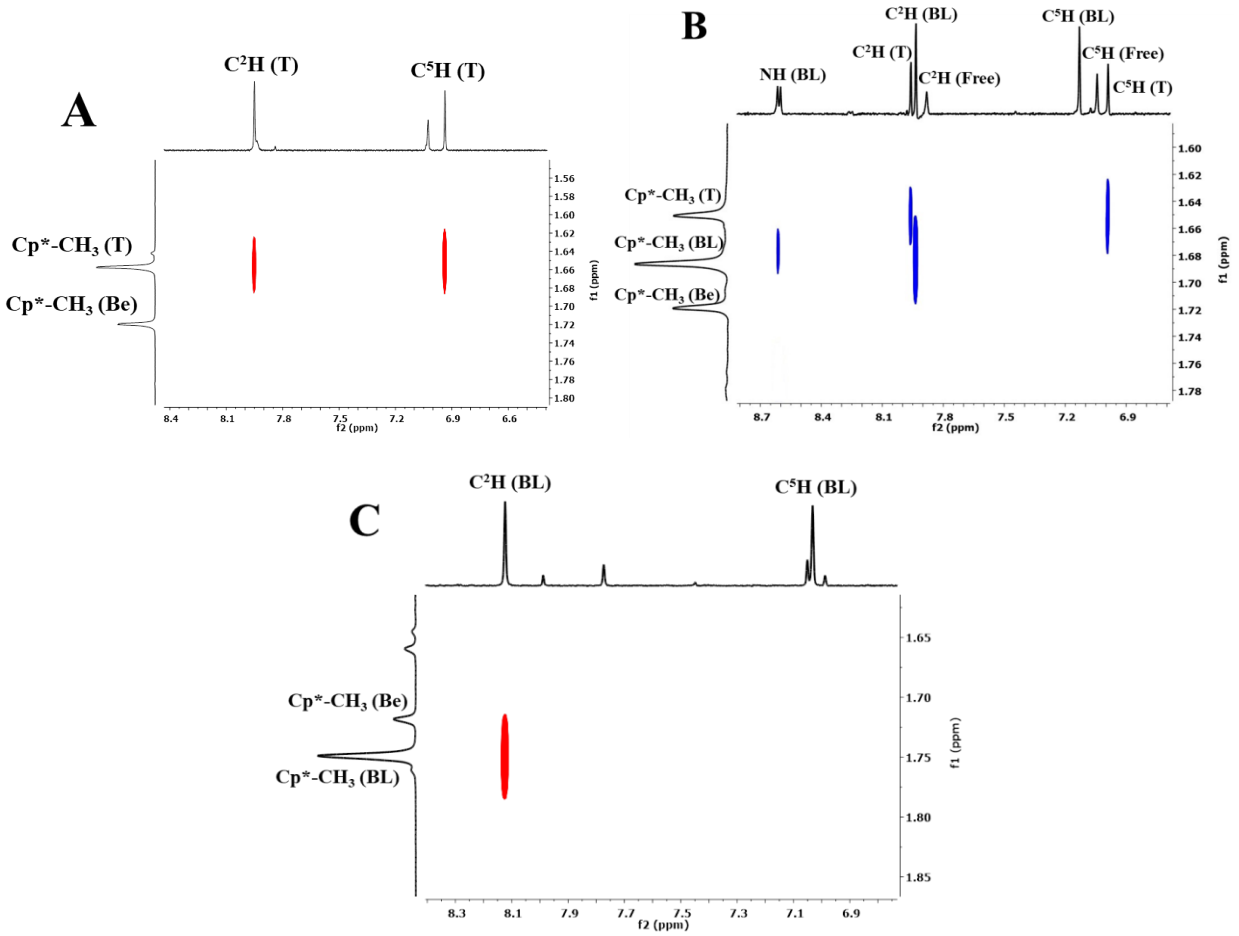

Figure A8. Parts of NOESY spectra of the (Cp*)Rh(III)-**L**[13]-en (A), (Cp*)Rh(III)-**L**[16]-en (B), (Cp*)Rh(III)-**L**[12]-en (C) ternary 1:1:1 systems at pH 7.40 (T, Be and BL denote ternary complexes, binary complexes of en, and binary complexes of histidine peptides, respectively).

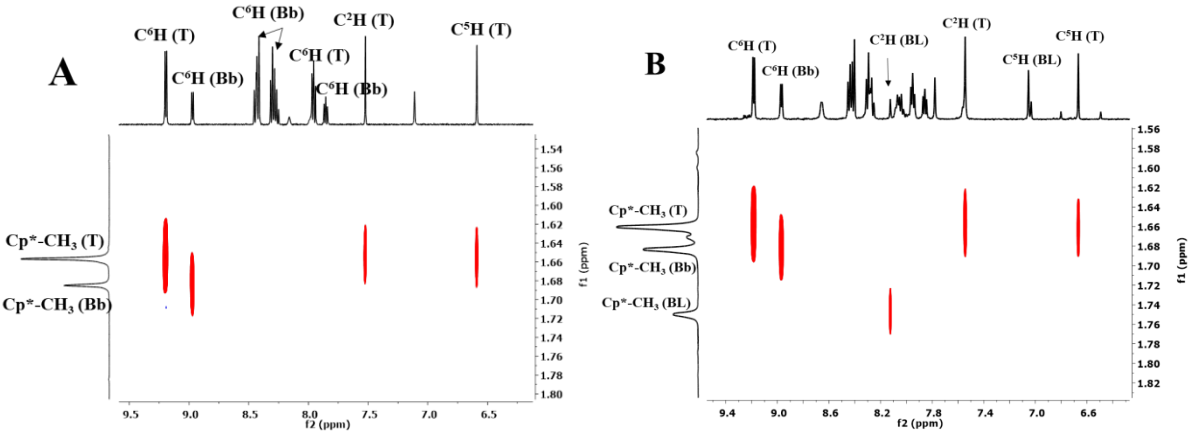

Figure A9. Parts of NOESY spectra of the (Cp*)Rh(III)-**L**[13]-bpy (A), (Cp*)Rh(III)-**L**[12]-bpy (B) ternary 1:1:1 systems at pH 7.40 (T, Bp and BL denote ternary complexes, binary complexes of bpy and binary complexes of histidine peptides, respectively).

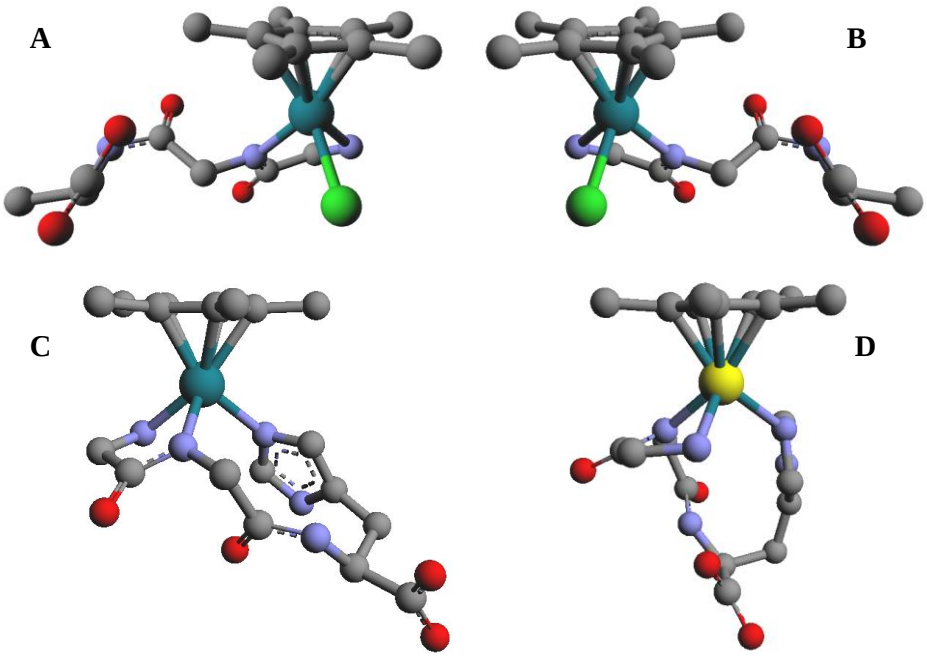

Figure A10. Optimized structures of $MH_{-1}\mathbf{L}^{6}$ $S_{Rh}S_{\alpha C}$ (A) and $R_{Rh}S_{\alpha C}$ (B), as well as $MH_{-1}\mathbf{L}^{6}$ $R_{Rh}S_{\alpha C}$ (C) $S_{Rh}S_{\alpha C}$ (D) diastereomers. Note that in structure D the rhodium(III) ion lies significantly out of the plane determined by the imidazole ring. (taken from [151])

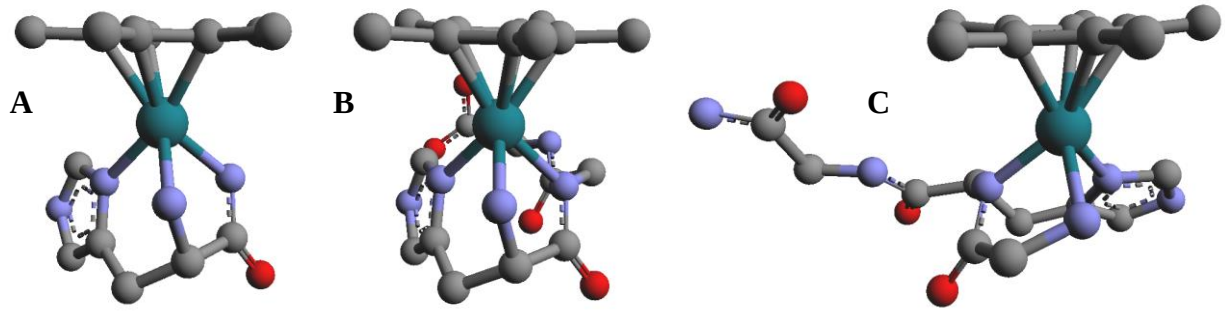

Figure. A11 Optimized structures of the $R_{Rh}S_{\alpha C}$ diastereomers of $MH_{-1}\mathbf{L}^{8}$ (A), $MH_{-1}\mathbf{L}^{8}$ (B) and $MH_{-1}\mathbf{L}^{10}$ (C) species. (taken from [151])

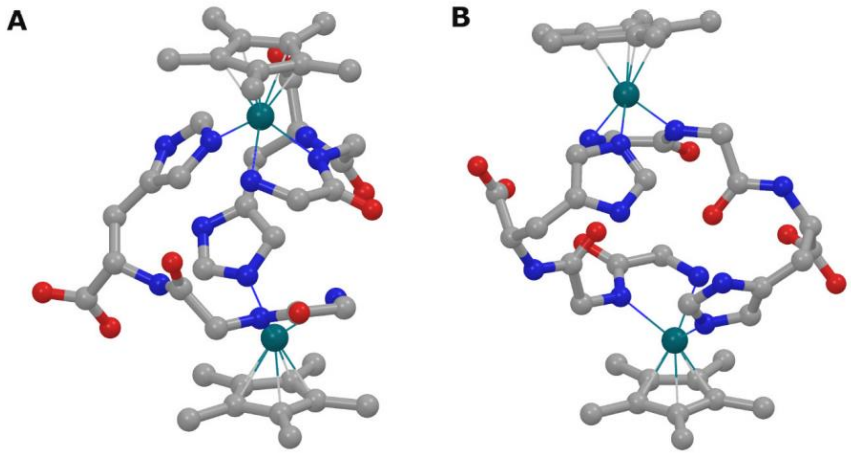

Figure A12 Optimized structures of the $R_{Rh}S_{\alpha C}/R_{Rh}S_{\alpha C}$ (A) and $R_{Rh}S_{\alpha C}/R_{Rh}S_{\alpha C}$ (B) diastereomers of the dimer $(MH_{-1}\mathbf{L}^{7})_2$ complex. Note that the rhodium(III) ions with S configuration (B) lie significantly out of the imidazole plane, similarly to the related monomeric $S_{Rh}S_{\alpha C}$ diastereomer (Fig. A10D). (taken from [151])

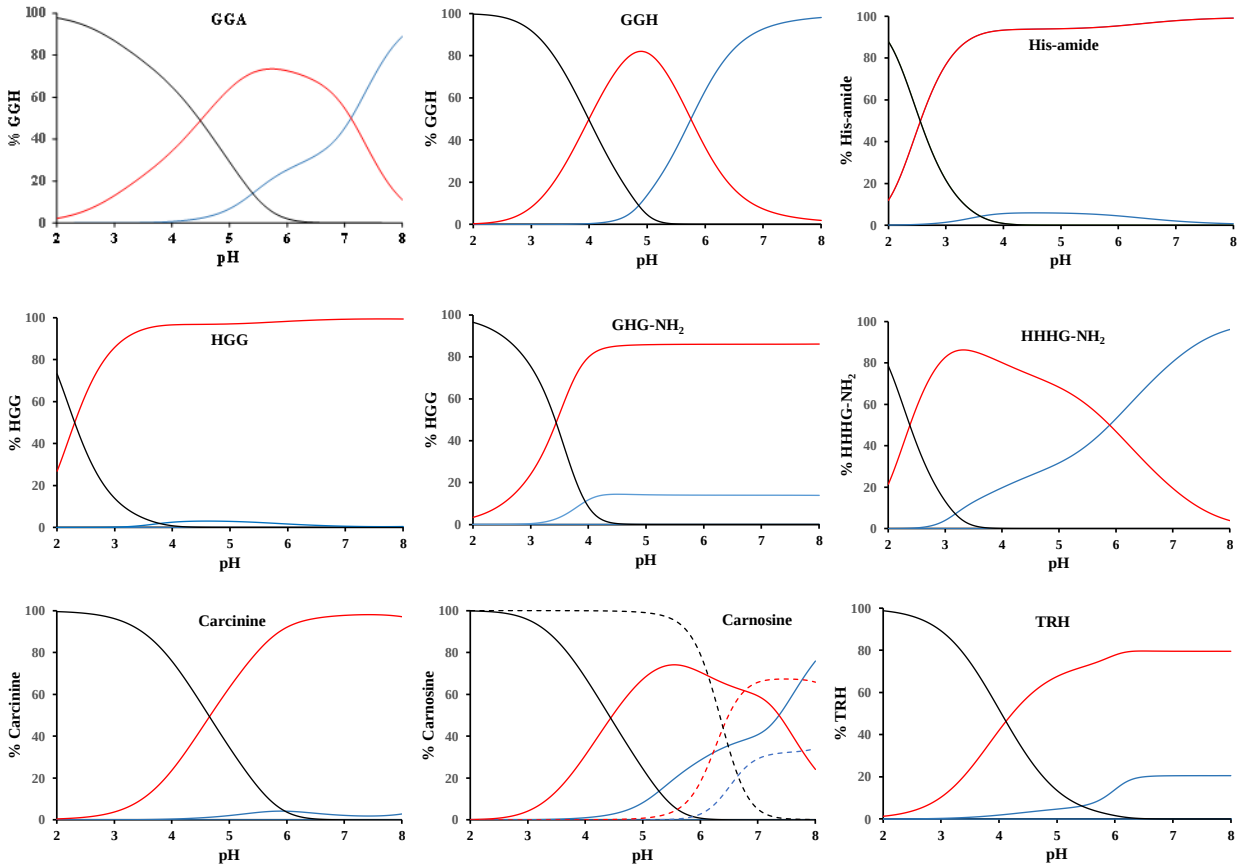

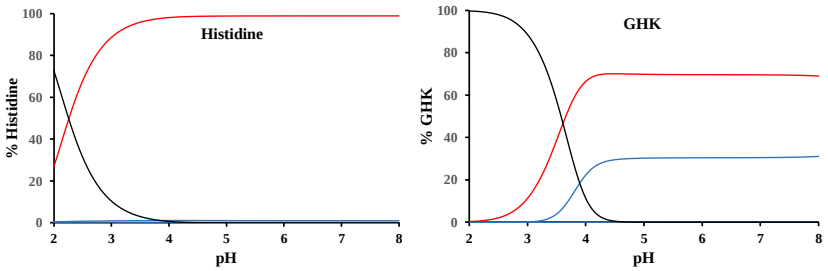

Figure A13 Predominance diagrams of the (Cp*)Rh(III)-Cu(II)-peptide 1/1/1 system at [peptide] = 1 mM (continuous lines) and [peptide] = 1 μM (dashed lines) concentrations

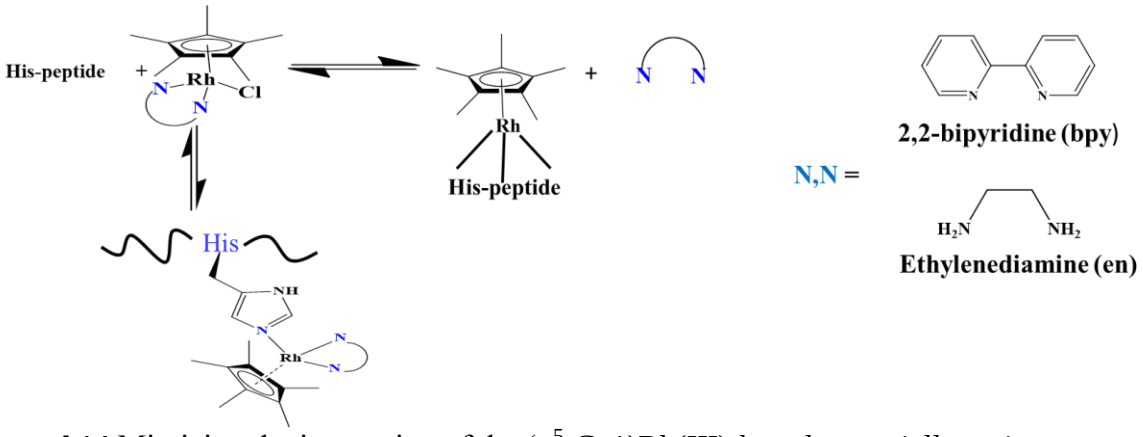

Figure A14 Mimicing the interaction of the (η^5-Cp*)Rh(III)-based potentially anticancer or drug delivery agents with peptides

Table A1. The concentrations of the studied systems, when the ROS production was followed by the oxidation of ascorbic acid ($c_{init.}$ = 100 µM). (taken from [[122])

	Cu(II)	Aβ		Ligand		Zn(II)	I
1.	-	-	-	EDTA	0µM-10µM	-	0.12 NaCl
2.	0-10 µM	-	-	-	-	-	-
3.	0-10 µM	-	-	-	-	-	0.12 NaCl
4.	10µM	-	-	-	-	10-1000 µM	0.12 NaCl
5.	10µM	1-16	0-30 µM	-	-	-	0.12 NaCl
6.	10µM	1-16	12 µM	-	-	5-1000 µM	0.12 NaCl
7.	10µM	1-40	0-30 µM	-	-	-	0.12 NaCl
8.	10µM	-	-	L*	20µM	-	0.12 NaCl
9.	10µM	1-16	12 µM	L*	20µM	-	0.12 NaCl
10.	10µM	1-16	12 µM	L*	20µM**	-	0.12 NaCl
11.	10µM	1-40	12 µM	L*	20µM	-	0.12 NaCl
12.	10µM	1-40	12 µM	L*	20µM**	-	0.12 NaCl
13.	10µM	-	-	PMPA	2-50µM	-	0.12 NaCl
14.	10µM	-	-	DPMGA	2-50µM	-	0.12 NaCl
15.	10µM	1-16	12 µM	PMPA	2-50µM	-	0.12 NaCl
16.	10µM	1-16	12 µM	DPMGA	2-50µM	-	0.12 NaCl

* The following ligands were studied (see SI-Chart 2): IDPA, NTA, GlyHis, DIEN, TREN, DPA and ENDIP.
** Delayed addition of ligands were applied.